University of Nottingham

PhD thesis

On the use of laser sources for microstructure modification, melting, and deposition of thermal barrier coatings

Author:
Dmitrii Ushmaev

This dissertation is submitted for the degree of
Doctor of philosophy

Faculty of Engineering

July 2023

Abstract

One of the most innovative technologies in the area of non-conventional machining, which is now used in a wide range of sectors, is laser processing. For the machining of difficult-to-cut materials like nickel superalloy and ceramic thermal barrier coatings (TBC), laser processing and pulsed laser ablation have been acknowledged as a practical processing technique in the aerospace industry. Thanks to its non-contact nature and ease of miniaturisation and delivery, laser become a desirable tool for material processing in difficult to access areas. Lasers, combined with a specially designed robotic carrier, may allow on-wing maintenance of turbine aero-engines.

One of the main reasons for engine overhaul is TBC spallation and oxidation of the components over the acceptable limits. To date, this results in a full replacement of the part and engine downtime. As a result, significant efforts have been made to address durability of the coatings by alternating coating composition and deposition methods. While durability of the coatings address the frequency of necessary repairs, on-wing coating application contributes to the duration of maintenance, and the ability to apply TBC on-wing has been recently demonstrated with the aid of combustion flame spraying process at the Nottingham UTC in On-Wing and Manufacturing Technologies. This study continues the trend in on-wing engine maintenance and is dedicated to addressing the problems with engine downtime.

Firstly, this study is dedicated to the development of a TBC modification technology. Inspired by the durable coatings produced by vapour deposition, its microstructure was attempted to replicate on a thermally sprayed coating with the aid of pulsed lasers. Vapour-deposited coatings are known for their better thermal cycling performance and resistance to erosion. In this work, columnar microstructure has been replicated with an array of laser-machined grooves. The next step of optimisation addresses resistance to abrasive action and chemical interactions by providing the coating with a dense continuous surficial layer. In order to asses the durability characteristics, the coating was compared against the state-of-the-art thermally sprayed coating in simulated in-engine environment.

Secondly, particular attention was paid to the solidification phenomena in laser melted TBC. Unusual behaviour of crystal growth, here referred to as ”grain surface sealing” and ”grain bending”, has been identified. While this may present an advantageous microstructure for various materials, e.g. to locally change crystal orientation dependant properties or guide microcrack propagation by adjusting the

grain boundary geometry, currently existing models fail to explain these phenomena. The responsible mechanism for both phenomena was identified as planar and dendritic grain growth modes. Therefore, by addressing both planar and dendritic solidification within a single model one can predict and control the grain bending and grain surface sealing phenomena. As a result, a predictive multi-scale model of solidification has been build with the example of laser-melted TBC. For this purpose, a three-dimensional finite-element thermo-capillary model has been developed, predicting the temperature distribution within the workpiece, which was coupled with a three-dimensional grain growth model based on cellular automata approach.

Thirdly, the possibilities of coating application with the aid of laser tool have been investigated. Current vapour deposition techniques are hardly suitable for on-wing coating application due to vacuum requirements, difficult to implement in-situ. In an effort to find a novel suitable deposition technology, various possibilities for coating generation in atmosphere have been identified and developed. While the properties of such coating are a subject for further optimisation, the main focus of this section is to study formation of the coating microstructure and interaction between the laser and absorbing target material. Two potential options for on-wing coating application with a laser source have been found and discussed. Resultant microstructures, possible formation mechanisms, and laser-material interaction in different deposition scenarios have been analysed and presented.

Keywords: laser-matter interaction, laser machining, laser melting, grain growth, liquid droplet laser deposition, atmospheric vapour laser deposition, cellular automata, dendritic growth

Acknowledgements

This thesis is the result of work of many people. I would like to express my gratitude to Prof. Dragos Axinte and Dr. Zhirong Liao who has always been interested in my work and available for discussions. I would also like to thank Prof. Tanvir Hussain and Prof. Paul Mativenga for the interesting discussion during my Ph.D. Viva and their helpful comments about the thesis. I also thank Dr. James Kell, Dr. Andy Norton, and Dr Gyaneshwara Brewster for sharing their industrial perspective on my research subject, providing the samples and helping out with tests.

Special thanks to my mother Natalia Ushmaeva and father Igor Ushmaev for being a constant source of support and encouragement, and to all of my special friends in Nottingham. Thanks to all of you!

Contents

Contents iv

List of Figures v

List of Tables vi

List of Symbols vii

1 Introduction 1
- 1.1 Motivation . . . 1
- 1.2 Research Problem . . . 6
- 1.3 Objectives of the study . . . 9

2 Literature Review 11
- 2.1 Thermal Barrier Coating system . . . 12
  - 2.1.1 TBC composition . . . 13
    - Substrate . . . 13
    - Topcoat . . . 14
    - Bondcoat and thermally grown oxide . . . 18
  - 2.1.2 Topcoat microstructure . . . 19
  - 2.1.3 TBC deposition methods . . . 21
    - Thermal spray techniques . . . 21
    - Vacuum deposition processes . . . 26
    - Other deposition techniques . . . 30
  - 2.1.4 Coating adhesion . . . 34
- 2.2 TBC degradation mechanisms . . . 36
  - 2.2.1 Oxidation and TGO spallation mechanisms . . . 38
  - 2.2.2 Sintering effects . . . 40
  - 2.2.3 Phase stability of topcoat materials . . . 40
  - 2.2.4 Effect of residual stresses on coating durability . . . 40
  - 2.2.5 Molten silicates penetration . . . 41
    - CMAS mitigation techniques . . . 43
  - 2.2.6 Foreign object damage (FOD) and coating erosion . . . 43
  - 2.2.7 Thermal barrier coating system modification techniques . . . 44
    - Pre-deposition TBC modification and modified deposition processes . . . 45
    - Post-deposition modification . . . 48
- 2.3 Laser Beam Processing . . . 51

2.3.1 Pulse length and physical process of material removal 51
2.3.2 Material removal mechanisms in laser ablation 53
2.3.3 Typical defects in continuous wave, long, and short pulse ablation 55
Recast layer and spattering 55
Microcracking 58
Hardness 60
Residual Stresses 60
2.3.4 Ultrashort pulse laser ablation for material removal 62
2.4 Fundamentals of solidification 64
2.4.1 Heat and fluid transport modelling 64
2.4.2 Modelling of laser melting for microstructure prediction 67
Phase Field Method 67
Stochastic Method 68
Cellular Automata Method 70
Thermal Gradient Method 70
2.5 Summary of the literature 71
2.5.1 Research challenges emerging from the literature review 72
Research Challenge 1 - Modification of thermal barrier coating microstructure for increased coating performance . . 72
Research Challenge 2 - Performance assessment and microstructure characterisation of laser modified thermal barrier coatings 73
Research Challenge 3 - Investigation of grain growth phenomena in laser-melted topcoats through modelling 74
Research Challenge 4 - Development of topcoat deposition technique in atmospheric pressure via a laser source . 75

3 Methodology **77**
3.1 Description of laser equipment 78
3.1.1 Laser sources 79
Continuous wave laser 79
Nanosecond pulsed laser 82
Picosecond pulsed laser 83
3.1.2 Beam and stage manipulation 84
3.1.3 Beam characterisation 85
Power meter 85
Beam profiler 86
3.2 Workpiece materials 87
3.2.1 Substrate 87
3.2.2 Thermal barrier coating system 88
3.3 Material analysis techniques 89
3.3.1 Metallographic preparation 89
3.3.2 Surface analysis 90
White light interferometry 90

3.3.3 Microstructural analysis . . . 92
Scanning electron microscopy and energy dispersive spectroscopy . . . 92
Electron back-scatter diffraction . . . 94
X-Ray crystallography . . . 96
3.3.4 Coating performance assessment techniques . . . 98
Thermal fatigue . . . 98
Erosion resistance . . . 98
CMAS infiltration . . . 99

4 TBC microstructure modification through laser ablation and laser melting approach 102
4.1 Introduction . . . 103
4.2 Theoretical aspects related to the improvement of thermomechanical compliance . . . 106
4.3 Laser grooving of thermal barrier coating system . . . 109
4.3.1 Ultrashort pulse laser grooving . . . 110
4.3.2 Short pulse laser grooving . . . 117
4.4 Laser glazing of thermal barrier coating system . . . 121
4.4.1 Laser melting process . . . 121
4.4.2 Optimised laser melting approach for continuous coverage of grooved TBC . . . 126
4.5 Summary . . . 128

5 Performance assessment and microstructure characterisation of laser modified thermal barrier coatings 131
5.1 Introduction . . . 132
5.2 Results and Discussion . . . 133
5.2.1 Effect of laser melting on surface roughness . . . 133
5.2.2 Resistance of the coatings to erosion . . . 134
5.2.3 Erosion mechanisms, microstructure, and morphology . . . 137
5.2.4 X-Ray diffraction analysis of the topcoat after erosive impact . 143
5.2.5 CMAS infiltration tests . . . 147
5.2.6 Thermal cycling tests . . . 152
5.2.7 Failure mechanics in as-sprayed and modified coatings and future outlook . . . 155
5.2.8 X-Ray diffraction analysis of the topcoat after thermal fatigue tests . . . 158
5.3 Summary . . . 161

6 Understanding microstructure formation within the glazed layer 163
6.1 Introduction . . . 164
6.2 Theoretical background of the interface stability . . . 169
6.3 Modelling approach for combined planar – dendritic growth . . . 171
6.3.1 Thermo-capillary model details . . . 172
6.3.2 Grain growth model of laser glazing of YSZ . . . 176
Nucleation model . . . 177

Mesoscopic dendritic and planar growth model . . . 177
Dendritic growth model for tetragonal crystals . . . 178
Planar growth model for the representation of the stable interface . . . 179
Coupling method for planar and dendritic models . . . 181
6.4 Experimental Methods . . . 182
6.5 Results and Discussion . . . 183
6.5.1 Influence of fluid flow on melt pool geometry . . . 183
6.5.2 Vertical columnar growth and horizontal columnar growth . . . 185
6.5.3 Morphology analysis and its influence on the crystal microstructure . . . 189
6.6 Summary . . . 193

7 Exploring new methods for local coating deposition 195
7.1 Introduction . . . 196
7.1.1 Initial experiments: spiral path and crack suppression in laser melting . . . 197
7.1.2 Substrate-to-substrate TBC re-deposition in atmospheric pressure . . . 203
7.1.3 High-speed imaging of laser-substrate interaction . . . 210
7.2 Experimental methods . . . 214
7.2.1 Substrate and target materials . . . 215
7.2.2 Deposition rig design . . . 216
Deposition rig v1: conductive heating design . . . 217
Deposition rig v2: radiative heating design . . . 217
7.3 Results and Discussion . . . 219
7.3.1 Initial deposition results (Deposition rig v1) . . . 219
Droplet deposition . . . 219
Whisker formation . . . 220
7.3.2 High-speed imaging of laser-target interaction . . . 224
7.3.3 Liquid droplet laser deposition (LDLD) method . . . 228
7.3.4 Atmospheric Vapour Laser Deposition (AVLD) method . . . 237
7.4 Summary . . . 244

8 General Conclusions 247
8.1 TBC microstructure modification through laser ablation and laser melting approach . . . 247
8.2 Performance assessment and microstructure characterisation of laser modified thermal barrier coatings . . . 248
8.3 On the importance of interface stability in cellular automata models: planar and dendritic solidification in laser melted YSZ . . . 250
8.4 Laser deposition in atmospheric pressure . . . 251

9 Future Work 252
9.1 TBC microstructure modification through laser ablation and laser melting approach . . . 252

9.2 Performance assessment and microstructure characterisation of laser modified thermal barrier coatings 253
9.3 On the importance of interface stability in cellular automata models: planar and dendritic solidification in laser melted YSZ 255
9.4 Laser deposition in atmospheric pressure 256

List of Figures

1.1 Evolution of Overall pressure Ratio in Rolls-Royce gas-turbine engines. Adapted from [73] . . . 2
1.2 Temperature and pressure distribution in Low Pressure Compressor(LPC), High Pressure compressor(HPC), followed by combustion chamber, High Pressure Turbine (HPT), Intermediate Pressure Turbine (IPT), and Low Pressure Turbine (LPT). Rolls-Royce Trent 800 Jet Engine. [294] . . . 3

2.1 Example of TBC application on a dynamic component. Cutaway view of Engine Alliance GP7200 aircraft engine, a photograph of a turbine blade (10cm long) with TBC from the high-pressure hot section of an engine, and a scanning electron microscope (SEM) image of the TBC cross-section. [52] . . . 12
2.2 Evolution of turbine entry temperature. [175] . . . 13
2.3 Variations in tetragonal allotropes of ZrO_2 according to their cell parameters. [329] . . . 15
2.4 (a) ZrO2–Y2O3 phase diagram.(b) YSZ phase diagram including stable and metastable boundary lines [329] . . . 17
2.5 Cross-section of (a) Atmospheric Plasma Sprayed Coating and (b) Electron beam physical vapour deposited thermal barrier coatings. [221] . . . 19
2.6 Morphology of EB-PVD P-YSZ TBCs in polished (left) and fractured cross-section (right) in as coated condition. [280] . . . 20
2.7 Comparison of different thermal spray processes in terms of particle velocity and temperature. [172] . . . 22
2.8 Schematic of Atmospheric Plasma Spray process and governing process parameters. [86] . . . 23
2.9 Classification of solid-solid particle interaction in terms of impact velocity and particle diameter.[172] . . . 26
2.10 Electromagnetic alignment in EB-PVD system. Modified schematics from [121] . . . 28
2.11 Schematics of a thermal CVD process.[372] . . . 29
2.12 Different routes and stages of the sol-gel technology. [368] . . . 31
2.13 Direct Laser Deposition for coating application. [368] . . . 32
2.14 Laser Assisted Pulsed Laser Deposition experimental setup [231] . . . 33

2.15 Columnar structure of YSZ, achieved by pulsed laser deposition in atmospheric pressure. (a) ion-beam milled cut for patch repair; (b) deposited columnar microstructure. [231] 34
2.16 Major failure categories of thermal barrier coatings [75] 38
2.17 Edge delamination and large scale buckling as a function of TBC modulus anisotropy [75] 39
2.18 The effect of deposition temperature on (a) residual stress at the coating surface and (b) elastic modulus [374] 42
2.19 Microstructure of 7YSZ TBC column tips infiltrated by synthesized CMAS at 1260°C for 4.25hrs. [241] 42
2.20 A schematic diagram of the failure modes for an APS and EB-PVD TBC.. [221] 44
2.21 Schematic of the orientation and dimensions of the 2D pores. [182] . . 46
2.22 Cross-sectional SEM morphology of laser-textured coatings. [64] . . . 49
2.23 Typical optical cross-sectional microstructure of TBCs: (a) plasma-sprayed; (b) laser-glazed. [317] 50
2.24 Long (a) and ultrashort (b) pulse laser ablation. Nanosecond and longer pulses do not prevent heat propagation and thermal effects, leading to heat-affected zone and collateral workpiece material damage [27]. (Typical removal mechanisms via long pulse ablation [80]: (c) melting and vaporisation, (d) melt displacement, caused by recoil pressure, and (e) melt ejection. 52
2.25 Surface imperfections in percussion drilling. (a)-(c) recast layer, oxidation and HAZ of nickel superalloy (Nimonic 263) [284] ; (d) cracking of the recast layer [49] ; (e), (f) recast layer and surface debris on Al-Si alloy after 5(e) and 100 (f) pulses [181]; (g) solidified microdroplets and vapour on the sides of the hole due to fragmentation and recondensation [350] ; (h) and (i) HAZ and recast layer after 5 and 50 nanosecond pulses on titanium surface [112] 56
2.26 SEM micrographs showing the typical spatter formation (plan view) of holes drilled with (a) oxygen assist gas and (b) argon assist gas[195] 57
2.27 Different grain morphologies found in the recast layer of laser-drilled Ni-superalloy. (a), cellular morphology of the recast [91]; (b) dendritic microstructure [90]; (c) and (d) fine columnar and equiaxed grains [358] 58
2.28 Surface integrity defects formed during laser drilling of Ni superalloys. (a) Cracks in the recast layer [9]; (b) transverse cracks in the oxide layer[136]; (c) longitudinal cracks in the oxide layer[136] 59
2.29 (a) Kerf surface micrograph of laser trepan drilled Ti–6Al–4V with a CO2 laser[363]; (b) distribution of in-plane residual stresses [199] . . 61
2.30 Micrographs of the laser-drilled holes on steel with long, short and ultrashort pulses. The pulse widths are (a) 3.3 ns, (b) 80 ps, and (c) 200 fs [245] 62
2.31 Percussion-drilled hole in Al-Mg alloy in the air with a femtosecond laser, revealing melt formation and hot cracking[66] 64

2.32 3D phase-field computation of polycrystalline equiaxed solidification of Ni-based superalloy [360]. 69
2.33 Microstructures of Laser Engineered Net Shaping additively produced stainless steel 304L. (a) EBSD measurement, (b) kinetic Monte Carlo simulations, and (c) conformal finite element mesh [81] 69

3.1 Organisation of methodology section 77
3.2 characteristic timescale of different processes. [311] 78
3.3 CW laser and its optical path 80
3.4 Possible fibre architecture for high-power application 81
3.5 Working principle of SPI-G3 fibre laser 82
3.6 (a) Relationship of pulse energy, average power, and pulse repetition frequency for the SPI-G3 fibre laser [321]; (b) Possible waveforms and the corresponding temporal profile of the SPI-G3 fibre laser [321] . . 83
3.7 Beam and sample manipulation systems, including galvoscanner and motorised stage. 85
3.8 Example of the raw intensity profile of defocused SPI-G3 laser having a Gaussian beam distribution measured with the CMOS beam profiler. The colour legend represents the normalised intensity. 86
3.9 Microstructure of as-sprayed TBC comprised of bondcoat and topcoat, covering a flat superalloy material. (a) Darkfield optical micrograph of the coating cross-section; (b) SEM image of the topcoat fracture surface revealing the lamellar structure of APS coating. 89
3.10 Schematic diagram of a white-light interferometer [290] 91
3.11 Schematic view of EBSD technique in the SEM environment, where the electrons are focused on a tilted sample, and diffraction pattern is collected on a detector plane. ND denotes the sample's normal orientation, and PC shows the pattern centre of the diffracted signal. 94
3.12 (a) direct diffraction pattern from the lattice on the phosphorus screen and (b) Hough space transformation of diffracted lines 95
3.13 (a) Cross-section view of X-ray interaction with crystal lattice and the Bragg equation below [29] (b) testing chamber of Bruker D8 Discover diffractometer. 97
3.14 Schematic diagram of the erosion test rig. 99
3.15 (a) Morphology of natural sand [100] and (b) AFRL 03 sand with size distribution typically entering the engine level [100](c) Schematics of CMAS infiltration along discontinuities, such as cracks, splat interfaces, and grain boundaries. 100

4.1 Key steps to enable pseudo-columnar architecture of the coating: (a) as-sprayed topcoat with pronounced thermal expansion mismatch stresses at the topcoat-bondcoat interface; (b) introduced grooves govern the in-plane Young's modulus of the coating minimising thermal expansion mismatch stresses; (c) coating with a dense top surface, resistant to mechanical impacts and reduced oxygen short path. 105

4.2 Schematic representation of thermal barrier coating modification. (a) thermally sprayed coating; (b) laser grooving via pulsed laser; (c) laser glazing via continuous or pulsed laser. 109
4.3 In-plane Young's modulus control through picosecond ablation of topcoat and incubation effect in picosecond laser texturing after 75 laser passes. (a) ablation with various scanning speeds, showing the selectiveness of topcoat removal. (b), (c): magnified topcoat-bondcoat interface showing no visible traces of bondcoat ablation; image (d) shows a light level of bondcoat ablation and (e) - unacceptable through-bondcoat cut with the affected substrate. Feature (I) shows the redeposited bondcoat after ablation. EKSPLA picosecond laser, PRF 4kHz, average power 1.2W 112
4.4 Influence of scanning speed and number of the line passes with picosecond laser ablation. EKSPLA picosecond laser, PRF 4kHz, average power 1.2W 114
4.5 Influence of high linear energy density input (6.8 J/mm^2) on the microstructure. (a) Low magnification image showing groove geometry; (b) high magnification of the groove tip. EKSPLA picosecond laser, PRF 4kHz, average power 1.2W, 5mm/s, 10 passes. Insert P1 from Fig. 4.4. 115
4.6 Selective YSZ removal with picosecond laser ablation applied to thermal barrier coatings. EKSPLA picosecond laser, PRF 4kHz, average power 1.2W,, 25 passes, 5mm/s (right) and 10mm/s (left). Insert P2 from Fig. 4.4. 115
4.7 Selective removal with 50 passes at varied scanning speeds, insert P3 from Fig. 4.4. (a) υ_s 40mm/s indicated with yellow arrow, υ_s 30mm/s indicated with green arrow, 10mm/s indicated with red box; 5mm/s indicated with green box. (b) high magnification insert of υ_s 20mm/s emphasising clear bondcoat-topcoat separation indicated with a green arrow; (c) high magnification insert of υ_s 10mm/s revealing a void between the layers. Red arrows indicate the assumed ray traces. EKSPLA picosecond laser, PRF 4kHz, average power 1.2W, 50 passes. 116
4.8 Influence of focal offset distance (FOD) on the groove geometry. EKSPLA picosecond laser, PRF 4kHz, average power 1.2W, 75 passes, scanning speed 25mm/s. 117
4.9 Process stability at a different number of scanning passes (indicated as "rep."). EKSPLA picosecond laser, PRF 4kHz, average power 1.2W; 50, 50, 90 passes, scanning speed is 25mm/s. 117
4.10 Cross-sectional SEM micrograph of thermal barrier coating system after nanosecond ablation. Scanning speed was varied in range 900 m/s to 50 m/s. (a) 10 passes; (b) 40 passes; (c) 50 passes. SPI G3 nanosecond laser. 118

4.11 Insert "n2" from Fig. 4.10 with 50 laser laser passes; scanning speed is (a) 200, 100, and 50mm/s. (b) High magnification micrograph of the tip of the laser ablated groove with 50mm/s scanning speed revealing thermal damage to the TBC. 119
4.12 Insert "n3" from Fig. 4.10 with 50 laser laser passes; scanning speed is 800mm/s. (b) High magnification micrograph of the groove revealing melting of the TBC. SPI G3 nanosecond laser. 120
4.13 Dark field optical microscopy of the TBC top surface showing defects in the laser melting process of YSZ topcoat typical for (a) high and (b) low heat input conditions. SPI RedEnergy CW laser, average power is 88W, spot size is 400 μm, laser scanning speed is (a) 2.5 mm/s and (b) 75 mm/s. 123
4.14 (a, c) Bright field Nomarski and (b) dark field optical microscopy of the TBC top surface showing coexisting planar and dendritic grains. SPI RedEnergy CW laser, the average power is 88W, spot size is 400 μm, the laser scanning speed is 25 mm/s. 124
4.15 Bright field microscopy of TBC top surface showing discontinuous melting. SPI RedEnergy CW laser, the average power is 88W, spot size is 400 μm, the laser scanning speed is 50 mm/s, the track pitch is 320 μm 125
4.16 Illustration of the strategy for continuous laser glazing of the thermal barrier coating. 126
4.17 Bright field microscopy of TBC top surface showing continuous melting. SPI RedEnergy CW laser, the average power is 88W, spot size is 400 μm, the laser scanning speed is 50 mm/s (pass 1) and 37.5mm/s (pass 2), and the track pitch is 320 μm 126
4.18 Compliant thermal barrier coatings with laser-ablated grooves sealed with a continuous layer. SEM image of cross-section (a) and fracture surface (b) showing the array of grooves and vertical microcracks aligning with the grooves. Optical images of the top-view in (c) dark-field mode and (d) bright field with Nomarski prism. 127
4.19 Optical transmittance spectrum of single-crystal YSZ [344]. 130

5.1 Surface topology of (a) as-sprayed and (b) laser-melted thermal barrier coating, showing significant reduction in surface roughness. . . 133
5.2 Average surface height of the samples after erosion tests in different conditions. (a) as-sprayed and (b) laser-modified samples. The light blue region of the 50% confidence interval (P value > 50%). 136

5.3 Microstructure analysis of as-sprayed sample after erosive particle impact via back-scattered SEM observations. (a) top view of the U2 sample, revealing splat decohesion; (b) magnified view of (a). (c) top view of U3 sample under low-magnification conditions. Dark surface indicates the bondcoat, and white coating is the top coat; (d) cross-section of U3 sample close to the centre of the erosive impact; (e) cross-sectional high magnification view of the surficial layer of U2 sample revealing surficial microcracking after erosion; (f) cross-sectional high magnification view of the sub-surficial layer of U2 sample revealing internal microcracking within the splat. 138
5.4 Microstructure analysis of laser modified sample after erosive particle impact via (a), (c)-(f): back-scattered and (b): secondary SEM observations. (a) polished cross-section after erosion of the L2 sample. Yellow arrows indicate eroded regions and red arrows indicate rounding of sharp edges at the solidification crack interfaces which initially resulted from the glazing process; (b) top surface of L2 sample after laser erosive particle impact revealing crack separation and appearance of internal microcracks, indicated as "perpendicular microcracking"; (c) magnified view of the red box in (a), showing the deformed surface of L2 sample; (d) top surface observation of L3 sample with signs of erosion; (e) top surface of L3 sample showing the partially removed surficial layer, revealing the underlying columnar microstructure after laser glazing (f) high magnification image of the red region in (d), with bands at the cracked region. 140
5.5 Surface morphology of the modified samples after erosion test. (a) texture and (b) height map. 142
5.6 Low angle XRD diffraction analysis of (a) laser modified and (b) as-sprayed coating after erosion. Notations 0, 1, 2, and 3 correspond to the samples after the impact of 0g (before erosion), 150g, 250g, and 400g, respectively. The blue arrow in (a) indicates an asymmetrical broadening of the peak. Blue and purple arrows in (b) indicate the central 2Θ angle of the U_0 and U_3 and peaks, respectively. 144
5.7 High angle XRD diffraction analysis of (a) laser modified and (b) as-sprayed coating after erosion. Notations 0, 1, 2, and 3 correspond to the samples after the impact of 0g (before erosion), 150g, 250g, and 400g, respectively. Blue and purple arrows in (b) indicate the central 2Θ angle of the U_0 and U_3 and peaks, respectively. $K_{\alpha 2}$ indicates the peak from secondary XRD wavelength (no postprocessing was used). 146
5.8 CMAS infiltration test results after 24h at 1121^oC. Optical photograph of the top surface (a) sample after proposed modification technique and (b) as-sprayed sample. (c) furnace chamber after the CMAS test with an explosion of as-sprayed coating; (d) SEM micrograph of the remaining as-sprayed coating; (e) modified structure after CMAS interaction. 148

5.9 Elemental analysis of the remained coating after CMAS infiltration into the as-sprayed coating. (a) SEM micrograph; (b) Si map showing homogeneous infiltration of silicon into the topcoat; (c) Al distribution map, showing Al depletion and formation of TGO; (d) Oxygen elemental map 149
5.10 Analysis of as-sprayed coating after CMAS interaction. SEM micrograph of (a) delaminated fragment of the coating after CMAS infiltration; high magnification image of the (b) top surface and (c) area close to the spallation interface, showing the interactions between CMAS and as-sprayed coating 150
5.11 (a) SEM image of the modified sample after CMAS test. red arrow indicates meniscus. (b) Si elemental map, showing infiltration of silicon through the porous part of the coating; (c) Zr elemental map; (d) Na elemental map; (e) Ca elemental map; (f) Mg elemental map. Yellow arrows indicate the high Ca-Mg concentration within the CMAS. 151
5.12 Radiation recorded during the cooling part of the thermal cycle shortly after the end of the heat exposure. Based on the part of the coating emitting light, coating adhesion to metallic substrate was evaluated. Amber arrows note samples close to failure, red arrows show the samples evaluated as failed. (a) 150 cycles; (b) 170 cycles; (c) 180 cycles; (d) 190 cycles; (e) 200 cycles; (f) 212 cycles; After 200 cycles, as-sprayed samples were removed from the furnace 153
5.13 (a) thermal cycling performance in isothermal tests of as-sprayed and laser modified samples. (b) optical picture after 200 cycles in the furnace with buckled laser-modified samples (labelled as L) and complete delamination of the topcoats of as-sprayed samples (labelled as U). Some of the topcoats were blown by air and changed their position. 154
5.14 Edge delamination and large scale buckling as a function of TBC modulus anisotropy [75] 155
5.15 Cross-sectional SEM micrographs of the as-sprayed sample after 185 cycles. (a) left, (b) middle, and (c) right sides of the coating 156
5.16 Cross-sectional SEM micrographs of laser-modified sample after 185 cycles. (a) left, (b) middle, and (c) right sides of the coating 156
5.17 Proposed failure mechanisms during thermal cycling of as-sprayed and modified coatings 157
5.18 Low angle XRD diffraction analysis of laser modified and as-sprayed coating after erosion. Notations 0, 160, and 185 correspond to the samples after 0, 160, and 185 thermal cycles, respectively. Blue and purple dashed lines indicate the central 2Θ angle of the U_0 and U_3 and peaks, respectively. 159

5.19 High angle XRD diffraction analysis of laser modified and as-sprayed coating after erosion. Notations 0, 160, and 185 correspond to the samples after 0, 160, and 185 thermal cycles, respectively. Blue and purple dashed lines indicate the central 2Θ angle of the U_0 and U_3 and peaks, respectively. $K_{\alpha 2}$ indicates the peak from secondary XRD wavelength (no postprocessing was used). 160

6.1 Grain inclination and grain bending in laser-melted YSZ observed in a transverse cross-section EBSD scan near the centre. Experimental conditions: SPI G3 laser, laser power 18W, scanning speed 2mm/s. . 165
6.2 Possible crystal morphologies as a function of temperature gradient G and growth rate R (adapted from Kou[161] and Kurz[173]). While low scanning speeds generally result in planar solidification front, with a constant thermal gradient the solid-liquid interface stability becomes disturbed with increasing scanning speed. As a result, the grain growth in a cellular or dendritic manner, until interface velocity reaches the velocity of absolute stability V_a. 171
6.3 (a) Laser glazing process of the workpiece material: heat absorption, phase change, surface tension-induced fluid flow within the melt pool. Modelling phenomena and the boundary conditions. (b) Schematic top view of solidification process during laser melting, depicting grain evolution across the solid-liquid interface. The solidification rate experiences its maximum at the trailing edge of the melt pool and can lead to the loss of interface stability. 173
6.4 Specific heat and thermal conductivity of YSZ [37] 176
6.5 Schematic representation of planar grain growth algorithm in variable heat flow conditions 181
6.6 Flowchart of grain growth modelling using combined planar-dendritic cellular automata route. 182
6.7 (a) Geometry of the melt pool with and without fluid motion within the pool. (b) Peclet distribution within the melt pool. Velocity vectors are shown in yellow. Energy density 10000 J/cm^2. 184
6.8 Micrographs of the top surface of the single track laser glazed thermal barrier coating at different laser scanning speeds: (a) 2.5mm/s, x5 magnification; (b) magnified backscattered SEM image of a marked region in a red box is shown in (a); (c) top surface of remelted track with a scanning speed of 25mm/s, x20 magnification and (d) x50 magnification of red box shown in (c). 186
6.9 Top view of modelled and experimental grain structure for scanning speed of (a) 2.5mm/s and (b) 25mm/s. 187
6.10 Illustration of the evolution of horizontal, vertical grains and grain surface sealing concept. (a) the top surface of the melt pool and solidification, indicating in-plane, or horizontal, columnar grains, and an area with vertically grown grains. (b) the cross-sectional sketch view. (c) EBSD of the transversal cross-section of track presented in Fig. 6.8c, showing vertical columnar grains and in-plane (horizontal) columnar grains. 189

6.11 Predicted solidification rate and morphology factor for scanning speeds (a-b) 2.5 mm/s and (c-d) 25mm/s; (e-f) stability of solid-liquid interface. Colorbars of morphology rates are shared for (a-b) and (b-c). 190
6.12 Grain evolution for (a) high energy density case (1000 J/cm2) and (b) moderate energy density case (100 J/cm2) 191
6.13 Grain boundaries and orientation map in longitudinal cross-sections (a) simulated microstructure; (b) EBSD scan. The corresponding energy density is 1000 J/cm^2. 192
6.14 Grain boundaries and orientation map in longitudinal cross-sections (a) simulated microstructure; (b) EBSD scan. The corresponding energy density is 100 J/cm^2. 193

7.1 An example of the spiral path and corresponding kinematic conditions. (a) XY spiral path; time evolution of: (b) velocity magnitude, (c) X coordinate; (d) Y coordinate; (e) X velocity; (f) Y velocity. 199
7.2 Slice of the temperature field in XZ direction with the standard line path, scanning speed $v_{travel} = 1.6\ mm/s$. (a) Temperature field, (b) temperature gradient in X direction (horizontal); (c) temperature gradient in Z direction (vertical). 200
7.3 Slice of the temperature field in XZ direction with the spiral path with the following parameters: $R = 1\ mm$, $n = 100$, v_{max}= 1000 mm/s, and $v_{travel} = 0.01\ mm/s$.(a) Temperature field, (b) temperature gradient in X direction (horizontal); (c) temperature gradient in Z direction (vertical). 200
7.4 microstructure comparison of (a) line scan, v=5mm/s and (b) spiral scan with $R = 1\ mm$, $n = 100$, v_{max}= 1000 mm/s, and $v_{travel} = 0.01$ mm/s.. SPI G3 nanosecond pulsed laser with a beam size of 0.6 mm, the average output power is 18.2W. 202
7.5 Optical and electron microscopy of spiral laser scans. (a) Bright field optical image, (b) SEM image. Performed with $R = 1\ mm$, $n = 3$, v_{max}= 1000 mm/s, and $v_{travel} = 0\ mm/s$, repeated 20 times for homogenous heating of the workpiece. SPI G3 nanosecond laser, laser spot size d=0.4mm 202
7.6 Vapour-grown YSZ, resolidified on the side of the molten pool (Region 1 in Fig. 7.5) 204
7.7 Schematic illustration of deposition process achieved via spiral path. (a) top view and the spiral trajectory of the laser beam; (b) cross-sectional view; (c) magnified view of the red box depicted in (b) illustrating the formation of the columnar microstructure. I denotes a column. 206
7.8 SEM images of spiral laser scans performed with $R = 1\ mm$, $n = 100$, v_{max}= 1000 mm/s, and $v_{travel} = 0\ mm/s$, repeated 20 times for homogenous heating of the workpiece. SPI G3 nanosecond laser, laser spot size d=0.4mm. (a) low magnification; (b) magnified view of (a); (c) magnified view of (b) with the coral-like structure of the material. 207

7.9 magnified view of the coral-like structure of YSZ depicted as I in 7.8 . 208
7.10 Microscope observations of spiral laser scans. (a) Top surface of the laser-affected surface of APS TBC with a 1D spiral path; (b)Cross-sectional micrograph showing material removal and melted layer. Laser parameters: $R = 2\ mm$, $n = 200$, v_{max}= 1000 mm/s, and $v_{travel} = 0.5\ mm/s$, SPI nanosecond laser. 209
7.11 Top surface SEM observation of YSZ after 1D spiral laser pass, as shown in 7.10. (a) X630, (b) x6500, (c)x1800, (d)x3300 210
7.12 High-speed imaging of laser ablation of APS-sprayed 8wt%YSZ coating. Frame rate 25300 frames/s, exposure time 10 μs. Time from the pulse denotes the time passed from a pivoting pulse at the beginning (initial pulses row), after 5 and 15 seconds of laser irradiation. SPI G3 laser, average laser power 18.2W, laser spot size 50.5 μm, pulse repetition frequency 35kHz. Static irradiation. 211
7.13 High-speed imaging of laser ablation of APS-sprayed 8wt%YSZ coating. Frame rate 17860 frames/s (56 μs frame-to-frame time), exposure time 45 μs. Time from the pulse denotes the time passed from a pivoting initial pulse. SPI G3 laser, average laser power 18.2W, laser spot size 50.5 μm, pulse repetition frequency 35kHz. Static irradiation. 213
7.14 High-speed imaging of laser ablation of APS-sprayed 8wt%YSZ coating with a picosecond laser irradiation. Frame rate 6500 frames/s (154 μs frame-to-frame time), exposure time 140 μs. Time from the pulse denotes the time passed from a pivoting initial pulse. EKSPLA 1064, average laser power 3.5W, laser spot size 35 μm, pulse repetition frequency 4kHz. Static irradiation 214
7.15 First design iteration of deposition rig, utilising conduction heating and wide range of target-substrate distances. 217
7.16 Final deposition rig setup utilising radiation heating and narrow of target-substrate distance range with fine control. (a) Equipment during the substrate heating; (b) apparatus after the experiment with deposited coating. 218
7.17 Calibration process of the heating equipment. (a) photograph of the heated substrate with a thermocouple. (b) the front surface temperature of a 0.8mm thick sample after thermal equilibrium. . . 219
7.18 Substrate surface (a) before and (b) after the deposition experiment with SPI G3 nanosecond laser. 220
7.19 Experimental deposition rig v.1 in action. (a) Normal operation with the substrate with visible laser spot and ablation plume; (b) Flipped sample rotating on its cylindrical side. 221
7.20 Deposition of sub-micron whisker-like YSZ with SPI G3 laser. 222
7.21 Deposition mechanism of whisker-structured YSZ 223

7.22 High-speed imaging of laser ablation of 4.9wt%YSZ target close to the focal plane. T Time step between images is 154 μs (frame rate is 6500 frames/s), exposure time 151 ms. Average power 88W, beam waist 30 μm (increased on a curved surface). Linear velocity at the target surface is 44 mm/s. 225
7.23 High-speed imaging of laser ablation of 4.9wt%YSZ target close to the focal plane. The time step between images is 154 μs (frame rate is 6500 frames/s), exposure time 151 ms. Average power 88W, beam waist 30 μm (increased on a curved surface). Linear velocity at the target surface is 44 mm/s. 226
7.24 A series of high-speed images laser ablation of 4.9wt%YSZ target with a laser spot size of 0.2mm. The orange arrow indicates the vapour plume. The Time step between images is 154 μs (frame rate is 6500 frames/s), exposure time is 151 ms. Average power 88W. Linear velocity at the target surface is 44 mm/s. 227
7.25 High-speed imaging of laser ablation of 4.9wt%YSZ target with defocused beam: (a) laser spot size of 0.2mm and (b) 0.4mm. The orange arrow indicates the vapour plume. Exposure time 151 ms. Average power 88W. Linear velocity at the target surface is 44 mm/s. 227
7.26 High-speed imaging of laser ablation of 4.9wt%YSZ target with a beam size of 0.4mm after prolonged irradiation. The orange arrow indicates the vapour plume. Exposure time 151 ms. Average power 88W. Linear velocity at the target surface is 44 mm/s. 228
7.27 Liquid droplet laser deposition (LDLD) process. (a) schematic view showing droplet formation; (b) photograph was taken during the experiment. 229
7.28 Various splat shapes achieved with LDLD method. Average power 88W, beam waist 30 μm. Linear velocity at the target surface is 44 mm/s, and target-substrate distance is 5mm. 231
7.29 BSE image and corresponding Fe and Zr elemental map of the substrate after LDLD process. Average power 88W, beam waist 30 μm. Linear velocity at the target surface is 44 mm/s, and target-substrate distance is 5mm. 232
7.30 BSE images showing cellular solidification of YSZ splays. Average laser power 88W, beam waist 30 μm. Linear velocity at the target surface is 44 mm/s, and target-substrate distance is 5mm. 233
7.31 BSE image and corresponding EDS map showing sample coverage with the coating at the side of the coating. Average laser power 88W, beam waist 30 μm. Linear velocity at the target surface is 44 mm/s, target-substrate distance is 5mm, and laser irradiation time is 120 seconds. 234
7.32 BSE images showing the surface topology and coating coverage at different magnifications and instances. (a) 522x; (b) 1000x; (c) 500x ; (d) 3066x. Average laser power 88W, beam waist 30 μm. Linear velocity at the target surface is 44 mm/s, target-substrate distance is 5mm, and laser irradiation time is 120 seconds. 235

7.33 BSE images showing surface topology and typical defects present in (a) LDLD coating; (b) APS coating. 500x magnification. 236
7.34 schematic view of Atmospheric Vapour Laser Deposition (AVLD) technique 238
7.35 Top view of the deposited coating via AVLD method, BSE SEM images at different magnifications: (a) x37; (b) x400; (c) x15 000. Substrate temperature 250°C, average laser power 88W, beam waist 200 μm. Linear velocity at the target surface is 44 mm/s, target-substrate distance is 200μm. 239
7.36 High magnification SE image of interconnected YSZ nanospheres deposited via AVLD method, x45 000. Substrate temperature 750°C, average laser power 88W, beam waist 200 μm. Linear velocity at the target surface is 44 mm/s, target-substrate distance is 200μm. 240
7.37 High magnification SE image of interconnected YSZ nanospheres deposited via AVLD method, x100 000. Substrate temperature 750°C, average laser power 88W, beam waist 200 μm. Linear velocity at the target surface is 44 mm/s, target-substrate distance is 500μm. 241
7.38 Top view of a long microcrack at different magnifications. (a) x2300 view showing crack propagation; (b) x100 000 view close to fracture surface; (c) x20 000 view fracture of a porous AVLD structure. Conditions: substrate temperature 750 ° C, average laser power 88W, beam waist 200 μm. Linear velocity at the target surface is 44 mm/s, target-substrate distance is 500μm. 242
7.39 Top surface SEM images of the central area of the substrate after deposition. (a) x1500 showing the formation of pseudo-columns; (b) close view of the columns (x4000); (c) Microstructure of the column consisting of sintered nanospheres. Conditions: substrate temperature 750°C, average laser power 88W, beam waist 200 μm. Linear velocity at the target surface is 44 mm/s, and target-substrate distance is 150μm. laser irradiation time 30 seconds. 244

List of Tables

2.1 Comparison of topcoat materials 18

3.1 CW laser parameters. [320] 79
3.2 Nanosecond laser parameters 82
3.3 Ekspla Atlantic HE 1064 laser parameters 84
3.4 Elemental composition of commercially available Nimonic C263 alloy [261] 88
3.5 Elemental composition (wt%) of bondcoat (Amdry 995C) powder [207] 88
3.6 Elemental composition (wt%) of topcoat (Metco 204B) powder [208] . 88
3.7 List of SEMs and corresponding parameters used throughout the investigation. 93
3.8 Elemental composition of AFRL 03 test dust used in CMAS tests [134] 100

4.1 Parameters for achieving selective TBC ablation and continuous dense layer. 128

5.1 Erosion resistance of as-sprayed and laser modified samples 135
5.2 Thermal cycling tests results 152

7.1 Elemental composition (wt%) of AISI 304L stainless steel used as substrates in the deposition experiment [234] 215
7.2 Elemental composition (wt%) of ZrO_2 deposition targets. 216

List of Symbols

Symbol	Unit	Description
C_0	mol/m^3	Equilibrium concentration far from the interface
C_L	mol/m^3	Concentration of Y_2O_3 in the liquid
C_p	$J/(kgK)$	Heat capacity at constant pressure
D	m^2/s	Thermal diffusivity
D_L	m^2/s	Thermal diffusivity of the liquid
d	mm	Laser beam diameter
d_f	mm	Laser spot size at the focal plane
E	GPa	Young's modulus
E_{dense}	GPa	Young's modulus of dense material
E_x	MPa	In-plane Young's modulus of TBC
E_z	MPa	Out-of-plane Young's modulus
F	N	External forces
f_{PRF}	Hz	Pulse repetition frequency
$\vec{g}$	m/s^2	Gravitational acceleration
G	K/m	Temperature gradient
k	$-$	Partition coefficient
k_{th}	$W/(mK)$	Thermal conductivity
l_{th}	μm	Thermal diffusion length
L	mm	Characteristic length
m_L	$Kmol/m^3$	Liquidus slope
p	Pa	Pressure
Pe	$-$	Peclet number
Pr	$-$	Prandtl number
PO	$-$	Pulse overlap
Q	W/m^3	incoming heat source
Re	$-$	Reynolds number
R	m/s	Solidification rate
T	K	Temperature
ΔT	K	Full temperature difference
T_{sol}	K	Solidus temperature
T_{liq}	K	Liquidus temperature
T_{ref}	K	reference temperature
$\boldsymbol{u}$	m/s	Velocity of the fluid
v_{planar}	m/s	Crystal growth speed in planar interface
v_d	m/s	Crystal growth speed in dendritic interface

Symbol	Unit	Description
α	K^{-1}	Coefficient of thermal expansion
$\alpha_{x\ TC}$	K^{-1}	In-plane linear coefficient of thermal expansion of the topcoat
$\alpha_{x\ sub}$	K^{-1}	In-plane linear coefficient of thermal expansion of the substrate
$\Delta\alpha_x$	K^{-1}	In-plane thermal expansion mismatch between topcoat and substrate
$\varepsilon_{x\ TC}$	K^{-1}	Thermal expansion induced strain in the topcoat
$\varepsilon_{x\ sub}$	K^{-1}	Thermal expansion induced strain in the substrate
ε_{laser}	J/m^2	Linear energy density within the laser track
γ	N/m	Surface tension coefficient
ν	$-$	Poisson's ratio
ρ	kg/m^3	Material density
ρ_0	kg/m^3	Reference density of the fluid
ρ_{geom}	$-$	Geometry factor of the pores
τ_p	s	Lattice heating time
τ_L	s	Laser pulse duration
υ_s	m/s	Laser scanning speed

Chapter 1

Introduction

1.1 Motivation

The first flight of a Heavier-than-air model is ascribed to the Italian inventor Tito Livio Burattini, who built an aircraft with fixed glider wings that lifted a cat as early as 1648 (however, not the inventor himself). Many years later, in August 1908, Wilbur and Orville Wright made the first public fights on the Wright aeroplane, which dispelled all doubt and showed great potential for a novel transportation system. Nowadays, the aerospace industry has become a well-established business with airline revenue of $876 billion and over 4,5 billion passengers departures in 2019 [132]. The industry trend of commercial flights is now oriented toward passenger safety and flight efficiency; this, combined with international standards for engine emissions and aircraft noise, formed a constant seek for innovative solutions in aircraft fabrication. An ambitious target of the European Union on environmental control over the new aircraft aims to cut CO_2 emissions by 75%, NO_x emissions by 90%, and reduce fuel consumption by 65% by 2050 [69]. Such objectives can be solved only in a highly-competitive environment open to innovative solutions, residing at the pinnacle of the world's technological advances.

It is common to describe turbine engine efficiency in thermodynamic terms. Gas-turbine engines obey to some extent the Brayton cycle, which starts with adiabatic compression of the inlet air. At this developed pressure, the heat is added to the turbine through combustion in the isobaric process. One of the ways to increase the turbine power output is to increase the pressure at which combustion takes place, i.e. increase the compression ratio. After the combustion, the gases adiabatically expand at the turbine stage and exhaust into the atmosphere, and the cycle continues. In an ideal Brayton cycle, thermal efficiency η_{th} depends on the pressure inside the combustion chamber, P_1, and the pressure outside P_2: $\eta_{th} = 1 - \frac{P_2}{P_1}$, thus it is useful to describe the engine with the Overall

Pressure Ratio (OPR), shown in Fig. 1.1. Modern turbofan engines, e.g. the Rolls-Royce Trent 7000, already work at an OPR of 50:1. In comparison with Trent 700, which reaches an OPR of 36:1, and together with a twofold increased air bypass ratio the fuel consumption of a higher-OPR engine improved by 11% [272].

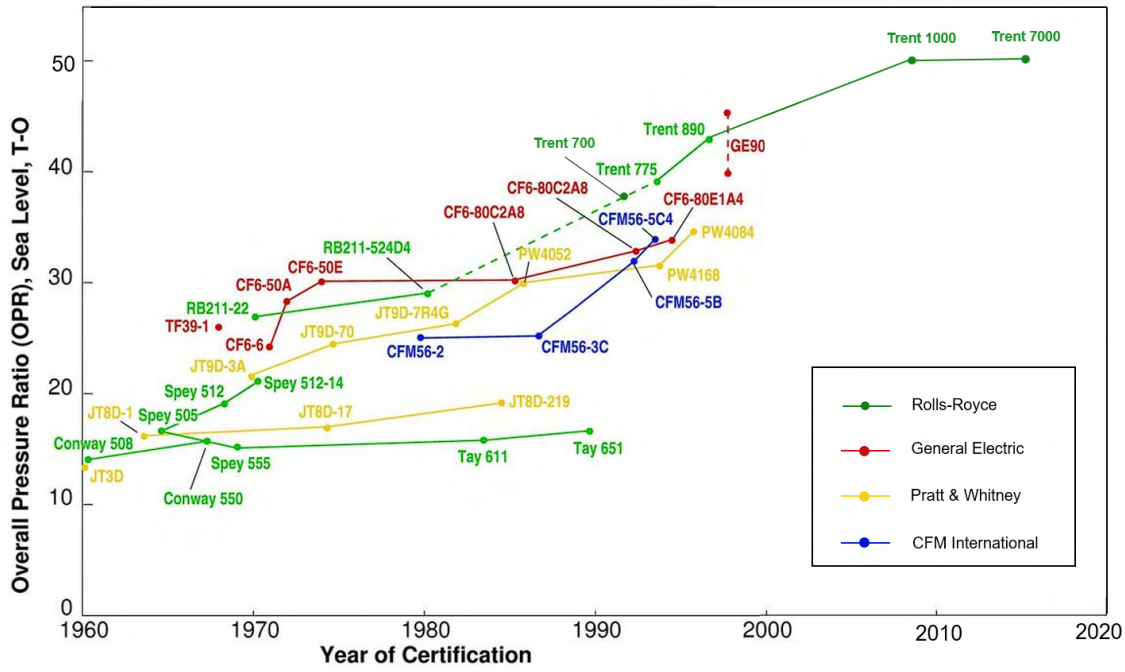


FIGURE 1.1: Evolution of Overall pressure Ratio in Rolls-Royce gas-turbine engines. Adapted from [73]
The line colours represent the engine manufacturer.

Higher compression ratio is associated with an increase in the internal temperatures of the engine. In the aforementioned engines, apace with increased pressure, the internal temperature increased by 200K, reaching more than 1835 K (1562 °C) at the turbine entrance. The latter is also called the Turbine Inlet Temperature (TIT) (also called turbine entry temperature, or TET), representing the highest temperature in the whole engine, e.g. see temperature distribution in Trent 800 engine in Fig. 1.2. While the overall pressure ratio is a useful measure of engine efficiency, TIT is in fact a rather similar way to describe engine performance, although linked to one of the main reasons limiting engine performance.

The everlasting race for higher efficiency had been driving the technology to develop novel materials with exceptional high-temperature properties. Ni-based superalloys had been used extensively in combustor and turbine sections, constantly undergoing further development. Manipulation with crystal structure allows for improving the properties of the engine components, i.e. by the transition from equiaxed crystals to directionally solidified, and eventually single crystal

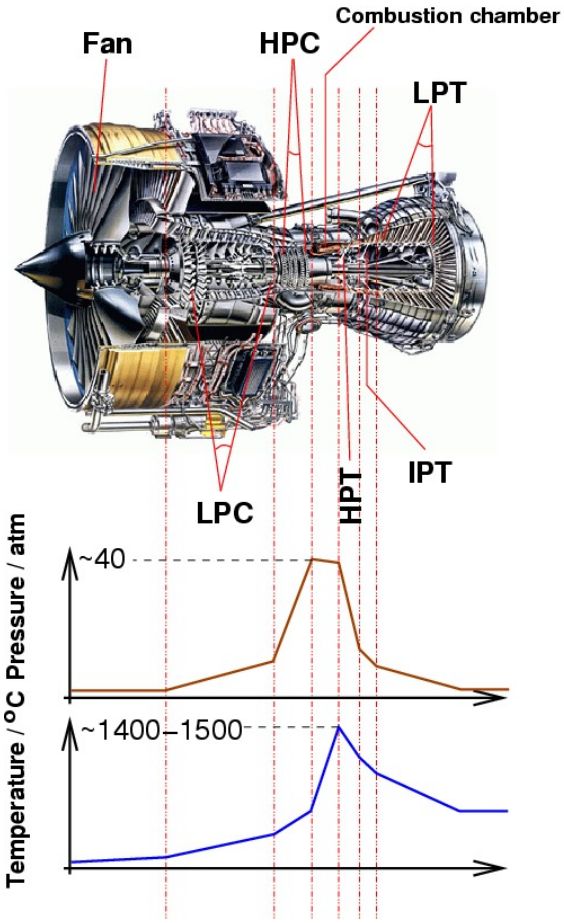


FIGURE 1.2: Temperature and pressure distribution in Low Pressure Compressor(LPC), High Pressure compressor(HPC), followed by combustion chamber, High Pressure Turbine (HPT), Intermediate Pressure Turbine (IPT), and Low Pressure Turbine (LPT). Rolls-Royce Trent 800 Jet Engine. [294]

blades. In order to overcome the limitations imposed by the metallic components, new concepts had been introduced over time and have already become state-of-the-art techniques. Nowadays, one of the implemented ways to increase the TIT is by applying a relatively thin (typically about 250 μm) temperature-resistant coating on the components in the turbine stage and combustion chamber. Combined with film air cooling, it will develop a temperature gradient inside a refractory material, and eventually can give a 100-300K increase in the turbine inlet temperature [235]. This coating just a few human hair thick allows the engine to withstand temperatures above the melting point of superalloys. Such coating, called Thermal Barrier Coating (TBC) also protects the underlying metal from a harsh engine environment. Resistance to high-temperature creep and oxidation of the metal, as well as protection of the metal from erosion and foreign object damage due to the high hardness of the coating material, also increases the durability of coated components. Besides,

novel materials such as silicon-based Ceramic Matrix Composites(CMC) and oxide-oxide CMCs are being studied extensively, which could withstand even higher temperatures.

Thermal barrier coatings have a limited lifespan, which goes down to several reasons. Most importantly, it is the oxygen diffusivity of current state-of-the-art ZrO_2-based coatings at elevated temperatures. Oxygen atoms can penetrate through the protective coating and react with the metal underneath, forming an oxide layer. In an effort to control the properties of the oxide, e.g. its composition and bonding strength, an intermediate metallic layer was introduced, called bondcoat. The reaction between oxygen and the bondcoat forms a layer of an oxide called thermally grown oxide (TGO). The TGO forms inevitably when the coated metal is in contact with hot gases and grows in a confined space. Eventually, high growth stresses of the TGO, combined with the mismatch of thermal expansion coefficient with the neighbouring layers, initiate cracks at the interface between bondcoat and topcoat, which will propagate through and cause coating delamination, leaving the metallic component unprotected. Alongside TGO growth, several other reasons can affect TBC properties and result in coating failure: high-velocity foreign objects erode TBC and cause wear and mechanical damage; fuel impurities and silicon-containing sand in runway strips and volcanic ash also play a critical role in TBC lifespan, which can infiltrate through the coating and cause its spallation.

The effects of coating deterioration alongside with other potential engine deterioration are captured during regular checks. The airworthiness of the engines is regulated by internationally agreed standards, such as the Maintenance Steering Group-3 (MSG-3) program, describing the "Operator/Manufacturer Scheduled Maintenance Development". The MSG-3 (Maintenance Steering Group) methodology is widely accepted and extensively used in the aviation industry for developing scheduled maintenance tasks and intervals. It has gained significant recognition and adoption by regulatory authorities, operators, and manufacturers worldwide. The frequency of engine overhaul and major maintenance inspections for aviation engines depends on several factors, including the engine type, manufacturer recommendations, operating conditions, and regulatory requirements. The specific intervals can vary between different engine models and operators. In general, engine overhaul and major maintenance inspections are typically conducted at predetermined intervals based on factors such as engine operating hours, cycles (takeoff and landing), or calendar time. These intervals are defined by the engine manufacturer and are outlined in the engine maintenance

manual or other technical documentation provided by the manufacturer. For commercial jet engines like the Trent 1000 or Trent 7000, the recommended engine overhaul intervals can range from several thousand to tens of thousands of engine operating hours, depending on the specific engine model and its design. Major maintenance inspections, which may involve comprehensive inspections, component replacements, or repairs beyond routine maintenance, are typically performed less frequently than engine overhauls.

Repair of thermal barrier coatings is one of the most time-consuming maintenance operations. To repair a failed coating, the part is usually taken off the engine and either replaced with a new part or sent to the overhaul centres for repair. Laborious engine disassembly leads to long downtimes of the turbine and requires time optimisation. One of the ways to optimise the engine repair process is to perform inspection and repair on-wing (or *in-situ*), without engine disassembly. On-wing technology is inherently difficult due to restricted access to the components and is currently limited to simple operations like borescope inspection, and compressor blade blending. In spite of all the difficulties associated with the on-wing repair, the area is undergoing substantial research. An example of such is the FLARE project, developed at the University of Nottingham in collaboration with Rolls-Royce, which utilises a "snake"-like robot for in-situ patch repair of failed components via combustion flame spraying approach [273, 78].

Coatings properties, and thus their durability, depending on the microstructure developed during deposition. Although limited TBC lifespan is a repair issue, one of the approaches to cut the maintenance cost is by developing a coating with superior properties and a longer coating lifespan. Eventually, a more durable coating repair and inspection will become less frequent, given the technology readiness level is adequate. This can be done via improvement of deposition methods, or by modification of the coatings, and microstructure after, during, or prior to coating deposition.

The utilisation of laser beams is favourable for in-situ application: the energy can be delivered in a "pure" form of photons with the aid of a thin optical fibre, or an array of fibres. One of the promising approaches for coating modification uses laser-beam energy for remelting the topcoat, called glazing [317]. The topcoat melts and creates a network of cracks upon crystallisation, which allows for increasing its thermomechanical compliance. Besides, it creates a protective dense layer resistant to erosion and chemicals. However, some studies have controversial results on this technique, revealing similar thermal shock performance of modified

coatings without any noticeable effect [367]. A thorough understanding of the mechanisms governing TBC degradation involves various physical and chemical phenomena: diffusion, oxidation, phase transformation, elastic and plastic, and creep deformation, sintering, thermal expansion, and fatigue [235]; this list, although incomplete, makes TBC operation one of the most complex interplays of physical phenomena, which is yet not fully understood.

1.2 Research Problem

Novel solutions for coating durability are yet to be found. With the focus on coating susceptibility to environmental damage and oxidation, a potential step forward is provided by tailoring the properties of thermal barrier coatings by a two-stage post-treatment process. While the ceramic coating confronts different degradation causes at its surface, at the bulk, and at the interface with metal, this feature can be utilised to smartly adjust the microstructural properties. For example, TGO growth and thermal mismatch stresses occur at the interface between bondcoat and topcoat; topcoat reaction with chemicals takes place first at the component's surface which further infiltrates through the coating and reacts with it as a whole; mechanical interaction between the coating and foreign particles happens at the surface of the TBC. Therefore, different strategies can be applied to adjust the coating properties.

A step forward in this direction is provided by combining pulsed laser ablation (PLA) and laser melting approaches to generate TBC resistance to environmental damage. To increase thermomechanical compliance, PLA generates voids in the bulk of the coating, eventually decreasing the stresses generated at TGO and making the coating less susceptible to buckling. After such laser ablation, TBC consists of a discontinuous column replicating the electron beam deposited thermal barrier coatings on a larger scale. Such coating with through-thickness trenches, however, is not integral, and has still the same problems related to the interaction with active chemicals and silicates, as well as the same or potentially worsen coating resistance to erosion. Moreover, open voids in the coating provide a short path for oxygen to the bondcoat, potentially leading to its higher oxidation rates. In this study, such an approach was combined with laser glazing, which provided the coating with a dense surface layer. In contrast with laser glazing, such a combination can effectively remove stress concentrators from the network of cracks, in which the latter is connected with PLA-generated voids. Such a combined approach has not been reported in the literature and is a potentially highly beneficial approach for coating modification.

The research of laser glazing, although being a popular approach, had been mainly focused on the coating response to the environment, in other words, the coating as a whole had been extensively tested in thermal fatigue, burner rig, erosion tests, and interactions with molten silicates. From a scientific point of view, research attention to the physical phenomena occurring during the laser glazing process was limited. Understanding a complex problem during heating involves consideration of laser absorption and energy transport, leading to melting, vaporisation, ionisation, and eventually plasma recombination, vapour condensation, vapour deposition, and liquid freezing, i.e. solidification. Besides, the crystal growth process of laser-melted TBCs has not found any attention in literature. The latter represents a significant challenge in appreciation of the present phenomena and constitutes a multi-scale problem, involving macro-scale temperature transfer and fluid motion, and a micro-scale problem, governing grain initiation and growth.

One of the previously mentioned transitions in laser-glazing is a vapour-to-solid transition, or deposition. Effectively, such a transition is utilised for the formation of state-of-the-art coatings with the best properties among all the other deposition techniques, namely Electron Beam Physical Vapour Deposition (EB-PVD). This technique uses high-energy electrons to evaporate the target material, which will later propagate to the substrate and be deposited, forming a coating layer. EB-PVD method requires the use of high vacuum, which is absolutely necessary for electron transport, and important for vapour propagation, reducing the scattering of vaporised particles in the ambient environment. Such a method creates a coating consisting of separate columns with great adhesion to the substrate, and has superior properties compared to deposition methods in an ambient air environment; although the technique is rather expensive and hardly possible for in-situ implementation due to vacuum requirements. In fact, a careful examination of laser-glazed TBC with a particular beam path revealed that a rather similar columnar structure was deposited on the neighbouring area of the substrate. Although deposition with the aid of lasers, which can be used in the atmosphere in contrast with an electron gun, has been developed into Pulsed Laser Deposition (PLD[276]), it had never been applied for complete coating deposition under atmospheric pressure. Certainly, deposition in atmospheric pressure is rather unfavourable for its own reasons (mainly due to a short mean free path of molecules in the atmosphere, where approximately one collision happens every 100 nm). Based on the initial experiments, the atmospheric deposition could represent a scientific and industrial opportunity for both research and application, and very few studies have been dedicated to such exploration. Complex phenomena such as

coating formation mechanisms, particle adhesion and cohesion, as well as thermomechanical compliance have never been addressed in an atmospheric vapour deposition process. Recognition of determining the aspects of the deposition process in the atmosphere constitutes a major problem involving different aspects of physics vital for the coating application process, which could be eventually exploited as an in-situ coating application technique.

The development of post-deposition coating modification, control of the modified coating structure, and coating deposition with in-situ potential is rather challenging due to the following reasons:

- Coating durability in a real engine environment is rather complex. Understanding the underlying reasons for coating failure and the influence of coating microstructure on its performance is vital to avoid a time-consuming trial-and-error approach and long tests of the specimens with unfavourable microstructure. A comprehensive analysis of the failure reasons of both as-sprayed and coatings that underwent modifications is essential for further implementation of the modification strategy; neither of them has been fully understood yet.

- Laser-matter interaction in case of laser ablation must be optimised in order to produce minimal collateral damage to the part and coating itself. PLA is a non-contact method for material removal, which, combined with changing the thickness of the coating due to heterogeneous deposition, represents a major challenge to affect the ceramic material only, leaving the substrate material and/or bondcoat uninfluenced. This will allow the component to be recoated again and continue service operation after coating reapplication. Moreover, vaporisation and plasma formation induce high pressures and cause severe cracking and even local spallation, which must be addressed in order to achieve a coating with adequate properties.

- Achieving a continuous protective layer through laser melting is important for protecting the coating from mechanical and chemical impact. This manufacturing problem is challenging due to the complexity of the melting and solidification phenomenon itself and becomes particularly problematic on uneven grooved surfaces. One of the main physical obstacles on the way to a continuous glazed layer is overcoming the Plateau-Rayleigh instability of liquids simultaneously maintaining an acceptable level of thermal damage to the TBC. Changing optical, thermal, and mechanical properties with raising temperature make the process difficult to predict; optical transparency of the

coating in the near-infrared spectrum, which is the typical spectrum of common industrial lasers, becomes especially pronounced after remelting and represents a challenge for its further application on a large area and limits the carpet laying strategies.

- Crystal structure of the materials is of great importance for material properties. Grain boundary design often plays an important role in achieving superior mechanical properties. Grain size is known to influence the yield strength of materials (via the Hall-Petch effect), crystal orientations and the relevant misorientation angles within the grain boundary affect stress-driven grain boundary motion, while the morphologies of crystals, i.e. dendritic, cellular, or planar, can affect surface topology, as it was observed with ZrO_2. Understanding the grain formation during solidification is essential for further ability to control material properties, which however had never been addressed for laser glazing. Unusual habits of grain development were found during the work on the laser glazing; although grain growth modelling is a rich scientific field of predictive tools, existing models could not capture observed phenomena, namely grain surface sealing and grain bending. A predictive multi-scale model for energy transfer and fluid motion within the molten pool combined with a correct grain growth model is necessary for understanding grain formation and vital as a future predictive tool for crystal formation.

- Careful examination of laser-melted patterns under certain conditions revealed the formation of EB-PVD-like columnar microstructure at the sides of the laser-melted grooves. To date, the very possibility of a vapour deposition under atmospheric conditions of TBCs found limited attention in the literature. Such work has likely been avoided due to the nanoscale length of the mean free path of atoms in atmospheric conditions, difficult to replicate in a macroscopic experiment.

1.3 Objectives of the study

The aim of the study is to advance current knowledge on thermal barrier coatings, expand the range of potential range of modification techniques, and understand the crystal formation of ZrO_2 upon solidification and deposition. This is motivated by the industrial need for optimisation of thermal barrier coating lifespan and maintenance costs, allowing to commit modification on deposited coatings *in-situ*, as

well as investigate new possible deposition techniques of ceramics in the atmospheric environment with a laser energy source. The specific objectives of the study are listed below:

- Investigate the possible ways for improving thermomechanical compliance of thermally-sprayed coatings by modifying existing structures with in-situ potential. Analyse the coating microstructure and minimise the damage by adjusting parameters and strategy of laser ablation and laser melting.
- Asses the properties of the modified coating in simulated in-engine conditions, and analyse the microstructural changes within the coating. A comparative study of performance characteristics, failure mechanisms, and microstructure transformations would allow for a better understanding of the benefits and drawbacks of the proposed microstructure. Analysis of the failure mechanisms enables further development of the proposed modification technique.
- Understand the governing mechanisms controlling grain boundary geometry, and grain morphology in laser-melted thermal barrier coatings. This objective is followed by the chosen modification approach which involves melting of TBC via an energy source, i.e. laser. This will be done by multi-scale modelling of laser melting and solidification. First, temperature distribution will be obtained via finite-element modelling of coupled heat transfer and fluid flow with a moving laser source. Temperature distribution will be further analysed and used for explanation of unusual crystal growth directions and grain morphology, found during laser glazing; to predict the crystal orientation and grain boundary geometry, temperature distribution will be used as an input for the microscale crystal growth model based on Cellular Automata methods with particular attention to the different solidification in planar and dendritic regimes.
- Investigate the possible TBC deposition techniques of ceramic materials with a laser tool in atmospheric conditions. To date, nearly every laser-based deposition technique utilising a laser requires a vacuum chamber, which is unsuitable for an *in-situ* deposition process. To close this gap, various deposition concepts in atmospheric conditions, in particular, deposition from the vapour phase and from liquid phases. The examination of the deposited coating microstructure and explanation of the deposition and microstructure formation mechanisms are necessary to enable further development of the technique in future studies.

Chapter 2

Literature Review

In this chapter, a comprehensive literature analysis of advances in thermal barrier coating systems and laser processing is presented. An overview of the thermal barrier coating system will be provided, including layers' purposes and functions. An overview of state-of-the-art deposition techniques, including thermal spray and vapour deposition methods, as well as techniques in research and development is arranged. This will be followed by a detailed look at the degradation mechanisms associated with TBC systems. Particular attention was paid to current techniques allowing for coating modification. The main tool used in this work is laser-based. The current state of laser microfabrication technologies, as well as the defects associated with laser-fabricated components, are summarised in this chapter. Different modification techniques are provided, including laser remelting and laser grooving approaches, their current state and comparison. Finally, solidification phenomena are discussed, with a focus on multiscale physical modelling of microstructure upon phase transformation. The chapter is concluded with a summary of current research gaps that have motivated the present work.

2.1 Thermal Barrier Coating system

Thermal barrier coating (TBC) is an advanced multilayer system found in a variety of applications ranging from the nuclear and aerospace industry to power generators. The aim of TBC is to protect components from harsh thermal and mechanical conditions and to increase the operating temperature above the melting point of the component material [235]. Combining different materials in a multilayer system and providing internal cooling of a component, it is possible to significantly reduce the temperature at contact with the substrate material, and protect it from oxidation in the hottest parts of the engine (Fig. 2.1).

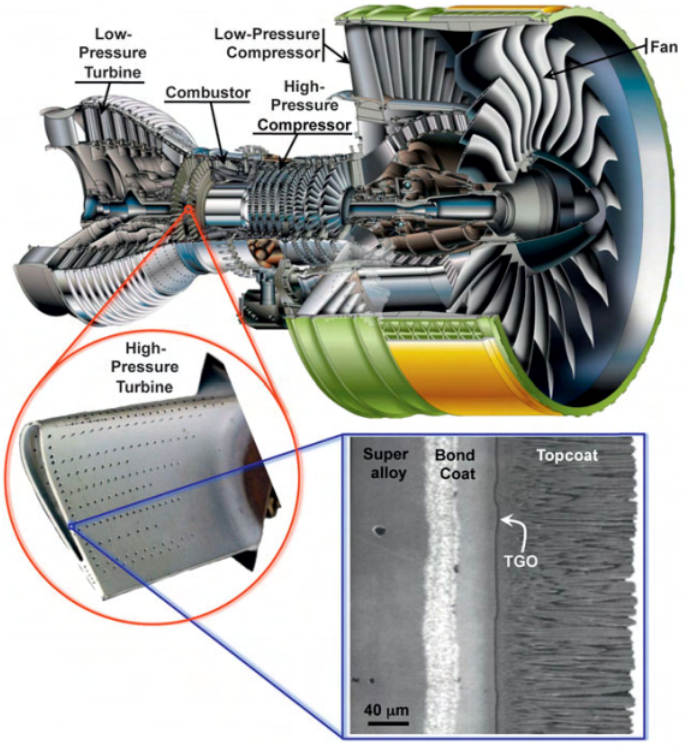


FIGURE 2.1: Example of TBC application on a dynamic component. Cutaway view of Engine Alliance GP7200 aircraft engine, a photograph of a turbine blade (10cm long) with TBC from the high-pressure hot section of an engine, and a scanning electron microscope (SEM) image of the TBC cross-section. [52]

The first TBCs were implemented in the early 1960s, and the first burner-rig tests of a multilayer TBC system with a NiCrAlY bond coat and a porous Yttria Stabilized Zirconia (YSZ) topcoat were conducted at the National Aeronautics and Space Administration's (NASA) in mid-1970s [298]. This coating composition remains

the state-of-the-art system for some components of the engine, As mentioned above, the TBC system is a crucial technique for the increase in turbine engine efficiency (Fig. 2.2). Initially, this TBC system was introduced to extend the lifetime of stationary engine parts, e.g. combustor, turbine vanes, and was first used on dynamic components in the late 1980s [52, 175].

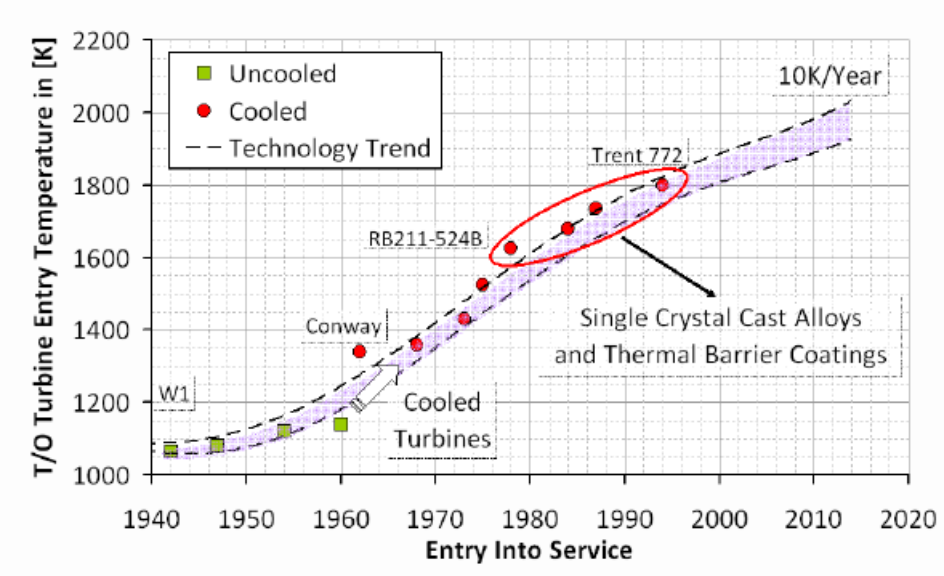


FIGURE 2.2: Evolution of turbine entry temperature. [175]

2.1.1 TBC composition

A typical TBC system on a Ni-based superalloy substrate consists of three layers (Fig. 2.1): metallic bond coat (BC), ceramic topcoat (TC), and thermally grown oxide (TGO), growing between the BC and TC due to high-temperature exposure and oxygen penetration through the ceramic topcoat.

Substrate

Typically, hot stage components are made of Ni-based superalloy with internal cooling. The material itself is a sophisticated alloy with different microstructural attributes, i.e. grain size, phase content and distribution, and grain boundary morphology, directly related to their thermal and mechanical properties [83]. The component may be cast as a polycrystalline piece or a single-crystal form. The polycrystalline structure is typically used in the cooler stage of the turbine and

combustor chamber due to potential damage accumulation at the grain boundaries and faster diffusion at high temperatures, and single crystals, due to the absence of grain boundaries at all, are used in the harshest engine parts, i.e. at the early turbine stage [250]. The γ' is an intermetallic phase, based on Ni_3(Al, Ti, Ta) phase, coherent with the matrix (γ phase) of the superalloy to strengthen the alloy matrix [160]. Carbides and borides improve creep performance of the alloy through grain boundary sliding resistance improvement [83]. Overall, modern Ni-based superalloys contain up to 12 additional elements for the sake of enhancement of specific properties, such as oxidation resistance, hot corrosion resistance, high-temperature strength, ductility, and castability [93].

However, metallic superalloys are not the only materials of interest for high-temperature components, a modern trend in research and industry is focused on Ceramic Matrix Composite (CMC) materials with even higher operational temperature and extremely promising properties for the use in higher-performance turbine engines [19]. However, even this material needs a protective coating for preventing it from oxidation and volatilization and is used with Environmental Barrier Coatings (EBCs). Nevertheless, the use of CMCs today is limited due to the lack of some key technologies, such as material processing, the establishment of design method and material evaluation techniques, that are currently being extensively developed [252, 226].

Topcoat

Topcoat (TC) is a relatively thick (usually 100 to 500 μm) low thermal conductivity layer of ceramic material, that provides thermal insulation. The most typical material for a TC is zirconium dioxide stabilised with yttrium (III) oxide, or Yttria Stabilized Zirconia (YSZ). Zirconium, being a transition metal, has several oxidation states: normally the IV state is the most stable, giving the Zr^{4+} cation. Zirconia ceramics are based on this principal oxide of zirconium, zirconium dioxide (ZrO_2), which is one of the most stable oxides, meaning that it has a large negative Gibbs function of formation (ΔG_{298K}=-1040 kJmol^{-1}) [266]. Zirconia has a melting point of 2710 °C [158], which made this material suitable for

high-temperature applications. The high thermal expansion coefficient of this material ($11{\cdot}10^{-6}$ K^{-1}) is close to the one of metals and helps to reduce thermal expansion mismatch stresses in the metal-ceramic interface.

Pure zirconia is a polymorphous crystal, where three allotropes are possible: cubic, monoclinic, and tetragonal. In cubic crystal, a-axis of the crystal was reported to be 5.167, while the monoclinic crystallographic phase has a=5.167, b=5.212, c= 5.317, and the angle between a and b axes is 99.02°[329]. Stable tetragonal zirconia is not used for thermal barrier coatings due to its possible spontaneous transition from tetragonal to monoclinic phase at elevated temperatures. Such transition is diffusionless martensitic, accompanied by volumetric expansion and can lead to catastrophic damage. However, the high-temperature morphs of zirconia, tetragonal and cubic, can be stabilised by addition of oxides, such as Yttria Stabilised Zirconia. At least three kinds of tetragonal phases can be distinguished in YSZ system: transformable, or stable, tetragonal (t phase), non-transformable tetragonal prime (t'), and a non-transformable tetragonal (t"), depending on the axes ratio c/a, (see Fig. 2.3).

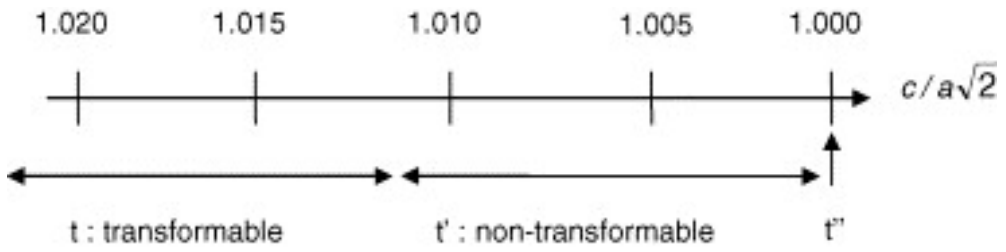


FIGURE 2.3: Variations in tetragonal allotropes of ZrO_2 according to their cell parameters. [329]

The transformable tetragonal zirconia is known for its high hardness and strength, and the hardening mechanism associated with the tetragonal to monoclinic transition is accompanied by a large (4.4%) [246] volume change associated with pseudoplasticity [301, 282]. The volumetric expansion, often called transformation toughening [48] has high importance for structural application: a bending strength of 2 GPa [318] at room temperature was obtained in tetragonal zirconia stabilized with calcium oxide. In contrast, zirconia having a purely monoclinic phase has a bending strength of just 250 MPa [92]. At the same time, the transformable t

phase undergoes the tetragonal to monoclinic transition at high temperatures, which also leads to volumetric expansion and leads to damage in the heated region, which limits the high-temperature application of the transformable YSZ.

The non-transformable *t'* phase does not undergo the transformation to the monoclinic phase under stress, thermal cycling, or ageing at temperatures up to 1200°C [114], which makes it desirable for TBC application. Instead, the proposed mechanism for superior properties of *t'* over its cubic allotrope is known as ferroelastic domain switching. In the study on large *t'* grain 3mol%YSZ, which corresponds to 5.5wt% of yttria, the fracture toughness was 7.7 MPa $\cdot$ $m^{1/2}$, compared 2.4 MPa$\cdot m^{1/2}$ for the cubic 8mol%YSZ [144]. By XRD, no monoclinic phase was detected, instead, a 90 °change in grain orientation was found, which was attributed to ferroelastic domain switching. The governing mechanism behind domain switching is the ability of the tetragonal unit cells to flip when the appropriately aligned external stress is applied, which happens through the movements of the zirconium and oxygen atoms. [127, 324].

The *t'* phase can only be achieved via high cooling rate techniques, e.g. plasma spray or electron-beam physical vapour deposition. Zirconia in this case is stabilised through a mechanism known as displacive transformation, enabled by quenching liquid or cubic phase from high temperature, or methods involving non-equilibrium syntheses, such as sol-gel and mechanical alloying[114].

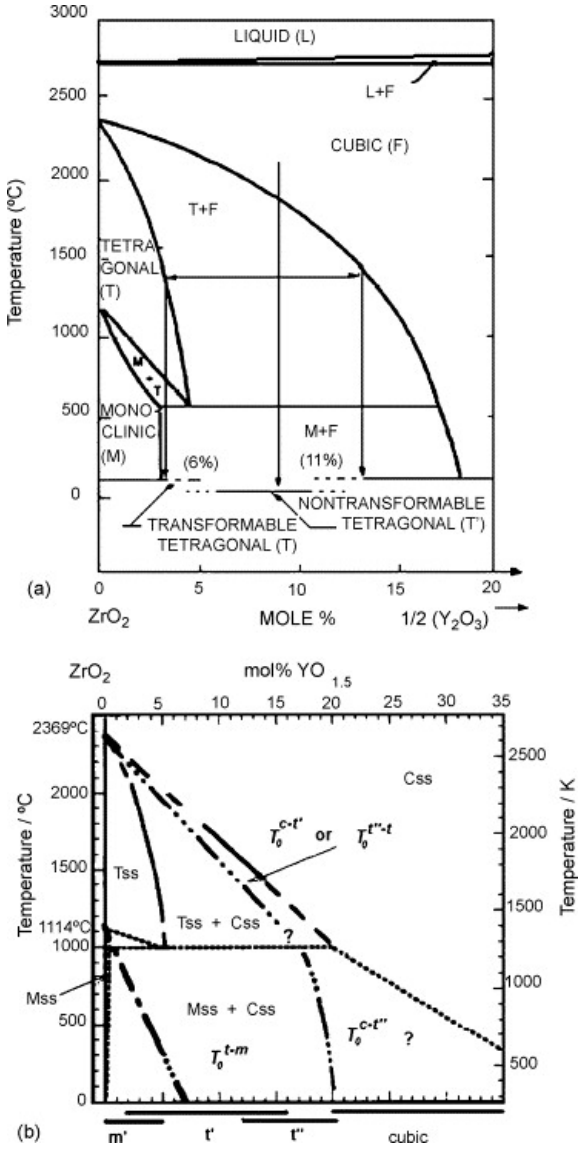


FIGURE 2.4: (a) ZrO2–Y2O3 phase diagram.(b) YSZ phase diagram including stable and metastable boundary lines [329]

YSZ has one of the lowest thermal conductivities of all ceramics, about 2.3 $W \cdot m \cdot K^{-1}$ at 1000 °C [123] for a fully dense material, and can be even smaller in a porous media. Zirconia topcoats can transfer the oxygen atoms to the underlying layers: interconnected porosities and cracks always exist in the material, providing a short path for oxygen to the bond coat. Moreover, because of the relatively high ionic diffusivity of oxygen in the ZrO_2-based ceramics, the layer is "oxygen transparent". On the other hand, this high ionic conductivity further reduces the already low thermal conductivity: oxygen vacancies, essentially being lattice defects, limit the phonon mean free path to approximately the dimensions of the unit cell [123]. It

also has a relatively low density (about 5.7 g/cm^3 in fully-dense crystal), which is important for the parasitic weight of the engine and centrifugal forces on the dynamic components.

The search for new materials for the TBC application is ongoing. Besides a possible increase in a coating lifespan, yet another driving force is the temperature limit of tetragonal zirconia. In order to provide a more complete picture, some of these materials are summarized in table 2.1.

TABLE 2.1: Comparison of topcoat materials

Materials	**Advantages**	**Disadvantages**
YSZ [36]	•High Thermal Expansion Coefficient •Low Thermal Conductivity • High Fracture Toughness	• Phase transformation at T > 1200°C
Pyrochlores (e.g. $Gd_2Zr_2O_7$, $La_2Zr_2O_7$) [36] [124]	• High thermal stability •Low Thermal Conductivity •Low sintering tendency	• Low thermal expansion • Low fracture toughness
Hexaaluminates (e.g. $LaMgAl_{11}O_{19}$) [325]	• High Melting Point • High Thermal Expansion Coefficient •Low Thermal Conductivity •High Sintering Resistance •Phase stability up to 1800°C	• Shrinkage caused by recrystallization
Perovskites (e.g. $SrZrO_3$) [36] [325]	• High melting point • Good thermal cycling performance above 1250°C	• Phase transformation • Low fracture toughness

Bondcoat and thermally grown oxide

The bondcoat (BC) is an oxidation-resistant metallic layer, typically 75 to 150 μm in thickness, and its composition and geometry substantially dictate the spallation failure of the TBC [235]. Since the topcoat is oxygen transparent, the composition of the bond coat is chosen such as to grow a consistent layer of an oxide with

high adhesion both to the topcoat and bond coat, which will also block further penetration of oxygen; for these purposes, aluminium oxide is used in both thermal sprayed and electroplated coatings.

Due to the high temperature of the bond coat during thermal cycling, and also the increase of oxygen diffusivity with temperature, the oxide grows under a temperature load, thus its name - Thermally Grown Oxide (TGO). The state-of-the-art bond coats are NiCrAlY or NiCoAlY alloys [235], the material is engineered to ensure that the TGO consists of α-Al_2O_3, grows uniform, slow and defect-free. α-Al_2O_3 has a low oxygen diffusivity and prevents further bond coat oxidation. The TGO layer can grow up to 1 - 10 μm. Another important property of the bond coat - its high adhesion - is achieved via reducing the sulphur (S) content to 1 part per million and addition of sulphur "getters" - Y, Zr [292]: segregation of S at the interface TGO-BC drastically reduced the TGO adhesion [291].

2.1.2 Topcoat microstructure

The microstructure of thermal barrier coatings is fully dependent on its manufacturing process and creates a significant difference in its properties and durability. Two common processes for topcoat manufacturing are Electron beam physical vapour deposition (EB-PVD) and atmospheric plasma spraying (APS) techniques. Typical microstructural features of both types are illustrated in Fig. 2.5.

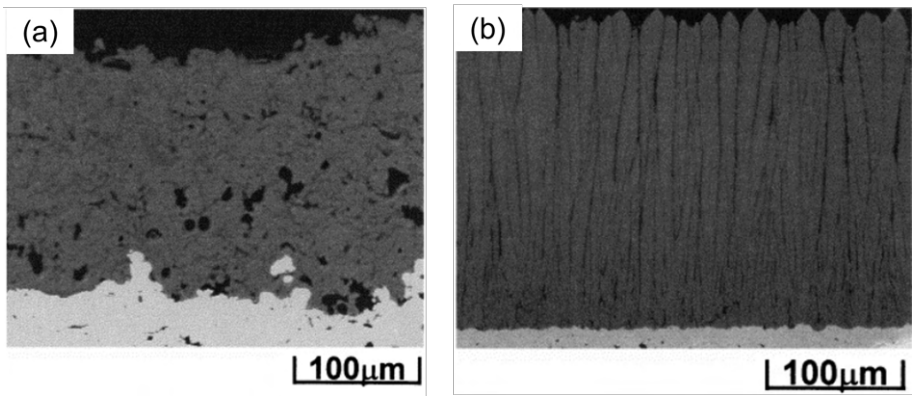


FIGURE 2.5: Cross-section of (a) Atmospheric Plasma Sprayed Coating and (b) Electron beam physical vapour deposited thermal barrier coatings. [221]

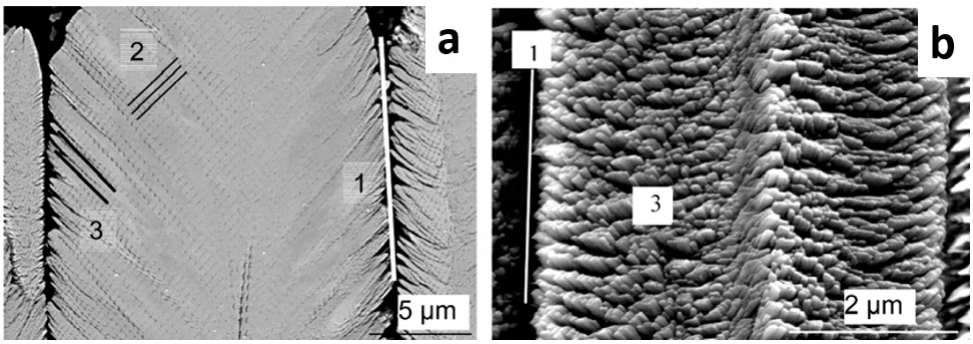


FIGURE 2.6: Morphology of EB-PVD P-YSZ TBCs in polished (left) and fractured cross-section (right) in as coated condition. [280]

APS morphology is usually called "lamellar", "splat-like" structure. An array of molten ceramic droplets, or splats, with the usual size equal or less than 100 μm, are moving towards the substrate, deforms and adheres to the substrate and previously deposited splats. This results in coating porosity, microcracks between and inside the splats. The cavities reduce the elastic modulus of the coating, therefore diminishing the thermally induced stresses. On the other hand, gaps and cracks reduce the resistance of the coating to mechanical damage, such as particle erosion and foreign object damage.

Coatings produced by EB-PVD consist of an array of separated columns. These gaps, as well as intracolumnar porosity, shown in Fig. 2.6, provide the matter with free space and decrease stress accumulation, eventually leading to an improved strain tolerance of the coating, since the columns under mechanical or thermal load can move relative to each other.

A significant difference in the microstructure, as well as the different bonding mechanisms between the topcoat and bond coat produced by different methods, influenced the application of TBC and limited the APS coating to static components. EB-PVD produced structure, more durable, strain tolerant, and more erosion-resistant [221], can be applied on all the components of engines where needed, however, due to the higher cost of this type of coating, it is usually deposited on dynamic components of an engine, where the working conditions are more severe.

2.1.3 TBC deposition methods

Constant seek for a reliable coating resistant to the harsh environmental conditions of the combustor and turbine stages have been driving the research and industry for decades. Besides the coating material itself, the coating microstructure plays a crucial role in the overall lifespan of the coatings. Coating adhesion, its estimated lifespan and resistance to erosion and foreign object damage, as well as deposition speed, has divided the coatings into two main types, providing different coating microstructure: thermal spray methods and physical vapour deposition methods. While thermal spray methods are cost-effective and provide a fast deposition, generally they show lower performance characteristics compared to PVD-produced ones. Here, different thermal spray and vapour deposition techniques will be discussed, as well as new concepts being researched. While the aim of this subsection is to provide a broad overview of deposition techniques, the subsection is mainly focused on deposition techniques suitable for topcoat application.

Thermal spray techniques

Thermal spray techniques are based on the idea of accelerating and/or heating the feedstock material it via a heat carrier (plasma source, combustion gases, high-velocity gas) [289], and delivering it to the substrate material, where kinetic energy will be delivered simultaneously with the heating energy.

Based on the heating principle and the particle acceleration level, the most common thermal spray techniques can be divided into the following groups: Atmospheric Plasma Spray (APS), Combustion Flame Spray (CFS), High-Velocity Oxy Fuel Spray(HVOF), Solution/Suspension Precursor Plasma Spray (SPPS), Detonation Gun (D-Gun), Cold Spray, and Warm Spay techniques. Two main process parameters, namely carrier gas temperature and particle velocity, are compared in Fig. 2.7 for some thermal spray processes.

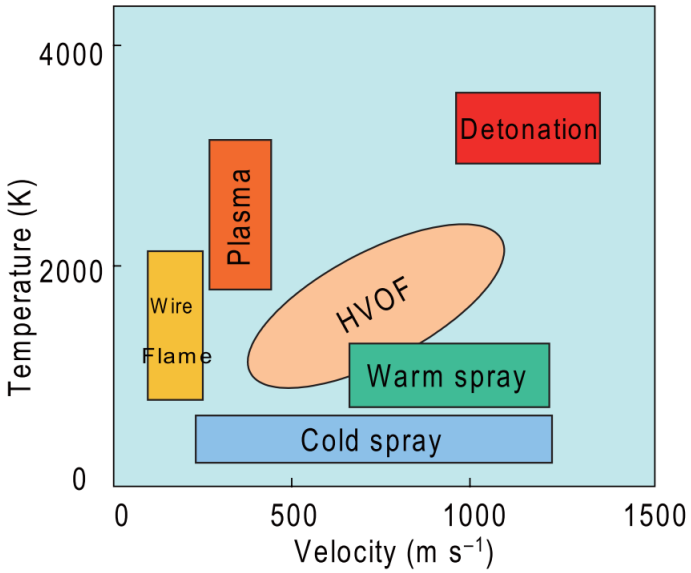


FIGURE 2.7: Comparison of different thermal spray processes in terms of particle velocity and temperature. [172]

Thus, coatings produced by thermal spraying techniques have a splat-like structure, porosity between splats, microcracks, and a fine columnar grain structure due to the rapid solidification of the splat.

Atmospheric Plasma Spray (APS) The most common example of topcoat deposition is atmospheric plasma spray (APS), where inert gas (typically an Ar-He mixture) is heated by an electronic discharge, creating a high-temperature plasma plume. The powder feedstock with characteristic size up to 100 μm is injected into the plasma jet where it melts and accelerates and is delivered to the substrate (Fig. 2.8). The majority of static components of gas-turbine engines, such as combustor tiles, are applied via this method.

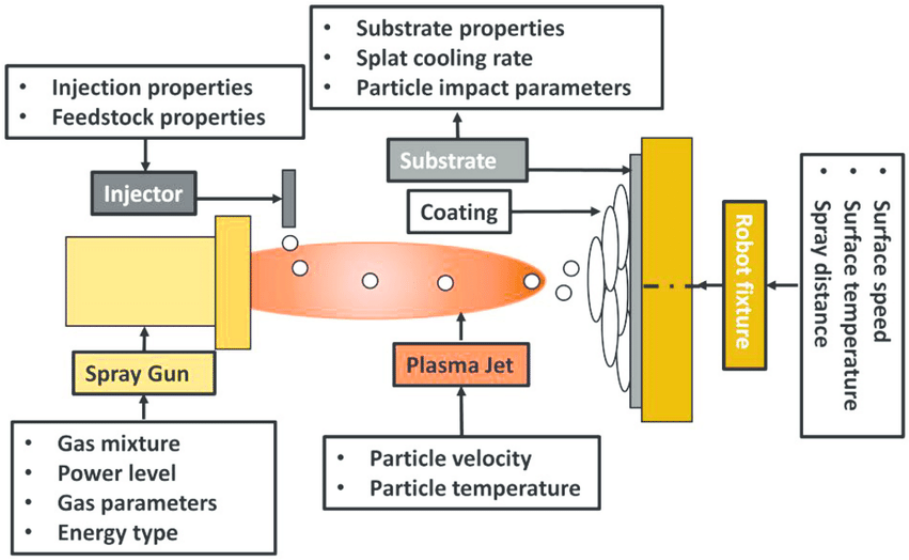


FIGURE 2.8: Schematic of Atmospheric Plasma Spray process and governing process parameters. [86]

To increase the temperature of the plasma jet, molecular gases such as hydrogen and nitrogen are added to the inert gas. In plasma spray, jet temperatures can exceed 14000 K [313].

Feedstock material can be added to the jet coaxially or radially just at the exit of the nozzle. The arc-heated plasma is accelerated in a converging nozzle and exchanges its kinetic energy with the powder feedstock material. To reduce particle oxidation issues (in the case of metallic materials) and modify the flame shape, the jet can be shielded with a secondary inert flow [289]. For the APS process, the selection of appropriate feedstock particle size is important; the upper size boundary is dictated by the ability to melt the particles before reaching the substrate. Deposition of submicron particles is limited due to its low effective cross-section, resulting in limited particle acceleration [142].

APS process can develop particle velocities of 130-180 m/s and requires high power inputs, typically 50-100 kW [278, 354]. By varying the process parameters, the coating porosity can be adjusted in the range of 5-15% and above [200, 55]. APS process is widely used for coating static components of aero-engines, providing thermal conductivity lower than the dense material, however, having poor bonding strength and resistance to mechanical impact. Compared to

vapour-deposited topcoats, APS topcoats have lower thermo-mechanical compliance and generally lower durability [235], which also applies to all coatings produced via thermal spraying methods.

Solution/Suspension Precursor Plasma Spray (SPPS) In order to overcome the lower particle boundary limitation for the APS process, SPPS technology can be used. Relying on the same physical principle as APS, SPPS heats and accelerates the particles with an inert gas plasma jet, the particle size is artificially increased by creating a solution or suspension of the particles. The mixture (solution or suspension) is first atomised and the sub-micron or nanometre-sized particles are coated with the binder; when the atomised feedstock reaches the jet, the liquid solvent with the particle is propelled and heated, during which the liquid evaporates and then the solid material melts. The benefit of the SPPS technique compared to APS lies in its ability to deposit fine columnar coating, similar to one produced by vapour deposition in vacuum. [236, 143, 26].

Combustion Flame Spray (CFS) Instead of accelerating the carrier through electric heating, as is the case in the APS process, the energy can be taken from an exothermic chemical reaction between a fuel and an oxidant. This process, a predecessor of APS, is called Combustion Flame Spraying (CFS). The maximum temperature combustion products can develop is limited by the adiabatic flame temperature, dictated by the fuel and oxidiser. Commonly, the feedstock is melted and accelerated by burning acetylene in oxygen with at $3100^{o}C$ [128]. Due to the lower combustion temperature, it is generally challenging to deposit a coating of high melting point materials, such as ceramics, and the powder is fed axially into the flame to increase its in-flight time. In CFS process [119]. The particles in the CFS process typically reach velocities in the range of $30 \div 120$ m/s and are characterised by a high level of porosity.

High-Velocity Oxy-Fuel Spray (HVOF) HVOF is the successor of the CFS process, where the spraying gun is modified with a combustion chamber followed by a convergent-divergent nozzle, where the combustion products are accelerated to

supersonic speeds. This allows reaching particle velocities of 1000 m/s [319]. The stand-off distances are typically higher compared to CFS and APS techniques due to the high velocity of the particles and consequently shorter periods of heat exchange between the jet and particles. The HVOF coatings are typically characterised by high density and are often used to apply metallic bond coats ([309, 139].

Detonation Gun (D-Gun) In D-Gun spraying, the feedstock material is accelerated by a discontinuous combustion process. Among all thermal spraying techniques, detonation gun reaches highest temperatures (4000^{o}C) and jet velocity (up to 3300 m/s shockwave that propels the feedstock), which allows to obtain particle velocities exceeding 1200 m/s [125]. The fuel for a detonation gun, like CFS, is typically acetylene with oxygen as an oxidiser. Combustion mixture together with the feedstock material is injected into acceleration tube, where the mixture is ignited at frequencies 1-100 Hz. Due to high particle velocities, the such method produces dense coatings with high bonding strength and limited in-flight oxidation [150, 356].

Cold spray For oxygen-sensitive materials, the cold spray technique is often applied. In this method, powder feedstock is accelerated to high velocities below melting point temperatures, which allows reducing in-flight time and oxidation rate. This method was developed accidentally while experimenting the high-velocity particle erosion, and the rapid coating formation was observed [172]. The solid-solid particle interaction can be summarised in Fig. 2.9.

Instead of combustion gases, cold spray relies on high pressure, ≈4MPa, process gases (nitrogen or helium and air), which is accelerated in a convergent-divergent nozzle. Since the cold spray is an all-solid-state process which relies on plastic deformation of the material, its use with ceramics is limited [137]. With the combination of very high velocities and low temperatures (below 800 ^{o}C), cold spray is able to produce very dense and well-adhered coatings with limited or no oxide strings within the coating[215, 296, 42].

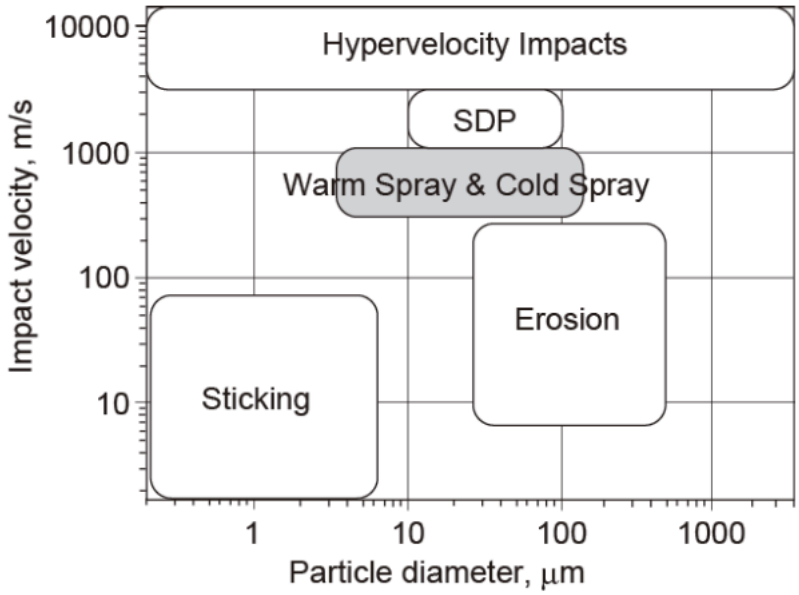


FIGURE 2.9: Classification of solid-solid particle interaction in terms of impact velocity and particle diameter.[172]

Warm spray In order to deposit a wider range of materials without thermal deterioration (e.g. purity, crystallinity), it is beneficial to have solid-state interaction. For some applications, it is beneficial to increase the temperature in the range of 800 - 1500 ^{o}C, since adhesion, cohesion, and densification behaviour relies on the mechanical properties depending on the temperature [148].

In warm spray, a supersonic jet is used which reaches speeds in the range of 900-1600 *m/s*. A warm sprayed coating is typically characterised by high density and low oxidation levels compared to the APS process. Highly-active metals, metallic glasses can be fabricated with high purity and high density; besides, metal oxide TiO_2 deposition was reported which kept the original crystal structure [149].

Vacuum deposition processes

Physical Vapour Deposition (PVD) Physical Vapour Deposition processes are atomistic deposition processes in which the target material undergoes phase transitions from solid or liquid to vapour phase in form of atoms or molecules and travels to the substrate in form of vapour through a vacuum or low-pressure gaseous environment, where it condenses onto the substrate surface. Since

deposition happens atom-by-atom, deposition rates are much lower compared to spraying techniques; typical deposition rates of PVD systems are 1-10 nanometers per second, and PVD is utilised for thin film application [204]. By far, the most common technique from this branch for topcoat application is the electron beam physical vapour deposition (EB-PVD) technique.

Electron Beam Direct Vapour Deposition (EB-DVD) EB-PVD is a vacuum deposition(evaporation) technique, where the energy source for material evaporation are accelerated electrons, typically from a thermionic source. The electron beam is accelerated with a potential of several kilovolts and bombards the surface, acting as an energy carrier and is absorbed by the material, where it interacts with the crystal lattice, and its kinetic energy is eventually surrendered by it. This energy breaks the lattice bonds, melting and evaporating or even sublimating the material [121]. Typical pressure during deposition process is 10^{-5} - 10^{-9} Torr.

EB-PVD process is used for topcoat application on the dynamic components of the engine. ZrO_2 undergoes a dissociation reaction, creating a positively charged cation of zirconia with oxygen vacancy; sometimes, it is beneficial to apply a negative potential to the substrate material (substrate biasing, [355]), thus increasing the energy of the particles, which may result in higher adhesion of the layer. The substrate is usually heated, which allows to an increase in the coating adhesion, i.e. adatom–substrate and adatom–film diffusion by giving the adatoms additional energy.

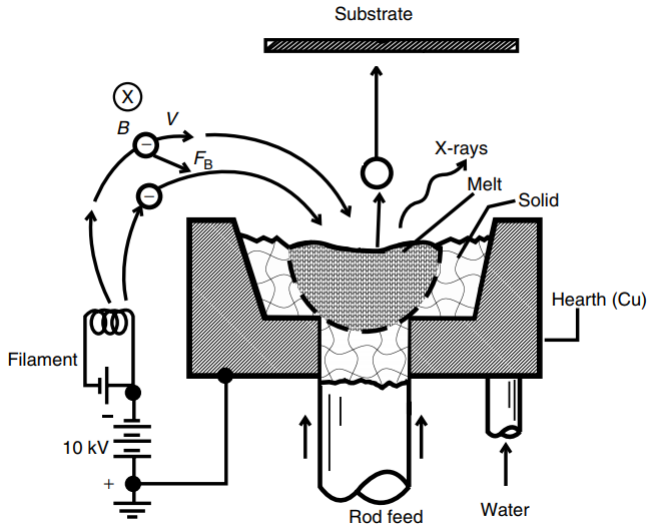


FIGURE 2.10: Electromagnetic alignment in EB-PVD system. Modified schematics from [121]

Plasma-Spray Physical Vapour Deposition (PS-PVD) PS-PVD is a low-pressure deposition technique from the vapour phase, where a high-energy plasma gun is used and operates at reduced work pressure of 0.1 kPa (compared to conventional vacuum plasma spraying (VPS) and low-pressure plasma spraying (LPPS) in the range between 3 and 20 kPa) [333]. Due to the high energy plasma and reduced work pressure, the deposition process happens from the vapour phase. By varying the process parameters, both splat-like and columnar microstructure can be obtained. At such low pressures, the plasma plume expands and therefore creates more homogeneously distributed temperatures and velocities of the particles. At the same time, the working pressure of 0.1 kPa is still much higher than that of other PVD, e.g. EB-PVD, techniques (10^{-3} - 10^{-7} Pa). Strain tolerant topcoats with comparable performance to EB-PVD coatings can be achieved [47, 333].

Chemical Vapour Deposition (CVD) Previously discussed thermal spray and PVD techniques, although some of them have been widely utilised, have a limited capability to coat complex-shaped components due to their line-of-sight nature. An alternative family of processes, chemical vapour deposition methods, can coat components with excellent conformal coverage[74, 89]. In CVD, the coating is formed

from the reaction of volatile precursors on the substrate surface (Fig. 2.11). There are many CVD methods for YSZ deposition.

One of the most common processes is thermal CVD, where the precursor (most commonly, a metalorganic mixture of $Zr(dpm)^4$ $Y(dpm)^3$, or $Zr(thd)^4$ $Y(thd)^3$, where dpm is dipivaloylmethanate and thd is tetramethyl-heptanedionate) with the oxidiser carried by inert gas is heated by a hot wall or hot filament, which causes decomposition of gas and generates radical species that can reach the substrate by diffusion. Activation temperature is usually high (773-1173K), and leads to cubic and mixed monoclinic and cubic phase morphologies of deposited YSZ used for the production of solid oxide fuel cells, gas sensors, and gas separation membranes.

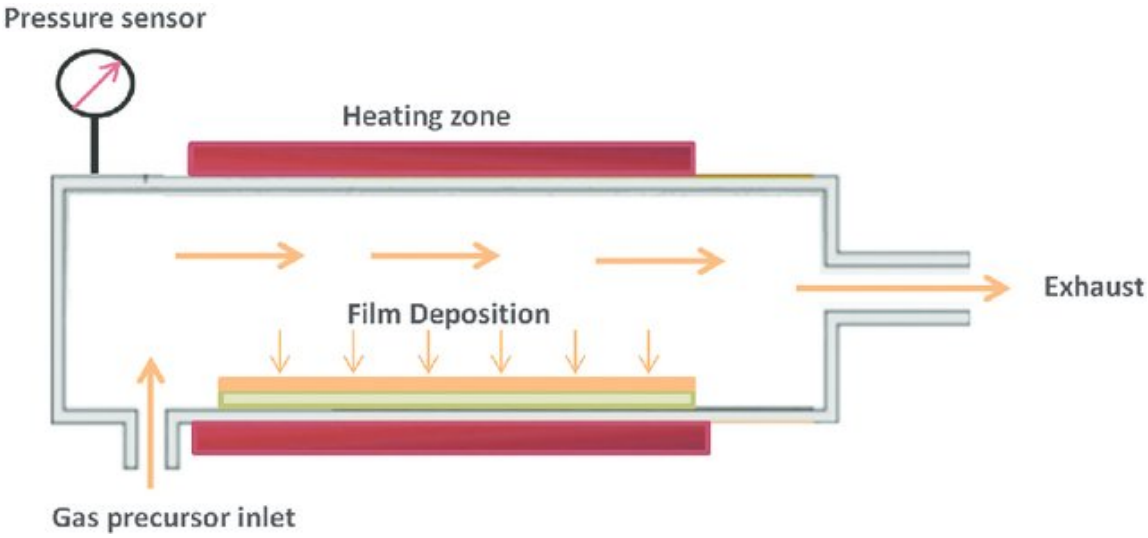


FIGURE 2.11: Schematics of a thermal CVD process.[372]

Thermal CVD typically has low deposition rates, 0.5-20 μm/h, and after thorough optimisation deposition rates of 108 μm/h were achieved [107]. Later, Betrand and Mevrel [25] developed a more effective process by adding an auxiliary microwave generator. In this process, called Plasma Enhanced CVD (PE-CVD), the chemical reaction was energy-enriched by means of microwave plasma, and higher deposition rates, 250 μm/h and above became possible. In PE-CVD, the coating consisted of a preferable metastable *t'* phase; the deposition temperature is high for most of the CVD processes and plays a crucial role in the phase and microstructure formation, where higher deposition temperatures (1173 ^{o}C) create

regular well-developed columns similar to those produced by EB-PVD. Another popular way to control the deposition process is by means of laser heating, laser-assisted CVD (LA-CVD), developed in the early 1980s [227]. In LA-CVD, the reaction takes place at the substrate heated by the laser in a cold-wall CVD chamber. The combination of relatively high precursor concentration and laser power of 250W created deposition rates of 660 μm/h, and can potentially become a new state-of-the-art method for TBC deposition [89, 105]

Other deposition techniques

Wet chemical deposition: sol-gel Slurry deposition techniques fall into the category of wet chemical deposition wherein the material to be deposited is mixed with a solvent, creating a solution, and the slurry is applied on the surface, dried, and sintered [54, 62]. The most common slurry deposition routes are suspension slurry and sol-gel slurry. In suspension slurry, YSZ powder, typically in the submicron range, is mixed with a binder, such as water pr 1-propanol, creating a suspension. In sol-gel, the particles are fabricated from metal alkoxide solutions, for instance, zirconium (IV) propoxide ($Zr(OPr)_4$), yttrium (III) nitrates hexahydrate, and 1-propanol acting as a solvent [247]. Such composition is used to generate submicron YSZ powder upon supercritical drying of a solvent, creating a gel [328]. The following heat treatment (sintering) is an essential step in promoting particle agglomeration and enhancing coating cohesion and adhesion. Heat treatment is often performed in a furnace or by means of laser radiation, with the temperatures reaching 1150 °C, limited by the melting temperature of the substrate [336, 328]. Various routes of sol-gel manufacturing techniques are presented in Fig. 2.12.

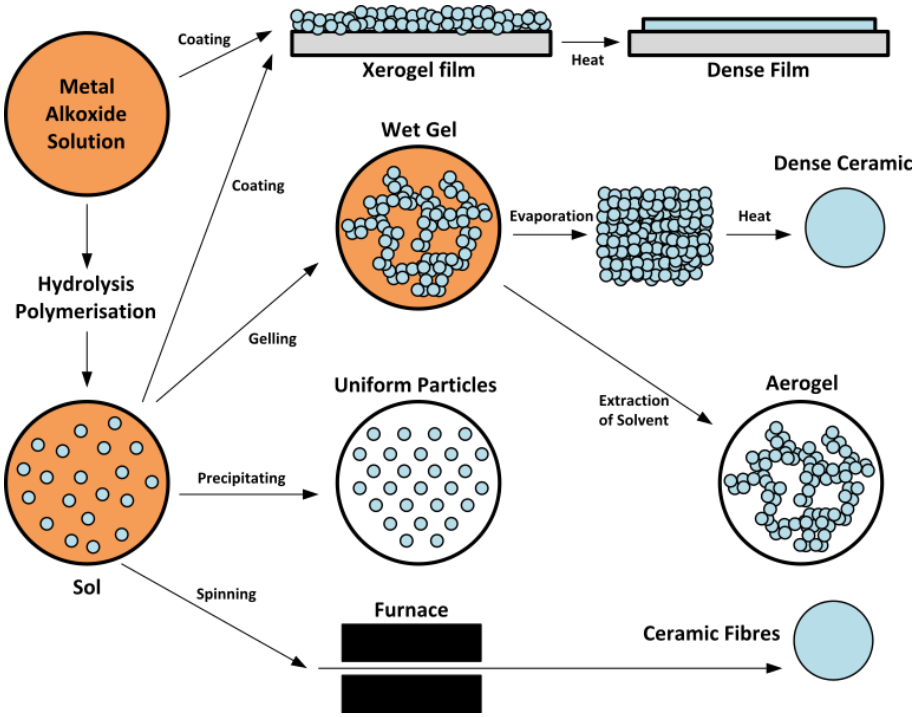


FIGURE 2.12: Different routes and stages of the sol-gel technology. [368]

Slurry deposition techniques can coat complex surfaces, and have been widely implemented for sensor fabrication, UV-inhibiting sunscreens, laser optical elements [62, 39]. The durability of sol-gel-produced coatings can overcome those produced by the EB-PVD method in certain tests [63].

Direct Laser Deposition (DLD) Direct laser deposition is a method of manufacturing components in bulk or depositing coatings by means of laser melting (Fig. 2.13). In DLD, the powder material is delivered by a carrier gas to the substrate, where it is heated and melted by a laser beam. The coatings typically have a dense structure with high hardness and excellent erosion resistance [20, 230]. Typically, DLD-produced ceramics suffer from poor bonding, cracking, and lowered fracture toughness [131, 130].



FIGURE 2.13: Direct Laser Deposition for coating application. [368]

Vapour deposition in atmospheric pressure Very few studies were conducted on the possibility of laser deposition in atmospheric pressure [288, 159]. Zihao Ouyang [231, 232, 233] developed a YSZ deposition system based on a nanosecond Nd:YAG laser and a 6kW microwave plasma torch and achieved a columnar structure on a René N5 superalloy, Fig. 2.14. In his study, Zihao used high-temperature plasma for both delivering the ablated particles to the substrate and for heating up the substrate to temperatures from 20 °C to 1300 °C. The study was mainly focused on plasma characterization of plasma with limited attention paid to material characterisation. Adhesion of such coating is questionable since the vaporised molecules leave the target to collide with molecules of the ambient environment, resulting in loss of energy and lower adhesion.

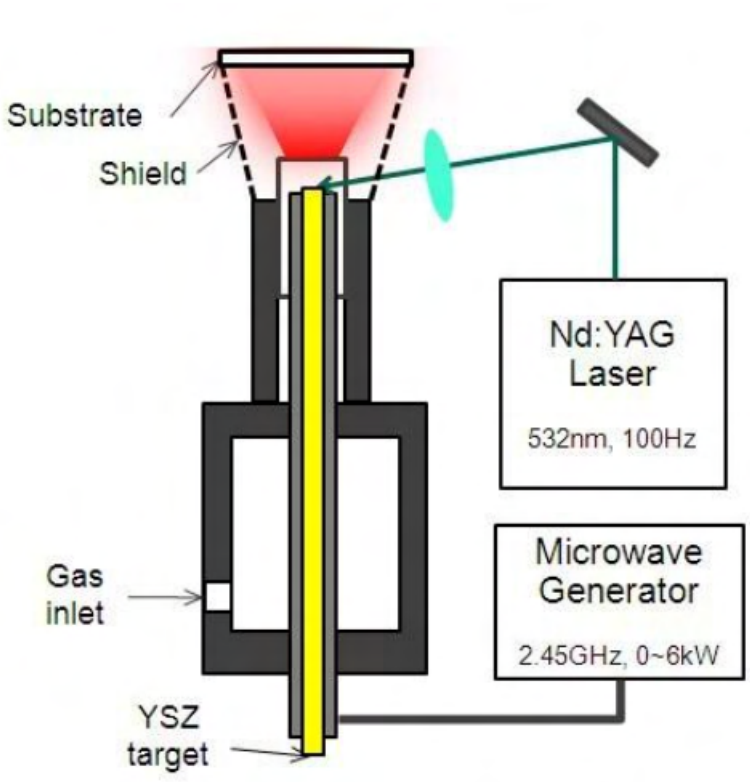


FIGURE 2.14: Laser Assisted Pulsed Laser Deposition experimental setup [231]

.

Adhesion strength was tested by scratching the coatings with a thin plastic stick [233]. Due to deposition setup limitations, it was impossible to achieve separate control of the substrate temperature and plasma torch flow and temperature, which is presumably beneficial to control independently. This research work demonstrated the potential possibility of columnar structure deposition in atmospheric pressure. The microstructure consisted of separated columns (Fig. 2.15). believed to enhance thermomechanical compliance of the coating, recreating the microstructure of vacuum-based deposition processes.

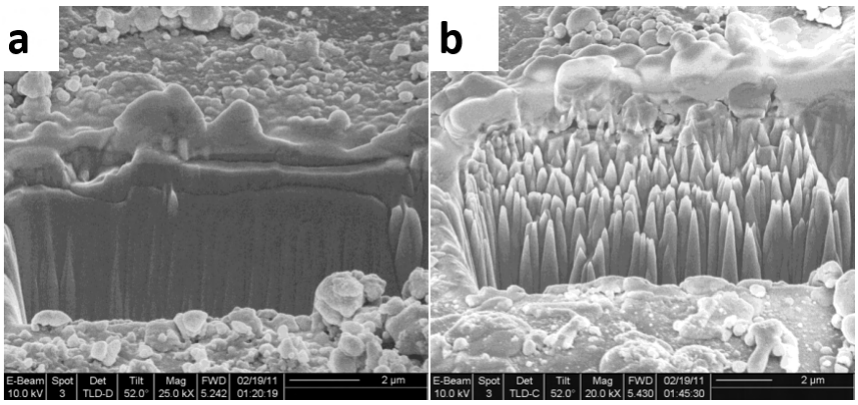


FIGURE 2.15: Columnar structure of YSZ, achieved by pulsed laser deposition in atmospheric pressure. (a) ion-beam milled cut for patch repair; (b) deposited columnar microstructure. [231]

.

2.1.4 Coating adhesion

Adhesion is the property of two dissimilar materials sticking to each other. Usually, it refers to two different meanings: in coating technology, adhesion is usually meant the mechanical force or energy that is required to separate the coating material from the substrate. The physical or chemical meaning of adhesion corresponds to the forces between molecules forming the contact. When two bodies are brought to close contact a new interface is formed, and the nature of interaction at the interface determines the adhesion energy [219].

Adhesion energy (E_a) can be defined as the difference between the initial state (E_i), i.e. before the contact, and energy in the final state (E_f), when the bodies are in intimate contact [212]:

$$E_a = E_i - E_f, \tag{2.1}$$

According to the equation above adhesion, energy must be in the order of magnitude of the surface energies of the bodies, in order of mJm^{-2} [219]. Here, adhesion is a purely interface phenomenon defined by a few surficial layers.

Coating adhesive properties can be described by the following theories:

(i) Mechanical theory;

(ii) Diffusion theory;

(iii) Electronic theory;

(iv) Dispersive adhesion theory.

Mechanical interlocking theory is based on topographical irregularities of the surface. The potential bonding area is higher on a rough surface, that on a smooth one. In thermal spraying techniques this bonding mechanism is believed to be the dominant one, and in order to increase coating adhesion the surface is "roughened", e.g. by shot blasting. Nevertheless, the topographical properties of the prepared surface must correspond to the applied coating, more precisely - with its viscosity. When the viscosity of the coating is too high, there is a chance that the coating material will not penetrate into the deep and narrow surface irregularities, or will solidify faster than the time necessary for the movement, resulting in poor adhesion.

Diffusion theory can be explained as the motion of *adatoms*, i.e. adsorbed atom, molecules and atomic clusters at surfaces [229]. This motion is generally driven by thermal energy and increases with temperature. This type of adhesion is affected by surface-adsorbed particle bonding strength, crystal lattice orientation, the difference in chemical potentials, and attraction or repulsion between the materials.

The main concept describing the kinetics of diffusion theory is known as nearest-neighbour adsorption (which further developed into next-nearest-neighbour), where the adsorbed atoms are residing at adsorption sites, which is changed by a jumping process. This is a probabilistic process, characterized by attempt frequency and a thermodynamic factor, defining the probability of a successful jump attempt.

Diffusion of adatoms is defined by different mechanisms, that dictate kinetics, adatom mobility, and temperature dependence. The jumping mechanism, the most basic one, explains the motion through the successive jumps from the adatom residence place. Atomic exchange, the second mechanism, is the exchange of surface vacancies fulfilling with an adatom and a surface atom. After this event

took place, the surface atom becomes an adatom and vice versa. Besides, diffusion of adatom congestions, or clusters, is possible, their movement can be a result of individual atoms displacement, section or the entire cluster at once [229].

Electronic theory. This type of adhesion is based on the idea of charge contrast between dissimilar materials because of the difference in Fermi levels [219], resulting in a double layer with an electronic potential difference. Here, apart from the electronic potential difference, charge separation plays a role.

Dispersive adhesion, or Van der Waals adhesion, is the type of attraction caused by so-called dispersive forces: It includes London forces and dipole-dipole forces. Among others, van der Waals forces are characterised by the weakest of all intermolecular forces. Dipole-dipole forces occur between polar molecules due to charge separation, such as in hydrogen chloride molecules. These forces are similar to ionic chemical bonds but incomparably weaker. The London force, called after Fritz London, is a type of intermolecular force occurring between nonpolar molecules and atoms as a result of the motion of electrons due to uneven distribution of the latter, therefore temporarily creating a dipole. Such a weak dipole can influence neighbouring atoms and molecules causing electrostatic repulsion or attraction and inducing a dipole on neighbouring atoms. Van der Waals forces frequently occur in nature, allowing geckos to adhere to walls and molecularly smooth surfaces through hierarchically structured setae [14, 88] to interplanar bonding in some crystals such as graphite [286] and MoS_2 [382].

2.2 TBC degradation mechanisms

The lifespan of thermal barrier coatings is limited. Due to a wide variation of the processes occurring within the coating is why TBC failure is not completely understood. The physical phenomena occurring during the lifetime of TBCs involve thermal conduction, thermal expansion, elastic, plastic, and creep deformation, diffusion, oxidation, phase transformation, radiation, sintering, fracture and fatigue [235]. It is known that depending on the microstructure of the

coating, or the deposition method, the coating failure mechanisms may differ [236]. Besides the typical heating/cooling cycles and subsequent TGO growth, TBCs are also susceptible to mechanical impacts, such as foreign object damage and erosion [352, 103]. Infiltration of molten sand, corrosion by molten Calcium–Magnesium–Alumino Silicates (CMAS), is a damage mechanism which can be expected in working conditions at sufficient temperatures [331, 253]. Fuel impurities, such as vanadium, sulfur, and sodium, in form of sulfate and vanadate salts and known to cause the TBC failure during service through the process known as hot corrosion [138, 209]. Sintering effects and phase transformation are particularily pronounced at temperatures above 1000 ℃ and also known to contribute to TBC failure [377].

Evans et al. [75] distinguished five major failure categories for thermal barrier coating systems, summarised in Fig. 2.16. 1. Spinels can form between the TGO and the bond coat or between the TGO and the TBC in some cases [299]. When this occurs, it is assumed (but not proven) that the spinel's "brittleness" causes delamination. 2. In other cases, particle impact and foreign object damage (FOD) cause local compression of the TBC, resulting in hot spots in the underlying bond coat that contribute to failure [222]. 3. Thermomechanical spallation at TGO, which includes the energy density in the TGO as well as imperfections in its vicinity. The failure scenario, in this case, obeys the following process: (a) Imperfections in (or near) the TGO form the nucleus of small cracks and separations. The growth is governed by the tensile stresses that form around these imperfections and the associated energy release rates. (b) The small cracks extend and coalesce once nucleated, but the TBC may remain attached to remnant ligaments. (c) Failure occurs when the ligaments detach over a large enough area to create either a large-scale buckle (designated LSB) or edge delamination that eventually spalls from the substrate [50].

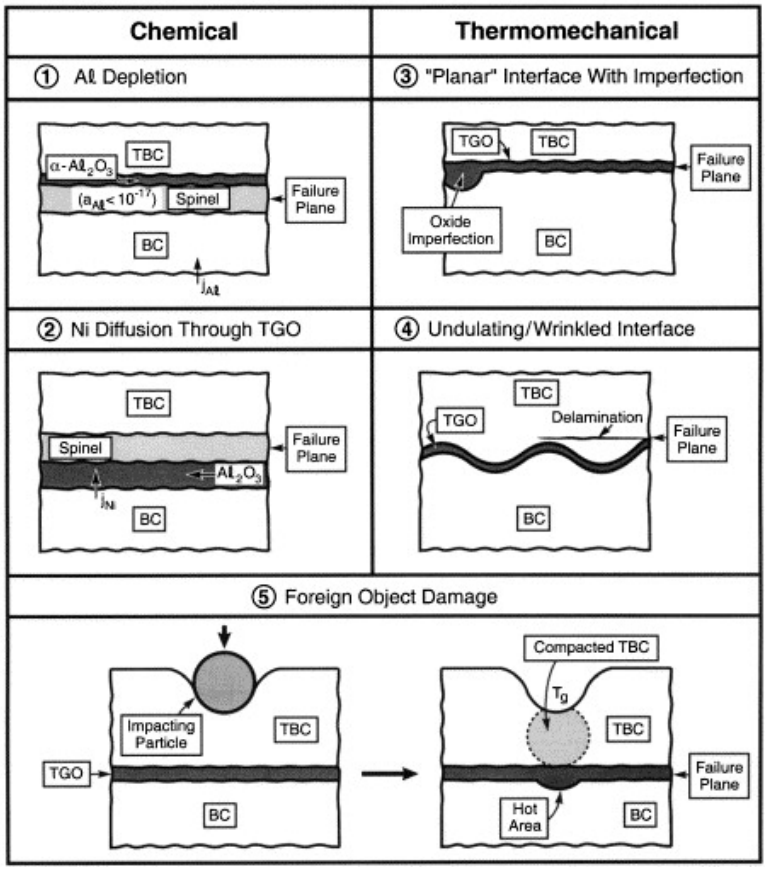


FIGURE 2.16: Major failure categories of thermal barrier coatings [75]

2.2.1 Oxidation and TGO spallation mechanisms

As the mechanisms of TBC failure, edge and buckle-driven delamination compete. The basic elements of this competition are represented by the failure map (Fig. 2.17) [75]. The TBC in the upper right has relatively high in-plane stiffness and limited strain tolerance, resulting in large residual stress and a high strain energy density. This energy density augments the TGOs and provides a strong driving force for edge delamination, which is resisted by mode II toughness along the most brittle pathway (among the TBC, TGO or interface).

The low in-plane modulus of the TBC in the lower left of the map does not resist small-scale buckling of the TGO, causing the system to fail under conditions similar to those for the TGO in the absence of the TBC. Small-scale buckling and edge delamination are suppressed at the intermediate levels of in-plane modulus, and the system resides in a "fail-safe" domain until degradation phenomena operate on either

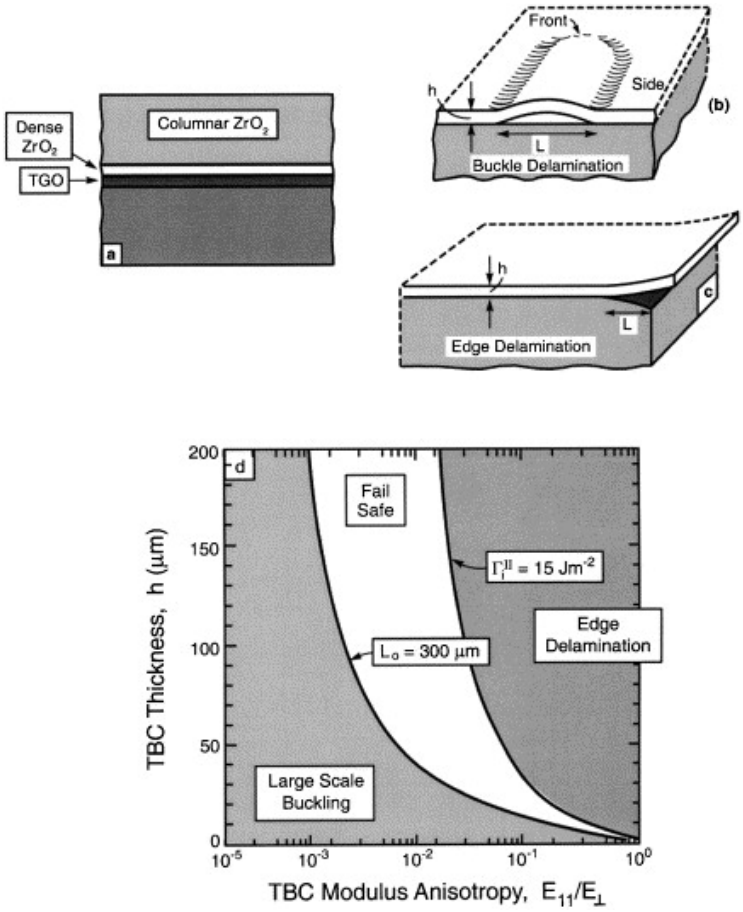


FIGURE 2.17: Edge delamination and large scale buckling as a function of TBC modulus anisotropy [75]

of these mechanisms. TBC systems operate in the following two main domains:

i. When the TBC is subjected to thermomechanical loadings typical of "power generation," with long high-temperature exposures and minimal thermal cycling, the cracking patterns are dominated by a combination of TGO growth stresses and thermal expansion misfit stresses.

ii. Aero-engines loadings, where extensive thermal cycling is more likely to be affected by strictly cyclic phenomena such as ratcheting, in which cyclic displacements of the TGO into the bond coat create delamination strains in the TBC.

2.2.2 Sintering effects

Most of the coating microstructures exhibit a certain level of thermomechanical compliance. In the case of thermally sprayed coatings, compliance is achieved by the internal porosity, intra-splat cracks opening and closure, and inter-splat sliding [153, 46]. With time, these characteristics deteriorate during the service life resulting in increased thermal conductivity and densification [53]. As a consequence, higher thermal stresses a generated within the coating-superalloy system. Zhu and Miller [383] studied the sintering of a free-standing plasma-sprayed ZrO_2 coating, and sintering was characterised by measuring shrinkage; other approaches utilise the measurements of elastic modulus change [177].

2.2.3 Phase stability of topcoat materials

At temperatures above 1200 ℃, the metastable tetragonal t' phase is partitioned to the stable tetragonal t and cubic c phases as a result of yttria diffusion within the material. The stable tetragonal phase can be further transformed to monoclinic m phase upon cooling with associated detrimental expansion of the lattice[210, 279].

Overcoming phase stability and sintering issues lead to the exploration of new stabilising materials. For instance, Gd_2O_3 stabilised ZrO_2 was investigated by Rahaman et al. [259], and higher phase stability of t' and lower sintering rate was found for gadolinia-stabilised zirconia. The effects of alternative stabiliser material were summarised in the table 2.1.

2.2.4 Effect of residual stresses on coating durability

The failure of YSZ TBCs is caused by a combination of residual loads and service stresses. Cracking and delamination of YSZ coatings are caused by residual strains induced in the coatings. Segmentation cracks are frequently detected shortly after thick coatings have been applied [110, 374]. The two major sources of residual stresses in plasma sprayed coatings are quenching, which is caused by rapid shrinkage and contraction of the molten splats during the coating deposition process [171, 170],

and thermal stresses, which are caused by a thermo-mechanical mismatch between the substrate and the coating during the post-deposition cooling stage.

Zhang et al. [374] used an analytical model and experimental data from four-point bend tests to evaluate the influence of residual stresses on the fracture properties of YSZ TBCs. The effect of thickness, elastic modulus, and residual stresses on coating fracture qualities can be described in this mathematical model (Fig. 2.18). The critical strain at which the first transverse crack formed was lower for coatings with low compressive stress and porous microstructure deposited at low deposition temperature, according to an investigation of the fracture properties of plasma sprayed YSZ TBCs on stainless steels deposited at different deposition temperatures. The deposition temperature has an effect on the fracture characteristics of TBCs. The coatings with the best crack resistance were those that were deposited at a high temperature and had a high level of compressive residual stresses. The fracture energy and mode of fracture toughness of the coating increased as the compressive residual stress rose.

2.2.5 Molten silicates penetration

Among all the failure reasons, in-service erosion caused by the deposition of a significant amount of calcium–magnesium–alumina–silicate (CMAS) at high temperature was found to be one of the most prevalent failure modes in EB-PVD coatings [45]. Sand particles, reaching the TBC-protected engine components during engine operation, become molten and adhere to the surfaces. This layer can significantly decrease the strain tolerance of the coating [45, 253] because of the excellent wetting characteristics of these glasses (can bee seen in Fig. 2.19), it penetrates the surficial pores and gaps, solidifies, creating a dense surficial layer and linked porosities, holding down the hole structure and increasing the elastic modulus of the system as a whole, especially in case of EB-PVD structure. Furthermore, the high-temperature CMAS-coating interaction was found to cause destabilisation of *t'* phase due to yttria depletion, and subsequent tetragonal-monoclinic transformation [253].

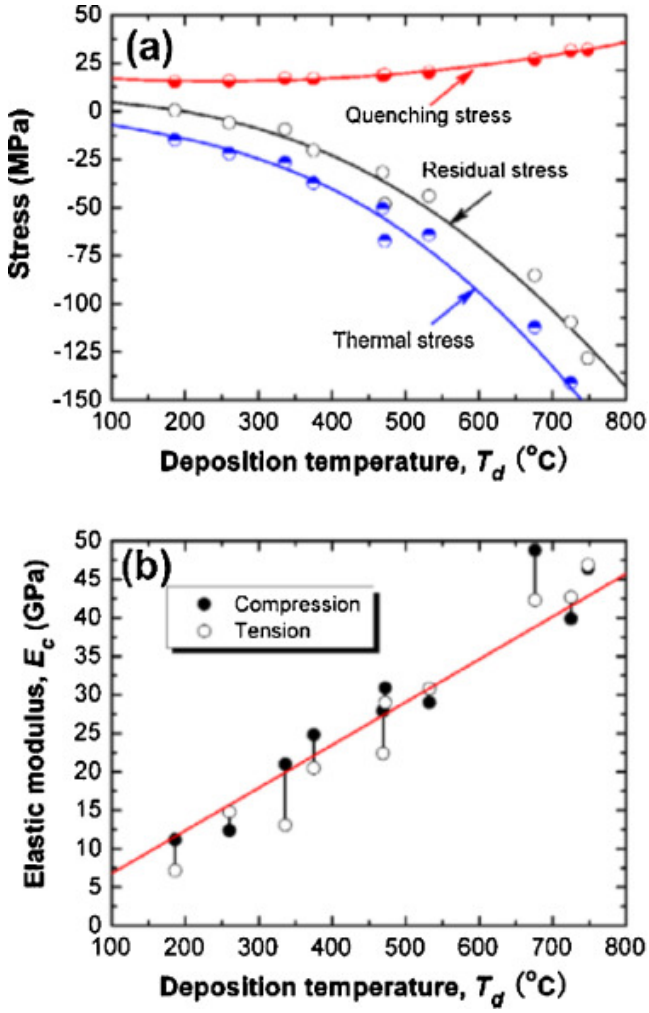


FIGURE 2.18: The effect of deposition temperature on (a) residual stress at the coating surface and (b) elastic modulus [374]

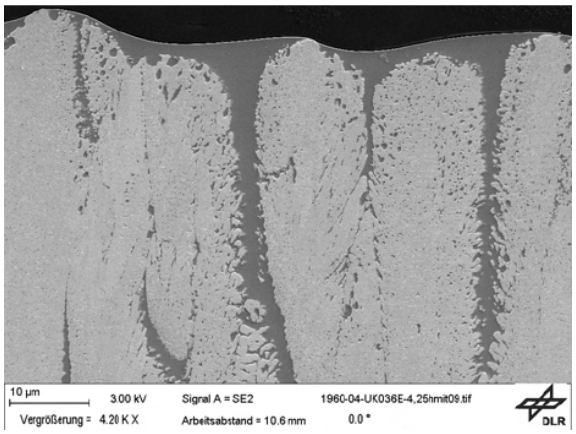


FIGURE 2.19: Microstructure of 7YSZ TBC column tips infiltrated by synthesized CMAS at 1260°C for 4.25hrs. [241]

CMAS mitigation techniques

To mitigate the CMAS attack on TBCs, Aygun et al.[16] incorporated 20 mol % Al_2O_3 and 5 mol % TiO_2 in the solid solution form of YSZ TBC (and not as a discreet second phase as described in some other works). The results reveal that the YSZ with Al_2O_3 + TiO_2 is efficient against CMAS assault by completely destroying the CMAS glass piercing front at 1121 °C.

Drexler et al. [68] employed the more adaptable APS technique rather than SPPS to deposit a solid solution with the same composition for testing thermal stability and CMAS resistance. At 1200 °C, the results showed that YSZ + 20Al + 5Ti APS TBC was extremely resistant to CMAS attack. The CMAS penetration depth was about one-third of the coating thickness before being thwarted by crystalline anorthite production at the leading edge. The CMAS attack mitigation strategy employed by the APS technique was comparable to that of the YSZ + 20Al + 5Ti TBC deposited by the SPPS approach in previous research. The success of the APS process coating, on the other hand, provides advantages in terms of process diversity, simplicity of processing, and reduced cost.

2.2.6 Foreign object damage (FOD) and coating erosion

The impact of high-velocity objects results in entire thermal barrier destruction, whereas erosion can cause incremental thickness loss during operation. Depending on the size of the impacting object, three modes can be distinguished [351]:

• small particle erosion. Damage is restricted to the TBC's near-surface region, and material removal comes from cracking of neighbouring columns in case of EB-PVD coating, and from splat loss in case of APS coatings. After impact, generally at a depth of 10–20μ m, and the concurrent loss of material from a cluster of nearby columns. Plastic deformation of the near-surface region is evident at high temperatures, and this limits the depth to which cracks spread.

• transition mechanism that occurs between erosion and FOD, called compaction damage, exists for EB-PVD TBCs. It entails column compaction without the

cracking that happens during erosion or the massive column deformation that occurs with FOD.

• Foreign Object Damage (FOD), involves gross plastic damage and the propagation of shear bands down to the BC-TC interface.

The findings of Nickolls et al. [221] suggest that erosion resistance of EB-PVD coatings is ten times higher than that of APS coatings, both at room temperature and at 910 °C. Significant difference in erosion resistance is attributed to poorly bonded splats in APS coatings.

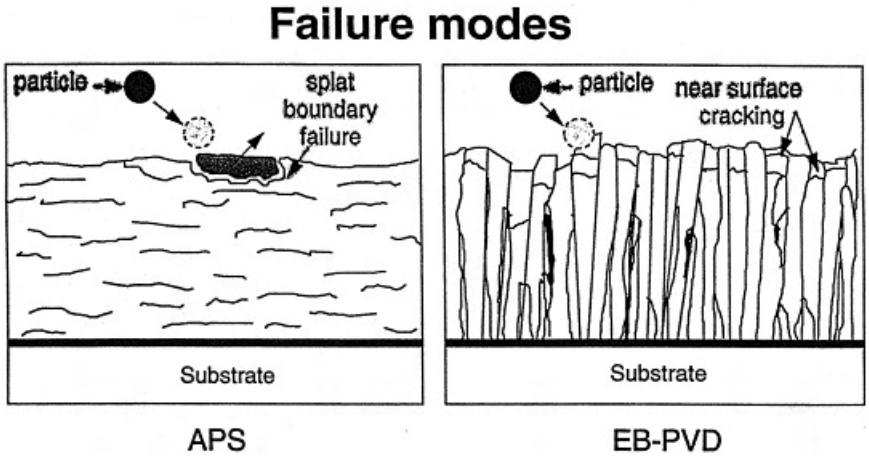


FIGURE 2.20: A schematic diagram of the failure modes for an APS and EB-PVD TBC.. [221]

Erosion and foreign object damage resistance can be potentially improved, for example by densification of the surficial layer, also known as "glazing" [317], adding an additional layer of alumina or chromia particles or precipitates, which will increase the wear resistance of the coating by increasing micro-hardness of the coating[265, 140].

2.2.7 Thermal barrier coating system modification techniques

To tackle the durability issues and adopt the properties of the coatings to comply with the engineering requirements, the thermal barrier coatings system has been constantly evolving. First, the two most important sources of durability are coating

composition and coating microstructure. In order to increase the fracture toughness of the oxide, the composition of the ceramic coating was adjusted to stabilise its tetragonal *t'* phase. The microstructure of the coating, in its turn, is dictated by the manufacturing method of the coating, mainly divided into two groups: vertical columnar grains with high adhesion for vapour deposited coatings, and lamellar structure for thermal spray coatings.

Pre-deposition TBC modification and modified deposition processes

Nanoheap TBC design Engineering nanostructured YSZ TBCs to mitigate sintering effects has been the subject of several studies. Because of the smaller powder size, nanostructured coatings offer significant increases in TBC service performance, allowing for improvements in physical and mechanical qualities. To generate nanostructured air plasma sprayed YSZ coatings, the spray parameters must be carefully controlled to avoid complete melting of nanostructured YSZ agglomerates in the plasma jet and to maintain the agglomerates' nanostructure in the coating microstructure, schematically shown in Fig. 2.21. Controlling the number of molten and porous semi-molten particles previously incorporated in the coating microstructure can significantly alter the coating's mechanical response [187, 188]. The thermal shock tests were conducted out at temperatures ranging from 1000 to 1300 degrees Celsius and showed significant improvement in thermal cycling life [184]. This approach shrinks down the spraying parameter window [187, 182].

Lima and Marple [186] studied the microstructure of air plasma spray coatings made from nano-agglomerated YSZ powders in order to avoid sintering effects. The results revealed that heat treatment increases the coarse porosity levels of the nanostructured coating. After 20 hours at 1400 °C, the coarse porosity level of the nanostructured coating was 3.5 times that of the original conventional coating. Because the sintering rates of the matrix and nano-zones in the nanostructured coating differed at high temperatures, an unique behaviour emerged. Nano-zones have a stronger driving force for sintering due to their bigger surface area. As a

result, the nano-zones shrank more quickly than the matrix, resulting in coarse pores.

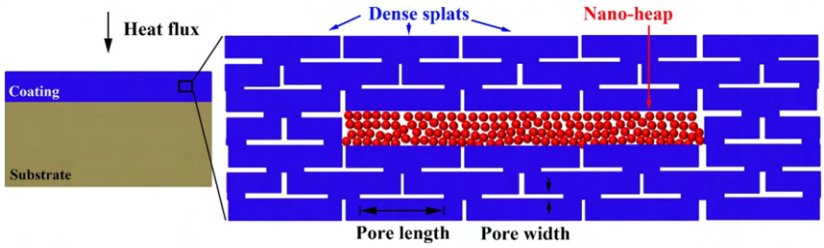


FIGURE 2.21: Schematic of the orientation and dimensions of the 2D pores. [182]

The coarsening of the nanoparticles, as well as sintering due to their greater surface area, are challenges for nanostructured coatings at higher temperatures [255]. Sintering effects cause irreversible changes in coating structure, resulting in a decrease in heat conductivity [104]. Nanostructured coatings have lower heat conductivity due to increased porosity. Because of the sintering of the coating, the microstructure changes significantly with heat treatment duration, and the grain size of the nanostructured zirconia coating grows dramatically with annealing time [146]. This suggests that the sintering of the nanostructured coating contributes more to its thermal conductivity than the traditional coating. The thermal barrier effects of nanostructured coatings are more sensitive to the temperature. In effect, this modification technique acts as a discontinuity and can be seen as a filled pore. However, such advantageous modification approach can lead to a decreased erosion resistance of the coating.

Graphene protective coatings for enhanced oxidation resistance Refined metals, which are frequently utilised in academia and industry, are chemically reactive and hence require a protective coating to prevent contact with the reactive environment. Ultra-thin coatings such as graphene are known to act as an oxidation barrier.

Graphene has outstanding thermal and chemical stability at significantly higher temperatures (>1500 °C) [59]. Graphene's characteristics make it excellent for protective coatings. Graphene has been utilised to coat metal surfaces as a protective layer [42].

Nayak et al. [220] showed the use of CVD-grown graphene sheets on the surface of a Ni substrate to shield it against air oxidation. There were 2 types of samples used. The first set of samples consisted of pure Ni foils with a thickness of 0.1 mm, whereas the second set of samples consisted of graphene-coated Ni foils with the same dimensions, both manufactured at low temperatures (800 °C). Nayak found excellent oxidation resistance up to 500 °C, after which the coating disappears. Although graphene and graphene oxide can present an excellent oxidation barrier, the temperatures are far below the temperatures used in aero-engine environments. To date, no reports were found for graphene-TBC systems, nonetheless, graphene-enhanced coatings can increase the oxidation resistance of the topcoats.

Pre-deposition substrate/bondcoat Texturing Besides the classic surface preparation methods such as grit blasting, non-traditional surface modification approaches have been utilised. Given the thermomechanical stress distribution as well as mechanical adhesion depends on the geometry of the substrate, the bondcoat - topcoat interface can be modified in a beneficial way. The study of Kromer et al. [165] evaluated the impact of laser texturing on a bondcoat-less TBCs in oxidation and creep tests and found some improvement in coating durability and coating adhesion, compared to grit-blasted samples. In their study on thermo-mechanical fatigue of the same system, [164] cracks were found to propagate above the bondcoat-topcoat interface, and the reported crack bifurcation in the vicinity of holes was attributed to compressive stresses in the vicinity of laser-patterned holes. Kromer also reports tripled adhesion strength for laser-patterned surfaces [163]. Wang et al. [340] utilised a one-dimensional array of grooves at the bondcoat surface prior to topcoat deposition. Wang reported an increased mechanical interlocking strength of the topcoat-bondcoat layers, and records different crack propagation paths for varied surface patterns, guiding the cracks to the bondcoat - substrate interface at high values of roughness.

Controlled TGO growth (pre-oxidation) As spinels and nickel oxides are known to reduce the thermal cycling life of the coatings, pre-oxidation treatment is a beneficial technique to suppress their formation by growing a continuous TGO

layer in a controlled environment. Chen et al. [44] in the study of APS-deposited coating found that a pre-grown TGO layer in vacuum and low-pressure oxygen atmosphere can suppress the formation of spinels, reduces the growth rate of the TGO and show an increase in thermal cycling life of the coating. A more recent study by Takahashi et al. [305] with air- and vacuum-grown TGO layers find that vacuum-oxidised samples exhibit a higher level of surface roughness compared to air-exposed samples.

Post-deposition modification

Grooving approach One of the approaches for durable thermally sprayed TBCs - segmenting the coating into patterns. This can be done, for example, by creating a grooved, or segmented, texture at the surface via laser ablation (Fig. 2.22) [155, 64], waterjet [111, 145], or conventional machining. This approach was probably inspired by the columnar structure, achieved by the EB-PVD technique. The idea of matter separation leads to a decreased effective elastic modulus leading to overall stress relaxation within the coating, crack arrest at the artificially created gaps, and surficial stress reduction, as proposed by Khan et al. [155]. This powerful technique hasn't found a particular research interest but found its application in industry [111, 145, 302]. Furthermore, the mechanism responsible for TBC service elongation was explained ambiguously, and perhaps can be further expanded. The proposed groove design in the works of Khan had limited investigation, based on the design of experiments and trial and error approach; to date, a fundamental study on TBC grooving is still absent and can open new possibilities in designed coating microstructures.

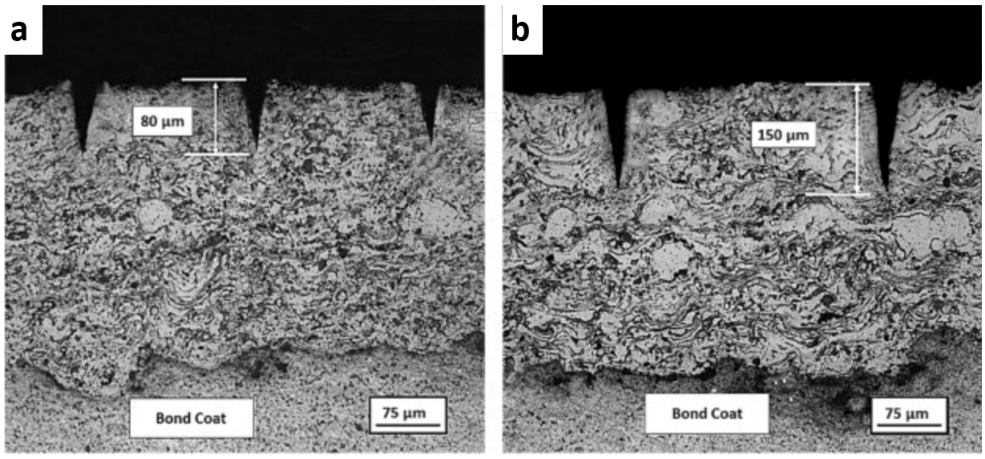


FIGURE 2.22: Cross-sectional SEM morphology of laser-textured coatings. [64]

In general, strain tolerance improvement will reduce thermal expansion stresses as well as thermal expansion mismatch stresses by:

(i) providing a pattern of gaps. Separated columns in the EB-PVD cross-section provide the structure with space and new degrees of freedom, letting the structure accumulate less stress.

(ii) Elastic modulus reduction. These two properties are actually two sides of the same coin: separated columns in EB-PVD can be described as a layer with decreased "effective" elastic modulus: in such a coating, the ratio between horizontal and vertical elastic modulus can reach the values of 0.2 (for further understanding of the values, $E_{vertical}$ of YSZ EB-PVD coating = 215 GPa at 25°C [197]).

Glazing approach One of the approaches involves surface remelting of the coating, or laser-glazing, creating a dense layer with decreased roughness and a network of cracks. There are many reports of the improved properties of a coating with such a microstructure modification: X. Zhong et.al. [381] reported that a laser-glazed layer enhances hot-corrosion behaviour of TBC in V2O5 environments, Petitbon et.al. [242] reported that the plasma-sprayed ZrO2 coating had exhibited a higher thermal shock resistance after laser-glazing in diesel engine conditions. Wang and Tian [338] showed the enhanced microhardness of the remelted region and improved erosion resistance. Tsai et.al. reports an increase in microhardness from 550 HV for an as-sprayed APS coating to 1550 HV on a glazed layer [316].

However, a deep microstructural analysis of the laser-remelted TBC and TBC solidification phenomena found little attention from researchers, generally reporting the existence of cracks, dense layers, and fine-grained structures.

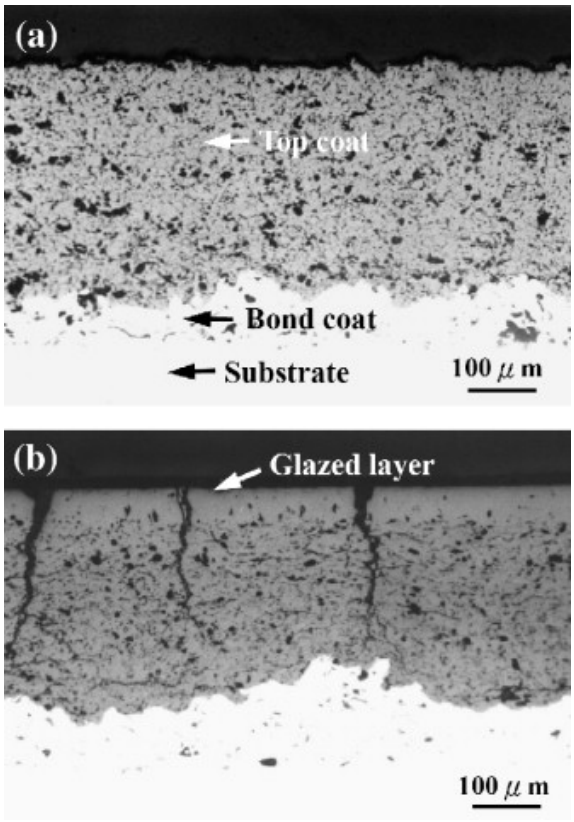


FIGURE 2.23: Typical optical cross-sectional microstructure of TBCs: (a) plasma-sprayed; (b) laser-glazed. [317]

In order to control the microstructure, it is necessary to understand the physical phenomena of solidification, which has been investigated scrupulously for metals in welding, directional solidification casting, etc.. Grain size, geometry, and orientation can play an important role in the mechanical properties of the material, therefore it is important to understand, control and predict the resultant grain structure of the remelted layer.

Laser glazing as a physical process is similar to laser welding: a moving energy source breaks the bonds in a crystalline lattice, creating a pool of molten material. The molten material will eventually solidify due to the heat exchange with the matter itself and the environment, which is the key parameter in obtaining the control of the microstructure: solidification, conduction, and convection dictate the properties of

the affected material, and both microstructural properties, such as grain geometry, such as size and shape [348, 349] and macrostructural features, such as geometry if the molten pool and the surface shape, appearance cracks [341] and generated residual stresses [33].

However, grain growth has never been investigated in for TBC surface remelting, neither the effect of grain size, which can vary significantly, depending on the heat input, from microns to several tens of microns nor its shape and geometry.

2.3 Laser Beam Processing

Laser processing of solids is a direct, local, and material-selective process, which has been employed for machining difficult-to-machine, hard and brittle materials. With the aid of lasers, it is possible to remove material without mechanical damage, with weakly expressed or absent thermal effects, while having no tool wear and excellent dimensional accuracy. In the following chapters, laser beam processing is used as the main tool for the modification of TBC structures: due to its non-contact nature and indifference to material hardness, the laser presents a great tool for machining difficult-to-cut ceramic materials, such as refractory oxide ZrO_2. This section contains an overview of laser-beam processing and its influence on the surface integrity of machined parts. Due to a limited number of studies of laser machining on TBC, the section aims to provide a general overview of laser beam processing of materials, as well as its potential impact on the microstructure and properties of laser-machined workpieces.

2.3.1 Pulse length and physical process of material removal

When laser interacts with a material, photon energy, in the case of metals, is absorbed by free electrons in a thin superficial layer, typically about 10 nm, and leads to melting, vaporisation, and ionisation of the absorbing media [361, 353]. Dielectric materials absorb the energy either directly if the photon energy is larger than the band gap, or by means of non-linear absorption by the defects in the lattice

[37]. Depending on the ratio between pulse width and characteristic lattice heating time, the lattice will experience different levels of heat-related effects, exemplified in Fig. 2.24, a-b. For most metals, lattice heating time is on the order of 1-100 ps and 1-2 orders of magnitude longer for dielectrics [23, 22], representing a border between thermal and non-thermal removal mechanisms.

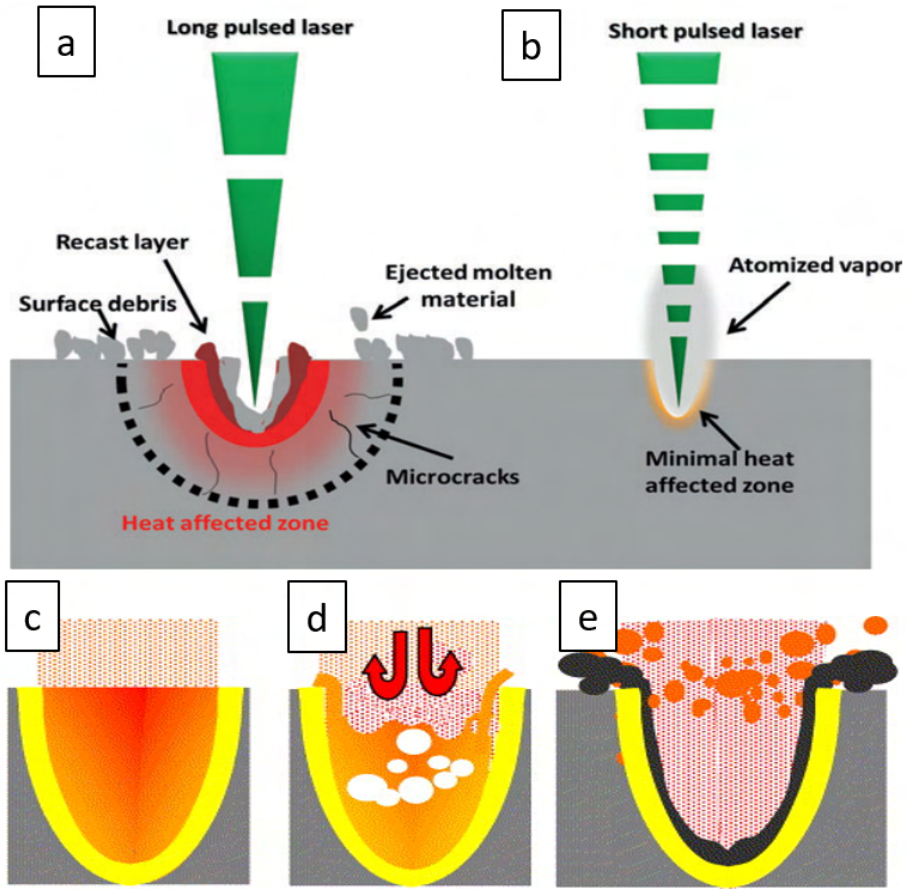


FIGURE 2.24: Long (a) and ultrashort (b) pulse laser ablation. Nanosecond and longer pulses do not prevent heat propagation and thermal effects, leading to heat-affected zone and collateral workpiece material damage [27]. (Typical removal mechanisms via long pulse ablation [80]: (c) melting and vaporisation, (d) melt displacement, caused by recoil pressure, and (e) melt ejection.

In long pulse ablation (nanosecond and above) and continuous wave cutting, heat is absorbed by electrons and followed by fast energy transfer to the lattice by collisions, diffusion, or electron-phonon coupling. This results in various thermal effects. Laser irradiation first heats localized volumes to the melting point and then to vaporization. During long pulses, absorbed energy propagates into the workpiece by heat conduction. The presence of heat-affected zones, melted zones,

recast layers and is typical for long pulse ablation and continuous wave cutting. The depth of heat propagation into the workpiece is determined by the thermal diffusion length $l_{th} = 2\sqrt{D\tau_L}$, where D is thermal diffusivity and τ_L is the pulse duration [297]. Heat-affected zones depend not only on thermal diffusion lengths, but also on the ability of such irradiation to ablate material, i.e. laser fluence, ablation thresholds, heat accumulation effects, and pulse repetition rates. Regarding high power density irradiation, melt pool formation is followed by material vaporization. Sufficiently long and intensive pulses can be absorbed by vapour, often leading to its ionisation. The vapour/plasma plume creates large recoil pressures and produces a shock wave that propagates through the material. This often leads to collateral damage and generates compressive residual stresses when pulse energy is sufficient. Recoil pressure induces melt pool flow that extrudes melt from the irradiated area. This forms pits on the crater sides and dictates recast layer shapes.

Ultrashort pulses (ps-fs), are the only way to achieve high-quality surfaces in conductive materials by pulsed laser ablation. At femtosecond scales, photon energy is absorbed by free electrons and is primarily exchanged among them. Electron-lattice interaction is governed by relatively slow electron-phonon interactions [297]. Therefore, heat transfer becomes non-equilibrium with high electron temperatures and the cold lattice, described by the two-temperature model [11]. Non-equilibrium temperature distribution leads to significant surface evaporation, preventing heat propagation into the workpiece. Therefore, the process progresses directly from solid to vapour/plasma, allowing precise material processing in the absence of molten material, recast layers, and heat-affected zone.

2.3.2 Material removal mechanisms in laser ablation

The main removal mechanisms for long and short pulse ablations are [297]:

- *Melt expulsion*, or liquid displacement to the crater sides resulting from recoil pressure (Fig. 2.24d). This is the typical removal mechanism in continuous wave to nanosecond long pulse ablation. [297, 80].

- *Spallation*, or material disintegration due to high tensile stresses associated with rapid expansion. Can occur in all thermal ablation regimes. However, its relative contribution to material removal is higher in nanosecond pulse ablation [179].
- *Explosive boiling*, sometimes referred to "*phase explosion*" or "*melt ejection*", is the disintegration of overheated liquid, leading to subsurface nucleation of vapour bubbles and ejection of the liquid material from the melt pool. This is the typical removal mechanism in short ablation, i.e. nanosecond to picosecond (Fig. 2.24, e) [194].
- *Fragmentation*, or dissociation of the *surface* of supercritical liquid into fine droplets due to rapid thermal expansion. Fragmentation suppresses the phase explosion mechanism and tends to dominate removal mechanisms with shorter, pico- and femtosecond laser pulses [194]
- *Direct vaporisation*, often with the absence of thermal effects. Becomes the distinguishable mechanism in ultrashort femtosecond pulse ablation (Fig. 2.24, b) [297, 80].

Fishburn et al.[80] studied nanosecond ablation with a molecular dynamics simulation and found material removal at low fluencies is solely caused by melt displacement. With increased laser fluence, the melt displacement is accompanied by vaporisation, and after a critical laser fluence, explosive boiling dominates the removal mechanism. Nevertheless, the characteristic removal mechanism is a complex interplay between material properties (absorption, characteristic lattice heating time and thermal properties), and incident beam conditions (pulse duration, fluence, and wavelength). The contribution of each is a field for rich and often controversial scientific discussion [179], [239, 240, 211, 380, 380].

2.3.3 Typical defects in continuous wave, long, and short pulse ablation

Surface integrity of laser machined material, summarised in Fig. 2.25, is dependent on the dominating material removal mechanism and heat transfer within the material which, in its turn, depends on the laser irradiation parameters, and especially on the duration of the pulse (including continuous lasers). *Melt expulsion* results in the recast layer on the sides of the workpiece surface and newly generated surface, generating an elevation on the sides of the hole in case of laser drilling (Fig. 2.25, a, d, e, i). *Explosive boiling* (Fig. 2.25, f) and *fragmentation* (Fig. 2.25, g) eject liquid droplets, which can then solidify and form spatter on the sides of machined feature and be ejected from the melt pool in case of explosive boiling, or its surface in case of fragmentation. *Vaporization* is responsible for material *recondensation* [237] and generation of recoil pressure that can induce mechanical damage. Reactive molten metal covers with an oxide layer upon solidification [284], especially when the material includes more reactive ingredients, such as chromium, nickel and niobium in Inconel 718 (Fig. 2.25, b). Solidification of the generated melt pool, recast layer or debris generates high stresses due to thermal shrinkage, often resulting in the formation of microcracks (Fig. 2.25, d) [49]. Propagated heat can result in heat-affected zone (Fig. 2.25, c, h) and phase transformation [262] , which is, in general, unfavourable result of laser machining.

Recast layer and spattering

Microstructure of the ejected material, forming recast layer and spatter, is typically columnar and perpendicular to the surface due to high solidification rates, however different grain morphologies are also found within recast layers [90, 91, 358]. Mechanical properties of recast layers and spatter can be different from the bulk material, being brittle in nature due to oxidation, micro cracked and having hardness different from the base material. Various attempts have been made to reduce recast layers. Low et al. [195] investigated the influence of assistant gas on spatter generated during laser percussion drilling. The authors

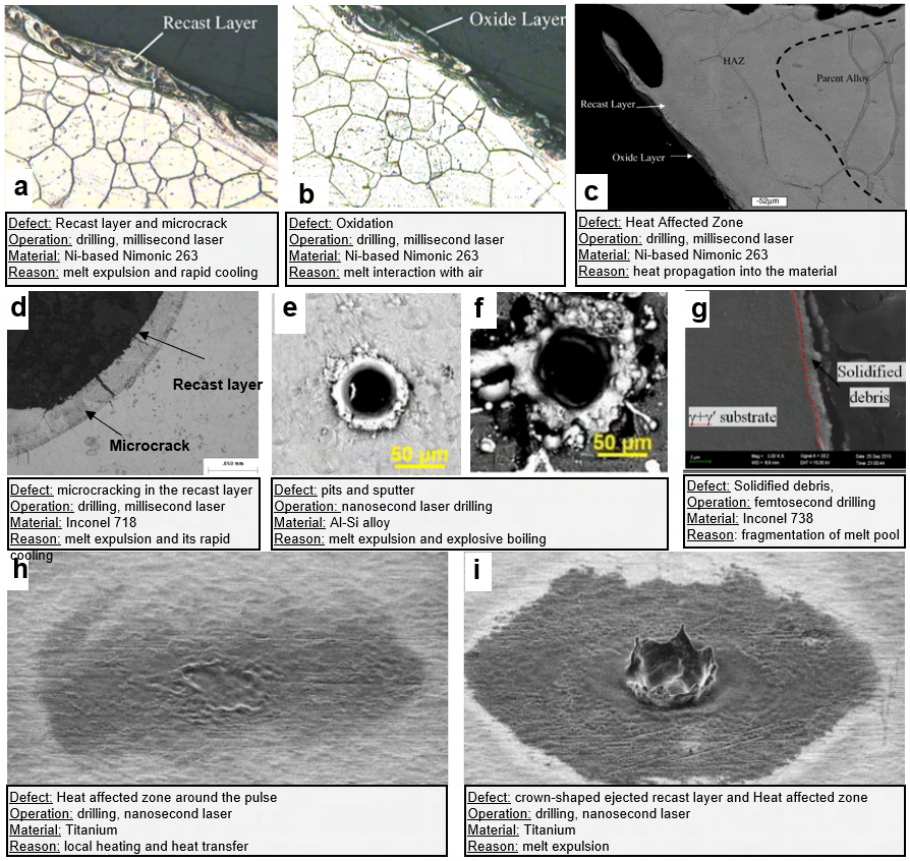


FIGURE 2.25: Surface imperfections in percussion drilling. (a)-(c) recast layer, oxidation and HAZ of nickel superalloy (Nimonic 263) [284] ; (d) cracking of the recast layer [49] ; (e), (f) recast layer and surface debris on Al-Si alloy after 5(e) and 100 (f) pulses [181]; (g) solidified microdroplets and vapour on the sides of the hole due to fragmentation and recondensation [350] ; (h) and (i) HAZ and recast layer after 5 and 50 nanosecond pulses on titanium surface [112]

found that spatter depends on the reactiveness of the assisting gas. Spatter bonding in N2 and Ar atmospheres is higher than in O_2, and therefore material removal is more difficult. Ejected spatter is thinner when oxygen assisted the drilling, shown in Fig. 2.26, a-b, and had lower bonding strength, compared to Ar assistance. Zhao and Yu [376] revealed recast layer self-cleaning during picosecond percussion drilling when the energy of the tail of the Gaussian laser beam was sufficient to remove generated melt from the hole sides.

One technique utilized for heat, and therefore recast layer, management during ablation is wet ablation. Nisar et al. [8] investigated dry and wet environments (deionised water and propanol), finding that recast layers are absent in wet environments. Due to active cooling being more pronounced in wet environments,

higher thermal gradients develop in water and propanol, leading to fine subsurface microstructures or their complete absence. Kudryashov and co-workers studied pressures developed in underwater ablation, where recoil pressure was 5-times higher, due to dynamic water confinement [167]. High recoil pressure collapse explains high removal rates and spatter-free surfaces in wet ablation. Kang et al. compared removal rates in air and water, finding that ablation performance increased by 700% in water [147]. Kang attributed this increase to thermal desorption of the target (induced by thermal stresses), resulting in material fracture and crack formation, and spallation dominated the process.

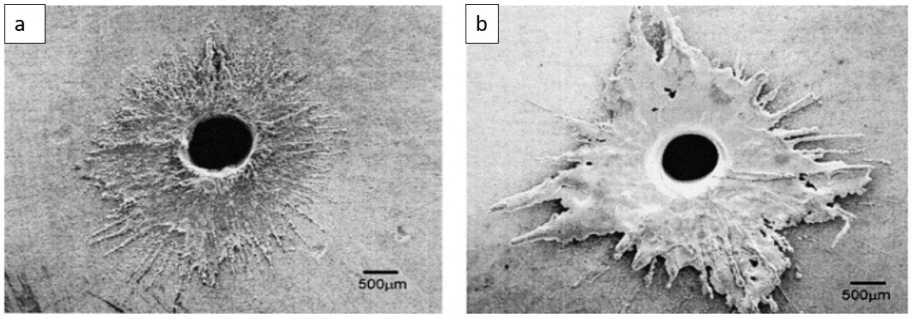


FIGURE 2.26: SEM micrographs showing the typical spatter formation (plan view) of holes drilled with (a) oxygen assist gas and (b) argon assist gas[195]

The microstructures of recast layers vary significantly from one case to another. While laser cutting can develop cooling rates of 10^3 K/s, thin recast layers can develop at cooling rates as high as 10^{11} K/s [57]. This wide range of cooling rates, possible during laser drilling, are responsible for the varied grain morphologies. Variation in cooling rates depends on material properties, ablation regime, and most importantly pulse duration, pulse energy and repetition rate. Rapid solidification often leads to fine columnar grains (see Fig. 2.27, b and c) [339]. Shorter pulses increase solidification rates leading to fine columnar cellular, columnar dendritic and equiaxed recast microstructures Fig. 2.27, a, b, d) [90]. Compositional changes can be also found in recast layers. Garofano et al. revealed the formation of nanoscale Ti-rich carbide precipitates between dendrite arms in Ni-based superalloys[91], which was attributed as a strengthening obstacle. Compared to the base material, the recast layer was softer due to the domination of microstructural influence on the properties.

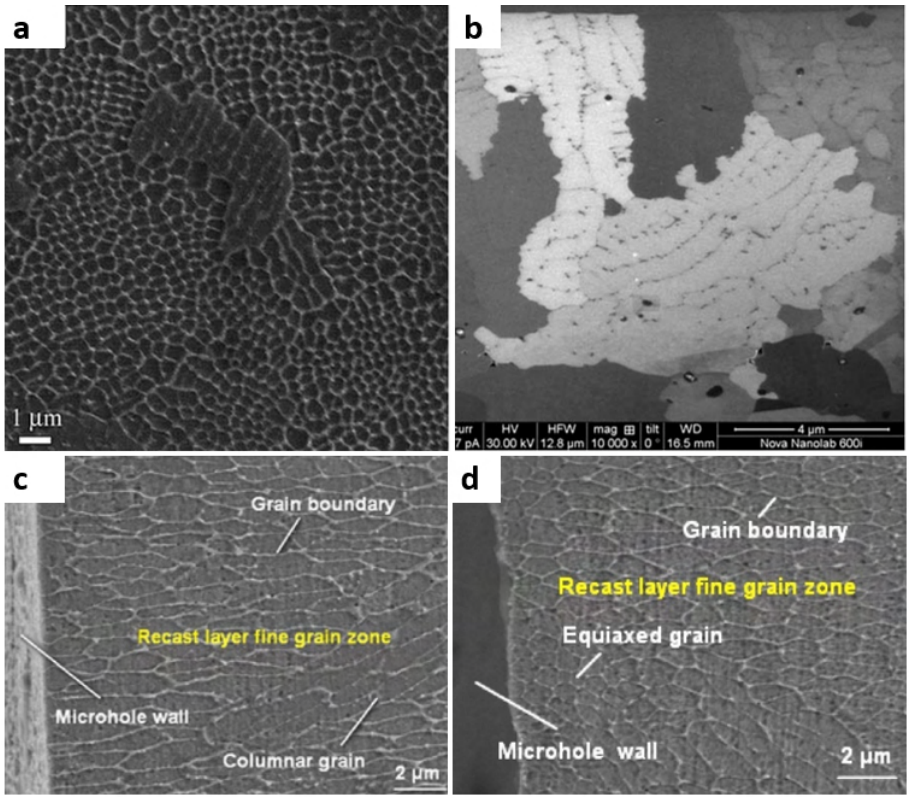


FIGURE 2.27: Different grain morphologies found in the recast layer of laser-drilled Ni-superalloy. (a), cellular morphology of the recast [91]; (b) dendritic microstructure [90]; (c) and (d) fine columnar and equiaxed grains [358]

Microcracking

At high cooling rates, high tensile stresses can be generated in the material. The yielding of these stresses to the tensile strength of a given material causes solidified layer cracking. This often combines with the formation of brittle oxide layers, influencing the development of cracks, as shown in Fig. 2.28. Microcracks are developed in the oxidized layer and propagate further into the recast layer or parent material [9, 365].

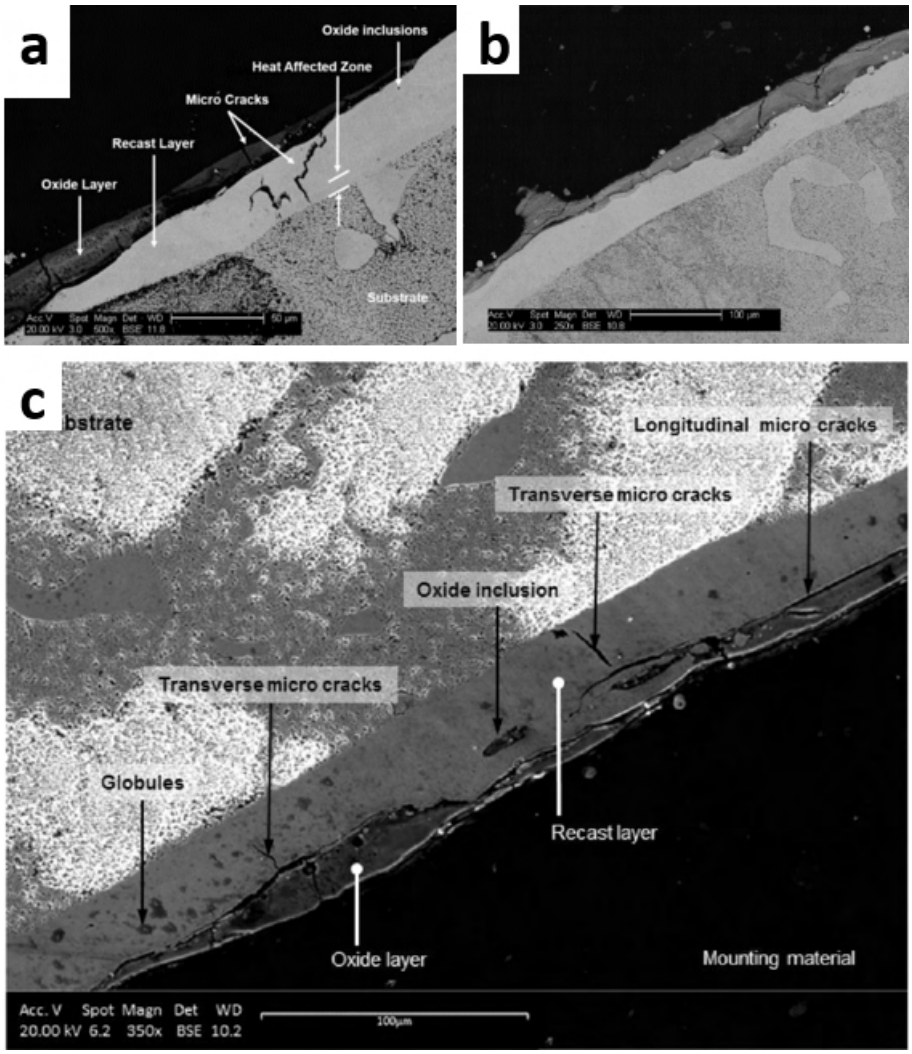


FIGURE 2.28: Surface integrity defects formed during laser drilling of Ni superalloys. (a) Cracks in the recast layer [9]; (b) transverse cracks in the oxide layer[136]; (c) longitudinal cracks in the oxide layer[136]

Thermal management, for instance with assisting gases, can influence the cracking behaviour of the oxide and recast layer. Transverse microcracks, perpendicular to the processed surface, are formed due to in-plane thermal gradients upon solidification. These cracks accumulate Griffith energy during propagation and are easier to propagate within recast layers and parent materials, and can cause component failures as indicated by Morar et al.[136]. Authors studied crack formation in laser trepanning drilling of Nickel-based superalloy. The authors acknowledged that pulse energy and pulse duration are the main parameters dictating microcrack formation and recast layer. Their findings revealed the formation of both transverse and longitudinal cracks (shown in Fig. 2.28).

Transverse cracks, caused by in-plane thermal gradients during machining, were considered an essential defect since can penetrate through the recast layer into the workpiece. However, it is important to acknowledge the importance of longitudinal cracks, caused by out-of-plane thermal gradients; these cracks propagate parallel to the surface, and potentially cause delamination of oxide and/or recast layer.

Hardness

Recast layer hardness is usually different from the base material. Recast layer hardness can be higher than the base material, for example, Inconel 718 alloy cut with a continuous-wave CO_2 laser, which results in carbide and carbonitrides formation on the surface after laser cutting operations, and high cooling rates during solidification of the recast[122]. Surprisingly, recast layer hardness can be also lower than that of the base material, as it was found in the work of Ahmed et al. on microsecond laser drilling of the same alloy [3]. Authors attributed this to the low density of γ' and γ'' precipitates at the surface and grain sliding. A possible reason for such a divergence in findings can be ascribed to the difference in the formation of the recast: continuous wave melting creates a continuous, dense surficial layer, while pulsed lasers eject material in series. This can lead to higher porosity of the recast and loss of the lamellar layers, eventually decreasing hardness. Overall, the relative change in surface hardness is a complex interplay among various phenomena, including recast microstructures, ambient environments during laser processing and laser output characteristics, and material parameters.

Residual Stresses

Several mechanisms can lead to residual stresses upon laser machining. Solidification, accompanied by material cooling and shrinkage, promote tensile stresses in surface and sub-surface layers. The formation of expanding vapour and plasma induces shock waves, which can lead to plastic deformation of the material if pulse energies are sufficient for such deformation[196]. Thermal gradients and material plasticity, metallurgical transformations, and chemical reactions can also be responsible for residual stress generation in subsurface areas. Yilbas et al.

studied laser trepan drilling with a high-power CO2 laser [364, 363, 12], developing several numerical models combining heat transfer with a viscoplastic model, validating stress fields with XRD measurements. Tensile stresses of 330 MPa were measured at the vicinity of the cut surface in Ti–6Al–4V, more than a third of the material yield strength. Melting and subsequent cooling of the material created striations, shown in Fig. 2.29, which were bent at the surface due to gas flow. This was attributed to the presence of assisting gas, leading to melting accumulation and solidification in a periodic manner, and should not be confused with mechanically induced strain. This also helped recast layer removal, which was estimated as 5µm. Considering XRD penetration depth is ca. 10-20 µm from the free surface, developed residual stresses propagate deeper than the recast layer, supported by numerical results. Maeda et al.[199] also found tensile residual stresses (150MPa and higher) after laser cutting, resulting from material cooling.

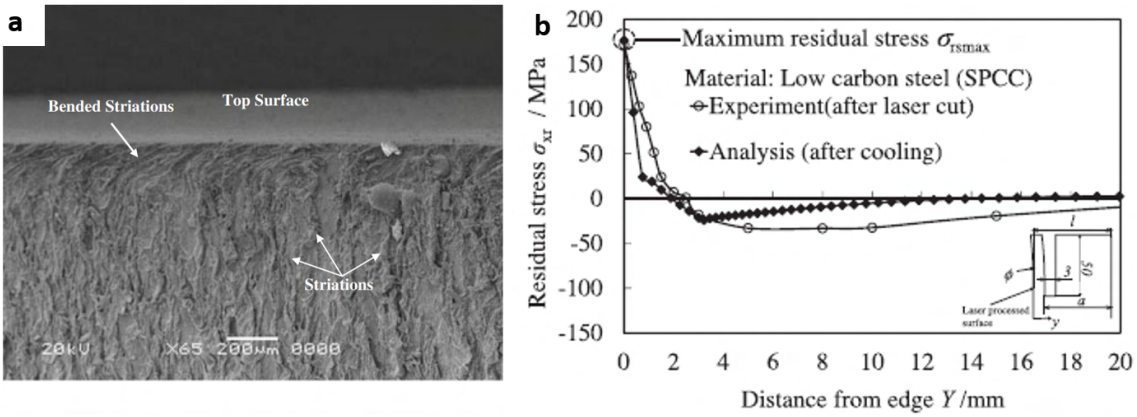


FIGURE 2.29: (a) Kerf surface micrograph of laser trepan drilled Ti–6Al–4V with a CO2 laser[363]; (b) distribution of in-plane residual stresses [199]

The work of Cha et al.[38] investigated residual stresses formed upon laser ablation of compressor blades with a nanosecond pulsed laser. On contrary, residual stresses were not different from the bulk material, evaluated through a local misorientation map. This could signify the absence of residual stresses, or rather the small penetration depth, undetectable with the selected method. Plasma-induced pressure waves can lead to plastic deformation and generate residual stresses. This phenomenon becomes noticeable only when the pulse energy is sufficient for rapid ionisation, typically in the Joule range in a nanosecond scale pulses [196]. These

pulses are used to generate favourable compressive residual stresses on workpiece surfaces, which can be enhanced by adding a transparent confining layer like water or glass. Laser shock peening is the subject of widespread investigation. Typically used pulse energies (mJ range) for laser microfabrication do not induce surface damage. This is why little attention was paid to the investigation of residual stresses in laser machined workpieces. Nevertheless, the generation of compressive residual stresses in-situ during laser machining is an attractive field for research and industrial application.

2.3.4 Ultrashort pulse laser ablation for material removal

Compared to continuous wave irradiation and long pulse ablation, the physical process changes significantly in the case of ultrashort femtosecond laser ablation. Ultrashort pulses have negligible thermal diffusion and direct vaporisation is often the prevailing material removal mechanism [240], [193]. However, fragmentation and explosive boiling are also reported [194],[4, 245]. Rapidly removed material has a thin heat-affected zone, causing less material damage. Ablation of steel with different pulse durations, shown in Fig. 2.30, indicates a transition between pronounced thermal ablation regimes (nano- and picosecond ablation), and clean, defect-free ablation using ultrashort femtosecond laser ablation, due to evaporation, negligible heat conduction, and absence of liquid phase [245]. However, in many cases, heat accumulation in the workpiece exists and affects resultant surface integrity [350], shown in figure 2.25,g and figure 2.31, a.

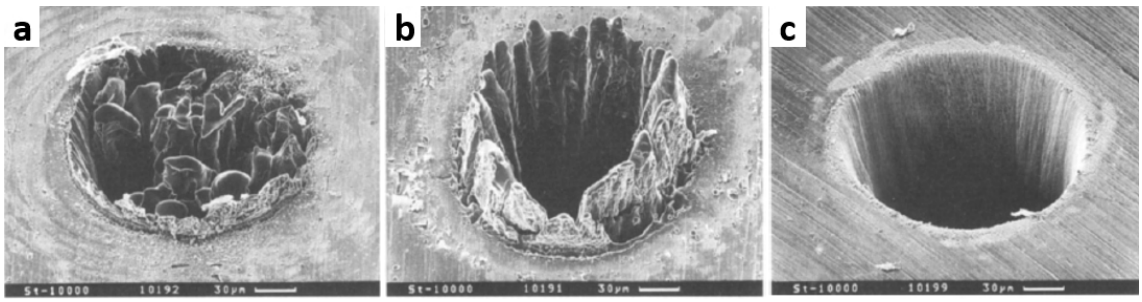
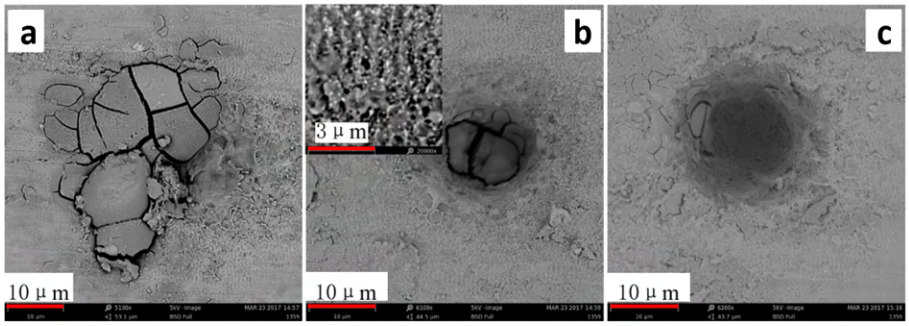


FIGURE 2.30: Micrographs of the laser-drilled holes on steel with long, short and ultrashort pulses. The pulse widths are (a) 3.3 ns, (b) 80 ps, and (c) 200 fs [245]

The choice of appropriate pulse duration is often a trade-off between process efficiency, an acceptable level of damage, and equipment cost. Although femtosecond ablation is an attractive technique for clean, defect-free machining, wide application of femtosecond lasers is limited due to the complexity of equipment able to produce ultrashort pulses with pulse energy sufficient for ablation[191]. While the ablation threshold fluence is independent of pulse duration in the sub-picosecond regime [101], the laser intensity is still inversely proportional to pulse duration. This is the limiting factor for machining with shorter pulses in mode-locked lasers. This limitation has been overcome via chirped pulse amplification (CPA), where the initial seeding pulse was first stretched by delaying different wavelengths in time, amplified at safe power densities, and then compressed back. The idea was proposed in 1985 [300], receiving the 2018 Nobel Prize in Physics, which is still the current state-of-the-art technique for a short pulse, high power density lasers already available for machining. Even in femtosecond regimes, melt pool formation due to heat incubation is possible in low melting point materials, which can result in recast layer cracking, shown in Fig. 2.31. Some studies on mode-locked femtosecond lasers without further chirped amplification utilize sub-threshold fluence for machining; in this case, ablation relies on incubation effect, i.e. when ablation threshold drops for multi-shot ablation [34] (especially pronounced with high repetition rates[206]). Heat accumulation enables material removal with lower fluences, but leads to noticeable melt pools [65], effectively changing the regime to thermal ablation. Interestingly, ultra-high repetition rate lasers can have behaviour different from typical ablation: recently, Kerse and co-workers [152] used ultra-high repetition rate ablation to exploit ablation cooling phenomena. In order to increase ablation efficiency and reduce material damage, the authors used ultrafast laser bursts (GHz pulse repetition rate). When the first pulse comes, it heats up the laser spot vicinity and reduces the ablation threshold and the energy necessary for ablation by the succeeding pulse. The work showed that by selecting a suitable pulse frequency, it is possible to utilise the thermal energy of previous pulses, therefore suppressing heat propagation into the bulk.



(a) F= 1.5 J/cm^2, N= 20 pulses (b) F= 1.5 J/cm^2, N= 50 pulses (c) F= 2.9 J/cm^2, N= 50 pulses

FIGURE 2.31: Percussion-drilled hole in Al-Mg alloy in the air with a femtosecond laser, revealing melt formation and hot cracking[66]

At present, femtosecond lasers are applied to machining, attracting interest in research and production. Due to non-thermal ablation with rapid material evaporation and the absence of workpiece thermal damage, it is used for defect-free microfabrication and is becoming a widespread industrial technique.

2.4 Fundamentals of solidification

2.4.1 Heat and fluid transport modelling

For all energy beam-based manufacturing techniques, heat movement in and around the melt pool has an unavoidable impact on melt pool dimensions, porosity and keyhole defects, surface roughness, and microstructure. As a result, during the last few decades, a lot of effort has gone into simulating this process. The Rosenthal solution for a moving point heat source across a material surface, omitting fluid movement, the latent heat of melting, and heat transmission from the top of the melt pool, is one of the simplest yet most practical approximations of these processes [275]. This solution in 2D and 3D has been used to calculate temperature gradients (G) and solidification rates (R) in different areas of the melt pool to relate process conditions to microstructure development [30, 31]. More precise solutions of heat transport can be obtained through finite difference or, more commonly, the finite element method, in which the domain is represented by a large number of simple geometrical shapes, in which the heat transfer equation is solved. The equation

describing heat diffusion within the workpiece can be represented as:

$$\rho C_p \frac{\partial T}{\partial t} = \nabla \cdot (k_{th} \nabla T) + Q, \tag{2.2}$$

where ρ is the material density, C_p is the heat capacity at constant pressure, T is the temperature, k_{th} are the thermal conductivity and the heat sink and heat source term (e.g. from incoming laser radiation) is Q. The latent heat of phase change between solid and liquid can also be included in the term Q. However, not all models account for latent heat; some simply treat regions above and below the melting temperature with phase-dependent densities or conductivities [267], but because alloy solidification occurs over a wide temperature range, other models incorporate this or a similar term in some way [258, 378]. The apparent heat capacity method allows to include the enthalpy of phase change in the specific heat directly by directly substituting apparent heat capacity, defined as $C_p^A = dH/T$, into the equation in terms of material enthalpy [332]. Together with the influence of the fluid flow, the generalised energy conservation law is [156, 217]:

$$\rho C_p^A \frac{\partial T}{\partial t} + \rho C_p^A \mathbf{u} \nabla T = \nabla \cdot (k_{th} \nabla T) + Q, \tag{2.3}$$

where $\mathbf{u}$ is the fluid velocity, which can be obtained by solving together Navier-Stokes and continuity equations:

$$k_{th} \frac{\partial \mathbf{u}}{\partial t} + \rho(\mathbf{u} \cdot \nabla)\mathbf{u} = \nabla \cdot (-pI + \mu \nabla \mathbf{u}) + F, \tag{2.4}$$

$$\rho \nabla \cdot \mathbf{u} = 0, \tag{2.5}$$

where p is the pressure, $\mu\nabla\mathbf{u}$ represents the viscous stresses, and F are the external forces. In laser welding, two forces are usually modelled, accounting for buoyancy and thermocapillary convection. Although the liquid is assumed incompressible and therefore the density deviations ρ from reference fluid density ρ_0 are negligible, small variations are still enough to induce motion within the melt pool. A common way to apply buoyancy forces is by using the Boussinesq approximation:

$$F_{buoyancy} = \rho_0(1 - \alpha(T - T_{ref}))\vec{g}, \tag{2.6}$$

where $\vec{g}$ is the gravitational acceleration, $-T_{ref}$ is the reference temperature, ρ_0 is the reference density of the fluid, and α is the thermal expansion coefficient.

Thermocapillary forces arise from the dependency of surface tension on surface temperature. Due to highly concentrated energy at the surface of the molten pool in laser melting application, high-temperature gradients occur at the top surface of the liquid. Typically, surface tension γ of the liquid decreases with increasing temperature, i.e. $\frac{\partial\gamma}{\partial T}$. Eventually, high-temperature gradients at the surface of the melt pool induce surface tension to generate shear stresses at the surface of the liquid, directed from the hottest point to the sides of the pool, where the liquid is cooler. This generates internal flow within the melt pool which, if this is of sufficient intensity, can become a dominating heat transfer mechanism. This process is also known as Marangoni convection or thermocapillary convection [162]:

$$F_{Marangoni} = \frac{\partial\gamma}{\partial T}\frac{\partial T}{\partial x}, \tag{2.7}$$

where $\frac{\partial\gamma}{\partial T}$ is the thermocapillary coefficient, γ is the surface tension.

2.4.2 Modelling of laser melting for microstructure prediction

The microstructure of the material, i.e. grain size and orientation, after laser processing can change significantly and result in the enhancement of mechanical[120], electric[5], magnetic[303] properties of the material. An example of laser processing techniques, laser melting, can vary grain morphology that allows tailoring specific application properties: fine equiaxed morphology to increase fatigue performance[283] and compromise creep lifetime[285], and columnar grains to exhibit longer times and higher creep strains[285]. Besides, the geometry of grain boundaries was found to influence crack propagation and fatigue properties in some research works[369]. Understanding of the microstructure, hence the properties, can allow tailoring the properties of the material in a way beneficial for a given application.

To understand the grain formation mechanism in laser-melted materials, at least two factors affecting the resultant microstructure, i.e. base material crystal size and orientation heat input conditions [61, 60], have to be considered. In the past, solidification found a lot of attention in welding application[82, 306], and the models were adapted to the additive manufacturing field, e.g. selective laser melting (SLM[6], electron-beam melting[357], direct energy deposition (DED)[189]). The vast field of possible heat input parameters is narrowed by the specific process used: higher energy density inputs are more typical in welding and DED, resulting in low solidification rates and eventually curved grain geometry[347, 161], while high solidification rates are typical for powder bed fusion processes and high-speed welding, resulting in vertical columnar grains[115, 248].

Phase Field Method

The front-tracking of a sharp interface was the standard simulation approach for solving free boundary issues. [274, 277, 10, 133]. However, due to the difficulties in tracing a sharp border of a complicated shape and detecting minor anisotropies, quantitative data were difficult to acquire. Despite these challenges, the

Müller-Krumbhaar group, for example, revealed conclusive quantitative assessments of the dendritic tip's functioning state [277, 133]. To limit the impact of computational artefacts, the authors utilised a front-tracking approach with rotating grids.

The phase-field (PF) technique, which was introduced in 1987 by Kobayashi for crystal growth in undercooled pure melt [254], made a substantial contribution to the modelling of phase boundary motion, morphology, and scale. This strong technique ultimately allowed the whole dendrite growth problem to be tackled after a decade of development: tip growth, secondary branching, microsegregation, and non-equilibrium effects. This is why it has become the favoured method for dealing with problems requiring phase transitions, an example of PF model capabilities is presented in Fig. 2.32.

The primary concept behind the PF model is to describe the phases using a non-conserved constant order parameter that fluctuates smoothly over the diffuse surface. This parameter evolves according to a governing equation that ensures the system's free energy decreases with time and is coupled to the diffusion field near the interface. Caginalp [35] and Langer [176] gave this notion a stronger quantitative foundation in the mid-1980s, demonstrating that the PF model converges to the free-boundary issue in the limit of diminishing interface width.

While the Phase-field method is the most accurate representation in terms of physical formulation incorporating the fine perturbations of the solid-liquid interface, phase-field is the most computationally intensive of all the approaches, typically limiting its application to small scales.

Stochastic Method

An alternative method for microstructural modelling based on stochastic models of grain boundary evolution. The steps in the computational technique are as follows: the domain is partitioned into a regular network of cells; variables and states are assigned to the cells; each cell has a neighbourhood, and transition rules governing the evolution of the cell's various states and variables are established [81]. Besides,

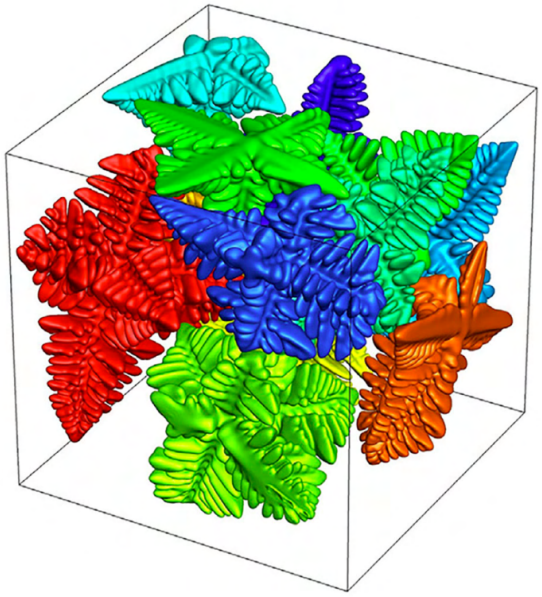


FIGURE 2.32: 3D phase-field computation of polycrystalline equiaxed solidification of Ni-based superalloy [360].

it is possible to mimic phenomena such as crystal transport in the melt and crystal remelting.

Kinetic Monte Carlo grain growth simulations [269] replicate abnormal grain morphology with variable microstructural characteristics, such as grain shapes and sizes, and interfaces. However, the simulation can only forecast qualitative aspects at this time, and there is still a lot of work to be done to figure out the physics of granular solidification nucleation and growth, as well as how to appropriately represent that physics inside simulation frameworks [81].

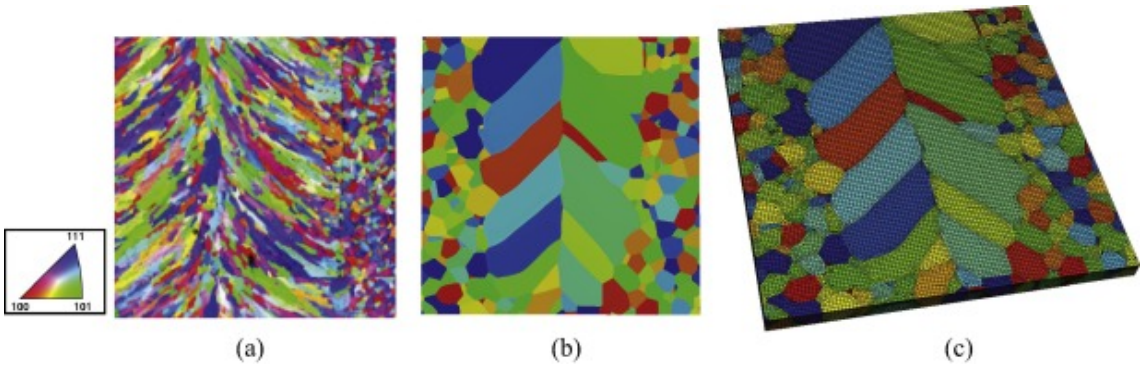


FIGURE 2.33: Microstructures of Laser Engineered Net Shaping additively produced stainless steel 304L. (a) EBSD measurement, (b) kinetic Monte Carlo simulations, and (c) conformal finite element mesh [81]

Cellular Automata Method

Cellular Automata (CA), arguably the most popular approach, have been designed for dendritic grain structures and can handle arbitrary forms and grain competition [260, 85]. The solidification domain is mapped with a regular arrangement of cells in this approach, and each grain is defined by a collection of cells, with those at the boundary being active for the growth process computation.The solution is based on calculating the length of an expanding octahedron, assigned to the cells at the solid-liquid interface. The octahedron approximates a growing dendritic crystal with 6 main growing axes, recognised for FCC and BCC materials. Currently, the most popular tool for predicting dendritic growth in CA models was established by Gandin and Rappaz [84], i.e., an algorithm allowing for reducing the influence of the mesh on grain propagation. These CA calculations, which included homogeneous and heterogeneous nucleation of new grains in the undercooled liquid, were connected to a FE approach for heat transfer and included homogeneous and heterogeneous nucleation of new grains. A decentered octahedron method was used to apply the Cellular Automata - Finite Element (CAFE) hybrid model to 3D grain formation for anisotropy-free generation of 3D grains with six-fold symmetry.

Thermal Gradient Method

A different approach was developed by Wei et.al. to predict the solidification microstructure of a solidified weld in pure aluminium on mesoscale [347, 346]. Based on the assumption that the direction of crystal growth is collinear with the local heat flow, the shape of the crystals was predicted with the aid of heat transfer and fluid flow model. Such an efficient approach, however, is valid only for the case of planar growth since the growth speed was defined by the laser. At the same time, growth in undercooled melts may not only be limited by the velocity of the melt pool. Growth velocity can be much higher than the melt pool velocity when the solid-liquid interface perturbations develop into dendritic solidification[314, 13]. A similar approach was used in several works of Han et al. [115, 118, 116], and in one of them, the difference in solidification behaviour in pure Al and binary Al-Cu alloy was emphasised [117]]. Dendritic growth of a binary alloy was found

even at low welding speeds of 2mm/s due to solute segregation. At the same time, both growth mechanisms usually coexist simultaneously [162]. Different growth mechanisms in planar and dendritic growth dictate different solidification velocities and characteristic crystal shapes have an influence on crystal growth, and therefore the shape of the crystals and their orientation. In an effort to capture these phenomena and demonstrate the influence of specific growth conditions, a predictive model for combined planar-dendritic growth is proposed in this work.

2.5 Summary of the literature

An encompassing literature review on the topic of thermal barrier coating systems and laser beam processing has been presented.

The research community has put forth significant effort towards understanding the mechanisms governing thermal barrier coating durability and accumulating the knowledge allowing for novel, durable thermal barrier coating systems. An interplay of different physical phenomena happening at elevated temperatures in the coating system is challenging to account for simultaneously. Besides oxidation, one of the primary reasons for coating spallation, mechanical and chemical interactions with the environment have also been addressed in various research works. Current knowledge of the degradation mechanisms, and current methods to address these issues by modifying the composition/microstructure of the coating, have been addressed in this chapter.

The main manufacturing tools used in this work are laser-beam based. Lasers present an incredibly versatile tool allowing one to perform a wide range of operations, such as cutting, drilling, and surface conditioning. Depending on the temporal-energetic parameters of the laser it is possible to control the laser-material interaction behaviour. In the simplest case, the transition from material removal through ablation to laser melting is when the laser energy is decreased. Literature provides a range of typical defects in laser micromachining as

well as current methods on microstructure modelling upon solidification, which will be directly linked to the following work.

2.5.1 Research challenges emerging from the literature review

To expand the current fundamental knowledge of thermal barrier coating systems and understand the interaction of laser irradiation with the latter, various research challenges must be addressed based on the current gaps in the literature. The research objectives and challenges are summarised in this section.

Research Challenge 1 - Modification of thermal barrier coating microstructure for increased coating performance

While thermal barrier coating systems have been continuously evolving in the past decades, there have been limited attempts to modify the internal microstructure of the coating system. A few studies on the coating texturing by Dhineshkumar and Khan [154, 64] shown a promising potential arising from stress relaxation on the surface. Laser glazing, a popular approach for thermal barrier coating modification, has been used for creating a dense surface for mechanical protection, and a network of vertical cracks for stress relaxation. While some works show significant enhancement in thermal barrier coating performance in terms of cyclic oxidation [79], others show the same [366] or even worse [371] performance. To date, there have been no reports on modification of thermal barrier coatings that could simultaneously increase thermomechanical compliance and its resistance to mechanical impact and interactions with silicates.

• **Objective 1.1.** Investigate possible scenarios of laser grooving of the TBC system within the limitations of the laser grooving methods.

• **Objective 1.2.** Understand melting mechanisms of TBCs upon laser irradiation. Find relevant physical parameters governing the geometrical and microstructural parameters of the coating upon laser glazing procedure.

• **Objective 1.3.** Optimise the combination of grooving and glazing procedures. Propose possible scenarios of the modification technique for varying conditions.

In an effort to combine the benefits of laser glazing and laser grooving, a novel modification approach is proposed in this work. While laser glazing provides a protective surficial layer, resistant to erosion and CMAS, the underlying structure of TBC can be tailored in a way to provide higher strain tolerance. Moreover, tuning the microstructure of the coating allows not only improves strain tolerance but also reduces the thermal conductivity of the coating. This novel approach for TBC modification will be presented in the relevant chapter.

Research Challenge 2 - Performance assessment and microstructure characterisation of laser modified thermal barrier coatings

Arising from the Research Challenge 1, the failure phenomena in TBCs was subjected to further studies. In order to understand the influence of the proposed modification technique on the durability, the coatings after modification will be tested in simulated in-engine environment.

• **Objective 2.1** Identify main failure mechanisms of thermal barrier coatings. Characterise the altered performance in as-sprayed and modified conditions in a comparative study.

• **Objective 2.2.** Recognise the difference in the governing failure mechanisms of the coating in each of the tests to better understand the influence of the compound microstructure.

• **Objective 2.3.** Provide in-depth analysis of the microstructure and crystal structure upon modification as well as after the simulated tests.

As with any technological novelty, its new properties and differences should be assessed to allow finding the best application thereof. Performance of the coatings will be assessed in thermal, mechanical, and chemical tests. Understanding of the changes in the crystal structure can be done using lattice diffraction techniques and reveal the stress response of the coatings on the environmental conditions.

Research Challenge 3 - Investigation of grain growth phenomena in laser-melted topcoats through modelling

During the work on objective 1.2, unusual behaviour of grain solidification was found. While the importance of grain microstructure is well-recognised in metals, limited attention was paid to grain formation in ceramic materials, and in particular in thermal barrier coatings.

While the current modelling methods do not allow the prediction of such behaviour, which will be discussed in detail in the corresponding chapter. Therefore, the aim of this chapter is to create a new method allowing for predicting particular behaviour found in laser-melted ceramics. Limited attention has been paid to this phenomenon, and to date, Fan et al. [76] were the only ones who analysed the thermal characteristic of the melt pool for laser melted TBC with different preheating conditions and crack suppressing by grain boundaries. In their study, close attention was paid to crack formation, however, grain growth and grain boundary formation mechanisms have not been explained. In this work, a preliminary selection of laser glazing capabilities revealed unusual grain growth behaviour in the subsurface layer: surficial grain curving, or bending, towards the heat source travel direction, and surface sealing, where the growth of the grains at the surface dominated growth at subsurface layer, leading to in-plane columnar growth of the grains. Besides, in this work, the existence of dendritic structures upon solidification was found and was assumed to strongly influence the solidification behaviour.

• **Objective 3.1.** Explain the grain growth behaviour based on state-of-the-art theories and models.

• **Objective 3.2.** Understand unusual behaviour found in the solidification of the TBC topcoat, and propose a comprehensive grain growth model. This will not only allow understanding the growth mechanics in topcoat solidification but can also be used as a predictive tool.

• **Objective 3.3.** With the aid of the model, elucidate the crystal formation found in Objective 1.2 and Objective 1.3.

• **Objective 3.4.** Validate the proposed model for grain growth by direct comparison of geometrical parameters, such as glazing width and depth, and by crystallographical analysis.

To date, CA dendritic growth models cannot capture the difference in planar and dendritic solidification, and a method to address these issues was proposed. While the standard decentred octahedron algorithm represents an option for modelling a dendritic interface, there are no reports of a complementary planar interface modelling using the cellular automata approach. The grain growth mode can significantly influence the final microstructure of the remelted layer. To explain these particularities in the solidification of laser-melted zirconia, a new computational method will be developed, considering the development of the dendritic interface, and the representative resolving the case of planar growth in three dimensions.

Research Challenge 4 - Development of topcoat deposition technique in atmospheric pressure via a laser source

In the studies towards objective O1.2, a close look was taken on the sides of the melted track, where the material was re-deposited from vapour and liquid state. Further, this unique feature was used for substrate-to-substrate coating deposition, where a number of possible coating microstructures were found. The aim of this chapter is to propose a novel deposition technique able to deposit coatings in atmospheric pressure based on these findings. Although the research on coating deposition methods is vast, and only a portion of deposition methods has been presented in the literature review. Depending on the manufacturing method, the coating microstructure can vary significantly, eventually resulting in varied coating performance. To date, the state-of-the-art method of coating production for dynamic components is vacuum-based (i.e. EB-PVD), and thermal spray for static components (i.e. APS). The major drawback of EB-PVD production is the high

vacuum required for coating deposition. While the columnar coating can be produced from vapour deposition, the possibility of vapour deposition in an atmospheric pressure environment is yet to be found. On the other hand, Solution/Suspension Precursor Plasma Spray (SPPS) method shows the ability to produce columnar-like topcoats with superior properties to APS coatings and attracted a lot of research attention. Besides, the SPPS method works in atmospheric pressure, and other methods can be used to achieve the same purpose.

• **Objective 4.1.** Investigate the substrate-to-substrate coating formation, i.e. deposition of the coating material on itself, generated by laser melting. Explore possible scenarios of substrate-to-substrate deposition.

• **Objective 4.2.** Understand the laser heating parameters governing melt creation, melt expulsion, explosive boiling, and vaporisation in heated ZrO2 target material.

• **Objective 4.3.** Expand the substrate-to-substrate coating deposition towards a target-to-substrate coating deposition. Investigate possible scenarios of coating deposition from the vapour phase and liquid phase.

• **Objective 4.3.** Analyse the generated microstructure and compare it to coatings deposited by other techniques.

A solution based on the laser, as opposed to SPPS or APS technique, can be miniaturised relatively easily, and allow for component re-coating *in-situ*. In the initial trials on laser glazing, the vapour plume present during the process was found to redeposit on the substrate itself. In an effort to utilise this as a coating deposition system, the fundamental understanding of laser-material interaction, vaporisation, condensation and adhesion, is crucial. To investigate the possibilities of atmospheric laser deposition and its influence on structure formation, a deposition setup must be established. To explore a wide range of parameters and achieve repeatable experiments, the experimental setup must attain sufficient accuracy over a wide range of processing conditions.

Chapter 3

Methodology

This chapter describes the equipment methods used throughout the present work. A detailed description of laser equipment and supplementary instruments for laser characterisation, material analysis equipment and the techniques used to evaluate the material response to laser irradiation, as well as to assess the performance of thermal barrier coatings, is presented. Due to the time limitations of the PhD, the evaluation of TBC properties does not include the analysis of coating adhesion and coating hardness, which however can be addressed in the future studies. The organisation of methods used is shown as a diagram in Fig. 3.1.

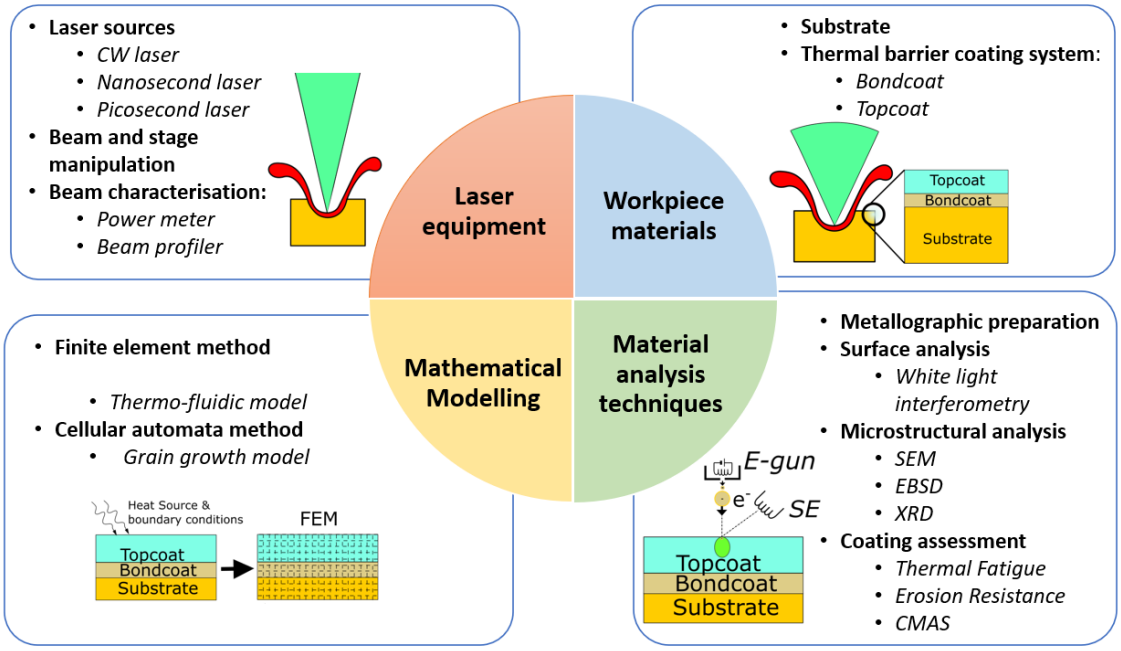
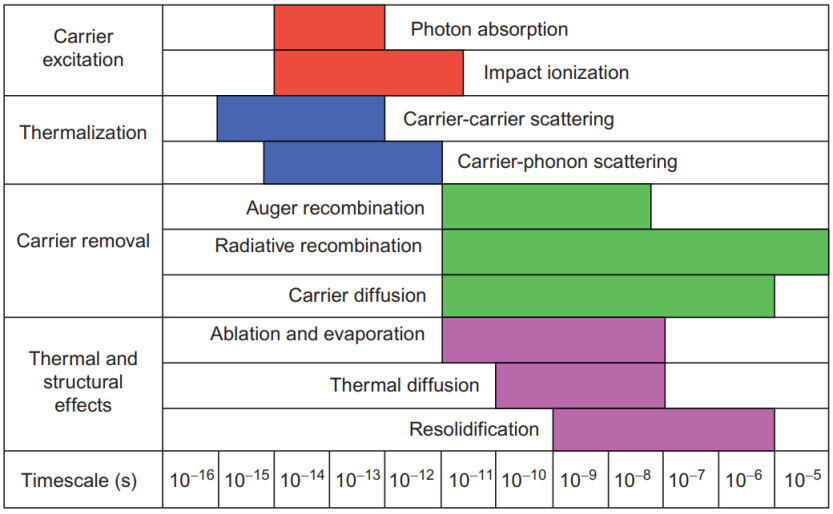


FIGURE 3.1: Organisation of methodology section

3.1 Description of laser equipment

In order to explain the significance of the difference in pulse duration, it is important to understand the characteristic timescales of the physical processes, shown in Fig. 3.2. Thermal processes are relatively time-consuming, especially in ceramic materials, and for pulse duration longer than the time of thermal diffusion, the ablation process is called thermal ablation. In contrast, if the laser pulse width is shorter, the lattice does not have enough time to respond, i.e. to deliver the energy deeper than the laser-affected area, and evaporates the material with negligible or absent molten phase. In contrast, long-pulse or continuous laser irradiation can be used for material heating with suppressed ablation or evaporation.



d

FIGURE 3.2: characteristic timescale of different processes. [311]

Thus, by controlling the duration of the laser pulse, laser fluence and laser optical power density (laser intensity), it is possible to achieve different material responses to the laser irradiation, and use it for creating high-quality micromachined features in ultrashort pulse regime, to generate steady or quasi-steady melt pool for surface conditioning in case of short-long pulse and continuous irradiation, and theoretically generate a clean, droplet-free, vapour plume.

3.1.1 Laser sources

Continuous wave laser

A laser with a nominally constant output over a set interval is called a continuous wave (CW) laser. During this period, the key parameters of laser irradiation, such as optical power and intensity, remain constant. Continuous-wave lasers can be found in a variety of applications ranging from laser cutting to surface conditioning. Moreover, due to the stable optical output, continuous wave irradiation is easier to predict and model, compared to pulsed irradiation. In this study, a Yb-doped, diode-pumped SPI-100C-0013 fibre laser (SPI lasers UK) was used. Some parameters of the CW laser are listed in the table 3.1.

Parameter	Specification
Wavelength, nm	1090 ± 5.0
Nominal pulse repetition Frequency , kHz	CW to 10^2 (modulated)
Average output power, W	up to 100
Mode	TEM_{00}
M^2	< 1.2
Beam divergence, mrad	< 2.8

TABLE 3.1: CW laser parameters. [320]

In this study, the laser was used both in continuous and modulated mode. In the modulated regime, the maximum optical power would vary with the duty cycle of the signal, i.e. the percentage of time the laser is on to the frequency of the laser. The input signal relies on transistor-transistor logic (TTL), i.e. the pulse signal can be supplied by square waves with the associated high (+2.7...5V) and low (0V...0.8V) level signals [320]. This will result in a modulated output of the laser, while the instantaneous power of the beam, or peak power, cannot exceed 100W.

Laser arrangement on the optical table is presented in Fig. 3.3. The laser is delivered to the optical table, where it exits from the laser aperture. Inside this aperture, a series of devices is situated: (1) beam collimator, in which the incoming diverging radiation after the fibre is aligned with the optical axis of the device and collimated; (2) optical diode, or isolator, ensuring the transmission of the light in only one direction and protects the optical gain media from back reflection; (3)

beam expander, which is used to increase the size of the laser from typically 10-50 μm (depending on the fibre type and diameter) to 5 mm in case of the used laser. After the laser aperture, the output beam is aligned with a Class 2 laser pointer, used for day-to-day alignment. To align the axes of the laser pointer and CW laser, a system of 2 irises (A1 and A2 in dig. 3.3) are used. To combine the axes of the CW laser and laser pointer, the optical axis of the CW laser is disturbed with a dichroic mirror, an optical filter with wavelength-dependent reflectivity. While being transparent to the infrared light, the dichroic mirror has a high reflectivity in the visible range, therefore simultaneously transmitting the CW light and reflecting the visible radiation from a laser pointer. After reflection from a series of dielectric mirrors, the laser is sent to the workpiece through a galvoscanner (discussed in section 3.1.2).

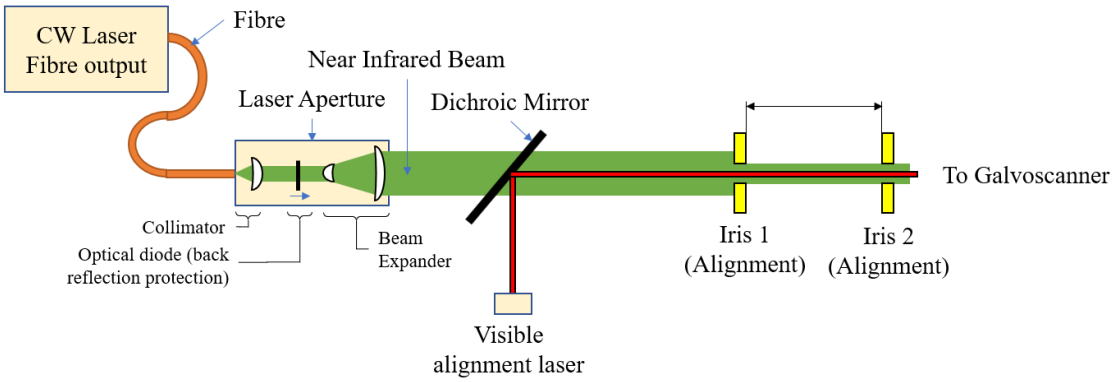
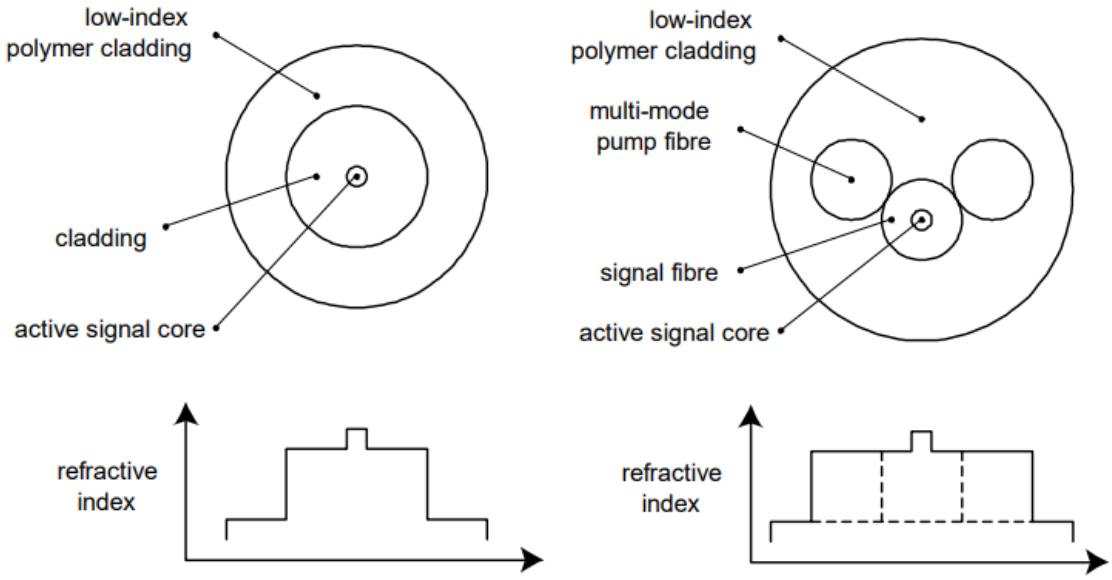


FIGURE 3.3: CW laser and its optical path

The benefit of using fibre lasers over solid-state lasers is the increased length of active media, which can be coiled and span for tens of meters, and the high surface-to-volume ratio allows providing efficient cooling. Rare-earth element doped silica fibre lasers have been reliably deployed in the industry with applications ranging from the telecom arena to welding and micromachining. Besides, silica fibres have a high thermal and optical damage threshold.

For machining applications, a double-clad fibre architecture is commonly used, schematically shown in Fig. 3.4a. The inner silica cladding and a coating with a low refractive index provide a high numerical aperture. The active core of the laser is heavily doped with lasing ions, such as Yb, Er, Nd, and Tm. In this

architecture, the pumping light is sent through the cladding of the optical fibre, allowing for multi-mode light propagation within the fibre, typically from laser-diode sources. Once the pump diodes are operating, the light propagates both through the cladding and the core, where it is absorbed by the active ions. The difference in refractive index effectively allows containing the light within the fibre through the total internal reflection phenomenon.



(A) Cross-section of a standard double-clad fibre and its refractive index profile [225]

(B) Cross-section of a GTWave fibre technology [225]

FIGURE 3.4: Possible fibre architecture for high-power application

A different approach for fibre configuration, used in the SPI-SP-100C, is shown in 3.4b. Instead of a coaxial geometry, the fibre consists of one active signal fibre and one or more multi-mode pump fibres that are manufactured to be in contact and are encased in a low refractive index polymer covering [225]. This concept allows for the creation of physically distinct pump and signal fibres that may be taken out from the common coating material and spliced into multi-mode high-power pump diodes independently from a single-mode transmission fibre separately.

Nanosecond pulsed laser

In this study, the SPI-G3 fibre laser was used to achieve laser pulses on a nanosecond scale. The laser's active medium is a Yb-doped crystal. In contrast with CW lasers, pulsed lasers are able to give high power density outputs. This results in a Gaussian beam with a diameter of 2.5mm at the aperture and a minor ellipticity along one axis.

The working principle of the laser is shown in Fig. 3.5. The fibre architecture utilises the same techniques described in the section 3.1.1. The initial seed laser diode is coupled into the single-mode fibre, which is then amplified by a series of pump sources based on laser diodes. The fibre configuration of the SPI-G3 laser is the same as the previously discussed pump fibre and signal fibre separation, shown in Fig. 3.4b.

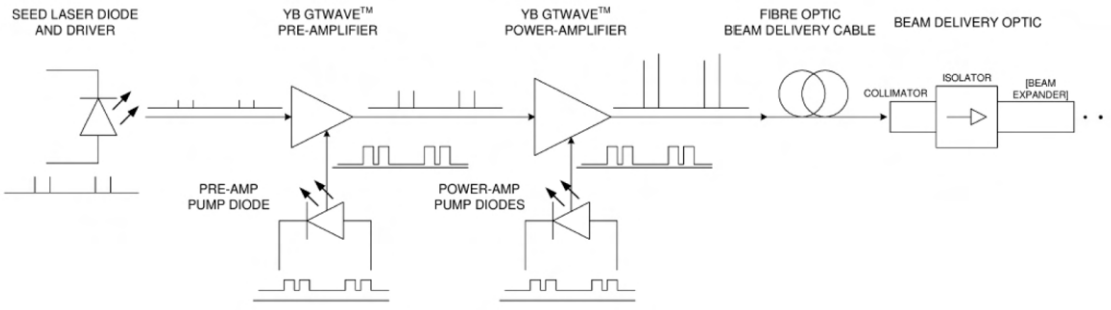


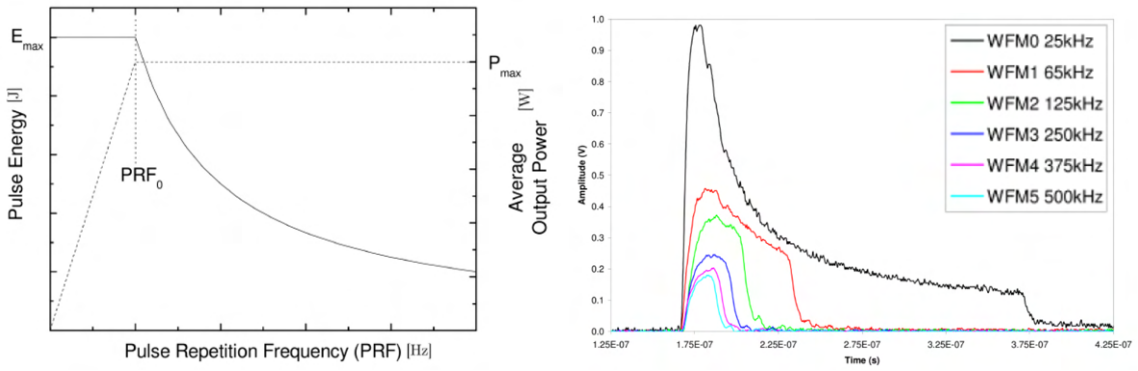
FIGURE 3.5: Working principle of SPI-G3 fibre laser

Parameter	Specification
Wavelength, nm	1062 ± 3.0
Nominal pulse repetition Frequency , kHz	1 to 1000
Average output power, W	up to 20
Maximum Pulse Energy, mJ	0.54
Pulse Duration, ns	$< 10 - 250$
Mode	TEM_{00}
M^2	< 1.6
Beam divergence, mrad	< 2.8

TABLE 3.2: Nanosecond laser parameters

The laser has an average power of 18.5 watts and may be operated in a variety of temporal patterns, as illustrated in Fig. 3.6b. Each "waveform" is associated

with certain pulse energy and pulse repetition frequency, ensuring constant power output. The experimental results in this work were obtained with the following default settings: waveform 0 was used for the temporal profile (WFM0, Fig. 3.6b) with maximum pulse energy of ∼0.54 mJ, the repetition frequency of 35 kHz, and pulse duration at full-width half-maximum (FWHM) was 50 ns. The repetition frequency may be varied between 1 kHz and PRF0 while preserving the same pulse energy; however, as shown in Fig. 3.6a, this lowers the average power generated by the laser.



(A) (B)

FIGURE 3.6: (a) Relationship of pulse energy, average power, and pulse repetition frequency for the SPI-G3 fibre laser [321]; (b) Possible waveforms and the corresponding temporal profile of the SPI-G3 fibre laser [321]

Picosecond pulsed laser

To achieve clean, debris-free ablation, an ultrashort pulse laser has been used. While the carrier-phonon scattering time, i.e. the time necessary for energy transfer from an energy carrier, i.e. electron, to the lattice, ranges from 10^{-14} s to 10^{-11} s (see Fig. 3.2), depending on the material. While a picosecond-long (10^{-12} s) pulse is nearly at the edge of carrier-photon scattering time, in principle it is possible to achieve high quality machining of ceramic materials due to a longer carrier-phonon energy transfer time, compared to metals.

The picosecond laser is a diode pumped solid state laser, assembled in the most common order for solid-state lasers: Master Oscillator - Regenerative amplifier.

Parameter	Specification
Wavelength, nm	1064
Repetition rate range, kHz	4
Average output power, W	4.5
Pulse Energy, mJ	> 1
Pulse Duration, ps	< 60
Mode	TEM_{00}
M^2	1.1
Beam divergence, mrad	< 2.5

TABLE 3.3: Ekspla Atlantic HE 1064 laser parameters

Master Oscillator is the initial seed laser based on Nd:YVO_4 crystal, which produces picosecond (about 6 ps) pulses with the repetition rate of 86 MHz [71]. Compared too the classic Nd:YAG crystals, the Nd:YVO_4 exhibits a much higher gain and higher pump absorption, and a broader pump wavelength range. The regenerative amplifier is based on Nd:YVO_4 crystal as well, the output pulse is formed by Pockels cell, letting the seed amplification in the cavity, eventually going through the regenerative amplifier towards the laser output.

3.1.2 Beam and stage manipulation

A synchronised system with a motorised stage for sample location in three spatial dimensions and rotation, and a galvoscanner to manipulate the beam in the 2 dimensions over the sample surface makes up the beam delivery. The motorised stage is a four-axis system designed by Aerotech that includes two planar linear stages ALS130H-025 for X and Y axis movement, one linear stage AVS125 for Z axis movement (in the beam propagation direction), and one rotating stage ACS-150-135. For the X, Y, Z, and rotation axes, the system has an accuracy of $\pm 1\mu$m, $\pm 1\mu$m, $\pm 1.5\mu$m, and $\pm 72.2\mu$rad, respectively. The manipulation system is shown in Fig. 3.7

Aerotech AGV-HP(O) is the galvoscanner used in this work, which allows the beam to travel at speeds up to 10000 mm/s with a peak acceleration of 288000 m/s^2 and position accuracy of $\pm 1.2\mu$m. It has a feedback mechanism that permits real-time data (position, velocity, and acceleration) for each individual mirror to be obtained.

To concentrate the beam and obtain a flat focal plane at the surface of interest, the galvoscanner is fitted with a 100mm f-Theta lens which transforms the spherical focal surface of simple lenses into a planar surface. When used in conjunction with the SPI-G3 laser beam, it creates a 54.5 μm diameter.

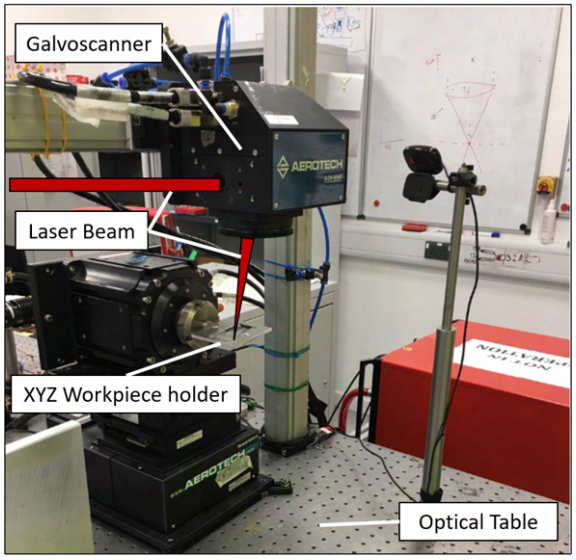


FIGURE 3.7: Beam and sample manipulation systems, including galvoscanner and motorised stage.

The system employs G-Code to design the beam path. This enables exact control of the system's behaviour, which is essential for accurate tests. The mechanism, for example, can be set to activate just when a specified speed is achieved, eliminating inaccuracies caused by mirror acceleration.

3.1.3 Beam characterisation

Power meter

An important metric of a laser is the optical power delivered to the workpiece. Thermal drift can cause the optical power of the laser to fluctuate by up to 10% in a short period of time. Degradation of optical components (e.g., mirrors along the optical path and the f-theta lens) can also result in a reduction in available power over time. It is vital to measure the power before and after each experiment to ensure that the right numbers are utilised for calculating the laser beam attributes.

The average optical power of the laser is measured using an optical power metre (Thorlabs S350C). The device converts optical energy to thermal energy using an absorbing material (Schott Glass), and an array of calibrated thermocouples measures temperature changes and converts them to a displayed average power.

For pulsed lasers, it is possible to obtain pulse energy E_p from the average power of the laser P_l and pulse repetition frequency f_l:

$$E_p = \frac{P_l}{f_l}, \tag{3.1}$$

Beam profiler

The spatial parameters of the laser beam are measured using a beam profiler (Cinology CMOS-1203). The beam processor is made up of an array of CMOS sensors with a pixel size of 4.5μm that enables precise beam diameter measurement. An example of the measured output is presented in 3.8. Before each measurement, the sensor is calibrated to account for the influence of external lighting, and an attenuator is employed to protect the sensor from overexposure. The beam profiler software then automatically post-processes the measurements after averaging at least 100 frames.

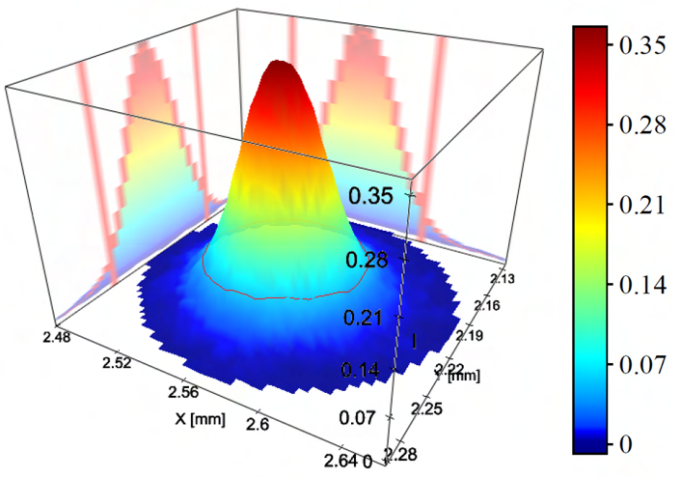


FIGURE 3.8: Example of the raw intensity profile of defocused SPI-G3 laser having a Gaussian beam distribution measured with the CMOS beam profiler. The colour legend represents the normalised intensity.

Throughout the experiments, the $1/e^2$ definition of beam diameter is applied. This is equivalent to the diameters of a fitted Gaussian with an intensity value of $1/e^2$ (i.e. 13.5%) of the maximum value. An ellipse can be used instead of a Gaussian for an astigmatic beam, as long as the beam does not stray too much.

Multiple measurements of the beam diameter for different places along the propagation axis are required to verify the beam diameter is measured at focus, and to correctly calibrate the mechanical stage used for sample placement.

$$w(z) = w_0 \left(1 + (\frac{z\lambda M^2}{\pi w_0^2})^2\right)^{1/2}, \tag{3.2}$$

where $w(z)$ is the beam radius at z, λ is the laser wavelength, and M^2 is the beam quality factor. The deviation of M^2 value from unity shows the difference between an ideal theoretical Gaussian beam, where M^2 is one, and the real beam with $M^2 > 1$.

Peak fluence, a parameter describing peak energy density for pulsed lasers, can be calculated as:

$$F = \frac{2EP_l}{\pi w_0^2} \tag{3.3}$$

3.2 Workpiece materials

3.2.1 Substrate

Polycrystalline Ni-based superalloy Nimonic C263 was used as a representative substrate material for thermal barrier coatings. C263 is a precipitation-strengthened alloy with excellent intermediate temperatures (∼1100K) properties such as ductility, strength, and oxidation resistance, and has found widespread use in aero-engines as a base material for combustors and

high-pressure compressor blades where high-temperature exposure is not expected [263].

The composition of the alloy is presented in table 3.4.

Elements	Cr	Co	Mo	Ti	Al	C	Ni
wt%	20.0	20.0	6.0	3.0	0.5	0.6	base

TABLE 3.4: Elemental composition of commercially available Nimonic C263 alloy [261]

3.2.2 Thermal barrier coating system

To represent static components of the turbine engine, i.e. combustor tiles, a thermal barrier coating system was deposited via the atmospheric plasma spraying process. The coating consisted of 75 μm metallic CoNiCrAlY bondcoat and 250 μm YSZ topcoat layer.

Both bondcoat and topcoat were sprayed with an 3MB plasma torch (Oerlikon-Metko). The composition of the powders used for CoNiCrAlY bondcoat and YSZ topcoat spraying are listed in the tables 3.5 and 3.6.

Commercial name	Co	Cr	Al	Y	Ni
Amdry 995C	base	18.0 - 24.0	5.0 - 11.0	0.1 - 0.8	29.0 - 35.0

TABLE 3.5: Elemental composition (wt%) of bondcoat (Amdry 995C) powder [207]

Commercial name	ZrO_2	Y_2O_3
Metco 204B	base	7.0 - 8.0

TABLE 3.6: Elemental composition (wt%) of topcoat (Metco 204B) powder [208]

Prior to spraying, the superalloy substrate was grit blasted and cleaned to promote adhesion of the bondcoat. The microstructure of the coating is shown in Fig. 3.9; topcoat microstructure, presented in Fig. 3.9, represents a typical lamellar structure formed flattening of spherical powders during the APS process with fine columnar grains, which is a typical result of air plasma spraying process.

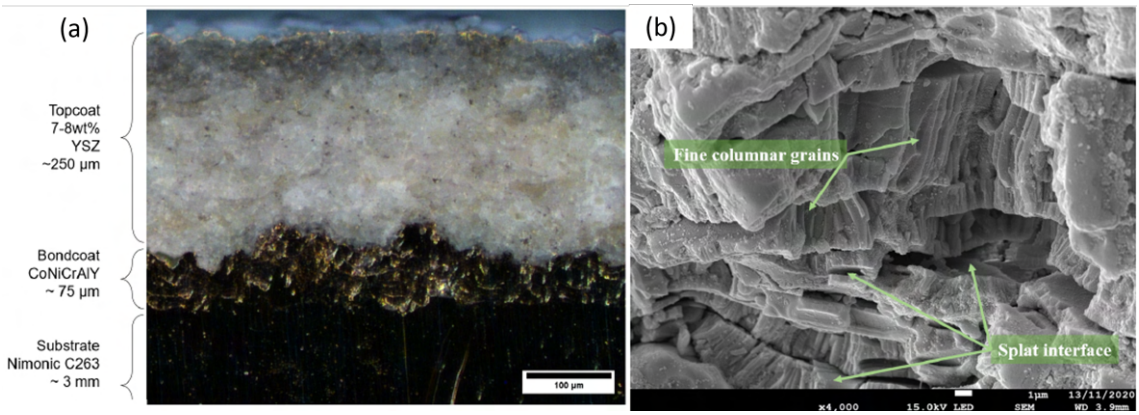


FIGURE 3.9: Microstructure of as-sprayed TBC comprised of bondcoat and topcoat, covering a flat superalloy material. (a) Darkfield optical micrograph of the coating cross-section; (b) SEM image of the topcoat fracture surface revealing the lamellar structure of APS coating.

The porosity of the as-sprayed topcoat was 13.1±1.5%, as measured by the ImageJ software from 3 SEM cross-sectional images, as described by [113]. In this method, the software analyses the cross-sectional image of the TBC by dividing the image on "white" and "black" portions, i.e. "material" and "pore" zones, based on the relative brightness of the spot. This method provides with an estimation of the porosity since the judgement can be affected due to the SEM scanning parameters and contrast settings, and limited to a 2-dimensional cross-section instead of the volume. While a better method to measure coating porosity using X-Ray tomography exists and provides with an accurate data, the porosity estimation using ImageJ analysis was sufficient for this study.s

3.3 Material analysis techniques

In this section, material analysis methods are described and used for the microstructural analysis, evaluation of coating performance, and model validation, are presented.

3.3.1 Metallographic preparation

Material response to laser irradiation as well as to the simulated in-engine conditions was evaluated by top surface or cross-sectional observations. The different nature

of the ductile substrate and brittle and hard topcoat makes material preparation challenging. Besides, the small thickness of the coating makes the layer particularly fragile. In order to diminish the mechanical influence of the tools used to obtain cross sections, aggressive cutting and grinding should be avoided. Instead, slow cutting conditions and low pressure during mechanical grinding and polishing should be used. In most of the experiments, the samples were mounted in epoxy resin which also helps redistribute stresses induced during sample preparation. The only exception was made for the preparation of the longitudinal cross-sections of remelted tracks; in that case, it was important to have a cross-section as close to the geometrical centre as possible, and the top surface was checked via an optical microscope between the grinding operation, particularly important on the first steps with low grit size number. These samples were mounted into a 3D-printed plastic fixture and manually ground on a low-number grit paper to get close to the track, and ground and polished automatically with the same procedure used for the rest of the samples, discussed below.

For surface preparation of the deposition substrates, annealed stainless steel AISI 304 of different thicknesses were waterjet cut to size, ground and polished through the same procedure used for all samples. Immediately before deposition, the samples were cleaned first in ethanol, then in acetone, and then in deionised water; prior to deposition, the sample was dried with a heat gun.

3.3.2 Surface analysis

White light interferometry

For obtaining the surface topography of the samples, white light interferometry has been used, which can reconstruct the 3D surface of the sample and can be used for calculations of surface topology parameters, such as roughness and waviness, as well as estimate the amount of removed material upon erosion. In this study, Bruker GTi white light interferometer has been used, which allows accurate mapping of a surface.

The following is a simple description of an interferometer's operation. A beam splitter splits a wave produced by a light source into two components. The first component hits a fixed reference mirror, while the second is directed at the surface and reflected back. After that, the two components are merged to create an interference pattern, which is subsequently photographed on a CCD detector. When the path difference between the two components is zero, the result is a distinctive fringe pattern, which is the brightest, in other words, when the mirror-target distance equals to the sample-splitter distance (see Fig. 3.10). Interference patterns are collected over a range of z locations by altering the vertical position of the target surface.

The surface data collected by the measuring equipment is subsequently processed using the MountainsMap software. According to the "National Physics Laboratory Measurement Good Practice Guide No.116 The Measurement of Rough Surface Topography using Coherence Scanning Interferometry" [243], each measured dataset undergoes a series of operations, which are listed in the following order:

- Filling isolated outliers and filtering;
- Remove surface tilt via 1st order polynomial;
- Automatic principal component analysis to rotate the measured surface to fit the principal axis of the measured feature.

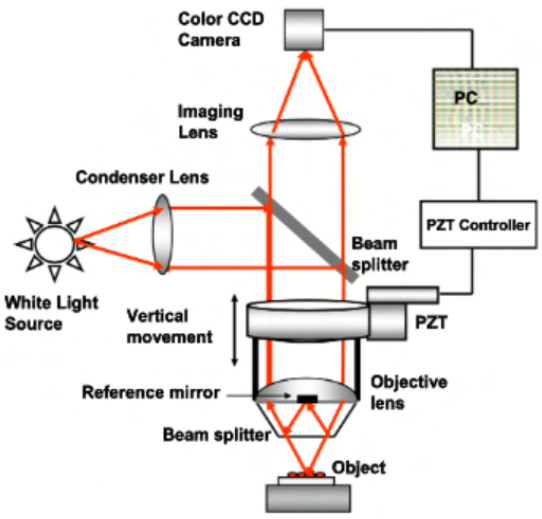


FIGURE 3.10: Schematic diagram of a white-light interferometer [290]

3.3.3 Microstructural analysis

Scanning electron microscopy and energy dispersive spectroscopy

The main tool to assess the impact of the laser beam on the microstructural transformations, be it material removal, laser melting, or interaction of the coating in tests, is Scanning Electron Microscopy (SEM). Diffraction-limited resolution of an optical microscope usually allows distinguishing features down to 1 μm. A way to overcome this issue is to decrease the characteristic wavelength. While decreasing photon wavelength is a challenging task, nanometre-scale observations are possible with high-energy electrons.

The Scanning Electron Microscope (SEM) operates on the premise of using kinetic energy to generate signals from electron interactions. Secondary electrons, backscattered electrons, and diffracted backscattered electrons are all types of electrons used to observe crystalline elements and photons. An image is created using secondary and backscattered electrons. The primary role of the secondary electrons generated by the specimen is to detect the shape and topography of the specimen, whilst the backscattered electrons exhibit a contrast in the composition of the specimen's constituents.

The working principle of a scanning electron microscope is comparable to that of a traditional light-based microscope. A light source (e.g., an electron gun) produces a beam (e.g., an electron beam) that is collimated by an electromagnetic condenser lens and directed at a specimen. The beam is scanned across the surface of the material in an SEM, generating a teardrop-shaped interaction volume.

Collisions with other electrons and atoms scatter electrons both elastically and inelastically within the interaction volumes. After multiple collisions, the elastically scattered electrons emerge from the surface and are captured by a detector. Backscattered Electrons (BSE) can be used to qualitatively differentiate between elements, such as a parent metal and its oxide because the quantity of scattering relies on the atomic weight of the element (heavier elements scatter more strongly than lighter elements).

The remaining electrons from the initial beam are elastically scattered. Only the electrons closest to the surface can emerge; these are low-energy electrons known as Secondary Electrons (SE), which are accelerated and captured by a second detector, usually situated close to the sample. SE can provide topographical information on the surface when the amount of SE grows at non-perpendicular incident angles (because of the bigger interaction volume).

Scattered electrons that do not form a secondary electron lose all of their energy within the lattice, which is converted to heat and also causes Bremsstrahlung radiation (due to contact between the nuclei and the electric field) or ionisation of an atom, which results in the emission of distinctive x-ray radiation.

The background signal captured by the EDX detector is composed of x-rays emitted through Bremsstrahlung, which have a continuous energy distribution up to the maximum energy of the primary electron beam; on the other hand, characteristic x-rays have a well-defined energy distribution, which is dependent on the electronic structure of the atom and can be indexed, allowing information about the elemental composition of a sample to be extracted.

Several SEMs have been used in this study. The type of emitter, available detectors, and parameters used throughout the study are listed in the table 3.7.

Microscope	**Emitter and detectors**	**Parameters**	**Comments**
Quanta Q650 eSEM	Tungsten-based thermal emitter. SE, BSE	20kV, WD 10 mm	low magnification day-to-day imaging
Quanta Q600 eSEM	Tungsten-based thermal emitter. SE, BSE, EDX	20kV, WD 10 mm	low magnification day-to-day imaging and elemental analysis
JEOL 7100F	Field-emission gun (FEG), EDX, EBSD	15kV, WD 10 mm	High magnification, high resolution imaging

TABLE 3.7: List of SEMs and corresponding parameters used throughout the investigation.

Electron back-scatter diffraction

To investigate the crystal characteristics upon laser melting, Electron Back-Scatter Diffraction (EBSD) has been used.

EBSD utilises an electron beam generated by an SEM column that is focused on the surface, resulting in back-scattered electrons. Because the lattice spacing in crystalline materials is constant along a crystallographic plane, some electrons can diffract, according to the Braggs condition $2d_{hkl}\sin\theta = n\lambda$, where d_{hkl} is the inter-planar distance and θ is the angle of incidence, and create constructive/destructive interference patterns that can then be imaged on a phosphorous screen, forming a Kikuchi pattern, shown in Fig. 3.11. The electron beam is directed onto a tilted specimen, usually at 70 degrees, to obtain the Kikuchi patterns. The crystal orientation map of the exposed surface can be reconstructed by scanning the beam across the surface, similar to how an SEM image is reconstructed.

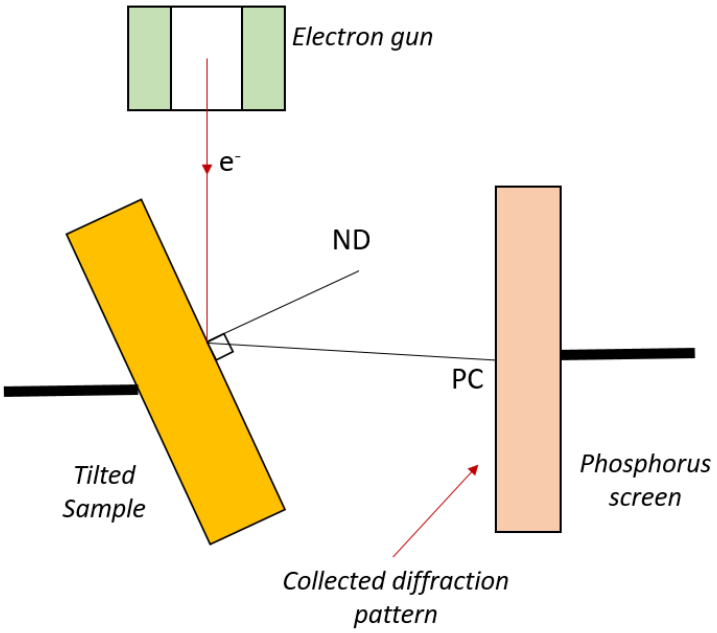


FIGURE 3.11: Schematic view of EBSD technique in the SEM environment, where the electrons are focused on a tilted sample, and diffraction pattern is collected on a detector plane. ND denotes the sample's normal orientation, and PC shows the pattern centre of the diffracted signal.

Each pattern has a zone axis with a sequence of intersecting bands, each reflecting

the projection of a different crystallographic plane. It is possible to match a Kikuchi pattern with an orientation angle and material phase if at least three crossing bands are present. This process is known as indexing, and it is carried out automatically by the EBSD's acquisition software, which first transforms Kikuchi band to a Hough space to determine the location and orientation of each band, and then compares it to a database. Hough transformation essentially represents the lines of diffraction bands (Fig. 3.12, a) as a set of points (Fig. 3.12, b) which are easier and faster to analyse, whereas the analysis consists of comparing the angles between bands and the lookup database.

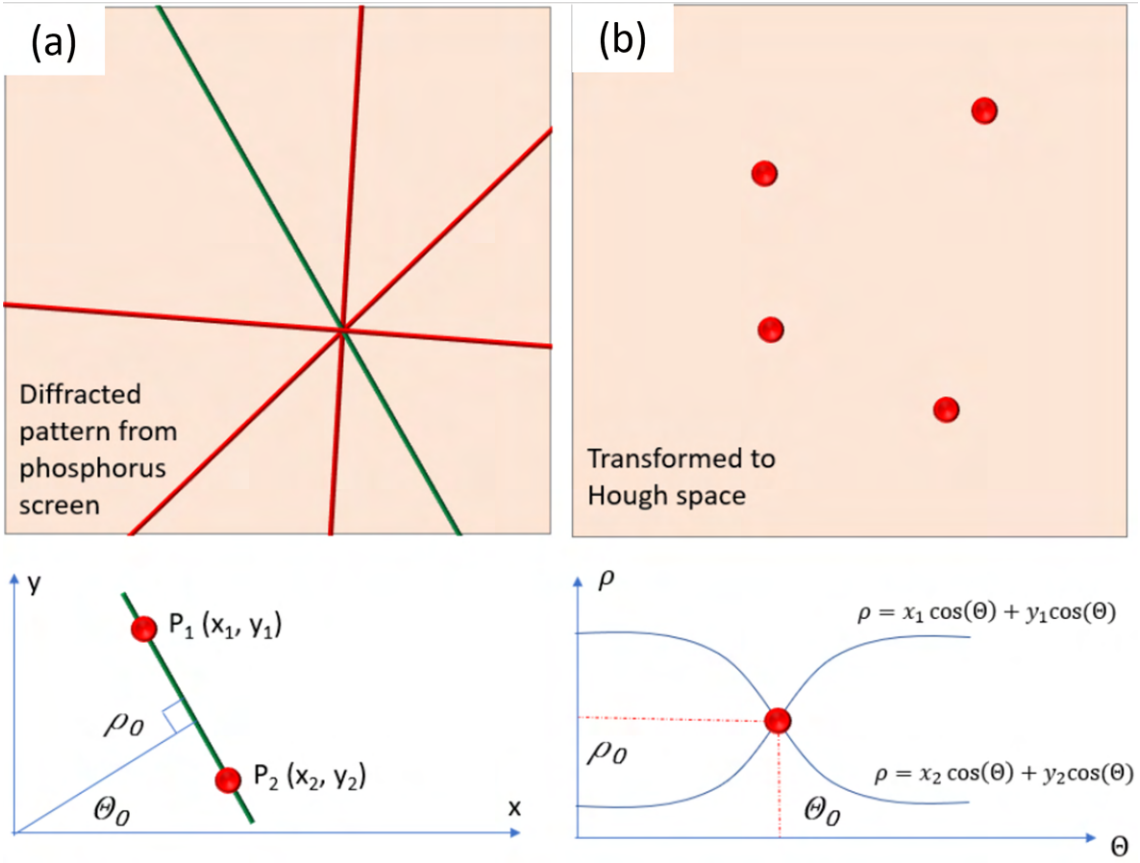


FIGURE 3.12: (a) direct diffraction pattern from the lattice on the phosphorus screen and (b) Hough space transformation of diffracted lines

The EBSD technique is a valuable tool for material characterization. The quality of the results, on the other hand, is ultimately determined by the quality of the patterns obtained, which is determined by the quality of the samples used. Because of the small sampling depth, the approach is particularly susceptible to surface

roughness and coating thinness, which might affect the quality of the Kikuchi patterns obtained. Furthermore, when the crystal lattice is significantly damaged due to extreme plastic deformation, the indexing algorithm frequently struggles to find a correlation between the data and the crystal reference database, resulting in a large percentage of non-indexed points.

An EBSD detector (Oxford Instrument Nordyl) linked to a JEOL 7100F SEM was used for the current experiment; the system additionally included an EDX detector for simultaneous elemental mapping. The capture parameters for capturing grain structure within the topcoat are as follows: step size of 30-300 nm, 2x2 binning, and a medium exposure period (100-250 ms) are utilised with the accelerating voltage of 15kV. Frame averaging (3 frames) was used for all the measurements.

Oxford Instrument's software AztecHKL indexes the Kikuchi patterns, which are then post-processed by Aztec Crystal software and MTex Matlab library. A variety of procedures are possible using both methods together, such as the removal of pseudo-symmetry and isolated outliers, generation of IPF and KAM maps, as well as pole figures. The maximum misorientation, defined as two indexed points belonging to the same grain, was set to 10 degrees, which was used for distinguishing neighbouring grains and revealing the grain boundary geometry.

X-Ray crystallography

X-ray diffraction is a localised, quick, and non-destructive diagnostic method for determining the phase of crystalline material. It is also possible to determine the residual stresses, crystal orientation, and purity. The lattice's high degree of periodicity and order is represented by a number of parallel planes, each of which has a distinct spatial orientation Fig.**??**. Each atom re-emits a small amount of its intensity as a spherical wave in response to the incident x-ray beam. Because of the crystal's high periodicity, constructive interferences are created for specified angles that are dependent on the distance between the planes and the common direction.

Similarly to EBSD, when $2d_{hkl}\sin\theta$ is equal to a multiple of the wavelength of the incident beam, the Bragg equation yields the precise angle for which the intensity

is maximal. The crystalline structure of the substance is fingerprinted by the XRD diffraction pattern. Typically, the diffraction pattern is compared to available databases. The proportion of crystal in a certain orientation was determined using XRD diffraction in the investigations reported. In the case of a random distribution of crystal orientation, the database normally includes the position of the peak and the ratio of the peak. As a result, a preferential orientation of the crystalline structure of the material can be obtained.

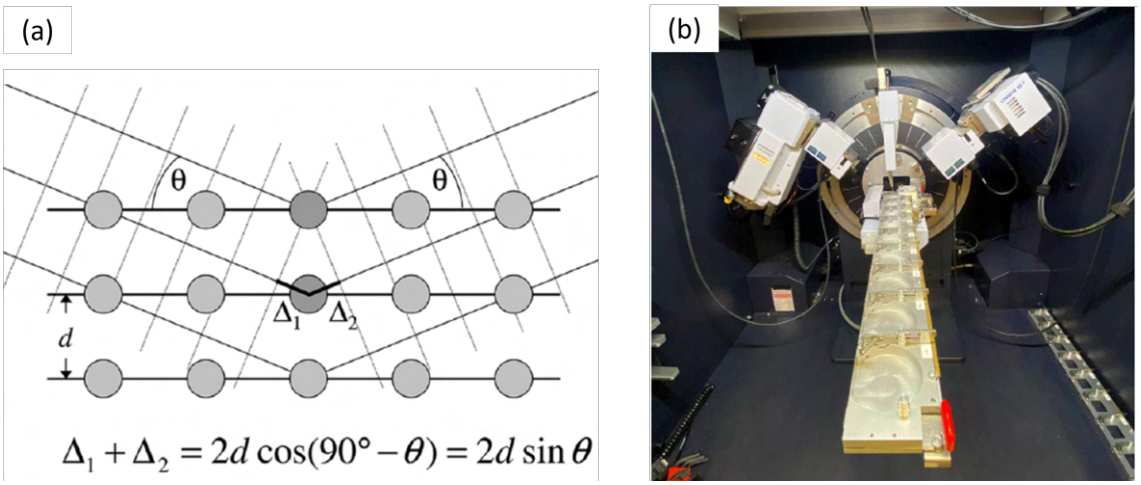


FIGURE 3.13: (a) Cross-section view of X-ray interaction with crystal lattice and the Bragg equation below [29] (b) testing chamber of Bruker D8 Discover diffractometer.

The crystal orientation of YSZ topcoats was measured using a D8 Discover diffractometer with a Cu K_α target (radiation source) for obtaining a full XRD spectrum and high-resolution analysis within a specific range of Bragg angles, allowing to distinguish between m, t, and t' phases. The broad range was obtained over a 2θ range between 5 °and 95 °with a step size of 0.5 °and dwell time of 10s. In refined spectrums, the 2θ ranges were between 27.5°to 32°, and 72.5°to 76 °, both obtained with a step size of 0.005 °and dwell time of 2s per step. In all the conducted experiments, the beam size was 1 mm.

3.3.4 Coating performance assessment techniques

Thermal fatigue

For static components, thermal fatigue resistance is one of the most essential attributes of TBCs. To determine thermal fatigue resistance of as-sprayed and modified coatings, 25x25x3 mm specimens were waterjet cut into cylindrical coupons ⌀of 24 mm, allowing to reduce the influence of stress concentration at the corners of the sample. The samples were heated to 1121°C in the air for 10 minutes, kept at this temperature for 40 minutes, and then cooled to 60°for ≈10 minutes, controlled by the thermocouple attached to the base of the furnace. The time spent between the start of the test and the delamination of 50% of the top coat area was used to calculate the thermal cycle lifetime, which was evaluated visually. 6 specimens per one measurement were used for statistically significant results. A similar procedure has been widely used in academic research articles (e.g. [198, 293, 238]).

Erosion resistance

The coatings were impacted with Al_2O_3 particles with 220 mesh size at a pressure of 0.175 MPa, a nozzle-workpiece distance of 101.6 mm, and a 20°impingement angle at room temperature on 25x25x3 mm as-sprayed specimens, according to the recommendation by Rolls-Royce. The erosion testing rig is schematically represented in 3.14. These parameters allow simulating conditions within the combustor chamber, where the flow of erosive particles impacts the sample with a low angle of incidence. At the standard procedure ASME G76-04 of "Standard Test Method for Conducting Erosion Tests by Solid Particle Impingement Using Gas Jets" limits the angle of incidence to 90°, which is of lower relevance for gas-turbine application.

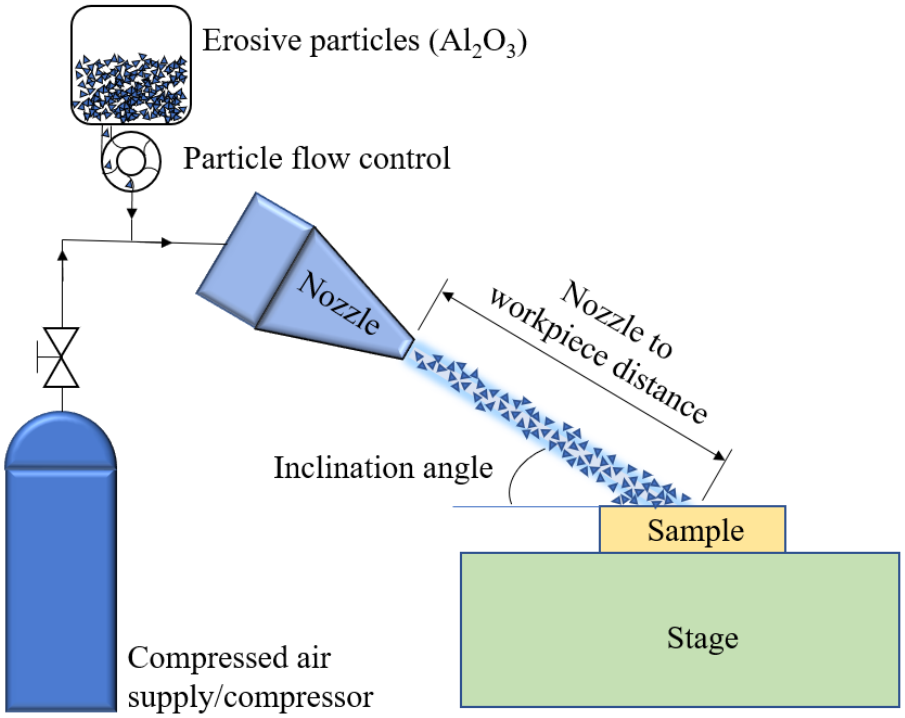


FIGURE 3.14: Schematic diagram of the erosion test rig.

Despite the fact that this feature was examined in this work. it should be noted that for the tiles within the confined area of a gas-turbine engine's combustor, foreign object damage (FOD) is a major issue within both compressor and turbine stage components, while erosion is more severe in the components situated at the turbine stage due to the higher angle of incidence.

CMAS infiltration

Components of aero-engines are exposed to a hostile combustible environment, as well as foreign particles in the air, such as volcanic dust, sand fly ash, fuel impurities, and others. The particles sediment on the surface of TBC, which often leads to sand infiltration and coating failure, schematically represented in Fig. 3.15. Typically, the sand represents a mixture of calcium-magnesium-aluminium-silicon oxide system (CMAS), which can interact with TBCs under high-temperature [168]. While in the cold sections of the engine, i.e. compressor region, the sand mostly causes erosion and air passage clogging, it melts mostly in the combustor region and was found to adhere and infiltrate the TBC on the combustor tiles and baffles, turbine blades,

vanes and shrouds [100]. The conditions simulating CMAS interaction with TBCs are yet to become standardised; in this work, the impact of CMAS was performed under high temperatures based on the parameters found in academic reports.

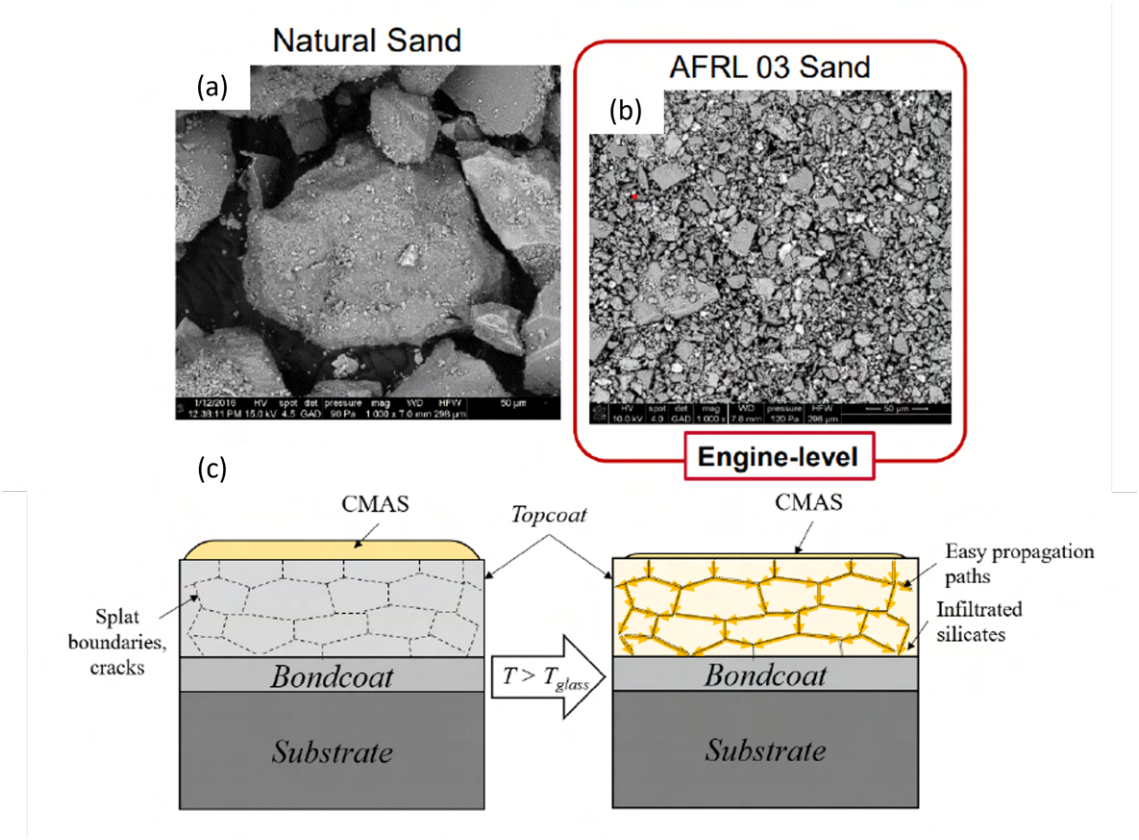


FIGURE 3.15: (a) Morphology of natural sand [100] and (b) AFRL 03 sand with size distribution typically entering the engine level [100](c) Schematics of CMAS infiltration along discontinuities, such as cracks, splat interfaces, and grain boundaries.

To simulate this, AFRL03 (Air Force Research Laboratory, US) test dust has been used (Powder Technology Inc., US), with the composition of 33CaO-9MgO-13$AlO_{1.5}$-45SiO_2 (mol %) [134]. The composition of the CMAS used is shown in the table 3.8.

Elements	Quartz (SiO_2)	Gypsum ($CaSO_4 \cdot H_2O$)	Aplite (quartz, feldspar)	Dolomite ($CaMg(CO_3)_2$)	Salt (NaCl)
wt.%	34	30	17	14	5

TABLE 3.8: Elemental composition of AFRL 03 test dust used in CMAS tests [134]

The sand particulates typically melt between 1050-1250°C [244]. Properties of AFRL 03 such as glass transition temperature and softening point were not measured in this study, and were estimated based on reports with similar powders; the reported glass transition temperature of desert sand with the composition of 27.8CaO-4MgO-5Al_2O_3-61.6SiO_2-0.6Fe_2O_3-1K_2O (mol %) is 706 °C, softening point is 764 °C, and coefficient of thermal expansion of $9.8 \cdot 10^{-6} K^{-1}$ [21]. Higher temperatures, typical for in-engine conditions, had been used in this study.

The AFRL 03 powder was mixed with ethanol to form a paste with a concentration of 0.5g CMAS/0.75ml ethanol. The paste was deposited on the sample with the concentration of 35 mg/cm^2 of CMAS powder. After deposition, the paste was dried on the substrate at room temperature in air for 30 min. The heat treatment procedure consisted of a slow temperature increase with the ramp rate of 10°C/min to a temperature of 1121°C. The samples were held at this temperature for 24 hours, slowly cooled down with the furnace without forced cooling, and taken out after 24 hours. Similar procedures can be found in various academic works, e.g. [16, 68, 15, 224].

Chapter 4

TBC microstructure modification through laser ablation and laser melting approach

This chapter provides a description of microstructure modification of thermal barrier coatings for improved durability. Starting with a brief summary of the failure mechanisms and proposed modification method, this will be followed by assessing the modification process of TBCs with laser tools. Laser machining and laser melting of thermal barrier coatings and damage to the material will be presented and discussed. Laser grooving was performed with short (nanosecond-long) and ultrashort (picosecond-long) pulse duration, and a particular material sensitivity of the ultrashort pulse lasers was found, allowing selectively remove topcoat material with no or minimal damage to the bondcoat while reaching the interface between the layers. Second step, laser melting, was optimised on the pre-grooved surface to achieve surface continuity and minimising the damage to the underlying topcoat material.

Understand melting mechanisms of TBCs upon laser irradiation. Find relevant physical parameters governing the geometrical and microstructural parameters of the coating upon laser glazing procedure.

4.1 Introduction

A constant seek for increased efficiency and durability of gas-turbine engines generated a high demand for reliable thermal barrier coatings (TBCs). TBCs are oxidation-resistant multi-layered structures typically having a metallic (Ni, Co)CrAlY bondcoat covered with an insulating ceramic topcoat. A commonly used topcoat material, 7-8wt% Yttria Stabilized Zirconia (YSZ), is suitable due to its low thermal conductivity, high thermal expansion coefficient comparable with that of underlying metals, high hardness and fracture toughness, as well as high-temperature phase stability.

Thermal barrier coatings protect the substrate from oxidation and chemical and mechanical (erosion and foreign object damage) attacks and improve the underlying component's expected lifetime. However, the lifespan of current state-of-the-art TBCs is limited due to oxygen ionic conductivity at high temperatures[157] allowing oxygen atoms to penetrate through the topcoat, eventually resulting in the bondcoat oxidation. Surprisingly, the internal porosity of the coating does not increase oxygen diffusion; conversely, internal pores act as a barrier and retard the diffusion of oxygen ions through the topcoat, as shown in the work of Wang et al.[342]. Besides, due to the mechanical nature of adhesion of APS coatings, they experience weak thermal shock resistance relative to EB-PVD-produced coatings.

Various attempts to modify thermally sprayed coatings have been undertaken and shown an increase in durability in thermal, chemical, and mechanical tests. For instance, the multilayer topcoat composition and porosity gradient of the coating showed the possibility of control of residual stresses in the coating [154]. Topcoat segmentation via direct material removal approach, for instance with a laser, waterjet, etc., found industrial attention, reflected in several patents [216], [359]

and a research work of Khan et al. [51]. Khan shows improved thermal shock resistance of coatings with a pattern of laser-ablated grooves at the near surface. 35% to 50% of the coating thickness and proved the advantage of grooving in thermal cycling tests; however, generated open voids might impair thermal insulative properties of the coating; to the best of the authors' knowledge, no further characterisation had been conducted for textured TBCs, hence the in-depth mechanisms of the thermal cycling improvement are still not clear.

The laser surface melting approach was also tested in a number of works [1], [366] and implemented during the deposition process[2], showing increased erosion resistance due to densification of the surficial layer. Thermal fatigue test of laser-melted thermal barrier coatings showed various results: while some studies reported increased thermal cycling performance [315], which was attributed to the network of vertical microcracks at the surficial layer; others found no improvement in thermal cycling life [98]. This process is also known as glazing because the dense layer becomes transparent. The influence of the microcracks network, as well as the relationship between thermal cycling life and the properties of the glazed layer, are yet to be established. Laser glazing also reduces surface roughness and increases microhardness but, on the other hand, slightly increased thermal diffusivity of the coating as a result of decreased porosity at the surface [317], which can also be attributed to the generated microcracks. The hot corrosion resistance of glazed coatings was also improved [98], [343] and believed to be a consequence of generated microcracks, which increased strain tolerance of the topcoat. However, microcrack morphology plays an important role in the TBC-chemicals interplay, and there is a field for further investigations of laser glazed TBCs; in more detail, TBC modification methods are discussed in the Literature Review section.

In summary, the main failure and degradation mechanisms of TBCs are as follows:

1. Stress development in the TGO, leading to coating spallation or buckling.
2. Erosion of the coating, a consistent loss of TBC thickness due to low splat-to-splat adhesion;

3. Chemical interactions of topcoat with an active environment, leading to destabilisation of YSZ and/or loss of thermomechanical compliance.

4. Sintering of the porous topcoat leads to deterioration of the thermal insulative properties of the coating.

To increase the durability of the coating in the harsh engine environment, the degradation can be retarded by addressing the abovementioned processes. In this chapter, combined laser ablation and laser melting modification technique is proposed (Fig. 4.1): hollow internal structure, created employing pulsed laser ablation, increases thermomechanical compliance of the coating at the bondcoat-topcoat interface; a dense surficial layer represents a protective surficial layer resistant to erosion, corrosion, and reducing the oxygen short-path to the bondcoat. The response of crystal lattice after mechanical erosion and thermal fatigue was studied and revealed no phase transformation within the affected area. Instead, the coating shows signs of ferroelastic domain switching and changed the residual stresses.

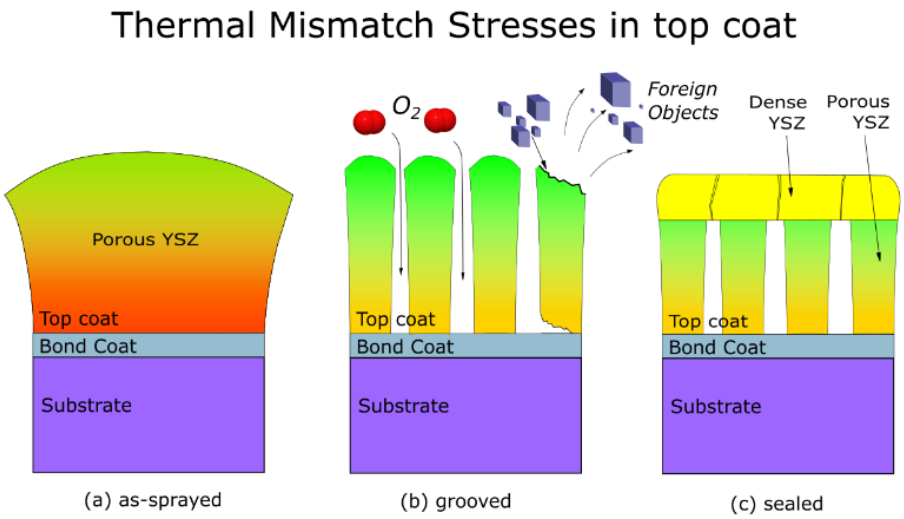


FIGURE 4.1: Key steps to enable pseudo-columnar architecture of the coating: (a) as-sprayed topcoat with pronounced thermal expansion mismatch stresses at the topcoat-bondcoat interface; (b) introduced grooves govern the in-plane Young's modulus of the coating minimising thermal expansion mismatch stresses; (c) coating with a dense top surface, resistant to mechanical impacts and reduced oxygen short path.

4.2 Theoretical aspects related to the improvement of thermomechanical compliance

As concluded in the previous section, one of the main reasons for coating spallation is the generation of high stresses at the interface with topcoat, induced by thermal expansion mismatch, shown in Fig. 4.1 a. The topcoat is subjected to micromachining in order to create a pattern of grooves, which will be later sealed with a dense protective layer by the laser glazing process. Firstly, the grooves physically separate the coating, allowing its free movement relative to each other, similarly to an EB-PVD-produced microstructure. Secondly, in such a process the solidification shrinkage cracks within the glazing layer will naturally follow towards the groove (which will be shown in this work), therefore removing the stress concentrator from the coating.

For the simplicity of further discussion, the bondcoat layer is neglected due to the similar coefficient of thermal expansion (CTE) with the substrate e.g. $\sim 14 \cdot 10^{-6}$ K^{-1} for Nickel-based superalloy [235] and in range of $15 \cdot 10^{-6}$ K^{-1} for bondcoat [223]), while the CTE of the topcoat is more different (for YSZ topcoat that is $11 \cdot 10^{-6}$ K^{-1}[235]); TGO strain input is neglected due to its small thickness (1-10 μm [235]). Based on work of Evans and Hutchinson [102] and assuming isothermal heating/cooling conditions, strain at the interface is given by:

$$\varepsilon_{x\ th} = \varepsilon_{x\ TC} - \varepsilon_{x\ sub} = \alpha_{x\ TC}\Delta T - \alpha_{x\ sub}\Delta T \tag{4.1}$$

where $\alpha_{x\ TC}$ and $\alpha_{x\ sub}$ are the linear CTEs in x direction of topcoat and substrate correspondingly; $\varepsilon_{x\ TC}$ and $\varepsilon_{x\ sub}$ are the thermal expansion induced strains in the topcoat and substrate respectively; ΔT is the full temperature difference.

From Hooke's law [94] the thermal mismatch stress in topcoat – bondcoat interface σ_{xx}, can be expressed as:

$$\sigma_{xx} = \frac{E_x \cdot \varepsilon_{x\ th}}{1-\nu} = E_x \cdot \frac{(\alpha_{x\ TC}\Delta T - \alpha_{x\ sub}\Delta T)}{1-\nu} = \frac{\Delta\alpha_x \cdot E_x}{1-\nu}\Delta T \tag{4.2}$$

where E_x is the *effective* in-plane Young's modulus of TBC, $\Delta\alpha_x = \alpha_{x\ TC} - \alpha_{x\ sub}$ is the thermal expansion mismatch between topcoat and substrate, and ν is the Poisson's ratio.

From Eq. (4.1) it is evident that thermal mismatch stresses can be minimised by minimising the thermal expansion mismatch between topcoat and substrate($\Delta\alpha_x$) as well as the *effective* in-plane Young's modulus of TBC (E_x). On a macroscale, the effective Young's modulus of a porous material E_{porous} is a function of its porosity, as proposed by Nielsen: [293]:

$$E_{porous} = \frac{E_{dense}(1-\nu)^2}{1+\nu\cdot(\frac{1}{\rho_{geom}}-1)} \tag{4.3}$$

Where E_{dense} is Young's modulus of initial material, ν is the Poisson's ratio, and ρ is the geometry factor of the pores, and higher pore content reduces Young's modulus. It is known that the coatings with higher porosity generally show better thermal cycling performance, on the other hand, greater porosity leads to a decrease in coating hardness and fracture toughness [16], therefore worse erosion characteristics. An effective way to decrease the in-plane E_x independently from out-of-plane Young's modulus E_z, without compromising coating hardness, is by creating grooves in one dimension, perpendicular to the interface of layers (see Fig. 4.1 b).

In this case, a gas short path to the underlying material, which might lead to increased thermal conductivity and faster bondcoat oxidation, and the topcoat is likely to have worse characteristics in terms of CMAS resistance, erosion, and particularly to foreign object damage. Hence, it would be beneficial to have a continuous protective layer, which would seal the grooves, creating a confined air bubble. Besides, the latter effectively decreases the thermal diffusivity of the coating. To address this, the top surface of TBC can be densified, "bridging" the columns

from the top, as shown in Fig. 4.1 c. These bridges, on one hand, reduce free penetration of combustion gases into the coating and reduce the thermal diffusivity of the coating. On the other hand, the sealed layer provides TBC with protection to mechanical and chemical damage, i.e. better erosion resistance and limited CMAS penetration through the coating due to the absence of interconnected microcracks at the dense layer.

As demonstrated in the literature, the possibility of modifying coating properties by performing post-treatment has been subjected to large interest in the scientific community over the last decades. At its most basic level, the idea of tailoring micro-macro structural properties of a coating by use of relatively simple and inexpensive techniques is very attractive. However, as could be expected, while each post-treatment is able to improve some characteristic properties of the target material, this often comes to the detriment of others. While numerous treatments have been proposed in the literature, a systematic approach to achieving precise control of coating properties has never been applied.

Manufacturing method of the modification technique is presented in Fig. 4.2. To reproduce the columnar structure of the EB-PVD topcoat on the macroscale, a pattern of grooves will be generated within the topcoat via a pulsed laser. For further protection of the coating from mechanical impact and CMAS infiltration, the coating is covered with a layer of dense remelted topcoat.

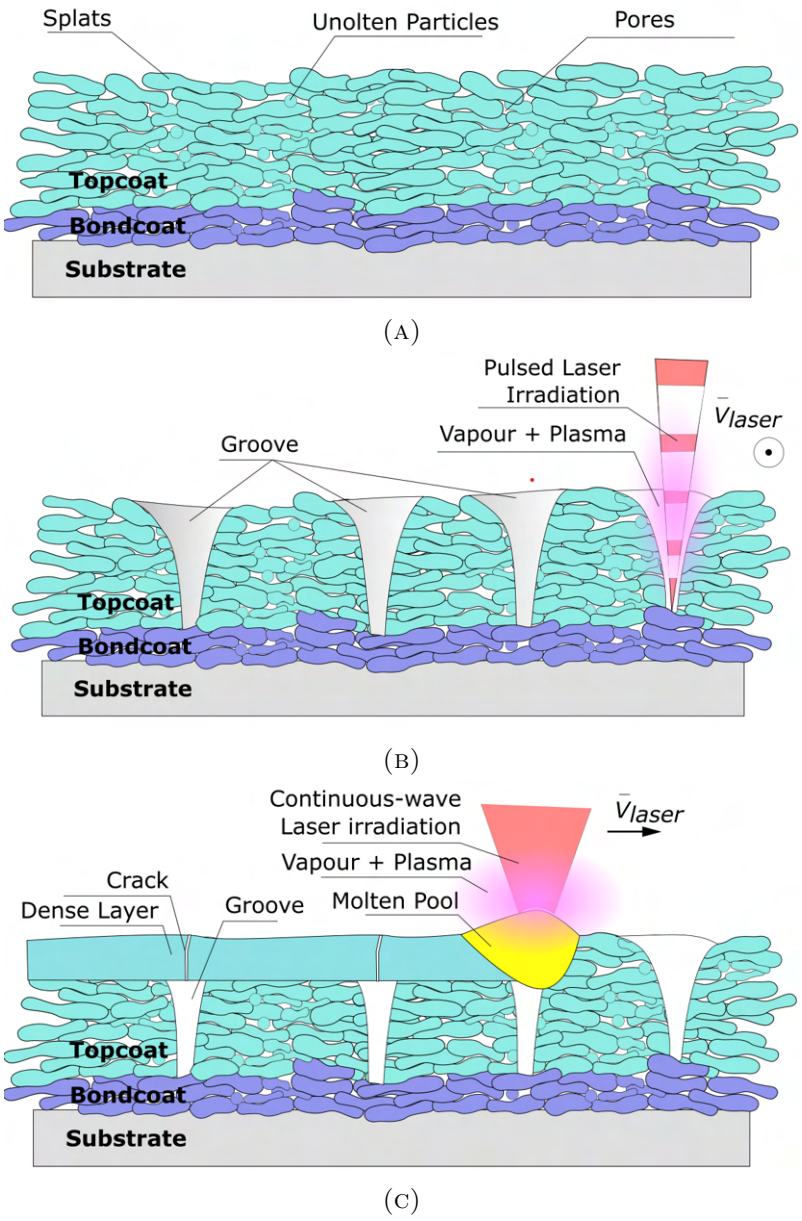


FIGURE 4.2: Schematic representation of thermal barrier coating modification. (a) thermally sprayed coating; (b) laser grooving via pulsed laser; (c) laser glazing via continuous or pulsed laser.

4.3 Laser grooving of thermal barrier coating system

The first step of modification aims to improve thermomechanical compliance by reducing in-plane Young's modulus, which is done by creating a pattern of

one-dimensional grooves in the topcoat. For the highest compliance of the layer and reduction of stress concentration at the groove tip, it was assumed that the grooves reaching the bondcoat interface is the preferred coating microstructure. This will ensure independent motion of each column as a consequence of thermal expansion and shrinkage and remove the stress concentrator at the tip of the groove. While optimising the laser grooving step, it is important to consider the following factors:

1. Collateral damage to the material. The laser ablation process can generate high thermal gradients, which is particularly undesirable for brittle materials prone to cracking.

2. Groove width at the top surface. Minimising the groove width allows to keep the structural integrity of the TBC and eases its further continuous melting.

3. Material selectiveness, i.e. ability to stop penetrating further through the coating once the topcoat was removed. While this can be performed actively, e.g. by continuously monitoring plasma emissions and measuring its spectrum, it was found that shorter pulse durations enable selective topcoat removal.

4.3.1 Ultrashort pulse laser grooving

To achieve groove penetration through the topcoat with minimal damage to the underlying material, ultrashort pulse lasers should be used. In long pulse ablation (nanosecond and longer) the absorbed heat is transferred to the lattice by heat conduction, which typically results in the melting of the material (unless the latter sublimates). The physical process of ablation consists of heat absorption (in metals absorption by free elections and by the valence electrons in ceramics) and heat diffusion to the lattice. With long pulses, the laser pulse length is sufficient for the thermal equilibrium of the electrons and lattice. When the laser pulse length τ_L is comparable to or shorter than the electron cooling time τ_e, the local equilibrium of the electron-lattice does not take place, and heating of the matter can be described with a two-temperature model. This results in significant evaporation once the energy is sufficient, which is typically the main material removal mechanism. Due

to the absence of free electrons in ZrO_2 and extremely low thermal conductivity compared to underlying nickel oxides, the removal mechanisms with a similar pulse length may be different. In metals, the thermalisation time within free electrons is typically between 10 fs to 1 ps [70] and the electron-lattice thermalisation is around 1 ps[345] and longer for ceramic materials [256]. Therefore, while a short pulse duration is used, it is possible to remove the topcoat material selectively without significantly affecting the bondcoat.

Results, shown in Fig. 4.3 a, were achieved with ultrashort pulse laser at a fixed pulse repetition frequency f_{PRF} of 4kHz and fluence of 8.3 J/cm^2 with the focal spot size d_f of 35 µm, and varied scanning speed v_s from 100 mm/s to 5 mm/s with 75 passes in each line. Such a high fluence was used due to the low absorption of the zirconia ceramic, and together with low pulse repetition frequency of the laser high values of fluence were used in order to improve machining speed. Rather a high number of passes was chosen to ensure minimal ablation of the bondcoat once the laser removes the topcoat. Pulse overlap PO, which can be found as $PO = \left(1 - \frac{v_s}{d_f \cdot f_{PRF}}\right) \cdot 100\%$. Varied scanning speeds changed the PO in the range of 96% and 29%, resulting in different heat accumulation attributes within the material. At low overlap values (29% to 71%, corresponding to v_s of 100mm/s to 40mm/s), laser patterning did not reach the bondcoat due to low energy input and insufficient heat accumulation. The depth of heat propagation, or thermal diffusion length, can be found as $l_{th} = 2\sqrt{D\tau_L}$, where D is thermal diffusivity. The diffusion length for a 60ps pulse for topcoat is just 16nm. At the same time, for a typical bondcoat and the same laser, the diffusion length becomes 45nm.

The lowest scanning speeds used in the experiments (10mm/s and 5mm/s), shown in Fig. 4.3 d-e, damaged the bondcoat, concluded from the bondcoat recast noted as I in Fig. 4.3 d-e, and penetrated through bondcoat and reached the substrate. Image (d) shows generated pore as a result of beam reflection from a metallic bondcoat. In further studies of laser modification, this feature of the bondcoat can be used to create large voids at the interface, potentially increasing coating compliance. Through bondcoat penetration, shown in Fig. 4.3 e, is an example of unacceptable

damage to TBC and substrate, leaving the latter unprotected and causing faster component failure.

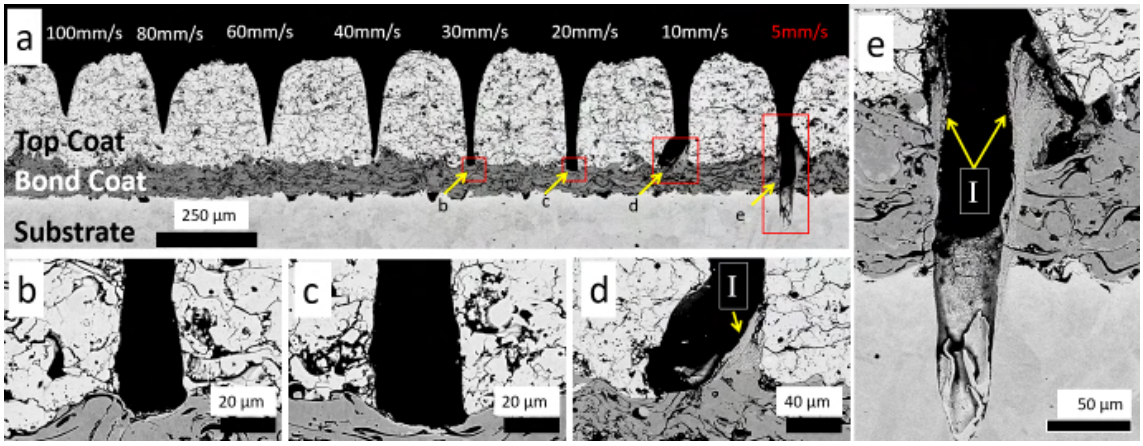


FIGURE 4.3: In-plane Young's modulus control through picosecond ablation of topcoat and incubation effect in picosecond laser texturing after 75 laser passes. (a) ablation with various scanning speeds, showing the selectiveness of topcoat removal. (b), (c): magnified topcoat-bondcoat interface showing no visible traces of bondcoat ablation; image (d) shows a light level of bondcoat ablation and (e) - unacceptable through-bondcoat cut with the affected substrate. Feature (I) shows the redeposited bondcoat after ablation. EKSPLA picosecond laser, PRF 4kHz, average power 1.2W

While the threshold fluences have not been measured in this study, literature data reports relatively high ablation threshold for single YSZ crystals in nanosecond regime, reported as high as 18.7 J/cm^2 [37]. Naturally, threshold fluence will reduce in picosecond ablation. Howeverm the ablation threshold of metals is typically close to 1 J/cm^2. For nickel superalloy DD6, ablation threshold in picosecond regime is only 0.11 J/cm^2 and 1.63 J/cm^2 in nanosecond regime [373].

Optimal cuts were be performed with scanning speeds between 30mm/s and 20mm/s (see Fig. 4.3, b-c), as these scenarios leave indistinguishable ablation of bondcoat. The difference in bond coat ablation can be explained in terms of the heat accumulation effect [281], [97]: low scanning speeds of the laser lead to smaller overlap between pulses, and therefore higher heat accumulation in the sample and higher energy of the lattice when the next pulse irradiates the surface. Moreover, the ablation threshold drops with an increase in the temperature of the affected material, known as the accumulation effect, potentially responsible for

increased ablation efficiency. However, the accumulation effect becomes pronounced at high repetition rates[221] and might not occur at 4kHz.

It is evident from Fig. 4.3 that the groove tends to have a V-shape, or a taper angle, ablating more material at the topcoat surface. The underlying reason for this is the Gaussian shape of the laser spot, and the tail of the Gaussian spot with smaller fluence also ablates the material, however at a lower rate. Multiple reflections from the perturbed surface can further increase the width of the groove. Since the second step of modification utilises the same topcoat without additional filling material, the ideal shape of the groove would be a rectangle with a little taper angle. Optimisation of the groove shape was carried out in terms of pulse energy and focal offset distance, aiming to minimise the taper angle and the groove width at the surface.

The general process window was studied by varying laser scanning speed v_s in the range of 5 and 140 mm/s, and the number of passes between 10 and 100, as presented in Fig. 4.4. It can be seen that the picosecond laser is able to remove the topcoat selectively at $v_s > 10$ mm/s.

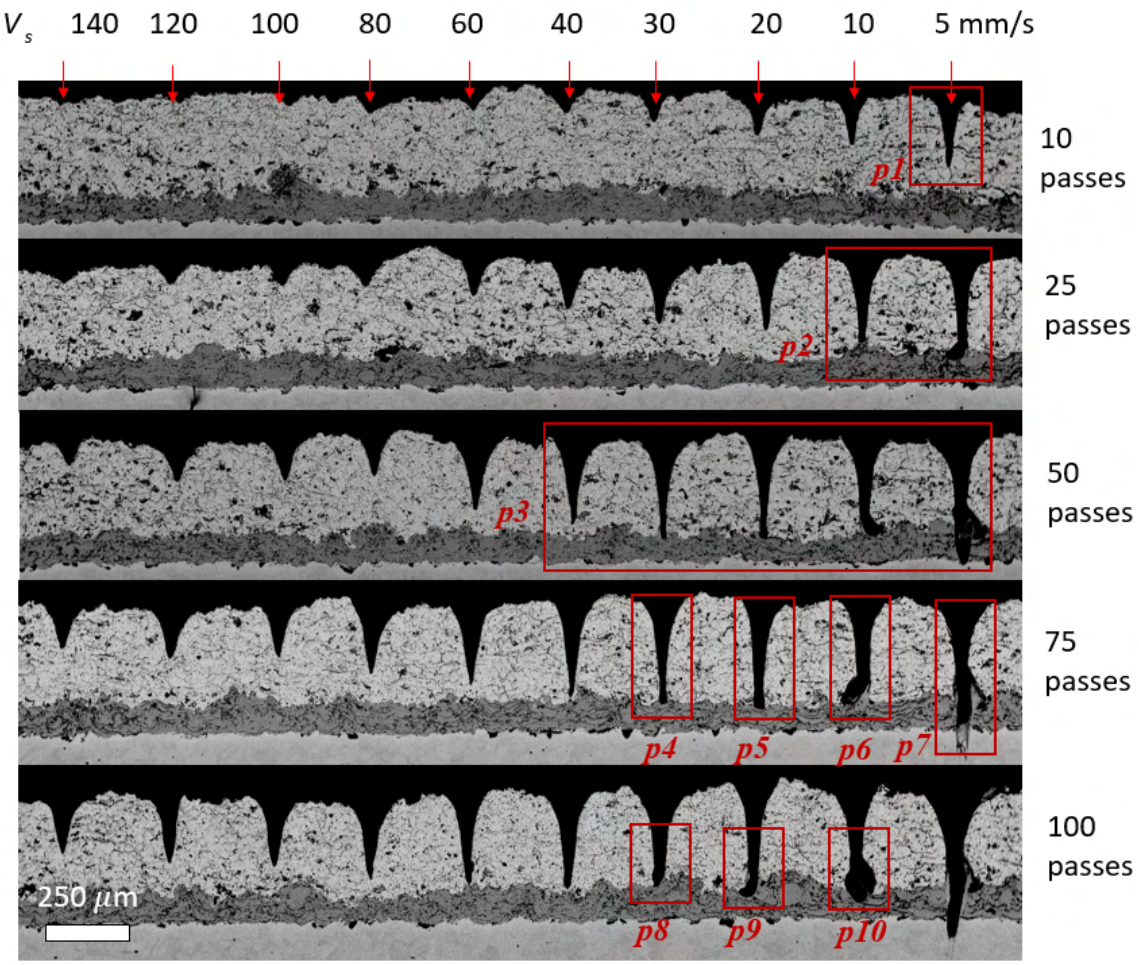


FIGURE 4.4: Influence of scanning speed and number of the line passes with picosecond laser ablation. EKSPLA picosecond laser, PRF 4kHz, average power 1.2W

A lower scanning speed of 5mm/s, corresponding to ε_{laser} 6.8 J/mm^2 linear energy density, results in localised heating and, consequently, in high thermal gradients. Region P1 in Fig. 4.4 is shown in Fig. 4.5 at higher magnification. Besides, high evaporation pressure is typical for ultrashort pulse ablation, and the amplitudes of compression wave on the order of 7 GPa, and corresponding aftermath region of tensile stresses of - 4GPa have been previously reported, which may lead to specimen spallation [135]. At the groove tip in Fig. 4.5 b, a crack appeared as a consequence of tensile residual stresses upon cooling. Moreover, the surface of the groove is covered with a 5 μm thick remelted layer occurred as a result of redeposition (indicated as "Affected zone").

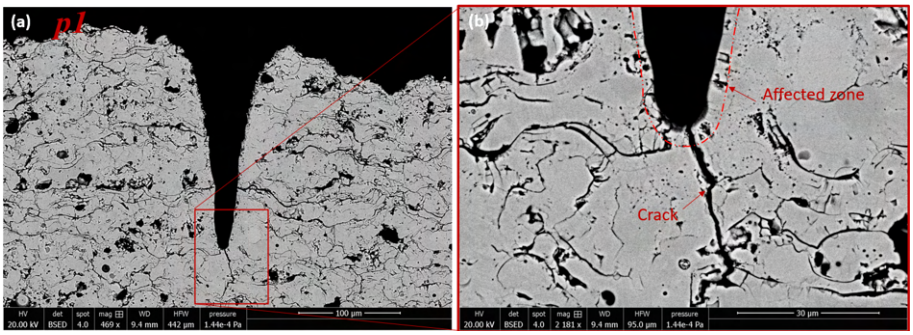


FIGURE 4.5: Influence of high linear energy density input (6.8 J/mm^2) on the microstructure. (a) Low magnification image showing groove geometry; (b) high magnification of the groove tip. EKSPLA picosecond laser, PRF 4kHz, average power 1.2W, 5mm/s, 10 passes. Insert P1 from Fig. 4.4.

After increasing the number of passes to 25, the crack is naturally removed by the incoming laser, as shown in Fig. 4.6. Even at such a high linear energy density even leading to cracking, it was still possible to remove the topcoat selectively, which resulted in a void at the bondcoat-topcoat interface (Fig. 4.6).

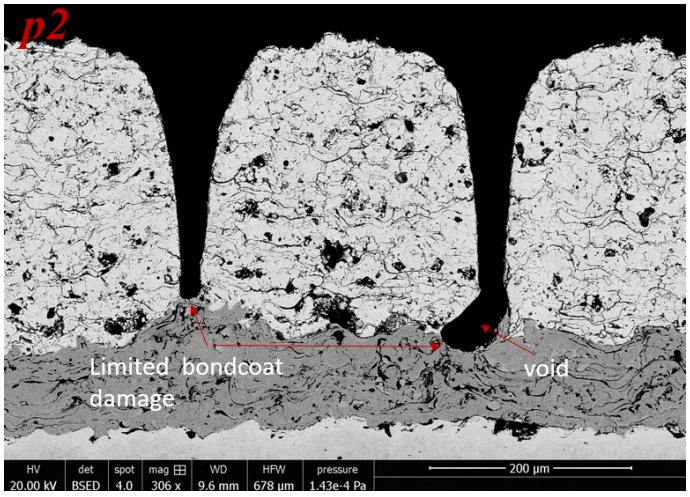


FIGURE 4.6: Selective YSZ removal with picosecond laser ablation applied to thermal barrier coatings. EKSPLA picosecond laser, PRF 4kHz, average power 1.2W,, 25 passes, 5mm/s (right) and 10mm/s (left). Insert P2 from Fig. 4.4.

However, when further increasing the number of repetitions, the bondcoat can be removed, as indicated with the red arrow in Fig. 4.7 a. Clear interfaces were achieved at 30mm/s and 20mm/s (Fig. 4.7 b) laser scanning speeds; similarly to the high linear energy density shown in Fig. 4.6. Besides, there are clear signs of bondcoat removal and redeposition in Fig. 4.7 c, which is a consequence of heat accumulation and melt expulsion of the bondcoat. The void, generated at the interface was

assumed to be a consequence of bondcoat redeposition: highly reflective in 1um spectrum metal redirects the incoming radiation back to the topcoat, as indicated with red arrows in Fig. 4.7 c. Presumably, the surface roughness after melt expulsion is low and contributes to surface reflectivity.

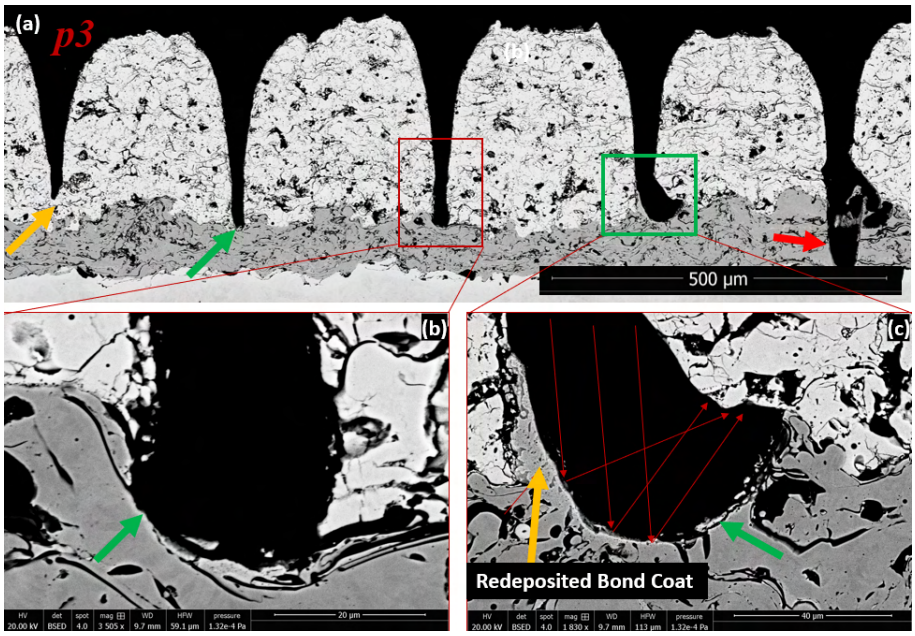


FIGURE 4.7: Selective removal with 50 passes at varied scanning speeds, insert P3 from Fig. 4.4. (a) υ_s 40mm/s indicated with yellow arrow, υ_s 30mm/s indicated with green arrow, 10mm/s indicated with red box; 5mm/s indicated with green box. (b) high magnification insert of υ_s 20mm/s emphasising clear bondcoat-topcoat separation indicated with a green arrow; (c) high magnification insert of υ_s 10mm/s revealing a void between the layers. Red arrows indicate the assumed ray traces. EKSPLA picosecond laser, PRF 4kHz, average power 1.2W, 50 passes.

Furthermore, the focal offset distance (FOD) was optimised in order to achieve a narrower groove opening at the top surface, shown in Fig. 4.8. The width of the groove at the top surface was measured from the edges of the laser-affected areas. This was done to compensate for relatively thick (0.3mm) material removal and change of the spot size, and a -0.25mm offset distance was chosen.

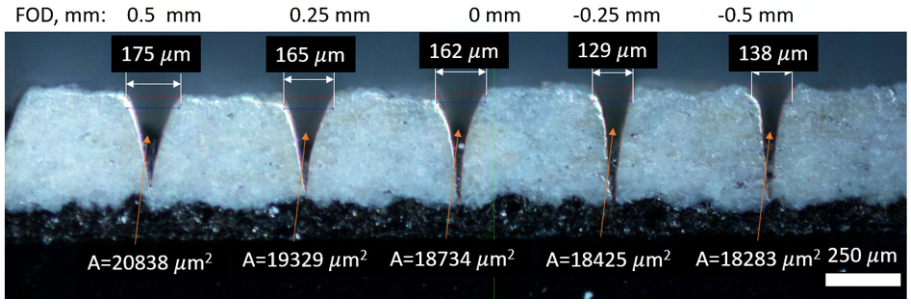


FIGURE 4.8: Influence of focal offset distance (FOD) on the groove geometry. EKSPLA picosecond laser, PRF 4kHz, average power 1.2W, 75 passes, scanning speed 25mm/s.

To confirm selective ablation of the topcoat, a different number of repetitions of scanning lines were used, as presented in Fig. 4.9 laser ablation can accommodate the variability of microstructural properties of the topcoat. Although the groove geometry is attributed to a change, the tip of the groove reaches the bondcoat interface within the tested range.

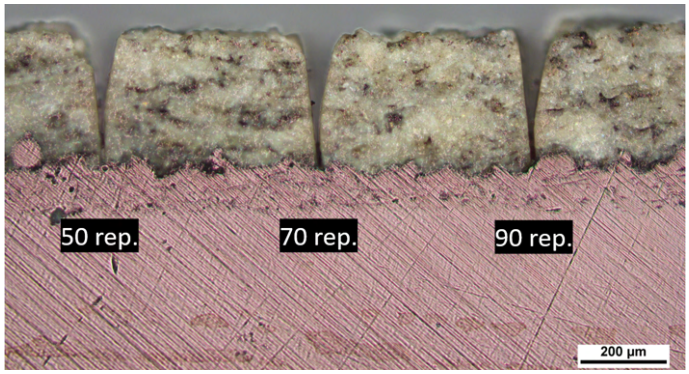


FIGURE 4.9: Process stability at a different number of scanning passes (indicated as "rep."). EKSPLA picosecond laser, PRF 4kHz, average power 1.2W; 50, 50, 90 passes, scanning speed is 25mm/s.

This effect was not observed when ablating material with nanosecond-long pulses, which can be a consequence of a more pronounced thermal effect of ablation and deep heat penetration, eventually removing both topcoat and bondcoat at a comparable rate.

4.3.2 Short pulse laser grooving

As shown above, the depth of heat propagation or thermal diffusion lengthl_{th} for a 60 ps pulse for topcoat and bondcoat are 16 nm and 45 nm, respectively and results

in a confined, localised material removal with little or no melting. Heat diffusion increases with increasing pulse duration, and for a 220 ns laser pulse that will be presented here, the thermal diffusion length becomes 1.2 μm and 2.9 μm for the topcoat and bondcoat layers, respectively. As a result of heat penetration, ablation of the thermal barrier coating systems exhibits thermal effects.

Nanosecond laser ablation of TBC is presented in the cross-sectional images in Fig. 4.10. Nanosecond ablation of YSZ TBC can cause melting and melt expulsion. Melt expulsion becomes pronounced at higher pulse overlap PO, i.e. lower scanning speeds, particularly noticeable with 50mm/s scanning speeds and noted in *"n1"* box in Fig. 4.10. Due to the long duration of the pulse, the incoming energy propagates into the coating and causes melting and vaporisation, eventually creating recoil pressure sufficient for moving the molten material to the sides of the groove. This removal mechanism was not observed at picosecond ablation of the TBC which was attributed to the drastic change in thermal diffusion length of the laser energy.

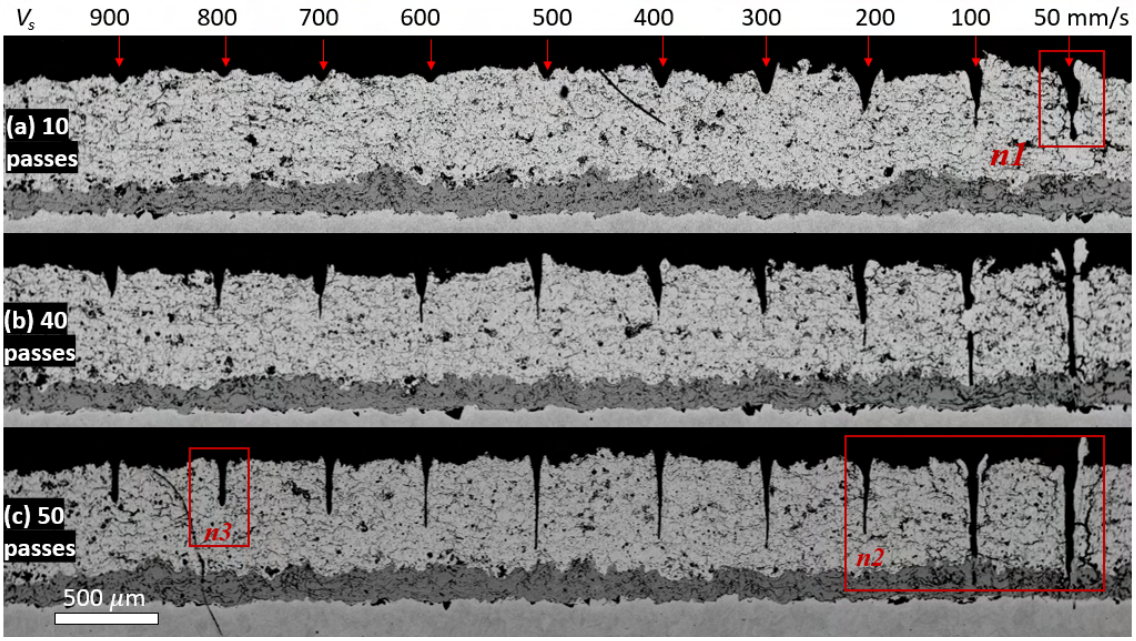


FIGURE 4.10: Cross-sectional SEM micrograph of thermal barrier coating system after nanosecond ablation. Scanning speed was varied in range 900 m/s to 50 m/s. (a) 10 passes; (b) 40 passes; (c) 50 passes. SPI G3 nanosecond laser.

Pulse overlap PO in case of 50mm/s is 97.4% which results in a pronounced heat effect on the TBC; highly localised heat from the laser source results in

microcracking, at the sides of the grooves, denoted in Fig. 4.11 b, as a result of thermal expansion of the TBC. Besides, recast formation at the surface of the topcoat was found at scanning speeds lower than 200mm/s (Fig. 4.10 and 4.11), which was attributed to the transition from melt expulsion to explosive boiling removal mechanism with increasing scanning speeds. Selective topcoat ablation found in the picosecond ablation regime was not found with longer pulse ablation within the tested range of parameters. In all the tested cases, bondcoat removal happened at a comparable rate with that of the topcoat.

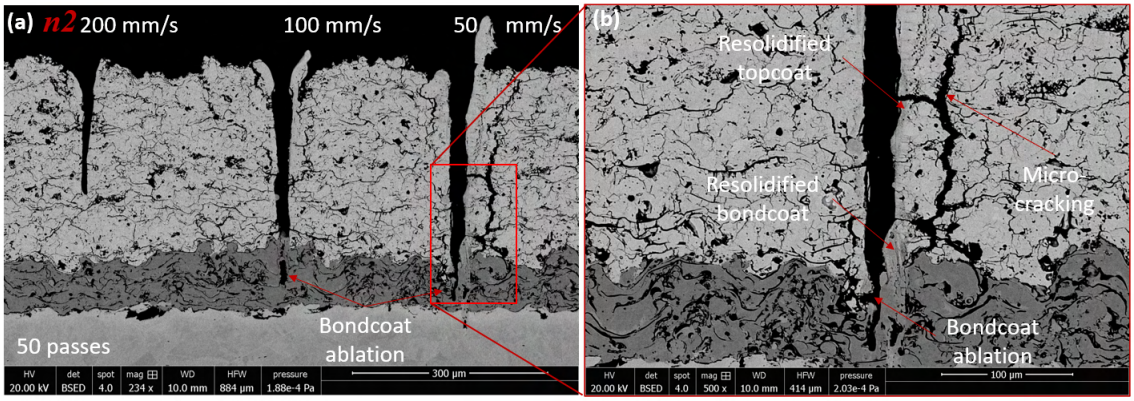


FIGURE 4.11: Insert "n2" from Fig. 4.10 with 50 laser laser passes; scanning speed is (a) 200, 100, and 50mm/s. (b) High magnification micrograph of the tip of the laser ablated groove with 50mm/s scanning speed revealing thermal damage to the TBC.

Melting of the sides of the groove and of the bondcoat was observed in both low (Fig. 4.11 b) and high (Fig. 4.12) scanning speeds. In both cases, a resolidified layer of the YSZ is formed at the sides of the groove (Fig. 4.12 b).

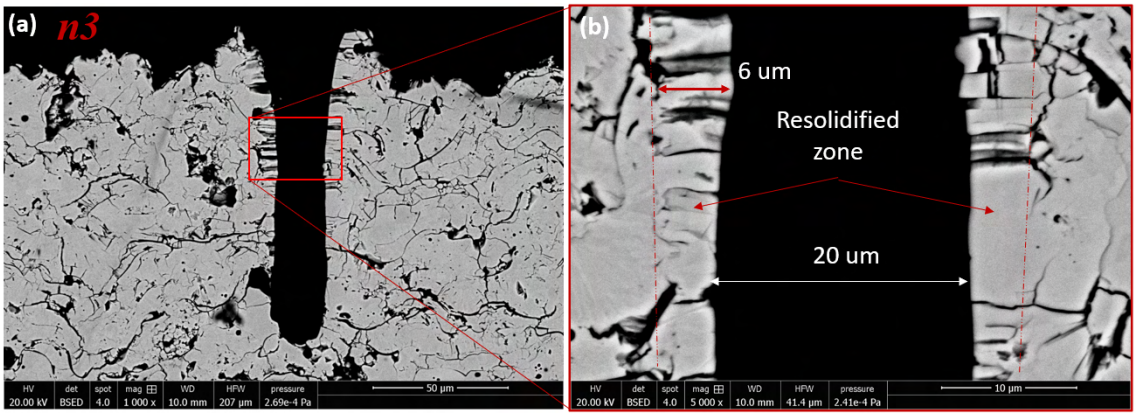


FIGURE 4.12: Insert "n3" from Fig. 4.10 with 50 laser laser passes; scanning speed is 800mm/s. (b) High magnification micrograph of the groove revealing melting of the TBC. SPI G3 nanosecond laser.

In the series of tests, the nanosecond ablation regime was found to ablate the topcoat without inducing significant thermomechanical damage and create shapes with nearly no taper angle, i.e. vertical walls of the ablated grooves, as was shown previously. The width of the groove in all the cases was smaller than the laser spot diameter, e.g. 20μm groove width shown in Fig. 4.12 b and even narrower grooves shown in Fig. 4.10, in part due to melt expulsion of the coating on the sides of the groove. However, under thermomechanical loads during heating/cooling cycles of the turbine, the tip of the groove may act as a stress concentrator within the topcoat material and may eventually result in partial loss of the coating. It was assumed that such effect can be minimised by ablating the whole topcoat until the bondcoat; in this case, the geometrical stress concentrator within the material will be diminished, however, it should be noted that the stress concentrator will be still present due to the thermomechanical mismatch between the bondcoat/topcoat layers. nevertheless, the introduced discontinuity at the topcoat/bondcoat interface would reduce the magnitude of the growth stresses within the TGO layer by allowing the expansion space. In this study, the influence of the groove depth on the performance of the TBC system was ignored, and the samples were grooved through the coating until the bondcoat was reached. Selective ablation was not found in the nanosecond ablation regime, and the samples were grooved in the picosecond regime, as discussed in the previous subsection.

4.4 Laser glazing of thermal barrier coating system

The second step of modification, laser glazing, was performed on pre-grooved thermal barrier coatings with one-direction grooves with the spacing of 200 μm with the following parameters: PRF of 4kHz, scanning speed 25mm/s, focal offset distance -0.25mm, with 75 passes per groove, pulse duration of 60ps, and the average power of 1.2W.

While the grooves within the TBC have increased the thermomechanical compliance (Eq. 4.2), such coating is exposed to mechanical and chemical damage and opens the oxygen short paths towards the bondcoat. To generate a continuous protective layer, the segmented topcoat was melted with a continuous wave laser. The sample must experience minimal thermal damage, i.e. thermal shrinkage microcracks and collateral damage to separated columns, and create a continuous dense layer, closing the surficial gap.

The main goals of glazing optimisation were considered to be:

1. *Continuity and uniformity of the top surface layer* to enable protective characteristics of the glazed layer, including CMAS and erosion resistance.
2. *Minimisation of the thickness of the remelted layer.* This would allow reducing potential buckling of the stiffened topcoat layer [75].
3. *Alignment of the solidification cracks with underlying grooves* in order to reduce stress concentration at the crack tip.
4. *Minimisation of thermomechanical damage* induced during laser melting.

4.4.1 Laser melting process

The solidification microcracks are an inevitable result of solidified zirconia in ambient conditions. They are generated due to the high coefficient of thermal expansion and a high melting point of YSZ, approx. 2600^{o}C [77], thus creating high tensile thermal stresses during rapid cooling and high-temperature drop. While the cooling is rapid,

the liquid zirconia solidifies on the existing substrate between the grooves, i.e. the column. In a simplified scenario, where liquid zirconia covers two neighbouring columns and solidifies, the heat flow is directed into the neighbouring columns. The thermoelastic strain is minimal at the surface of solidification and amplifies with the further propagation of the solid-liquid interface. In this scenario, the cracks will be always generated at the grooves as the accumulated strain between the columns is higher. This is achievable when the melt pool is elongated, i.e., larger than the groove width. Control over the melt pool elongation can be achieved by increasing the scanning speed of the laser. The diameter of the beam, in this case, should be decreased accordingly to compensate for the drop in the energy density and avoid discontinuous melting.

Ideally, the remelted layer would continuously cover the grooves, and the generally unavoidable solidification microcracks align with the grooves while remaining the minimal thickness. The width of the groove, especially at the top surface area, was found to significantly influence the laser melting process; large groove widths at the top surface would require a larger volume of the melt pool allowing it to move towards the next column, at the same time resulting in higher melting depths. Two examples of defects in non-optimal conditions are presented in Fig. 4.13 and include severe uncontrolled cracking of the topcoat with visible darkening of the molten track, which was found at low scanning speeds (Fig. 4.13 a). Besides, low scanning speeds allow for filling of the groove void with molten material, as indicated in Fig. 4.13 a. Conversely, high scanning speeds result in insufficient linear energy density of the laser $\varepsilon_{laser} = \frac{P}{\upsilon_s d}$, where P are the laser power, υ_s is the laser scanning speed, and d is the beam diameter; this result in discontinuous melting of the topcoat and bubbling, which was attributed to the effect of surface tension. At the same time, it was found that the solidification microcracks coincide with the underlying grooves, as indicated in Fig. 4.13 b.

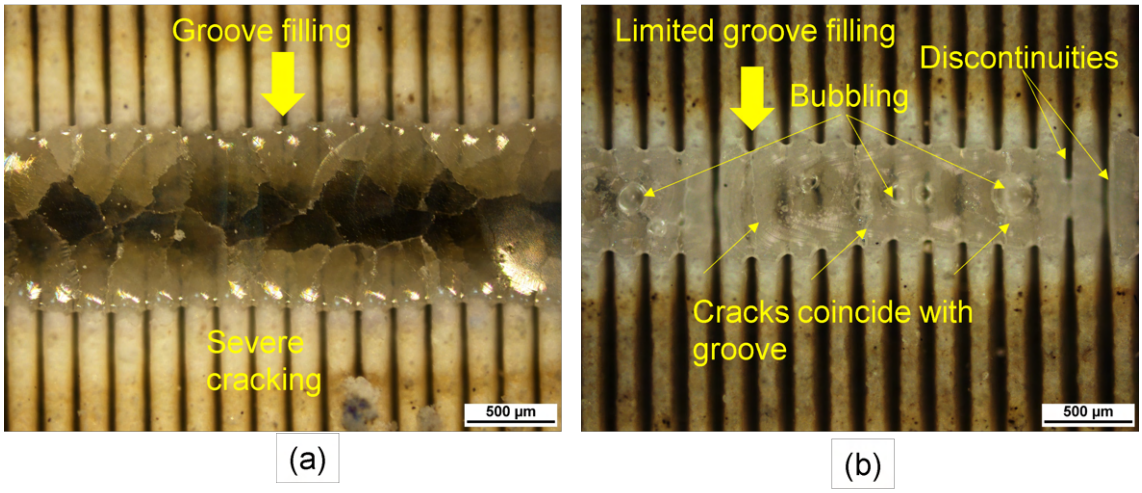


FIGURE 4.13: Dark field optical microscopy of the TBC top surface showing defects in the laser melting process of YSZ topcoat typical for (a) high and (b) low heat input conditions. SPI RedEnergy CW laser, average power is 88W, spot size is 400 μm, laser scanning speed is (a) 2.5 mm/s and (b) 75 mm/s.

A closer look at the surface of the remelted tracks revealed the formation of the unusual topology of the resolidified YSZ, presented in Fig. 4.14. Nomarski microscopy allows to capture of small variations of the surface topology by introducing a prism into the optical path of the microscope, and the varied colour of the image corresponds to changing distance between the objective and the examined surface, by which the dendrite formation was particularly clear (Fig. 4.14 a, c). However, the surface variation introduced by the tip of the dendrite was under 2 μm, as measured with the microscope stage. Dendritic grains were found next to planar grains with "equi-directional" shape and elongated in one direction, indicated as "planar elongated grains" and "planar grains" in Fig. 4.14 c. Interestingly, the sizes of the dendritic grains were much larger than the neighbouring planar grains, e.g. a 190 μm width of the dendritic grain indicated as "dendritic grain" in Fig. 4.14 c an sub- 30 μm grain size of the planar grains. These three unusual observations attracted more attention, and crystal formation in planar and dendritic solidification modes will be studied in Chapter 6.

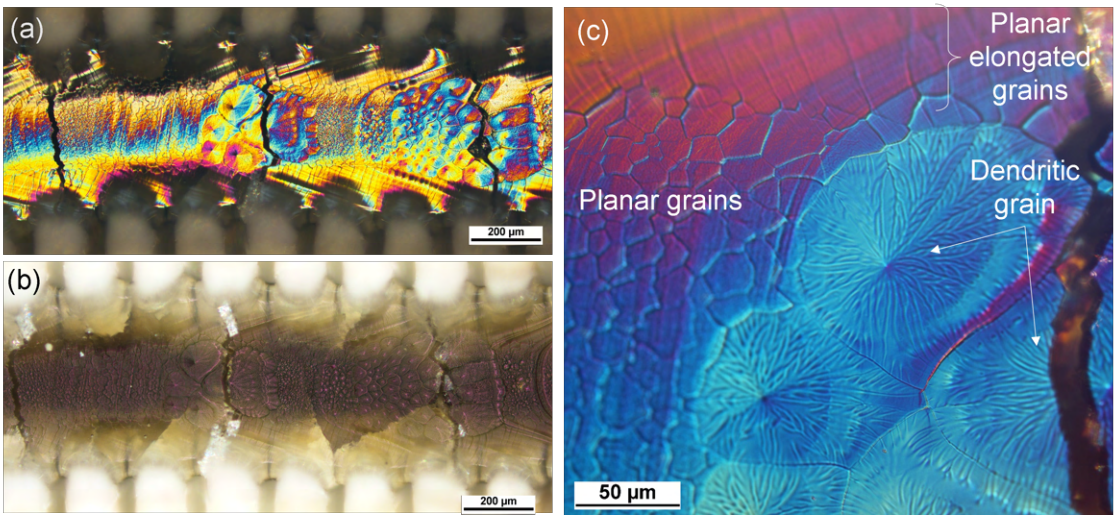


FIGURE 4.14: (a, c) Bright field Nomarski and (b) dark field optical microscopy of the TBC top surface showing coexisting planar and dendritic grains. SPI RedEnergy CW laser, the average power is 88W, spot size is 400 μm, the laser scanning speed is 25 mm/s.

Although the continuity of the single track melting was achieved, the whole surface of the grooved TBC must be remelted. The near-infrared laser was used for remelting, where YSZ has a low absorption coefficient of 1600 cm^{-1}[37], and inelastic light scattering at the defects such as pores, cracks, and splat interfaces, is largely responsible for energy absorption from the incoming laser. After melting, the amount of the scattering defects reduces significantly, therefore reducing the effective absorption of the laser light by the coating. This results in discontinuous laser melting, as presented in Fig. 4.15.

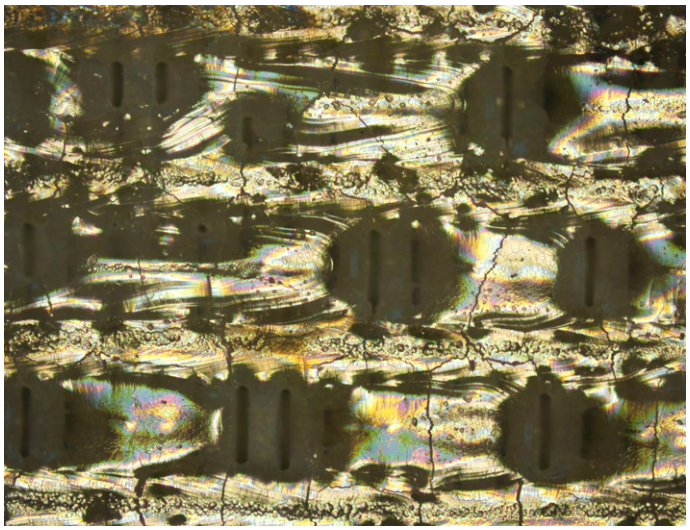


FIGURE 4.15: Bright field microscopy of TBC top surface showing discontinuous melting. SPI RedEnergy CW laser, the average power is 88W, spot size is 400 μm, the laser scanning speed is 50 mm/s, the track pitch is 320 μm

The dense layer lacks internal imperfections, that scatter the laser, and becomes optically transparent to the laser in the near-infrared spectrum. To create a continuous layer with low waviness, the surface was melted with the following routine. The sample was divided into an array of lines separated by hatch distance. Firstly, every second line was melted with optimal single-pass linear energy density $\varepsilon_{laser} = 4.4$ J/mm^2, calculated as $\varepsilon_{laser} = \frac{P}{v_{sd}}$. Secondly, the rest of the surface was melted with a slightly higher linear energy density input $\varepsilon_{laser} = 5.9$ J/mm^2, ensuring recrystallisation of the previously melted track, where the coating has increased transparency. Beam diameter of 0.4mm was chosen, scanning speed of main tracks are 50mm/s, of filling tracks were chosen 75% of the main track, and optimal hatch distance was chosen as 80% of the beam diameter.

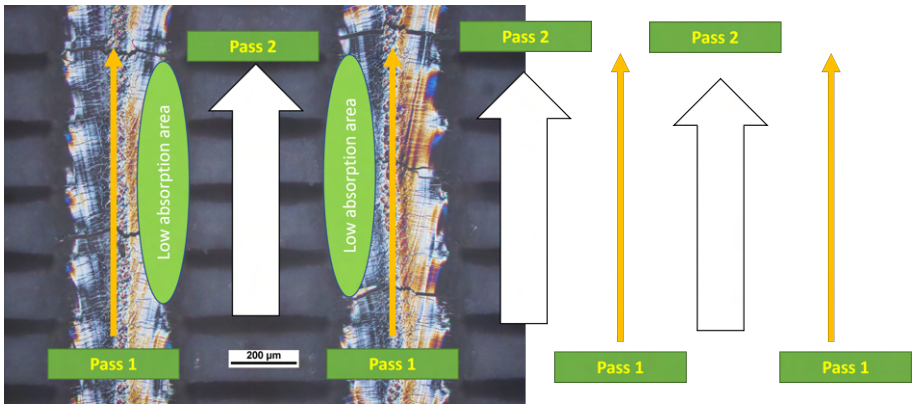


FIGURE 4.16: Illustration of the strategy for continuous laser glazing of the thermal barrier coating.

After utilising such a strategy with the above-mentioned strategy and parameters, it was possible to achieve a continuous coverage of the grooved surface, as shown in Fig. 4.17.

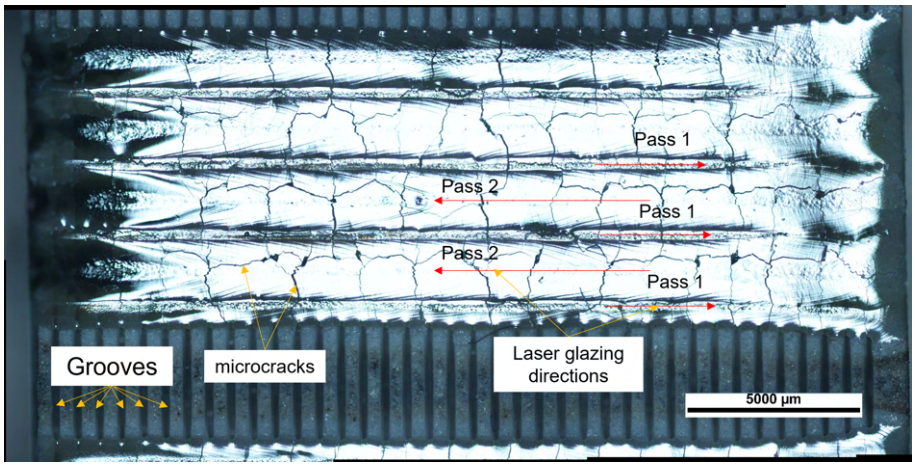


FIGURE 4.17: Bright field microscopy of TBC top surface showing continuous melting. SPI RedEnergy CW laser, the average power is 88W, spot size is 400 μm, the laser scanning speed is 50 mm/s (pass 1) and 37.5mm/s (pass 2), and the track pitch is 320 μm

4.4.2 Optimised laser melting approach for continuous coverage of grooved TBC

The final microstructure of the coating after optimisation is shown in Fig. 4.18 a-c. The modified coating consists of macro-sized grooves, approximately 10µm in width. The dense layer covers the as-grooved TBC continuously (Fig. 4.18 a), although

separated by narrow vertical microcracks, and no horizontal under the dense region was observed. The bulk of the remelted region consists of vertical columnar grains, while the top surface is covered with horizontal columnar grains, visible in Fig. 4.18 b. This phenomenon will be addressed in Chapter 6, dedicated to the crystal growth in the laser melting process, which will be referred to as "grain surface sealing". In the middle of the laser melted tracks the morphology of the solidified grains changed from planar to dendritic (Fig. 4.18 d, middle of the track). The thickness of the glazed layer was found to be in the range of 25 to 75 μm.

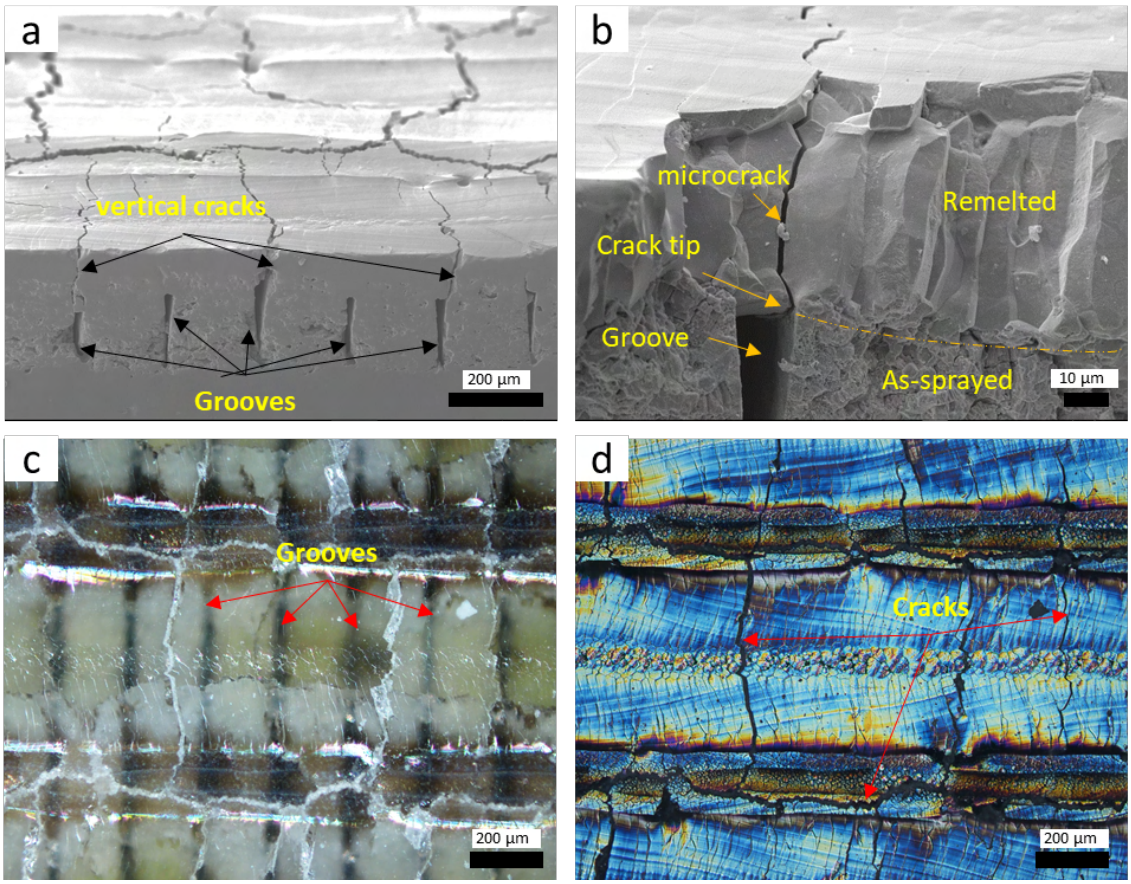


FIGURE 4.18: Compliant thermal barrier coatings with laser-ablated grooves sealed with a continuous layer. SEM image of cross-section (a) and fracture surface (b) showing the array of grooves and vertical microcracks aligning with the grooves. Optical images of the top-view in (c) dark-field mode and (d) bright field with Nomarski prism.

An additional feature of the modification technique is the alignment of microcracks with the underlying grooves. In the work of Ahmadi-Pidani et al. [315] and Ghasemi et al.[326], the increased performance of laser-glazed TBCs was associated with

strain relaxation at the top surface boundary due to the presence of microcracks, providing additional space for thermal expansion and accommodating the stresses. At the same time, microcrack presents a stress concentrator that can significantly deteriorate the mechanical properties of the coating. By creating a free void under the remelted surface, the solidification microcracks will naturally connect with the underlying grooves due to their mechanical independence. Once the microcrack is connected to the groove, the effective microcrack tip radius is increased to the size of the groove ($\sim$20μm), and the stress concentration is significantly reduced, while the structure of the coating can act independently. Since the current study considers only a one-dimensional array of grooves, the microcracks at the overlapping region of the remelted layer cannot be connected with the underlying grooves since the latter are perpendicular to the melt pool velocity.

The laser parameters for ablation and continuous melting of TBC are summarised in the table 4.1.

TABLE 4.1: Parameters for achieving selective TBC ablation and continuous dense layer.

Process	Pulse duration	Fluence, J/cm^2	Linear Energy density, J/mm^2	Scanning Speed, m/s	Focal Offset distance, mm
Grooving	60 ps	8.3	-	20	-0.3
Melting	CW	-	4.4-5.9	50	0

4.5 Summary

In this chapter, a new TBC modification approach has been discussed with particular emphasis on the manufacturing approach based on laser machining. Development of the idea of minimisation of in-plane Young's modulus of the topcoat lead to a two-step modification approach, creating an array of one-dimensional grooves within the coating for reducing the stresses arising from thermal expansion mismatch within the coating, later covered with a continuous glazed layer. In contrast with laser glazing of as-sprayed TBC, laser glazing of a pre-grooved surface requires careful attention to the geometrical parameters of the grooves.

The parameter window for continuous laser glazing is limited due to:
(i) Damage to the underlying coating as a result of thermal stresses
(ii) Surface tension effects, leading to discontinuous surface coverage.

One of the optimisation goals of laser glazing is the minimisation of the thickness of the glazed layer, which may reduce thermal cycling stresses within the dense layer. This further complicates the manufacturing process of such coating, as the thickness of the glazed layer in this scenario also depends on the width of the previously machined grooves. Other laser manufacturing approaches may be used in other studies. Minimisation of the laser spot size will eventually decrease the thickness of the glazed layer; this can be done by either reducing the numerical aperture of the focusing lens, i.e. increasing the beam width at the entrance and/or decreasing the focal distance of the lens. Another method of laser spot size minimisation is the decrease of the laser wavelength from 1064nm to higher harmonics, e.g. 532nm or 355nm.

The latter will also promote laser absorption within the TBC, as zirconia-based ceramics are known to have poor absorption of near-infrared irradiation [37]. It is known that most of materials will absorb light with shorter wavelengths. The plot in Fig. 4.19 indicates that the transmittance of YSZ decreases with decreasing wavelength, showing particularly low transmission in the 220-450nm region. This range of wavelengths potentially will not only reduce the spot size of the laser but also promote the absorption of the incoming laser radiation. In this study, the available wavelengths were limited to the fundamental harmonic of Nd:YAG Lasers 1064nm, which is the most common wavelength for industrial applications of the laser. Further reduction of the wavelength by frequency doubling/trippling is less common however finds its applications due to the better absorption of the laser and smaller feature sizes. However, this comes at a cost of reduced average power due to the limited conversion efficiency.

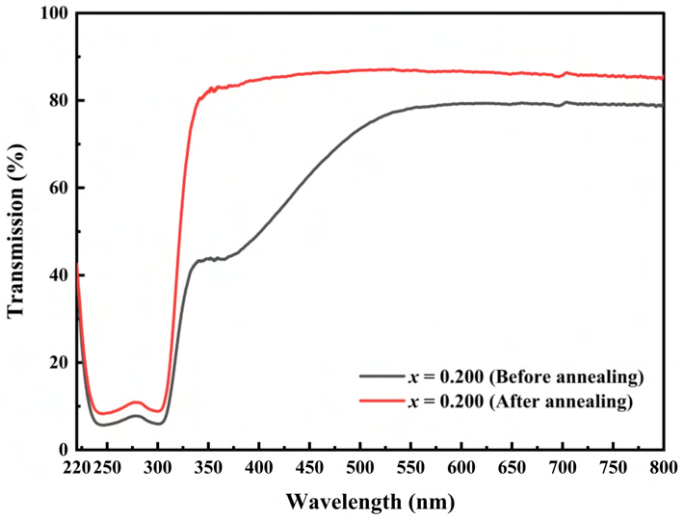


FIGURE 4.19: Optical transmittance spectrum of single-crystal YSZ [344].

Due to the limited number of coated samples available for the study, the number of possible experiments was limited with care, and therefore possible deviation have not been confirmed statistically in this study. Naturally occurring defects in the material, impurities, varied surface conditions such as roughness or even dust can affect both ablation and melting processes. For the further industrial use of this data, a statistical experimental study will be needed to further confirm the process window in manufacturing settings.

Chapter 5

Performance assessment and microstructure characterisation of laser modified thermal barrier coatings

The limited lifespan of protective coatings attracted interest in studying the failure phenomena and investigating various coating deposition techniques. Thermal barrier coatings must have a minimal mechanical response to temperature variations, i.e. thermal expansion-induced stresses while having low thermal conductivity and excellent resistance to environmental agents. This chapter reports a novel post-treatment approach allowing independent control of the elastic modulus in the coating and on its surface by creating hollow internal anatomy covered by a dense protective layer. Hollow internal microstructure aims to recreate the artificial columnar-like structure of electron-beam physical vapour deposited coatings, known for their excellent strain tolerance properties. To protect the coating from chemical and mechanical degradation and to cut the generated oxygen short path, the top surface of the coating is subsequently melted with a continuous-wave laser, creating a dense erosion and corrosion-resistant surface. The approach was comprehensively benchmarked against state-of-the-art thermally sprayed coatings in terms of thermal shock, erosion resistance and molten silicon sand penetration.

5.1 Introduction

Noticeable attention to TBC failure mechanisms was spawned shortly after TBCs were introduced in the 1970s[185]; nonetheless, as a consequence of the sophisticated interplay of physical and chemical phenomena, predictive models for TBCs still undergo improvements [174] even after 50 years of investigations. The generally recognised primary mechanism dictating the lifespan is based on the development of thermal expansion-driven stresses in the thermally grown oxide (TGO) at the bondcoat - topcoat interface. Padture et al. [235] summarised TBC failure mechanisms, indicating that compressive TGO stresses, combined with the interface imperfections, phase degradation, and thermal expansion mismatch between dissimilar materials lead to microcrack development, their coalescence, and coating spallation. According to Evans et al. [218], the coating spallation is a result of large residual compression in the TGO layer, amplified by interface imperfections.

Erosion of the coatings is another important problem, particularly severe in the turbine stage of the engine; high-velocity particles can damage the coating and remove material, leading to the loss of coating thickness and a shortened life of the component. It has been found that the material removal mechanism for the EB-PVD structure is based on microcracking at the near-surface region and removal of fractured pieces of TBC, while the erosion of APS coatings occurs due to the loss of poorly bonded splat boundaries, being 10 times less resistant to erosion [221].

Hot corrosion is especially severe for uncoated metallic components [379], [72], furthermore, even ceramic materials can degrade in a chemically active environment [141]. Sodium, vanadium, sulphur, and other contaminations can be usually found in low-quality fuels, which can form salts able to react with the substrate or coating material. In the case of YSZ TBCs, the salts react with Y_2O_3 provoking depletion of the latter from YSZ and eventually destabilization of YSZ. A YSZ decomposition under hot corrosion into monoclinic and cubic polymorphous zirconia has been found, where the YVO_4 spinels as a result of the reaction between yttria and vanadium and sodium salts were observed [295].

Coating corrosion can be caused by desert sand, volcanic ash, containing calcium-magnesium-alumino-silicates (CMAS), both for EB-PVD and APS produced coatings [68], [67]. Rapid CMAS infiltration through the EB-PVD coating and reaching the substrate once CMAS is melted, as was reported by Kramer et al. [166] and able to induce depletion of yttrium, which causes tetragonal-to-monoclinic phase transformation upon cooling. The work of Vidal-Setif et al. on CMAS - EB-PVD TBC interaction presents the occurrence of complex Zr-bearing phases, the formation of vertical microcracks, and decreased strain tolerance of the coating [331].

5.2 Results and Discussion

5.2.1 Effect of laser melting on surface roughness

The typical thermal spray rough surface, shown in Fig. 5.1 a, arise from the deposition process where a coating consists of stochastically deposited splats; laser melting here acts as a polishing process (Fig. 5.1 b). After laser melting, the coating roughness reduced from *Sa* 9.81 μm for the as-sprayed condition to *Sa* 0.75 μm for modified coatings. However, there is noticeable waviness at the overlapping region between the laser tracks.

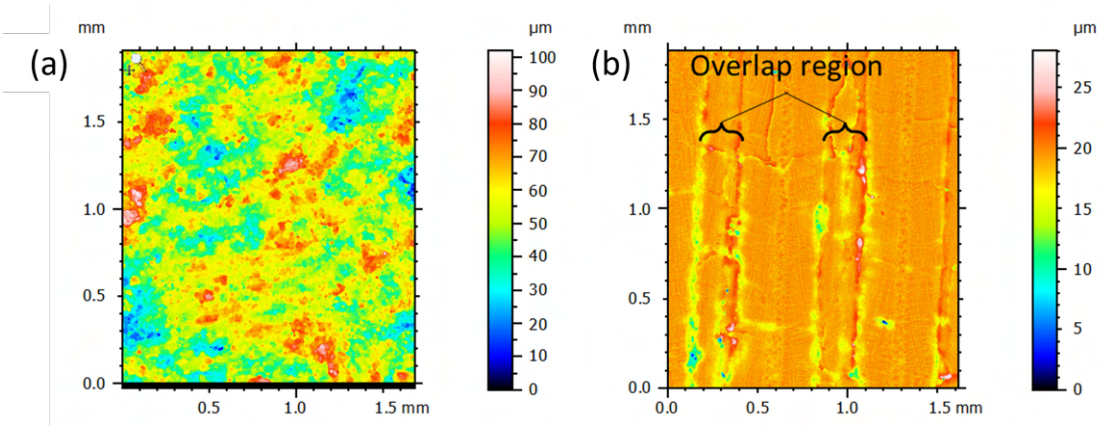


FIGURE 5.1: Surface topology of (a) as-sprayed and (b) laser-melted thermal barrier coating, showing significant reduction in surface roughness.

While the roughness of the sample after modification decreased significantly, there is a degree of surface waviness caused by the overlapping of the neighbouring trenches. After laser melting, the amount of internal defects is reduced significantly, which, in turn, affects internal beam scattering and, therefore, light absorption; melting becomes heterogeneous and creates bulges in the previously melted areas, indicated as the "overlap region" in Fig. 5.1 b. The *Sa* parameter captures the overall height change, while the maximum height difference *Rz* reaches the values of 102 μm and 28 μm for as-sprayed and laser-melted conditions, respectively. The laser-glazed surface appears glossy to the direct light, and the improvement in surface roughness after modification can enhance thermal and tribological properties of the coating absorbing less convective and radiative energy flow from the combustion products.

5.2.2 Resistance of the coatings to erosion

The threat of coating thickness loss due to particle erosion and foreign object damage is especially serious in nozzle guide vanes and turbine blades, where the incident angle of the gas flow is nearly perpendicular to the surface [221]. While the flow in the combustor chamber is almost parallel to the surface coating erosion occurs at a slower rate, the degradation of the coating due to mechanical impact still cannot be neglected, and the erosion resistance of as-sprayed coatings was compared with that of the coating after proposed 2-step laser modification, consisting of laser grooving and laser sealing.

The results, presented in Table 5.1, show a significant increase in erosion resistance of thermal barrier coatings upon modification. The average erosion rate, calculated as a ratio of the mass loss of the sample to the mass of erosive particles, for as-sprayed samples is 0.896 mg/g, and 0.104 mg/g for laser melted samples, and therefore the average erosion performance increased by nearly 8.6 times.

It should be noted that the number of samples was limited and therefore statistical significance of the erosion experiments will need further confirmation in future studies of the coating behaviour. To facilitate the future industrial utilization of

this data, a statistical experimental investigation will be required to validate the coating performance.

TABLE 5.1: Erosion resistance of as-sprayed and laser modified samples

Sample type	Sample ID	Erosion rate $\Delta m/\Delta M$ mg/g	Erosion rate $\Delta m/\Delta t$ μg/s	Average Erosion rate, mg/g	Erosion rate STD mg/s
As-sprayed	U1	0.90	6.72	0.895	0.065
	U2	0.97	6.09		
	U3	0.81	5.43		
Laser Modified	L1	0.11	0.82	0.104	0.003
	L2	0.10	0.64		
	L3	0.10	0.68		

The samples after erosion tests were analysed via white light interferometry. The surface data were averaged along the particle flow direction, and the corresponding average plot is presented in Fig. 5.2. The coating thickness is decreasing in the middle of the as-sprayed samples significantly (Fig. 5.2 a) and reaches the bondcoat interface in the U3 sample. According to the results presented in Table 5.1, the erosion rate of U3 sample, which was eroded up to the bondcoat interface, is lower than that of U1 and U2. This can be attributed to a higher bonding strength of the bondcoat splats, than that of the topcoat splats, and generally lower erosion rate of the bondcoat. At the same time, the erosion rate increased from 0.9 mg/g to 0.97 mg/g (samples U1 and U2), when the topcoat was not removed completely (Fig. 5.2 a).

Due to the limited number of samples available for the study, the number of samples for each repetitions was also limited and distributed carefully. For the erosion studies, only 1 sample for each experiment was taken and the statistical deviation should be addressed in the future studies. Nevertheless, a comparison can be made with the relative erosion rate since only the duration of the erosive act was changing; this was found as the ratio of mass loss and the mass of the deposited grit. It was found that the erosion mass loss also becomes more predictable with the standard deviation dropping from 0.065mg/g to 0.003mg/g. This was attributed to the different erosion mechanisms where for the dense coating the coating loses its mass

due to micro cutting process, while for the as-sprayed coating, mass loss can be a consequence of splat decohesion. Such behaviour of erosion rate can be explained as a consequence of damage accumulation within the underlying regions, as will be discussed below. At the same time, the surface of the laser-modified coating remained nearly unchanged (Fig. 5.2 b), and the impact of erosive particles is not as obvious as in the case of as-sprayed coating. The laser-modified sample L3, which underwent the longest erosion experiment, lost just 40.8 mg of the coating; taking the density of the glazed layer for 6075 kg/m^3 [50], this would result in the removal of just 6.0·10^{-3} cm^3, or, taking homogeneous removal of the coating, a layer of just 9.7 µm.

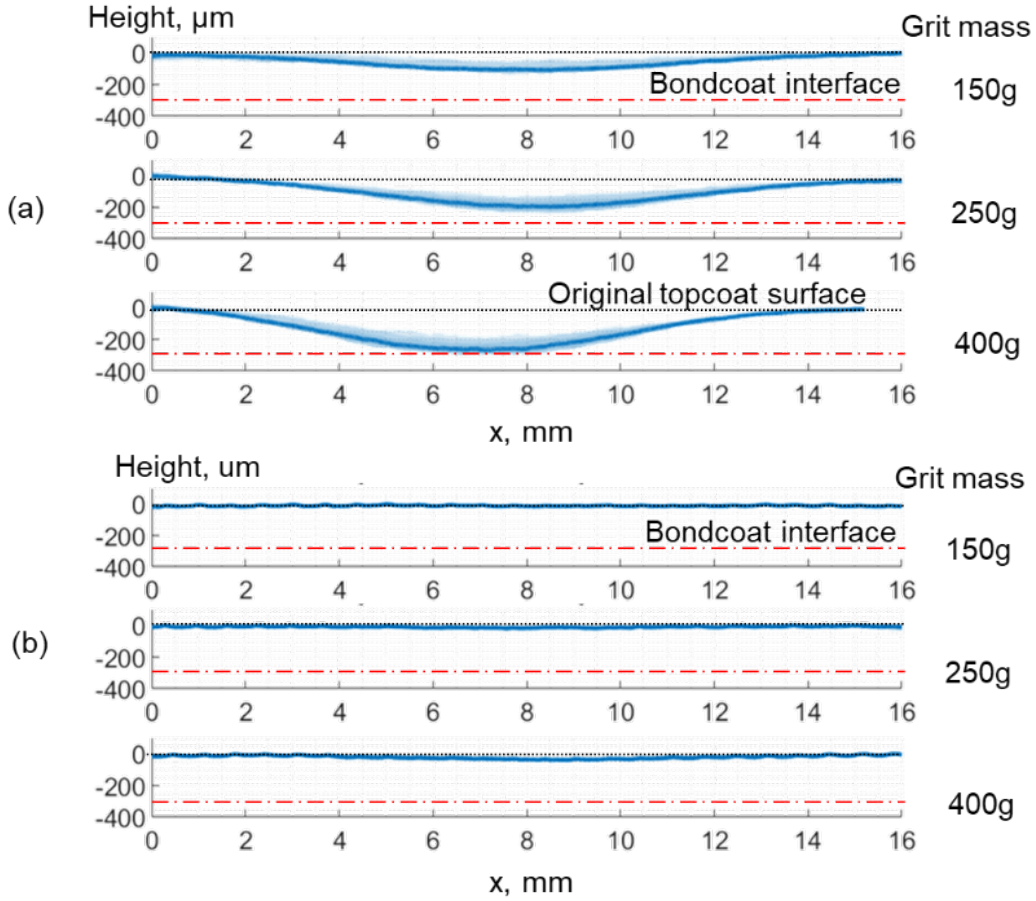


FIGURE 5.2: Average surface height of the samples after erosion tests in different conditions. (a) as-sprayed and (b) laser-modified samples. The light blue region of the 50% confidence interval (P value > 50%).

5.2.3 Erosion mechanisms, microstructure, and morphology

The abundance of structural imperfection, e.g., intra- and interspat cracks and pores, as well as poor splat-to-splat adhesion, led to a high erosion rate of thermally sprayed coatings, compared to laser-modified samples. In Fig. 5.3 a the surface of U2 sample is presented close to the middle of the erosion impact. The surface includes a smooth interface as a consequence of splat decohesion upon particle impact. The magnified view, shown in Fig. 5.3 b, reveals the fracture of the underlying splat with a typical for thermal spraying columnar grains. In a longer experiment, when the mass of erosive particles reached 400g, the topcoat was removed completely in the region of the highest impact, as presented in Fig. 5.3 c. The dark areas of the image indicate the exposed bondcoat, while the lighter areas correspond to the remaining topcoat, which is possible to distinguish in the backscattered mode of SEM. The cross-sectional analysis was also performed and shows a significant loss of coating thickness (Fig. 5.3 d). Besides, erosive particles induced mechanical damage to the surface of the splats, as shown in Fig. 5.3e, and the subsurface of the sample, presented in Fig. 5.3 d. The microcracks tend to propagate along the grain boundaries in the surface and the subsurface layers. It is worth mentioning that the microcracking of the splats are a typical defect after thermal spraying, and microcracks originating from thermal spraying are also present in the surface. However, the crack density upon thermal spraying is typically low (between 55 and 75 microcracks/mm[235]), while the presented results suggest much higher density of cracks, 300 microcracks/mm in the surficial layer and 210 microcracks/mm in the subsurface region. Accumulation of microcracks within the surface and subsurface layers can be responsible to the increased erosion rate, decreasing the necessary energy for splat decohesion.

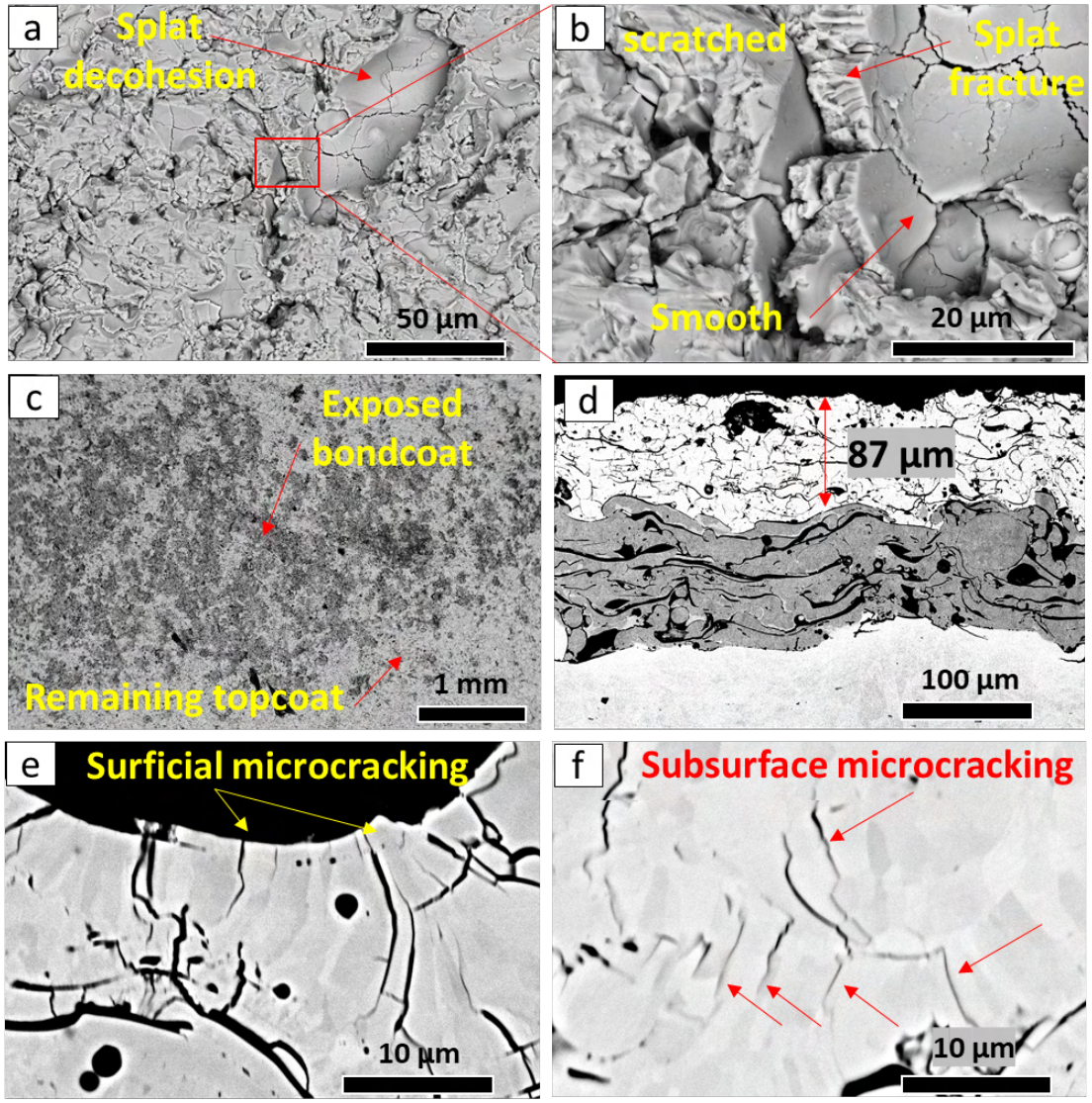


FIGURE 5.3: Microstructure analysis of as-sprayed sample after erosive particle impact via back-scattered SEM observations. (a) top view of the U2 sample, revealing splat decohesion; (b) magnified view of (a). (c) top view of U3 sample under low-magnification conditions. Dark surface indicates the bondcoat, and white coating is the top coat; (d) cross-section of U3 sample close to the centre of the erosive impact; (e) cross-sectional high magnification view of the surficial layer of U2 sample revealing surficial microcracking after erosion; (f) cross-sectional high magnification view of the sub-surficial layer of U2 sample revealing internal microcracking within the splat.

After laser modification, the response of the coating to erosive particles changed significantly: while the mechanism of coating loss in the case of thermally sprayed TBCs is mainly governed by splat decohesion, whether complete or partial, laser modified coatings degrade much slower and with a different mechanism. The cross-section of the modified coating, shown in Fig. 5.4 a, shows that there is no

significant change in the coating microstructure after erosion. The layer underneath the glazed region is not cracked, and all the damage is present only in the surficial region. The number of microcracks, generated at the glazed region of the modified samples is limited compared to that of as-sprayed samples (e.g Fig. 5.4e-f). Due to the large grain size, the damage does not result in cracking along the boundaries of micron-sized grains, but rather in permanent plastic deformation of the surface (Fig. 5.4 d). It should be noted that such behaviour was found at room temperature, suggesting the possibility of plastic behaviour of YSZ not only at elevated temperature. This can be explained as a consequence of dislocation motion within a single grain: assuming the number of dislocations the same within a grain of a splat and grain after laser glazing, due to the size difference of splat grains (∼1µm) and glazed grains (∼20 µm) the amount of possible lattice deformation is much higher for larger grains. This results in plastic deformation and an abundance of scratches at the surface of the glazed region (Fig. 5.4e). Accumulated damage still results in narrow microcracks that appear approximately in the middle of the solidification cracks in perpendicular direction, visible in Fig. 5.3 b, indicated as "perpendicular microcracking". It is interesting to note that underneath the eroded surface of the sample (Fig. 5.4e). It can be seen that in a smoothed, micro-cut layer, the coating consists of large columnar grains (Fig. 5.4 c). At the crack, which appeared within the dense glazed layer shown in Fig. 5.4f, an uneven surface morphology suggests the presence of dislocation motion and their propagation along the slip bands, eventually resulting in a specific surface shown in the indicated region.

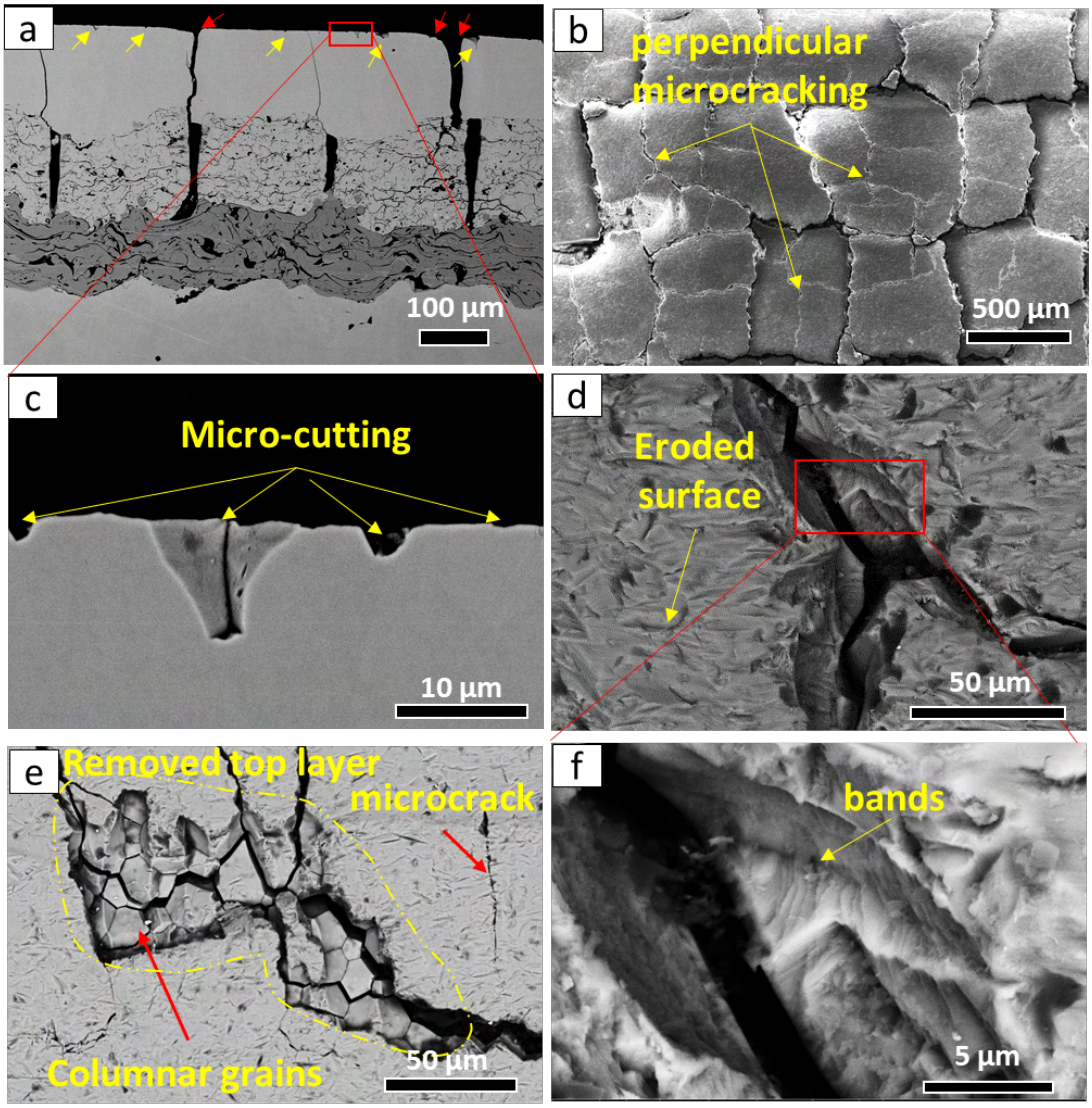


FIGURE 5.4: Microstructure analysis of laser modified sample after erosive particle impact via (a), (c)-(f): back-scattered and (b): secondary SEM observations. (a) polished cross-section after erosion of the L2 sample. Yellow arrows indicate eroded regions and red arrows indicate rounding of sharp edges at the solidification crack interfaces which initially resulted from the glazing process; (b) top surface of L2 sample after laser erosive particle impact revealing crack separation and appearance of internal microcracks, indicated as "perpendicular microcracking"; (c) magnified view of the red box in (a), showing the deformed surface of L2 sample; (d) top surface observation of L3 sample with signs of erosion; (e) top surface of L3 sample showing the partially removed surficial layer, revealing the underlying columnar microstructure after laser glazing (f) high magnification image of the red region in (d), with bands at the cracked region.

Lufeng Li [235] in a similar mechanical process, grinding, separated the effects of mechanical impact into groups including rubbing, ploughing, and cutting. The depth of penetration of the grains discriminates different material removal

processes, noting that cutting appears when the penetration depth d is higher than the cutting transition depth d_{pc}, and the material is removed via chip formation. The results presented in Fig. 5.4 c, d suggest that a portion of the top surface was removed presumably by a cutting mechanism. No surficial micro cracks around the depressions and scratched surface were detected, however, a 110µm long microcrack was found at the top surface (shown in Fig. 5.4e), much larger than the track of erodent particles, which appeared perpendicular to the particle flow. The maximum depth of particle penetration does not exceed 20 µm (Fig. 5.4 c) with the majority of depressions in micron and submicron levels. Since no microcracks were detected around the eroded depressions (or scratches) neither in cross-section nor top surface, large plastic deformation of the YSZ topcoat was assumed. It should be noted that the tests were performed at room temperature conditions and the surface represents a fully dense YSZ, usually seen as a material brittle in nature. The absence of piled-up material around the scratches suggests chip formation and their removal; however, during the erosion process, the formed chips escape the surface with the erodent particles, and their separation is a challenging task.

Surface morphology, presented in Fig. 5.5, supports the previously discussed cracking. Narrow microcracks, visible as thin lines in the texture map (Fig. 5.5 a, 0g of erosion particles), are present as a consequence of solidification shrinkage after laser glazing. Besides, surface undulations repeat the laser melting pattern (Fig. 5.5 b, 0g). After erosion, the undulations are smoothed out, the waviness of the surface is less apparent (Fig. 5.5 b, 150g), and the previously narrow cracks are widened. The density of cracks increases with the increase of erosive particles (Fig. 5.5 a and b, 250g) as a consequence of damage accumulation in the glazed layer. Erosive particles generate dislocation motion within the large grains and eventually result in massive cracking (Fig. 5.5 a and b, 400g).

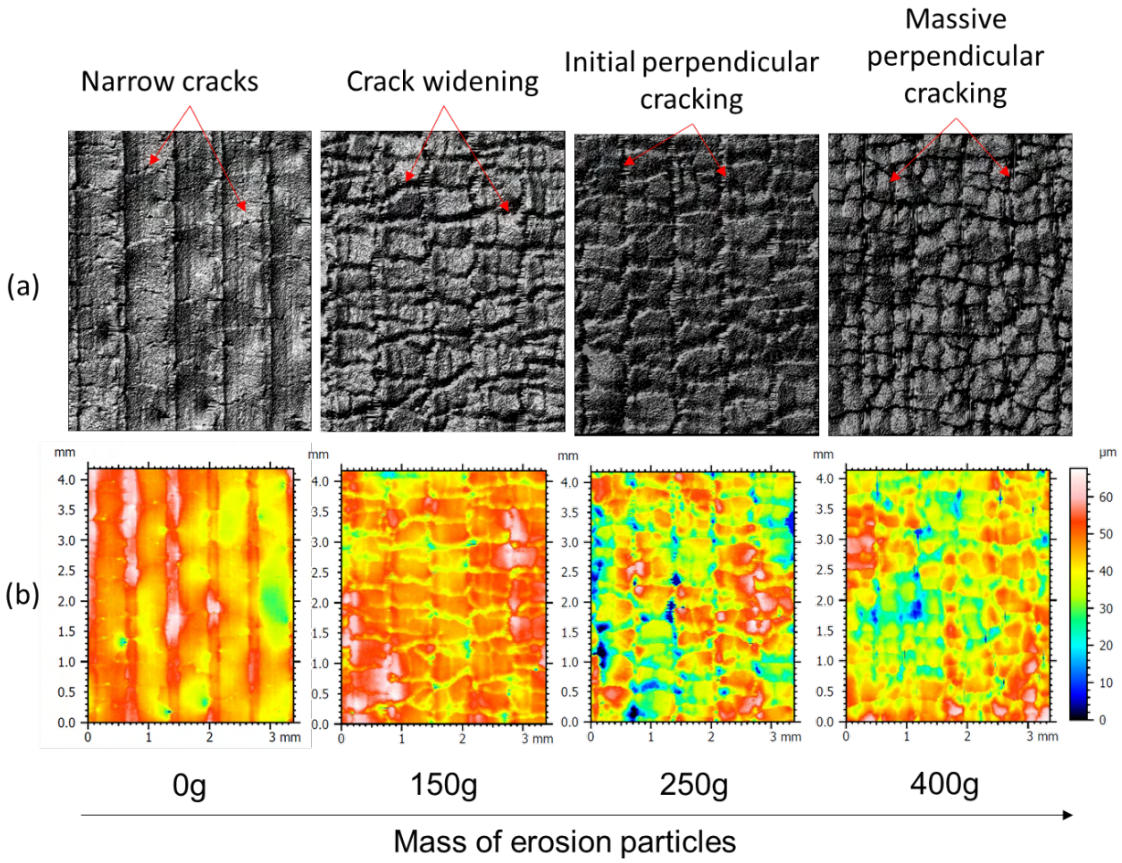


FIGURE 5.5: Surface morphology of the modified samples after erosion test. (a) texture and (b) height map.

The study of Tsai et al. [202] revealed that the laser glazed TBCs were losing large chunks of the densified coatings, and the spallation of this layer exposed the underlying splat structure, susceptible to erosion damage. The overall resistance improvement via their method was 1.5 times at low (30^o) impingement angles. In the case of the proposed modification method, the coating loses thickness gradually, and erosion resistance increased by 8.9 times. Spallation occurs rarely, and still exposes densified material; an example is shown in Fig. 5.4e.

Such a major difference in erosion performance of the proposed TBC microstructure and the traditionally glazed TBCs could be attributed to the confinement of cracks in the described method; the solidification cracks occurring after glazing, positively affecting thermomechanical compliance of topcoats, create a stress concentrator at the crack tip and can become transverse underneath the dense layer. Under mechanical loads, a stress concentrator propagates further

inside the material and coalesces just underneath the surface. In our method, crack tips are connected to the underlying grooves, reducing the stress concentrator from the coating. However, after significant erosion, secondary cracking occurs at the surface (noted as perpendicular cracks in Fig. 5.5). No large-scale spallation of the coating was observed in laser-modified samples. Erosion, similarly to literature reports[235], is happening by spallation failure of the poorly bonded splats and their fracture in the case of the as-sprayed APS coatings. After undergoing combined laser modification, the crack direction was controlled, and splat spallation as well as near-surface cracking was diminished. Instead, relatively large cracks were appearing in the energetically favourable spots of the coating.

5.2.4 X-Ray diffraction analysis of the topcoat after erosive impact

In order to understand the influence of mechanical impact on the crystallographic properties of the YSZ, x-ray diffraction measurements were carried out (Fig. 5.6 to Fig. 5.8). Typically, the X-ray spectrum of TBCs is taken over a whole range of angles, however, to capture the morphology of the YSZ, high-resolution spectrums were taken in low (27.5^o – 32^o) and high (72.5^d – 76^o) 2Θ angles. Texture and morphology of 8wt%YSZ are denoted with respect to the literature reports [235], [279]. In Fig. 5.6 a, the sample before erosion tests shows a strong peak at 30.1^o, which corresponds to *c*, *t* and *t'* phases. In the low angle of incidence, these phases are indistinguishable from each other. No monoclinic phase was observed in the as-sprayed and eroded samples. Interestingly, the XRD spectrum becomes asymmetric upon erosion of laser-modified samples (Fig. 5.6 a, denoted with a blue arrow). At the same time, samples upon erosion of as-sprayed samples, shown in Fig. 5.6 b, do not exhibit this behaviour. Instead, the peak does not change its shape but gradually shifts toward 30.1^o, which is the stress-free state of to *c*, *t* and *t'*morphs. According to Bragg's law, the shift of 2Θ peak towards the smaller values corresponds to smaller distances between the diffractive planes, i.e. (111) crystal planes, and vice versa. Qualitatively, the peak of the as-sprayed sample U0 before

erosion is shifted towards the higher values (Fig. 5.6 b, blue arrow), which can be a consequence of expected tensile residual stresses upon splat solidification. After erosion with various duration of the grit mass, the peak gradually shifts toward the stress-free state (U3 in Fig. 5.6 b, purple arrow).

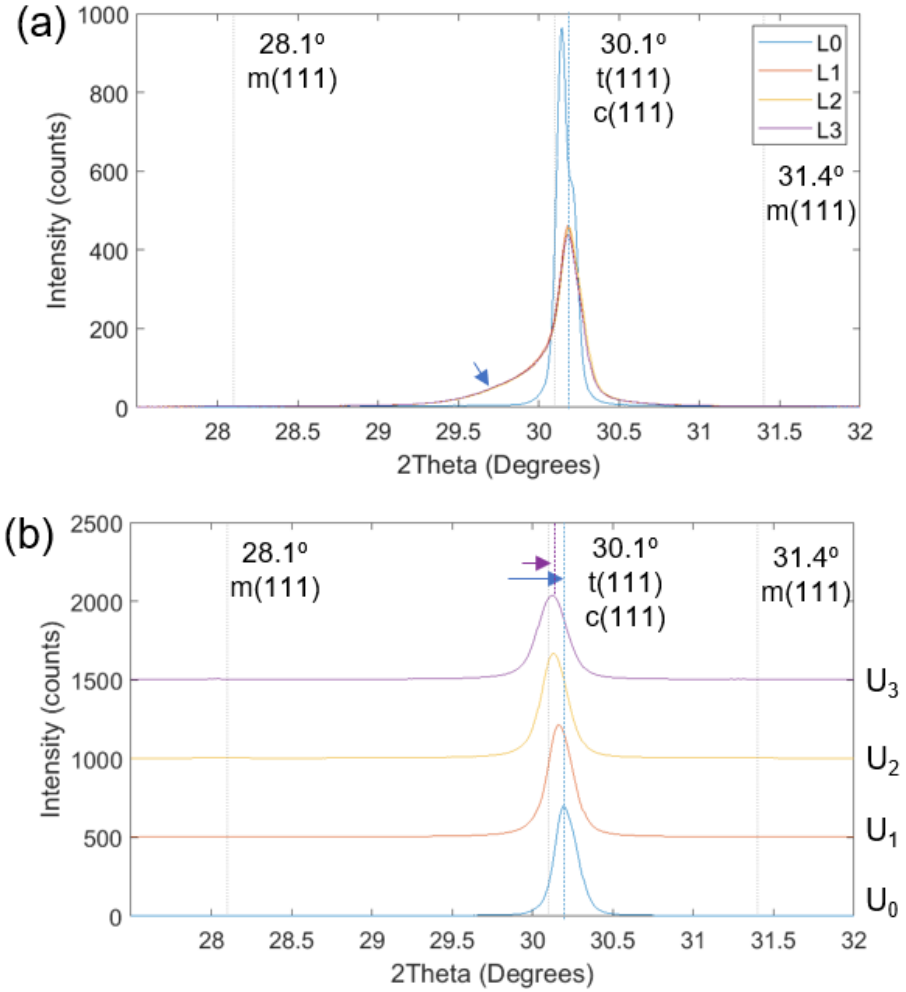


FIGURE 5.6: Low angle XRD diffraction analysis of (a) laser modified and (b) as-sprayed coating after erosion. Notations 0, 1, 2, and 3 correspond to the samples after the impact of 0g (before erosion), 150g, 250g, and 400g, respectively. The blue arrow in (a) indicates an asymmetrical broadening of the peak. Blue and purple arrows in (b) indicate the central 2Θ angle of the U_0 and U_3 and peaks, respectively.

The peak of the laser-modified sample before erosion L0 (Fig. 5.6 a) is close to its relaxed state, which is a consequence of stress relaxation within the cracks after laser solidification. After erosive impact, the left tail of nearly gaussian peak, disturbed by unfiltered $K_{\alpha 2}$ radiation of the x-ray source, propagates towards the smaller 2Θ angles. It was assumed that left-side peak asymmetry represents the increase

of compressive stresses, which are smaller than the penetration depth of x-ray radiation. The monoclinic phase content is indistinguishable from the noise level, and the samples before and after erosion dominantly consist of *t'* phase, typically occurring with high cooling rates.

It is possible to distinguish between *t, t'*, and *c* phases in the high angles of the diffraction spectrum, presented in Fig. 5.7. In this case, the diffraction of the second characteristic wavelength of copper $K_{\alpha 2}$ is particularly pronounced [235] denoted on the graphs. All of the as-sprayed samples before and after erosion have a strong *t'*phase preference, and the (400) orientation dominates over the 90^o rotated (004) orientation, see Fig. 5.7 b. It was assumed that such judgement can be made based on the relative intensity of the peaks since the *t'* (400) and *t'*(004) planes have roughly the same number of atoms at the diffraction plane. After erosion tests, there is a general trend toward increasing thermal stress. Surprisingly, the shift of the (004) and (400) peaks from the stress-free state is the opposite, suggesting that the *t'*(004) experiences compressive stresses, and *t'*(400) has residual tensile stress. This phenomenon could not be explained in the scope of the current work, however, similar behaviour was found in the work of Ballard et al. [235], where the *t'*(004) peak is at 73.1^o, while the *t'*(400) has signs of tensile residual stresses.

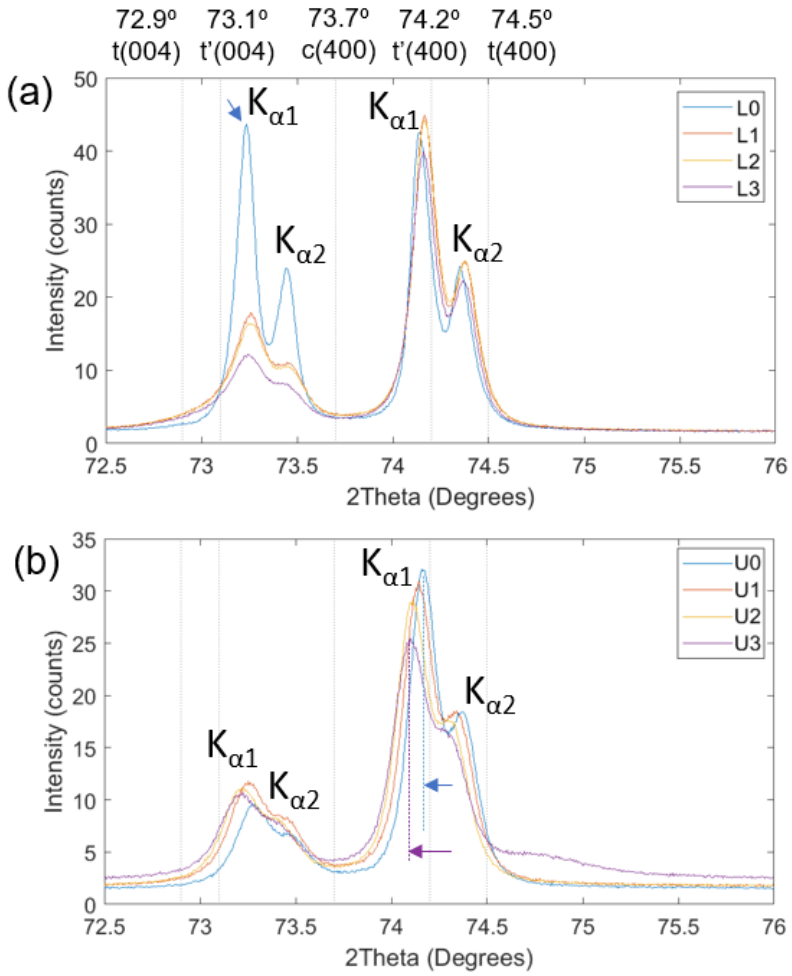


FIGURE 5.7: High angle XRD diffraction analysis of (a) laser modified and (b) as-sprayed coating after erosion. Notations 0, 1, 2, and 3 correspond to the samples after the impact of 0g (before erosion), 150g, 250g, and 400g, respectively. Blue and purple arrows in (b) indicate the central 2Θ angle of the U_0 and U_3 and peaks, respectively. $K_{\alpha 2}$ indicates the peak from secondary XRD wavelength (no postprocessing was used).

At the same time, the laser modified sample L0 shows similar $t'(004)$ and $t'(400)$ tetragonal peaks, shown in Fig. 5.7 a. Such change is a consequence of the laser melting and subsequent solidification. Interestingly, upon erosion tests, no significant shifts of the peaks along the 2Θ axis were noticed, which suggests that these phases did not change their stress state. On the other hand, the relative content of $t'(004)$ has increased significantly after the first erosive impact in sample L1 (Fig. 5.7 a), and the trend continued in samples L2 and L3, instead of naturally occurring trend towards compressing stresses (Fig. 5.7 b). A possible explanation for this observation could be a shift of the atoms $t'(004)$ to $t'(400)$ under external

stress, also known as ferroelastic domain switching, which was used to explain the unusually high toughness of the tetragonal zirconia with no transformation to monoclinic phase.

5.2.5 CMAS infiltration tests

After CMAS infiltration tests in the furnace, the samples reacted with a pronounced difference, visible in the optical photographs and SEM cross sections are shown in Fig. 5.8. While the as-sprayed sample underwent explosive spallation behaviour (fractured parts of the coating are denoted with red arrows in Fig. 5.8 c), most of the coating of the laser-modified sample remained (Fig. 5.8 a). To further understand the interaction mechanisms of the molten silicates and TBC, cross sections close to the centre of the samples have been taken, ground and polished. In Fig. 5.8 d it is possible to confirm the loss of thickness and spallation of the TBC. The Failure mechanism may include 2 factors. First, the loss of compliance of the coatings due to mechanical stiffening of the splat-like as-sprayed structure is a likely mechanism responsible for spallation. Secondly, yttria reaction with CMAS, its subsequent depletion from stable 8wt%YSZ causes a decrease in yttria content and loss of phase stability of *t'* YSZ. Finally, *t'*phase undergoes martensitic transformation to monoclinic phase with a volumetric increase, causing spallation of the coating.

Similar results have been reported previously by Ghoshal et al. [235] with rapid spallation after CMAS infiltration. In their work, rapid spallation was not observed after 30- and 60-min infiltration tests at 1100^{o}C, while complete coating fracture was reported after 24h test. While some of the coatings still remain on the as-sprayed sample (Fig. 5.8 b), cross-sectional observation show a significant loss of thickness of the remaining part of the coating to less than 100 µm, shown in Fig. 5.8 d.

Laser-modified samples, on contrary, show improved resistance to CMAS attacks. While some partial fracture of the coating was present (Fig. 5.8 a, denoted as "partial spallation"), the coating still remains adhered to the substrate. A cross-sectional micrograph shows little damage to the coating with CMAS situated at the top surface of the densified coating (Fig. 5.8e), which is a sign of decreased

infiltration ability of the molten sand. The small width of the solidification microcracks, generated after laser melting, reduces CMAS propagation significantly.

It should be pointed out that the properties of the CMAS-simulating powder have not been measured as a part of this study. However, for similar to AFRL-03 powders the reported glass transition temperature of desert sand with the composition of 27.8CaO-4MgO-5Al_2O_3-61.6SiO_2-0.6Fe_2O_3-1K_2O (mol %) is 706 °C, softening point is 764 °C, and coefficient of thermal expansion of $9.8 \cdot 10^{-6} K^{-1}$ [21]. Since the softening point of the CMAS is far lower than the dwelling temperature during the test (1121 °C), and the duration of the test is 24 hours, the CMAS is expected to melt and infiltrate through the coating.

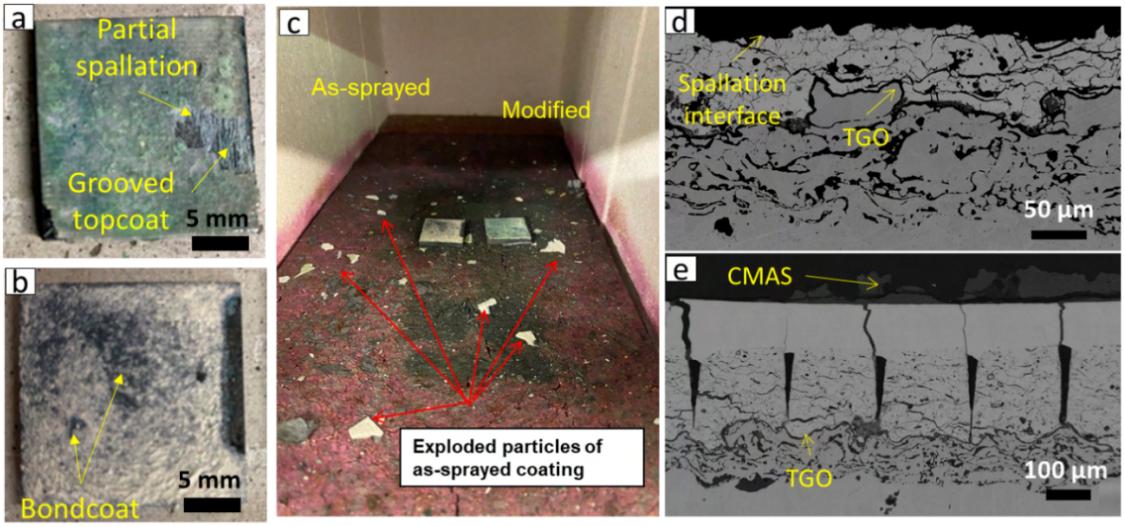


FIGURE 5.8: CMAS infiltration test results after 24h at 1121^{o}C. Optical photograph of the top surface (a) sample after proposed modification technique and (b) as-sprayed sample. (c) furnace chamber after the CMAS test with an explosion of as-sprayed coating; (d) SEM micrograph of the remaining as-sprayed coating; (e) modified structure after CMAS interaction.

In the as-sprayed coatings, the porous splat-like microstructure creates interconnected channels within the coating. EDS analysis of the remaining coating, presented in Fig. 5.9, reveals silicon infiltration even in the remaining coating (Fig. 5.9 b). Besides, a continuous TGO layer is visible at the bondcoat-topcoat interface, and the CMAS does not propagate through the TGO to the bondcoat.

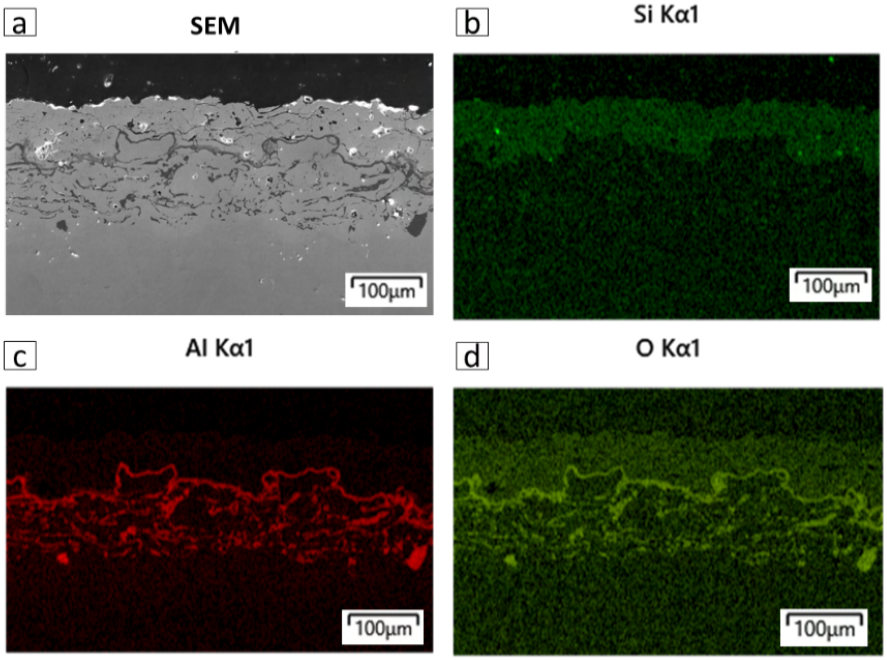


FIGURE 5.9: Elemental analysis of the remained coating after CMAS infiltration into the as-sprayed coating. (a) SEM micrograph; (b) Si map showing homogeneous infiltration of silicon into the topcoat; (c) Al distribution map, showing Al depletion and formation of TGO; (d) Oxygen elemental map

The cross-section of a spalled piece of the as-sprayed coating was also analysed, showing signs of CMAS reaction with the coating (Fig. 5.10). CMAS reaction can be distinguished by generated submicron porous structure, visible in Fig. 5.10 b. This is caused by the confinement of volatile SO_3, CO_2, and H_2O[235]. Splat interfaces, i.e. the discontinuities in the microstructure of the as-sprayed coatings, create a channel for fast CMAS propagation, and the traces of severe CMAS reaction with the coating are also visible along these paths (Fig. 5.10 b). At the same time, the CMAS has reacted close to the delamination interface, visible in the magnified view in Fig. 5.10 c.

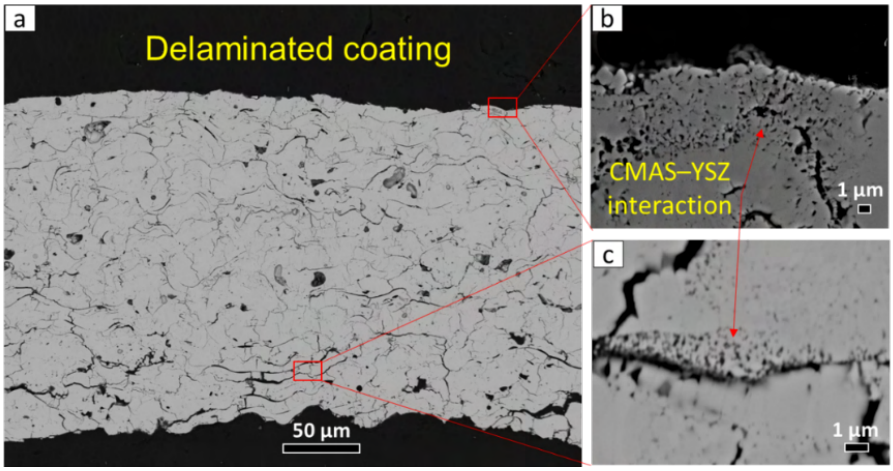


FIGURE 5.10: Analysis of as-sprayed coating after CMAS interaction. SEM micrograph of (a) delaminated fragment of the coating after CMAS infiltration; high magnification image of the (b) top surface and (c) area close to the spallation interface, showing the interactions between CMAS and as-sprayed coating

After laser modification, the surficial layer is dense and free from internal porosity, as it was shown previously. The only possible way for CMAS infiltration through the coating is the solidification microcracks. While the microcracks are beneficial for thermomechanical compliance, their width would control the flow of the molten silicates. Generally, the idea behind combined laser modification is to prevent further propagation of the silicates through the coating. Laser ablated grooves create a void that can contain the silicates within its volume and reduce its further infiltration. A high magnification cross-sectional micrograph of the groove interface with the dense layer is presented in Fig. 5.11. The dense layer is nearly free from silicon traces (Fig. 5.11 a-b), while the grain boundaries became pronounced. This can be a result of CMAS propagation through the grain boundaries of the dense YSZ. Inside the groove, the CMAS is contained close to the dense layer, and a concave meniscus is caused by surface tension forces, denoted with the red arrow. The concave meniscus displays a strong adhesion of the CMAS and YSZ and their high wettability.

After reaching the groove, CMAS continues its infiltration through the topcoat to the neighbouring regions (Fig. 5.11 a-b), at the same time, decreasing the Zr content in the areas of interaction (Fig. 5.11 c). Na, Mg, and Ca is generally contained within the void as a consequence of the lower viscosity of their compounds than that of Si glass.

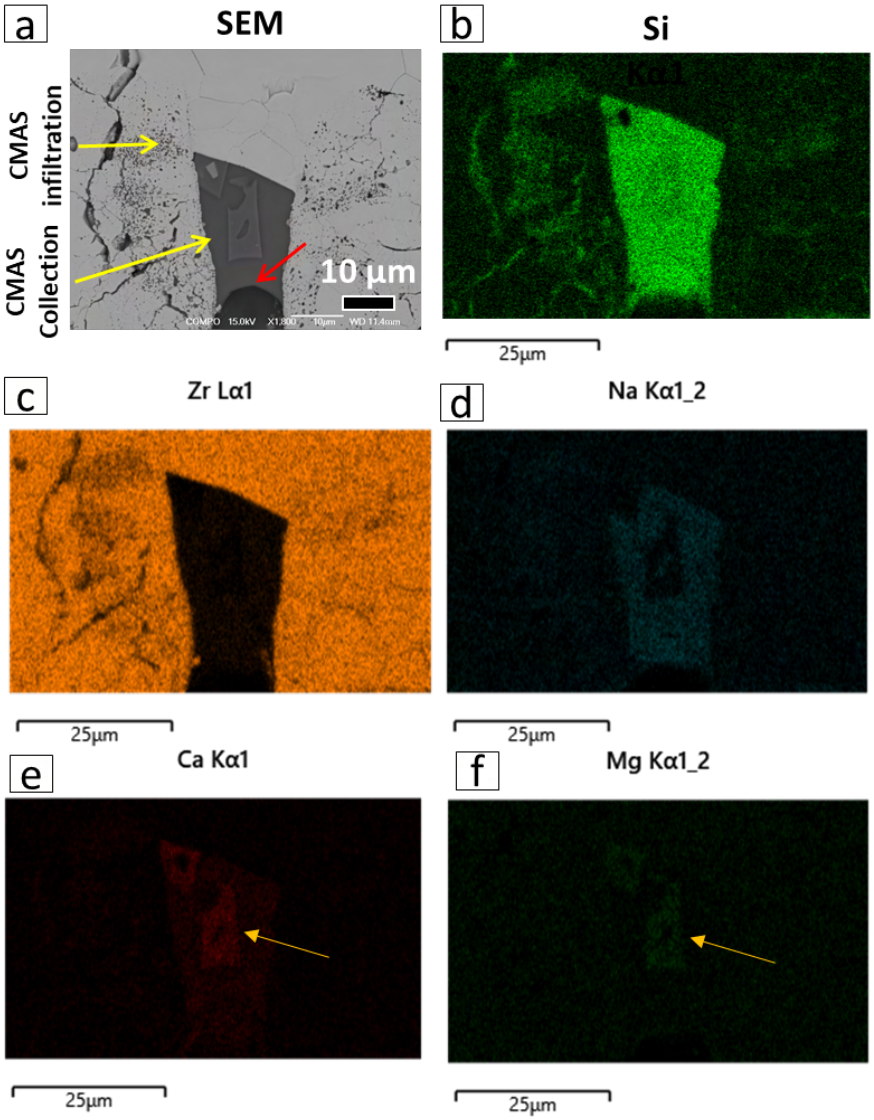


FIGURE 5.11: (a) SEM image of the modified sample after CMAS test. red arrow indicates meniscus. (b) Si elemental map, showing infiltration of silicon through the porous part of the coating; (c) Zr elemental map; (d) Na elemental map; (e) Ca elemental map; (f) Mg elemental map. Yellow arrows indicate the high Ca-Mg concentration within the CMAS.

While it is difficult to quantitatively compare coating resistance to CMAS, overall, the resistance of the coating to CMAS infiltration has increased significantly after combined laser modification.

5.2.6 Thermal cycling tests

Isothermal thermal cycling tests were completed in the furnace simultaneously, thus experiencing the same conditions in both as-sprayed and laser-modified coatings. Thermal cycling results are presented in Table 5.2, showing an insignificant increase in the thermal cycling performance of the coating.

Table 5.2: Thermal cycling tests results

	As Sprayed	Modified
Number of cycles to failure, mean	179	199
Standard deviation, %	17	9

In contrast with typically shown partial spallation of the coating and gradual thickness loss, which can be simply evaluated by either the area of remaining coating or by thickness loss, the samples underwent different failure behaviour, and this evaluation technique was not feasible. Instead, the coating remained at the surface/in its vicinity throughout the experiment, and no fracture of the coating into smaller pieces was detected. Instead, the as-sprayed samples lost their topcoat completely, which is particularly clear in Fig. 5.12 e (long red arrow pointing at the delaminated coating).

Thermal cycling performance in these conditions was evaluated based on the emission characteristics of the coating shortly after leaving the furnace after each cycle (Fig. 5.12). Hot objects emit electromagnetic radiation, which becomes visible close to 1000^{o}C, and a CCD camera usually can capture radiation in near-infrared spectrum. When the topcoat is disconnected from the substrate, the rate of temperature loss is higher due to lower overall heat capacity of the object. Therefore, it is possible to estimate the approximate area of the coating adhered to the substrate, and 50% of the adhesion loss by area was used as a failure criterion. Such a high value of coating loss was chosen due to the generally high thermal inertia of the 3 mm thick substrate with partially delaminated coating: while the spallation failure is straightforward for analysis, thermal delays of the substrate-TBC system make it difficult to find the exact moment when the edge

delamination or buckling has begun. However, coating delamination, in this case, becomes clearer with a higher percentage of the delaminated coating.

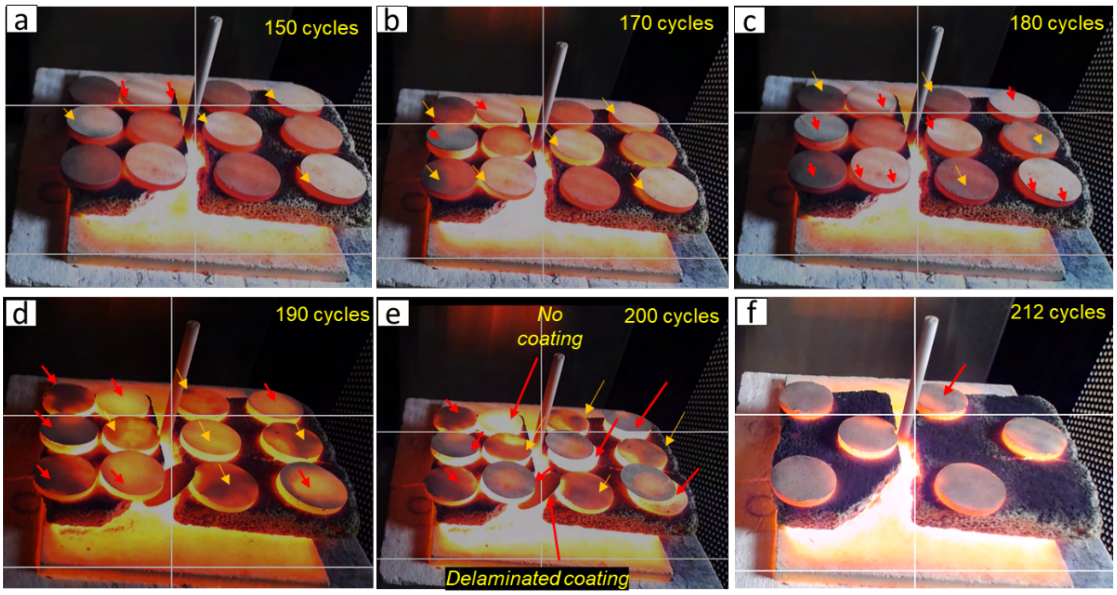


FIGURE 5.12: Radiation recorded during the cooling part of the thermal cycle shortly after the end of the heat exposure. Based on the part of the coating emitting light, coating adhesion to metallic substrate was evaluated. Amber arrows note samples close to failure, red arrows show the samples evaluated as failed. (a) 150 cycles; (b) 170 cycles; (c) 180 cycles; (d) 190 cycles; (e) 200 cycles; (f) 212 cycles; After 200 cycles, as-sprayed samples were removed from the furnace

After isothermal thermal cycling, every as-sprayed sample lost its topcoat (Fig. 5.13 b, label U), and the bondcoat with small islands of white topcoat is exposed to the environment. Laser-modified samples in the same figure (label L) remained at the substrate, however with visible signs of buckling.

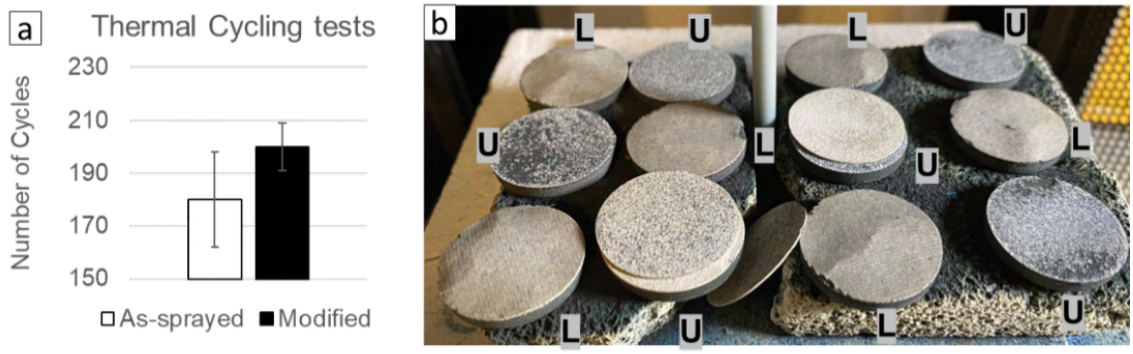


FIGURE 5.13: (a) thermal cycling performance in isothermal tests of as-sprayed and laser modified samples. (b) optical picture after 200 cycles in the furnace with buckled laser-modified samples (labelled as L) and complete delamination of the topcoats of as-sprayed samples (labelled as U). Some of the topcoats were blown by air and changed their position.

Fig. 5.13 a shows a slight improvement in thermal cycling performance of the TBCs after laser modification, however, the change was considered insignificant. Overall improvement of thermal cycling performance is 11%, which is comparable with the statistical deviation of the test. At the same time, the failure mechanism of the coating after laser modification changed to buckling, and further analysis is described in the following section.

Edge-driven delamination and buckle-driven delamination have been long recognised as two distinctive failure processes. According to Evans [75], the failure of thermal barrier coating with a given thickness will be dominated by either large-scale buckling or edge delamination, depending on the ratio of the in-plane and out-of-plane elastic moduli of the top coat, shown in Fig. 5.14). The TBC in the upper right has relatively high in-plane stiffness and limited strain tolerance, resulting in large residual stress and a high strain energy density, which corresponds to as-sprayed coating. This energy density augments the TGOs and provides a strong driving force for edge delamination, which is resisted by mode II toughness along the most brittle pathway (among the TBC, TGO or interface).

The low in-plane modulus of the TBC in the top left of the map does not resist small-scale buckling of the TGO, causing the system to fail under conditions similar to those for the TGO in the absence of the TBC, which is the case for

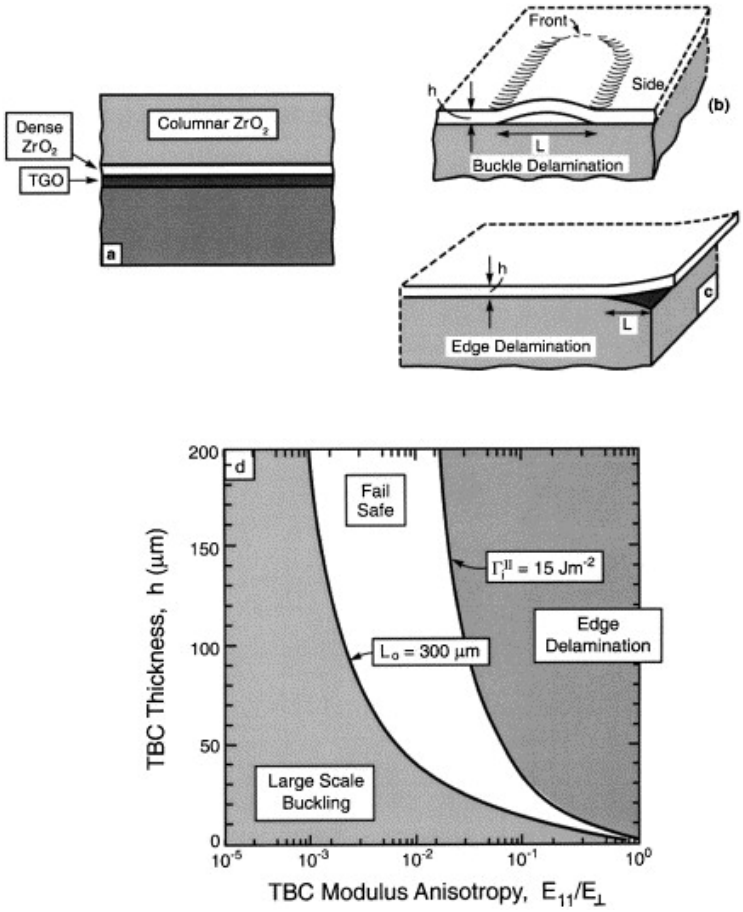


FIGURE 5.14: Edge delamination and large scale buckling as a function of TBC modulus anisotropy [75]

laser-modified coatings. Small-scale buckling and edge delamination are suppressed at the intermediate levels of in-plane modulus, and the system resides in a "fail-safe" domain until degradation phenomena operate on either of these mechanisms.

5.2.7 Failure mechanics in as-sprayed and modified coatings and future outlook

Since every sample experienced complete failure due to a large number of cycles, the experiment was repeated for 160 and 185 cycles. Cross-sectional observations of the samples closest to failure was taken close to the centre of the samples, and are presented in Fig. 5.15 and Fig. 5.16.

The as-sprayed sample after 185 cycles experienced edge delamination from one side

with a large crack opening (∼150 µm), shown in Fig. 5.15 a. In the middle of the sample, Fig. 5.15 b, the crack still exists and disappears on the right side (Fig. 5.15 c). Some initial cracks are present on the right side of the coating (noted with yellow arrows in Fig. 5.15 c) which did not coalesce. Moreover, the left edge of the topcoat has moved relative to the bondcoat (Fig. 5.15 a) as a consequence of creep within the topcoat.

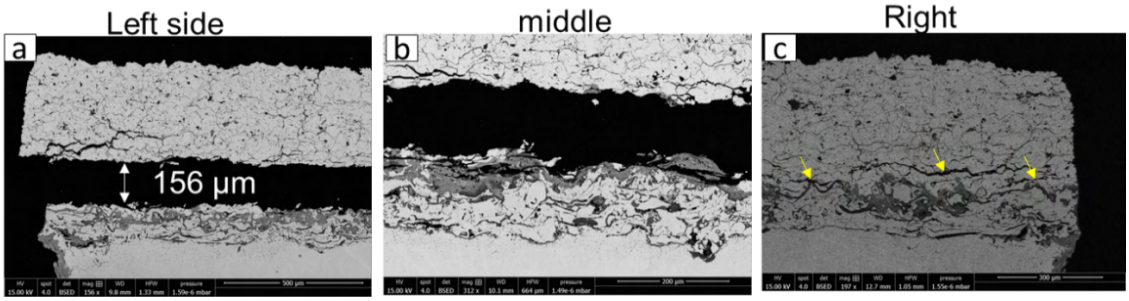


FIGURE 5.15: Cross-sectional SEM micrographs of the as-sprayed sample after 185 cycles. (a) left, (b) middle, and (c) right sides of the coating

The TGO thickness of the as-sprayed samples after 185 cycles was 4.3 ± 1.3 μm. In some areas, the formation of thick spinels was also observed. Similar values were found in laser-modified samples (3.9± 1.6 μm). After laser modification, the crack was discontinuous (Fig. 5.16 b), and the crack opening was the largest in the middle of the sample (∼ 40 μm). This was considered to be a buckling failure due to the high elastic modulus of the densified coating.

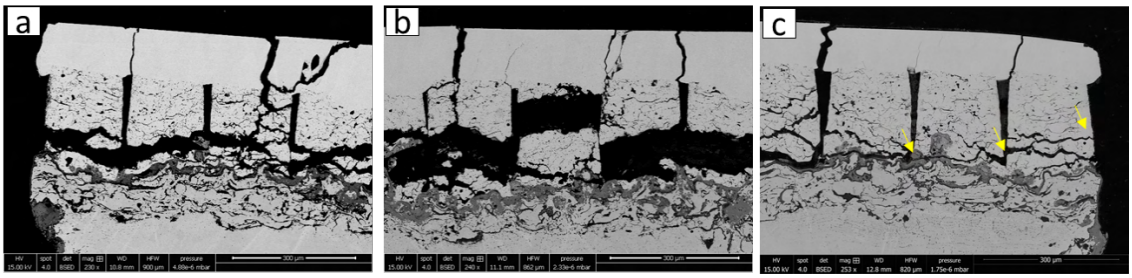


FIGURE 5.16: Cross-sectional SEM micrographs of laser-modified sample after 185 cycles. (a) left, (b) middle, and (c) right sides of the coating

During the thermal test, the following explanation is proposed, schematically shown in Fig. 5.17, separated into 4 stages. At stage 0, the coating experiences no damage and functions as designed with full functionality and begins developing

microcracks. At the next stage, microcrack initiation starts, and in the case of the as-sprayed coatings develops into a macrocrack close to the edge. This creates a combined crack front (noted with a red arrow in Fig. 5.17, "Stage 1"), and the sample enters the crack growth stage, where the crack front continues its expansion. Depending on the stress concentration, the relative speed of crack propagation and crack initiation may differ, resulting in one of the possible failure cases: (i) when the crack propagation speed is faster than crack initiation, the once initiated crack continues its development and continues its growth, as depicted in Fig. 5.17 and observed in the presented experiments; (ii) on contrary, the speed of crack initiation may be higher than the speed of propagation, which would result in crack initiation across the circumference of the sample, and then its propagation towards its centre. Eventually, in both cases, the crack propagates towards all the surfaces of the sample, and the substrate fails after losing the whole coating, noted as stage 3.

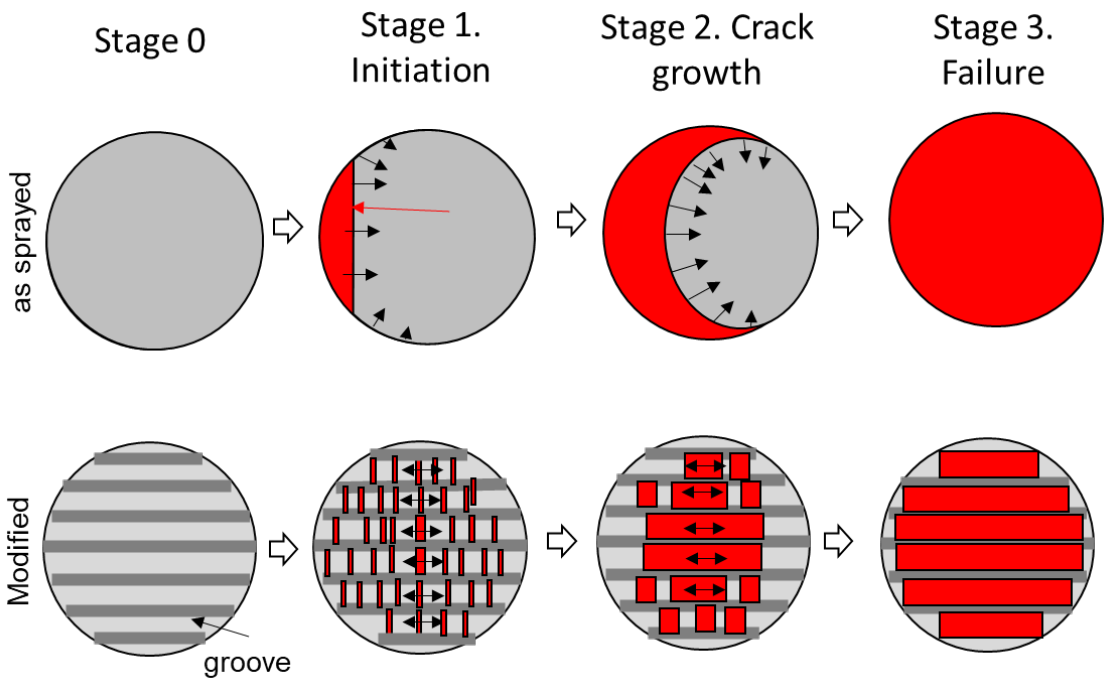


FIGURE 5.17: Proposed failure mechanisms during thermal cycling of as-sprayed and modified coatings

The amended microstructure of the coating upon modification changes its failure mechanism due to the dense layer of the topcoat and grooves. During stage 1, the coating develops microcracks at the stress concentrators at the sides of the grooves.

The direction of micro- or microcrack propagation is confined in one dimension: once a propagating crack front enters the groove, its further propagation, effectively, stops. In stage 2, the initiated cracks continue covering a larger portion of the sample until failure.

Choi et al. [235] distinguished the failure phenomena of the coatings based on the ratio of in-plane and out-of-plane elastic modulus of the topcoat, proposing that the dominance of the out-of-plane elastic modulus leads to edge delamination, and the relative decrease in the in-plane elastic modulus would lead to buckling spallation. Between the two, a "fail-safe" condition is met, when the initial delamination neither spreads nor buckles, eventually increasing the thermal shock resistance of the coating. With the proposed method, it has been shown that it is possible to tailor the microstructure of the coating in such a way that the edge delamination is suppressed by buckling, while the coating experiences similar thermal cycling characteristics. In this work, the microstructure design was limited by the manufacturing abilities and aimed to show the possibility of tailoring the microstructure and needs further optimisation.

5.2.8 X-Ray diffraction analysis of the topcoat after thermal fatigue tests

To understand phase transformation in as-sprayed and laser-modified states, the samples were analysed via X-Ray diffraction. The results presented in Fig. 5.18 suggest that no noticeable tetragonal-to-monoclinic phase was observed under 1121^{o}C. Nonetheless, further analysis revealed a small peak of less than 5% of the total content, which is not visible with the linear scale of intensity. As was discussed previously, the relative residual tensile stresses upon laser modification are lower than that in the as-sprayed case, however, after thermal cycling the coating experience the opposite behaviour. As can be expected, the peak of the as-sprayed sample U0 gradually shifts towards relaxation at 30.1^o after 160 and 185 cycles (samples U160 and U185) due to creep relaxation and splat sliding of

the coating. On contrary, the tensile residual stress of the laser-modified sample increases with increasing thermal cycles, shown in Fig. 5.18.

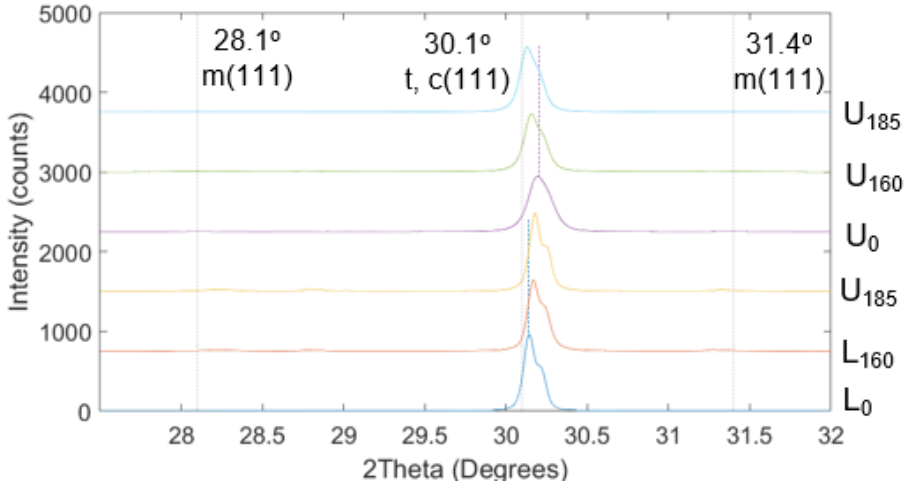


FIGURE 5.18: Low angle XRD diffraction analysis of laser modified and as-sprayed coating after erosion. Notations 0, 160, and 185 correspond to the samples after 0, 160, and 185 thermal cycles, respectively. Blue and purple dashed lines indicate the central 2Θ angle of the U_0 and U_3 and peaks, respectively.

This controversial result is a consequence of the changed creep mechanisms of the coating. Thermal relaxation cracks, typical for laser melting of thermally sprayed YSZ, are believed to be responsible for the increased lifespan of the coatings[315], however sometimes with no improvement in thermal cycling life [98]. Due to high microcrack density, controlled by the groove pitch, the width of the microcrack is smaller than that occurring naturally. During thermal cycling, the topcoat is separated by the microcrack with a width smaller than the linear thermal expansion of the coating, and the colliding parts of the dense coating generate compressive stresses. The underlying splat like as-sprayed topcoat still experiences splat sliding creep behaviour, in contrast with the dense layer. Together with the bondcoat, this combined effect results in tensile stresses at the topcoat layer in the case of laser-modified coating.

High angle XRD spectrum also shows relaxation of the coating in as-sprayed conditions, see Fig. 5.19 b. The *t'* crystals compressed in [001] direction and experience tensile stresses in [100] direction release the accumulated stresses due to creep relaxation (U160 and U185, Fig. 5.19 b). The laser-modified samples also

show some signs of relaxation with the general trend towards the stress-free state (Fig. 5.19 a). As was discussed previously, the initial texture of the laser-modified sample has a similar distribution of $t'(400)$ and $t'(004)$, i.e. [100] and [004] oriented crystals, which changed after erosion impact. Similar behaviour is present after the thermal cycling tests, where the relative peak height of $t'(400)$ to $t'(004)$ decreases after thermal exposure. Similarly, the possible explanation for this is the ferroelastic domain switch of the dense coating with increasing preference for the [100] orientation.

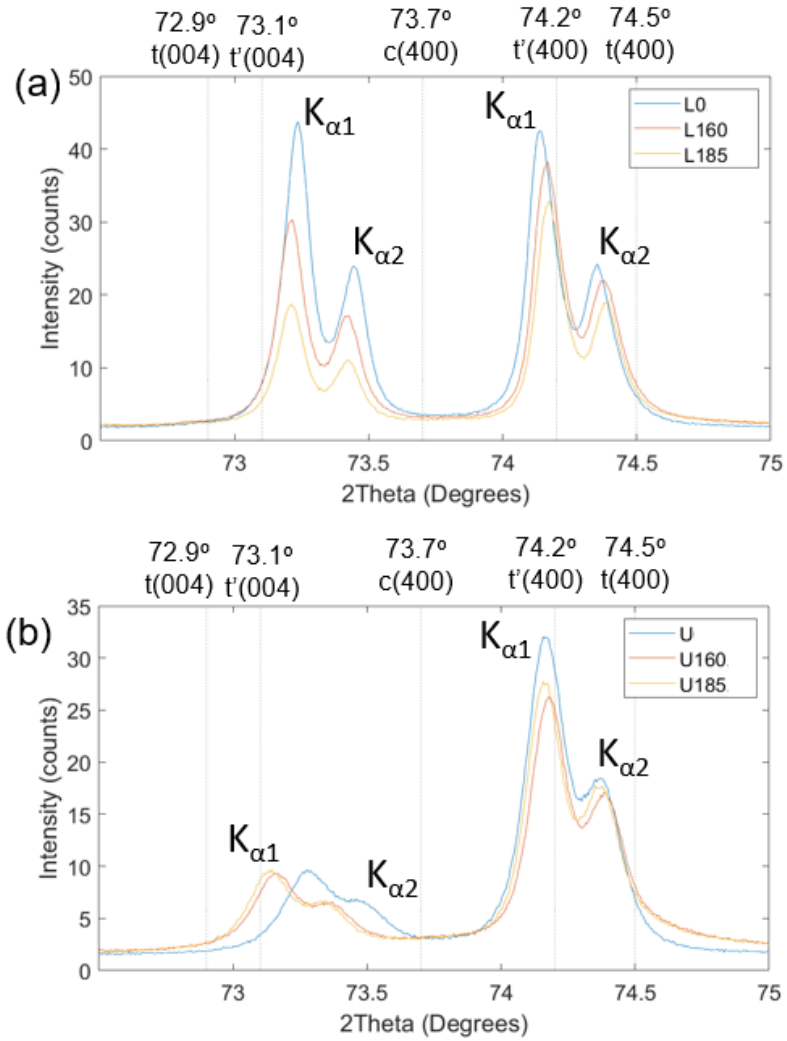


FIGURE 5.19: High angle XRD diffraction analysis of laser modified and as-sprayed coating after erosion. Notations 0, 160, and 185 correspond to the samples after 0, 160, and 185 thermal cycles, respectively. Blue and purple dashed lines indicate the central 2Θ angle of the U_0 and U_3 and peaks, respectively. $K_{\alpha 2}$ indicates the peak from secondary XRD wavelength (no postprocessing was used).

While the splat sliding does not occur in the dense coating, this decreased the rate of coating relaxation. Besides, the stresses generated during thermal cycling in laser-modified coatings are sufficient for ferroelastic domain switching of the dense coating.

5.3 Summary

This study showed the effects of artificially induced porosity after coating deposition, combined with surface densification, generating vertical and sealed pores via laser beam processing. Further work toward TBCs with desired elastic modulus ratio, in particular through thermomechanical modelling, should be carried out in order to obtain thermal barrier coatings with desired characteristics. Besides, the width of the microcracks at the dense layer after laser melting was recognised to be responsible for an increased thermal shock resistance [315]. Grooving the topcoat in perpendicular dimensions would potentially benefit the coating. Together with careful control of the thickness and geometry of the glazed layer, this can suppress buckling failure. A pattern of grooves generated at the dense layer can serve this purpose, thus decreasing compressive thermal stresses. Potentially, wider microcracks would increase the thermomechanical compliance of the topcoat. The width of these cracks may be controlled by the groove pitch and/or ambient temperature during laser melting. At the same time, there is a trade-off between the crack width and resistance of the coating to oxidation, i.e. larger cracks would be a better short path for oxygen penetration to the bondcoat. With regard to CMAS resistance, increasing the crack width would lead to a higher flow rate of molten silicates toward the grooves, and lower CMAS performance.

It should be noted that the number of samples was limited and therefore statistical significance of the erosion experiments will need further confirmation in future studies of the coating behaviour. To facilitate the future industrial utilization of this data, a statistical experimental investigation will be required to validate the coating performance.

The modified coating was comprehensively analysed in close to engine operating conditions. In all the tests conducted the modified coating showed increased durability in comparison with as-sprayed coating:

1. The coating after combined laser modification decreased its surface roughness from *Sa* 9.81 μm to *Sa* 0.75 μm, potentially improving tribological flow conditions within the aero engine.

2. Erosion resistance of the coating after modification was increased by on average 8.6 times in comparison with as-sprayed coatings, which is a consequence of surface densification and diminishing the influence of poor splat-to-splat adhesion of thermally sprayed coatings. No large volume fracture of the densified region was observed, which is a consequence of the increased depth of the glazed region.

3. Quasi-columnar coating has an increased CMAS resistance by reducing the propagation of the molten silicates inside the coating and containing the CMAS within the groove volume.

4. Thermal cycling life of the coating was increased by 11%, resulting from increased strain tolerance of the coating. The spallation mechanism of the coating changed from edge delamination to buckling.

5. No phase transformation of YSZ was found under 1121^{o}C after thermal cycling in either as-sprayed or laser-modified conditions.

6. X-ray diffraction revealed the existence of a ferroelastic domain switching in the laser-modified state of the YSZ coating as a response to particle impact and thermal cycling. Such behaviour was not found in as-sprayed coatings. Tensile residual stresses after thermal spraying were relaxed through laser melting. After erosion, signs of stress relaxation were observed in the as-sprayed coating, while the laser-modified coating generated compressive stresses within the thin surficial region.

Chapter 6

Understanding microstructure formation within the glazed layer

During the work on laser modification of TBC, discussed in the previous chapters, unusual solidification behaviour of the laser melted topcoats was observed. Particularly, formation of remarkable fractal-like dendritic grains is rarely discussed in the context of ceramics. Besides, two different phenomena have been identified, which will later called "grain surface sealing" and "grain bending". In grain surface sealing phenomenon, we found that in certain conditions the typical vertical columnar microstructure is "sealed" with horizontal columnar grains; "grain bending" refers to the change of the straight grain boudary to a curve. With the assumption that these three observations have a common physical reason, closer attention was paid to stability of the planar-liquid interface in the melt pool. With the aid of macroscopic thermal model, the interface stability of the interface was analysed, and was used in combination with a grain growth model which was developed based on cellular automata approach. With the aid of the models, three phenomena have been explained and accurately predicted, and compared against experimental data.

6.1 Introduction

Laser-based modification of thermal barrier coatings, discussed in Chapters 4 and 5, consisted of material removal via laser ablation and melting and consequent solidification via laser heating. While the ultrashort pulse laser ablation used in our case removes material, it incurs little change to the remaining material. Laser melted topcoat, on contrary, changes the properties of the coating significantly, including mechanical, i.e. roughness, density, and Young's modulus, thermal, i.e. thermal conductivity of the coating, optical, i.e. material absorptivity and scattering.

As-sprayed topcoats consist of mechanically interlocked lamellar splats and provides internal porosity. High cooling rates during as-sprayed process, 10^6 K/s [327] to 10^8 K/s [287], and leads to fine microstructure, and the grain morphology in sprayed coatings is planar columnar. However, laser melting allows to change these characteristic parameters: as it was shown in Fig. 4.15, various grain morphologies may be achieved with pronounced dendritic morphology. Besides, some unusual solidification effects were observed. Fig. 4.18 b and d, where the vertical columnar grains are covered with horizontal, or in-plane, columnar grains, therefore significantly altering geometry of grain boundaries compared to typical columnar grains. This phenomenon will be referred to as "grain surface sealing". Moreover, the very grain geometry was found to change its shape in certain experimental conditions, presented in Fig. 6.1. Te experimental evidence shows the existence of grain inclination, i.e. the angle between Z axis and grain within the straight region, and grain bending, i.e. change of the grain boundary shape from a straight line to a curve.

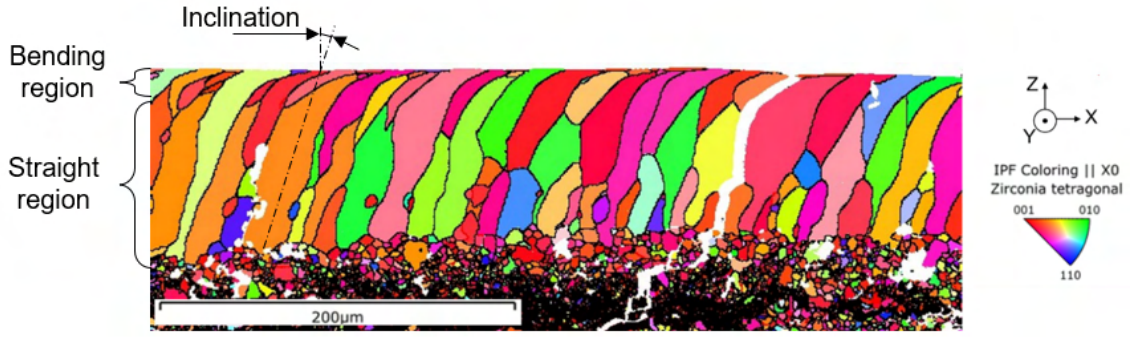


FIGURE 6.1: Grain inclination and grain bending in laser-melted YSZ observed in a transverse cross-section EBSD scan near the centre. Experimental conditions: SPI G3 laser, laser power 18W, scanning speed 2mm/s.

Such unusual behaviour has not been reported, and in general very few studies paid attention to microstructure formation of TBC upon laser melting. Nevertheless, laser processing is a continuously evolving field for tailoring surface properties of materials. Altering crystal structure allows tailoring specific application properties: fine equiaxed morphology to increase fatigue performance[283] and compromise creep lifetime[285], and columnar grains to exhibit longer times and higher creep strains[285]. Besides, the geometry of grain boundaries was found to influence crack propagation and fatigue properties in some research works[369]. Thus, the understanding of the microstructure, hence the properties, can allow tailoring the properties of the material in a way beneficial for a given application. While the importance of grain microstructure is well-recognised in metals, limited attention has been paid to grain formation in ceramic materials, including thermal barrier coatings.

To understand microstructural transformations within the grain region, the crystal growth kinetics must be taken into account. The change in the properties in the resultant coating was out of the scope of this work, instead, the goal of this chapter is to understand the following phenomena:

- Grain inclination;
- Grain bending;
- grain surface sealing.

Grain geometry can be studied experimentally, i.e. by direct analysis of the cross-section via EBSD mapping *post-mortem*, or predicted via mathematical modelling. While the experimental observation always provide with the "true" results of the process with given experimental conditions, such approach is resource-consuming and gives little understanding of the process. Modelling approach, instead, provides an idealised picture of the process with a number of assumptions and leads to certain inaccuracies as a direct result of considered assumptions. Such approach allows to directly observe certain parameters experimentally inaccessible, e.g. the shape of the molten pool and fluid velocity within the melt. At the same time, modelling approach allows to skip the experimental part and provide theoretical crystal structure as a result of laser melting with certain conditions, which may allow creating "microstructure by demand" for various materials. In order to understand the process and provide the ability to predict grain geometry and morphology, mathematical modelling approach will be used.

Generally, there are three major categories of methods for modelling the microstructure formations during the laser processing: Phase Field[32], Cellular Automation (CA) [270], [95], and Monte-Carlo[346] methods. The Phase-field method is the most accurate representation in terms of physical formulation incorporating the fine perturbations of the solid-liquid interface; however, phase-field is the most computationally intensive of all the approaches, limiting its application to small scales. Probability-based models, such as the Kinetic Monte Carlo method, which are based on grain boundary mobility [268], [228]; nevertheless, currently, it does not incorporate material texture. In this approach the representation of the physical model is limited, and the parameters are determined by experimental data. As such, CA approach is arguably the most popular technique for grain formation on large scales [248], [43]–[307]. The solution is based on calculating the length of an expanding octahedron, assigned to the cells at the solid-liquid interface. The octahedron approximates a growing dendritic crystal with 6 main growing axes, recognised for FCC and BCC materials. Currently, the most popular tool for predicting dendritic growth in CA models was

established by Gandin and Rappaz [84], i.e., an algorithm allowing for reducing the influence of the mesh on the grain propagation and became arguably. However, this approximation is valid only for the case of diffusion-limited aggregation in the undercooled melt [330]. Although it is known that this is not the only case of solidification, to the best of the author's knowledge, this assumption has been applied to all solidification models, limiting their application to dendritic mode only. At the moment, there are algorithms actively resolving dendritic growth which do not rely on decentred algorithm scheme. By actively solving the solute diffusion equation in the melt, it is possible to resolve the higher-order branching of the dendrites [118]. Due to computational complexity similar to phase-field models, these models are generally limited to 2-dimensional growth[116], [51], or growth of one/several dendrites in three dimensions[109].

Yet another approach was developed by Wei et.al. to predict the solidification microstructure of a solidified weld in pure aluminium on mesoscale [347], [346]. Based on the assumption that the direction of crystal growth is collinear with the local heat flow, the shape of the crystals was predicted with the aid of heat transfer and fluid flow model. Such an efficient approach, however, is valid only for the case of planar growth since the growth speed was defined by the laser. At the same time, growth in undercooled melts may not only be limited by the velocity of the melt pool. As it will be shown later, growth velocity can be much higher than the melt pool velocity when the solid-liquid interface perturbations develop into dendritic solidification[314], [13]. A similar approach was used in several works of Han et al.[115], [118], [116], and in one of them, the difference in solidification behaviour in pure Al and binary Al-Cu alloy was emphasised [117]. Dendritic growth of a binary alloy was found even at low welding speeds of 2mm/s due to solute segregation. At the same time, both growth mechanisms usually coexist simultaneously[162]. Different growth mechanisms in planar and dendritic growth dictate different solidification velocities and characteristic crystal shapes have an influence on crystal growth, and therefore the shape of the crystals and their orientation. In an effort to capture these phenomena and demonstrate the influence of specific growth conditions, a predictive model for combined planar-dendritic

growth is proposed in this work.

To date, CA dendritic growth models cannot capture the difference in planar and dendritic solidification, and a method to address these issues is proposed in this chapter. While the standard decentred octahedron algorithm represents an option for modelling a dendritic interface, there are no reports of a complementary planar interface modelling using the cellular automata approach. In order to explain and allow to predict the observed phenomena, cellular automata approach will be utilised due to its relative computational simplicity.

While the classical cellular automata approach fails to explain solidification in laser-melted TBC, a new computational method is proposed. The method considers the development of the dendritic interface, and the representative resolving the case of planar growth. With the aid of the model, we explain the grain surface sealing and grain bending phenomena, where the coexisting planar and dendritic solidification take place. In order to address this challenge, the following steps will be taken:

- *Theoretical background of the interface stability* will be analysed, which allows to distinguish between planar and dendritic solidification modes.
- *Modelling approach for combined planar – dendritic growth* will explain the particular method used to explain crystal growth. This will include the macroscopic thermo-capillary model, and microscopic grain growth model from the melt.
- *Influence of fluid flow on melt pool geometry* will be discussed
- The cases of *vertical columnar growth and horizontal columnar growth* will be analysed and distinguished, explaining the grain surface sealing effect
- *Morphology analysis* will be performed based on the thermodynamic characteristics at the solid-liquid interface, and its *influence on the crystal microstructure* will be discussed, allowing to explain why grain bending occurs in certain conditions and discuss the grain inclination angle within the straight grain region.

6.2 Theoretical background of the interface stability

The development of one of the morphologies is dictated by the heat input and its kinetic parameters, as well as the material properties. With regard to a compound of two or more components, 5 possible interfaces can be identified [201]:

1. *Mode 1. Full diffusional equilibrium*, when the phase compositions C are uniform, and the temperature gradient is zero.
2. *Mode 2. Interface equilibrium*, when the initial interface perturbations begin to develop due to Gibbs–Thomson effect
3. *Mode 3. Metastable interface equilibrium*, when the stable phase cannot nucleate sufficiently fast, and initial perturbation develops into cells.
4. *Mode 4. Interfacial non-equilibrium*, when the chemical potentials are not equal at the interface, and cellular perturbation develops into dendritic microstructures.
5. *Mode 5. Absolute interface stability,* when the interface becomes stable again at high solidification rate conditions.

As the driving force for solidification is the degree to which the liquid is undercooled, five types of solidification undercooling have been identified: kinetic undercooling, thermal undercooling, constitutional (solutal) undercooling, curvature undercooling, and pressure undercooling. In a two-phase material, the main driving force is usually constitutional undercooling [308], which occurs during the difference in melting points of the phases and redistribution of the solute in the liquid, and results in cooling a liquid is cooled below its melting point. In a simplified scenario, neglecting the influence of surface tension and fluid flow, liquid undercooling occurs when the liquidus temperature gradient at the interface is larger than the temperature gradient at the workpiece $\frac{\partial T_L}{\partial x} > \frac{\partial T}{\partial x}$, or

$$\frac{\partial T}{\partial x} < m_L \frac{\partial C_L}{\partial x} \tag{6.1}$$

where$\frac{\partial T_L}{\partial x}$ is the liquidus temperature gradient at the interface, m_L is the liquidus slope at the phase diagram, C_L is the concentration of Y_2O_3 in the liquid [173]. From Eq. (6.1) considering k as a partition coefficient defined as the ratio of concentration gradients of compound elements, G for the temperature gradient, R for velocity of the interface advance, or solidification rate, and D_L for thermal diffusivity of the liquid, the critical of the interface can be deduced as [173]:

$$\frac{G}{R} < \frac{m_L C_0 \left(k-1\right)}{k D_L} \tag{6.2}$$

where C_0 is the equilibrium concentration far from the interface. When the condition in Eq. (6.2) is met the interface is stable, and otherwise random perturbations can be amplified to cellular and dendritic morphologies. The $\frac{G}{R}$ ratio is often called the morphology factor and is a useful parameter describing the stability of the interface, shown in Fig. 6.2. High thermal gradients G and low solidification rates R result in indistinguishable undercooling and planar solid-liquid interface. With the increase of solidification rate R, liquid undercooling in the melt pool increases and the interface perturbations amplify, and result in cellular and later in dendritic morphology.

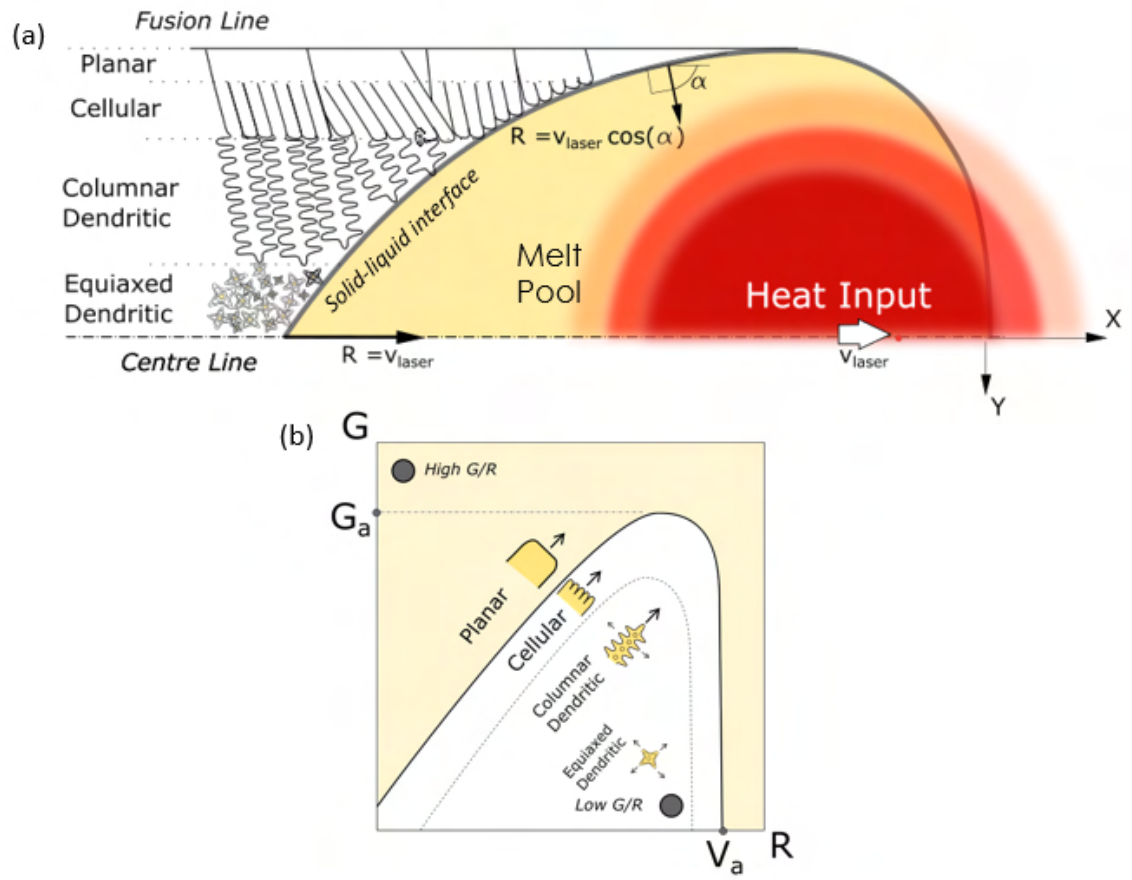


FIGURE 6.2: Possible crystal morphologies as a function of temperature gradient G and growth rate R (adapted from Kou[161] and Kurz[173]). While low scanning speeds generally result in planar solidification front, with a constant thermal gradient the solid-liquid interface stability becomes disturbed with increasing scanning speed. As a result, the grain growth in a cellular or dendritic manner, until interface velocity reaches the velocity of absolute stability V_a.

6.3 Modelling approach for combined planar – dendritic growth

When modelling the grain growth in the laser melting process, by far the most popular approach is decentred octahedron method, allowing to resolve grain growth in various two- and three-dimensional models on a large scale. When the assumption of dendritic growth is valid, it is possible to utilize existing models for the competition of columnar dendritic grains [43], [248] where the final orientation is dominated by the grains with easy growth directions. However, the models considering thermal undercooling without recalculations of front temperatures lead

to growth with a strong influence of grain orientation. Once the assumption of dendritic growth fails, the decentred algorithm can no longer represent the solid-liquid interface, since the growth mode is not limited by diffusion of adjacent liquid atoms[17], but rather by the velocity of the melt pool geometry. This, in turn, explains the straight grain boundaries, i.e. with no bending, formed during orientation competition in dendritic growth models[189], [183], which cannot capture the reality of possible grain curving.

Hence, in this work, a new and comprehensive method for capturing both growth modes, which can expand current models to capture grain bending (curving) and surface sealing with in-plane growing grains, is proposed and demonstrated on laser glazing of YSZ as a case study.

6.3.1 Thermo-capillary model details

To accurately model the solidified microstructure as well as the local thermodynamic parameters at the interface, i.e. temperature distribution, the melt pool shape, temperature gradient, and fluid motion in the molten pool of laser-glazed YSZ must be taken into consideration. Velocity magnitude in laser melting, induced by Marangoni convection, can reach the orders of mm per second [58] and effectively dominate the heat flow conditions from conduction to convection. In this study, a coupled heat transfer and laminar flow model was built to predict the temperature distribution accurately, schematically shown in Fig. 6.3. The semi-transparent nature of the coating material was taken into account by considering the Beer-Lambert law of absorption. The main assumptions of the thermal model are:

1. The fluid is Newtonian and incompressible;
2. Fluid flow is laminar;
3. The free surface of the fluid is flat;
4. Vaporisation is neglected.

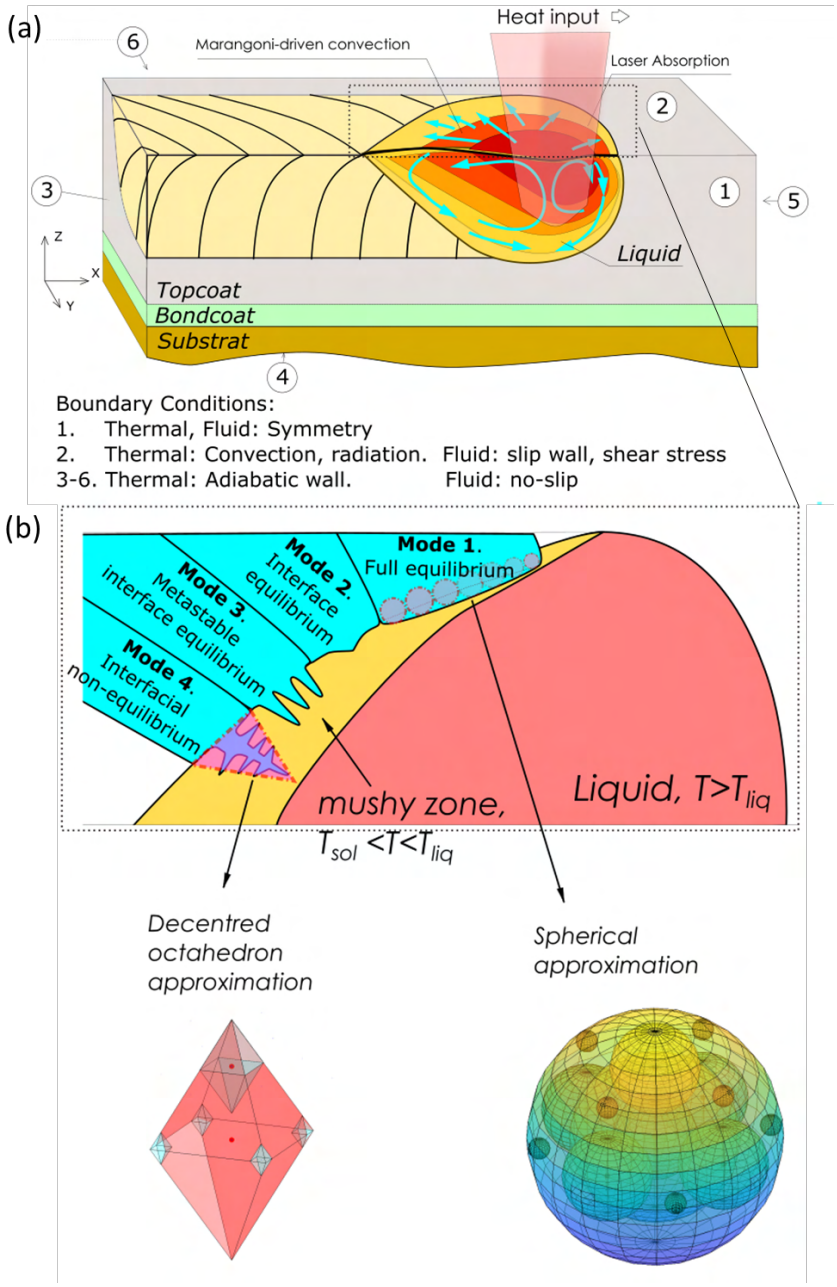


FIGURE 6.3: (a) Laser glazing process of the workpiece material: heat absorption, phase change, surface tension-induced fluid flow within the melt pool. Modelling phenomena and the boundary conditions. (b) Schematic top view of solidification process during laser melting, depicting grain evolution across the solid-liquid interface. The solidification rate experiences its maximum at the trailing edge of the melt pool and can lead to the loss of interface stability.

The energy transfer is modelled using the generalised energy law of energy conservation through the apparent heat capacity method [217], [156]:

$$\rho C_{app}\frac{\partial T}{\partial t}+\ \rho C_{app}\boldsymbol{u}\cdot\nabla T-\nabla\left(k_{th}\nabla T\right)=Q_{l} \tag{6.3}$$

Where ρ is the density, C_{app} is the apparent heat capacity, T is the temperature, $\boldsymbol{u}$ is the velocity vector, k_{th} is the thermal conductivity and the heat source term from incoming laser radiation is Q_l, Incoming laser radiation was modelled considering transparency in the layer via Beer-Lambert law[37]:

$$\begin{aligned}Q_{l}\left(z,t\right)=\left(1-R\right)\alpha\left(z\right)\exp\left(-\int_{0}^{z_{surf}}\alpha\left(z\right)dz\right)\cdot\\ \frac{2P}{\pi w^{2}}\exp\left(-\left(\left(\frac{x\left(t\right)-x_{0}}{w}\right)^{2}+\left(\frac{y\left(t\right)-y_{0}}{w}\right)^{2}\right)\right)\end{aligned} \tag{6.4}$$

Where R is the reflectivity of the coating (set to 0.2), $\alpha\left(z\right)$ is the absorption coefficient(1600 cm^{-1}[37]), $x\left(t\right)$ and $y\left(t\right)$ is the position of the centre of the laser beam, and w is the beam waist (0.2mm).

Heat loss through radiation and convection at the top surface are considered:

$$k_{th}\frac{\partial T}{\partial z}=h_{\infty}\left(T-T_{\infty}\right)+\varepsilon\sigma\left(T^{4}-{T_{\infty}}^{4}\right),\quad z=z_{surf} \tag{6.5}$$

where $h=10\ Wm^{-2}K^{-1}$ is convective heat transfer coefficient[99], emissivity ε is set to 0.8 [7], σ_0 is the Stefan-Boltzmann constant ($5.67\cdot10^{-8}\frac{W}{m^{2}K^{4}}$). The rest of the boundaries are considered adiabatic walls. The initial temperature of the material is set to $T\left(x,y,z,0\right)=293$ K.

Due to highly concentrated energy at the surface of the molten pool, high-temperature gradients occur at the top surface of the liquid. Typically, surface tension (γ) of the liquid decreases with increasing temperature, i.e. $\frac{\partial\gamma}{\partial T}<0$. Eventually, high-temperature gradients at the surface of the melt pool induce surface tension to generate shear stresses at the surface of the liquid, directed from the hottest point to the sides of the pool, where the liquid is cooler. This generates internal flow within the melt pool which, if this is of sufficient intensity, can

become a dominating heat transfer mechanism. This process is also known as Marangoni convection or thermocapillary convection[161].

The velocity of the fluid in the melt pool can be found by coupling the continuity and momentum equations, which can be written as[304], [40]:

$$k\frac{\partial \boldsymbol{u}}{\partial t} + \rho\left(\boldsymbol{u}\cdot\nabla\right)\boldsymbol{u} = \nabla\cdot\left(-pI + \mu\nabla\boldsymbol{u}\right) + \boldsymbol{F} \tag{6.6}$$

where p is pressure, $\mu\nabla\boldsymbol{u}$ represents the viscous stresses, and $\boldsymbol{F}$ are the external forces (gravity and surface tension, activated at the top surface).

The top surface boundary is considered as a slip wall $\boldsymbol{u}\cdot n = 0$ and is subjected to thermocapillary induced shear stresses $\sigma_{th} = -\gamma\nabla T,$. A standard way to numerically implement these stresses at the slip wall is done by introducing a volumetric force $\boldsymbol{F}_{\psi}$ acting at a thin subdomain with thickness ψ, producing the same amount of shear force[24]. Therefore, the boundary condition is implemented as:

$$\boldsymbol{F}_{\psi} = -\frac{\gamma}{\psi}\nabla \tag{6.7}$$

The rest of the boundaries have a no-slip condition $\boldsymbol{u} = 0$.

Temperature-dependent properties are assumed in the model, shown in Fig. 6.4. The model consisted of three layers, i.e. substrate, bondcoat, and topcoat. Navier-Stokes equations (A4)-(A5) were solved for the topcoat region only since no phase change occurs in the underlying layers. To suppress flow in the solid-state, dynamic viscosity of the media in solid-state μ_s was set to 10000 Pa·s. The model was meshed with tetrahedral elements with a maximum element size in the topcoat of 20 µm. The total width of the model (Y dimension) was 3mm, and the thickness of the layers was 300 µm, 150 µm, and 3000 µm for the topcoat, bondcoat, and substrate, respectively. Due to increasingly large length to depth ratios of the melt pool for high scanning speeds, the length of the modelled region was varied for each speed case. The length was taken for 5 mm. The governing equations for thermal and fluid models were

solved in a moving reference frame using the finite element method as provided by commercially available COMSOL Multiphysics 5.5 by fully coupling Non-isothermal Flow and Heat Transfer in Liquids[217].

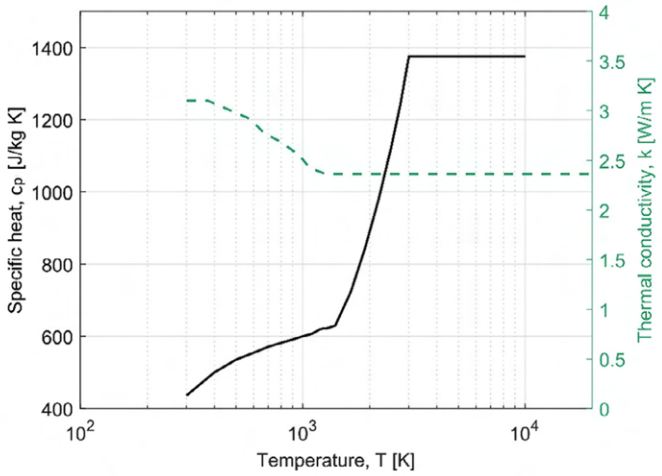


FIGURE 6.4: Specific heat and thermal conductivity of YSZ [37]

Once the thermal field is established, i.e., the shape of the melt pool has ceased to increase, it is assumed to be the same for the whole duration of the process. Then one-way coupling was used to couple the heat transfer and cellular automation models. However, as one-way coupling does not capture enthalpy changes due to grain growth and solidification, the FE was also employed to calculate the latent heat release induced by solidification explicitly through the apparent heat capacity method [37]. It should be noted that such approximation induces some level of errors on the thermal field and the melt pool, and therefore on the local solidification rate R and thermal gradients G.

6.3.2 Grain growth model of laser glazing of YSZ

A relatively coarse mesh used in the heat transfer model is bilinearly interpolated on a fine mesh with a constant step size dx of 3 µm. The space is initially assigned with the orientation of the crystals represented by Euler angles. To achieve an accurate representation of orientation, initial orientation was taken from an EBSD map of as-sprayed material. While the average grain size of the real grains with the mean value of 0.25 µm was smaller than the step size of the mesh (3 µm), the points

corresponding to the initial map were randomly mixed within the matrix and were used to fill the 3D space of the CA model.

Nucleation model

Several mechanisms of grain nucleation are possible: fusion boundary nucleation, epitaxial nucleation, and bulk nucleation ahead of the solidification front. In the sets of experiments, epitaxial growth was found to be the dominating mechanism for grain nucleation in laser melting. Although some level of equiaxed grains were found in the set of experiments, bulk nucleation in the undercooled liquid was neglected for numerical simplicity.

Epitaxial nucleation was implemented with a constant rate of nucleation[307], [214]. The space within the region $T_{sol} < T < T_{liq}$ was assigned with random nucleation probability $P \in [0, 1]$. The space within the undercooled melt is assigned to critical nucleation probability $P_{cr} = N \cdot (dx)^3$, where N is nucleation rate (taken for $10^{13} \frac{1}{\mathrm{m}^3}$). The points with nucleation probability $P > P_{cr}$ were subjected to nucleation. The cells ever experienced melting, i.e. when $T > T_{liq}$, were not subjected to nucleation and removed by storing an additional Boolean matrix $T > T_{liq}$.

Mesoscopic dendritic and planar growth model

As it was shown in Section 2, the development of the grain structure can depend on the local parameters within the solid-liquid boundary. The presented model combines two modes of development of grain structure: dendritic and planar growth, schematically shown in Fig. 6.3. The grain growth in dendritic mode is limited by the rate of the forward reaction, i.e. the rate at which atoms can join the solid [18], which is site-specific for most of the crystals[323]. This is the basic mechanism for orientation selection in competitive dendrite growth that can be captured by the dendritic growth model.

At the same time, the growth rate is limited by the velocity of the solid-liquid interface, and therefore the growth velocity is not limited by diffusion. This happens when the interface of the solid-liquid interface is planar, according to Eq. (6.2), the

solid-liquid interface can be split into planar and dendritic interfaces, and the growth modes should be treated differently. The approach proposed below allows resolving two growth modes simultaneously.

Dendritic growth model for tetragonal crystals

Due to the high computational costs of resolving dendrite branching, large-scale models are usually limited to approximating growing dendrite by some shape, typically an octahedron in three dimensions (e.g. [271], [307]). An octahedron represents the shape of a freely expanding crystal in the undercooled melt, particularly clear in the work of Mohebbi and Ploshikhin [214]. To reduce the influence of the mesh, a decentred octahedron scheme is widely accepted [84].

In decentred octahedron approximation, the crystal is free to expand in the mushy zone, and its growth velocity is defined by the level of liquid undercooling. As stated before, five types of undercooling can be distinguished, namely thermal, constitutional, curvature, kinetic, and pressure undercooling[173]. The majority of three-dimensional cellular automata models consider thermal undercooling only [307], however constitutional and curvature supercooling is often calculated [214]. To avoid calculation of solute diffusion equation, only thermal undercooling was considered, $\Delta T = T_{liq} - T^*$, *w*here T^* is the temperature of the cell obtained from eq. (6.8). Lipton-Glicksman-Kurz (LGK) model is widely used to relate the dendrite tip velocity (v_d) to local undercooling, and analytical approximation of dendrite tip velocity was used [307]:

$$v_d\left(\Delta T\right) = \mathrm{A}\cdot\Delta T^{2.5} \tag{6.8}$$

Where A is the dendrite growth velocity, which can be found as:

$$A = \frac{D_l}{5.51\pi^2(-C_0 m_l\left(1-k\right))^{1.5}\Gamma} \tag{6.9}$$

The length of the half-diagonal (L) of the octahedron at the time t' can be found as:

$$L(t') = \int_0^{t'} v_d\,(\Delta T)\,dt \tag{6.10}$$

The process is implemented by using decentred octahedron scheme (Fig. 6.3). Typically, FCC and BCC crystals are modelled by CA. In the case of YSZ, the grain structure upon solidification is tetragonal with a c/a ratio close to $\sqrt{2}$. Based on the work of van der Drift [323], the growth for t' YSZ crystal is an elongated octahedron. Numerically, this can be implemented by calculating the vertices of the octahedron *C6* and multiplying them by a rotation matrix with corresponding Euler angles:

$$C6 = \begin{pmatrix} a & 0 & 0 \\ 0 & a & 0 \\ -a & 0 & 0 \\ 0 & -a & 0 \\ 0 & 0 & c \\ 0 & 0 & -c \end{pmatrix} \cdot R_{ZYX} + P$$

Where R_{ZYX} is rotation matrix in three dimensions, P is the coordinate of origin point, a and c are the lattice parameters of the crystal (3.605Å and 5.18Å respectively [129]). Then, the vertex coordinates undergo Delaunay triangulation. Together with the coordinates of the neighbouring points, this allows checking if the point is inside the enclosing simplex within any given shape. Once the neighbour is inside the octahedron, its new coordinates are calculated according to the typical decentred algorithm procedure.

Planar growth model for the representation of the stable interface

To capture grain growth independent of its orientation, a spherical approximation of the growing element is proposed. Firstly, this ensures that the grain growth is independent of its preferred orientation. Physically, this means that the adsorbed atoms have no preference where they will land since all the possible states in the

crystal will be filled, until the interface with liquid (growth of initial seed in a planar manner is shown in Fig. 6.3).

The growth velocity, in this case, is equal to the solidification rate R, which can be found as a projection of the laser scanning speed vector to the solid-liquid interface. Since the solid-liquid interface is a surface of equal temperature, the temperature gradient vector $\overline{\nabla T}$ is perpendicular to the interface. Therefore, the planar growth velocity can be expressed as:

$$v_{planar} = R = \frac{dot\left(v_{laser}, \overline{\nabla T}\right)}{\left|\overline{\nabla T}\right|} \tag{6.11}$$

where v_{laser} is the scanning speed vector of the laser, and $\left|\overline{\nabla T}\right|$ is the L^2 norm of the vector. Similarly to Eq. 6.10, the length of the sphere representing planar grain can be found as follows:

$$L(t') = \int_0^{t'} v_{planar}\left(\nabla T\right) dt \tag{6.12}$$

Besides, the growth algorithm based on expanding spheres is far less computationally expensive than the decentred octahedron algorithm. The capturing condition, in this case, is simply $L - (N - O) > 0$, and the new length $r^{t0} = L - (N - O)$. This approximation does not include matrix products and can be easily vectorised.

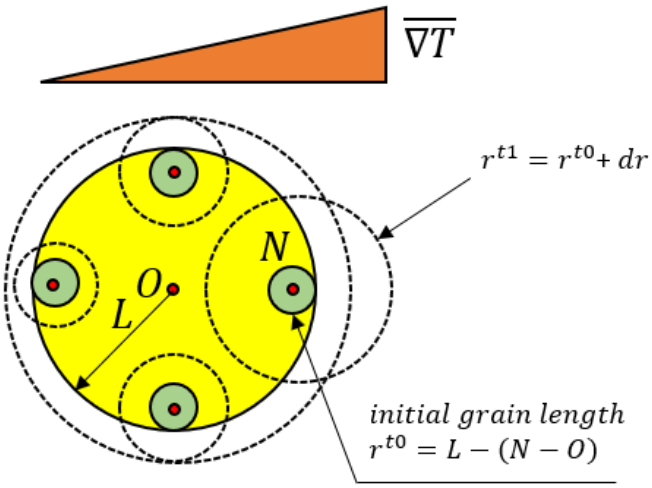


FIGURE 6.5: Schematic representation of planar grain growth algorithm in variable heat flow conditions

However, the growth process is also dependent on the mesh. Two neighbouring points representing different crystals will preferably propagate parallel to the chosen coordinate system. The shape of the real solid-liquid interface in the point connecting two planar grains and the liquid zone is different and can be influenced by capillary effects [312]. In this study, grain mobility is increased by changing the initial length of the cells at grain boundaries to zero, and the length of their neighbours to half of its initial length each time the interface is shifted.

Coupling method for planar and dendritic models

Once the nucleation process has passed, each nucleated cell (active cell) is assigned with its growth rate R and mean thermal gradient value $\left|\overline{\nabla T}\right|$. The ratio $\frac{\left|\overline{\nabla T}\right|}{R}$ is compared with the critical G/R ratio, which can be obtained from Eq. (6.2), and the active cell is assigned to either dendritic or planar growth modes. The velocity of the grain is calculated according to (6.8) or (6.11), and the following procedure of checking the neighbouring cells is performed according to the growth mode. To define the cells around the active cell, the first Moore neighbourhood is used in this study, consisting of 26 neighbouring elements in 3-dimensional space [248]. The model flowchart is presented in Fig. 6.6.

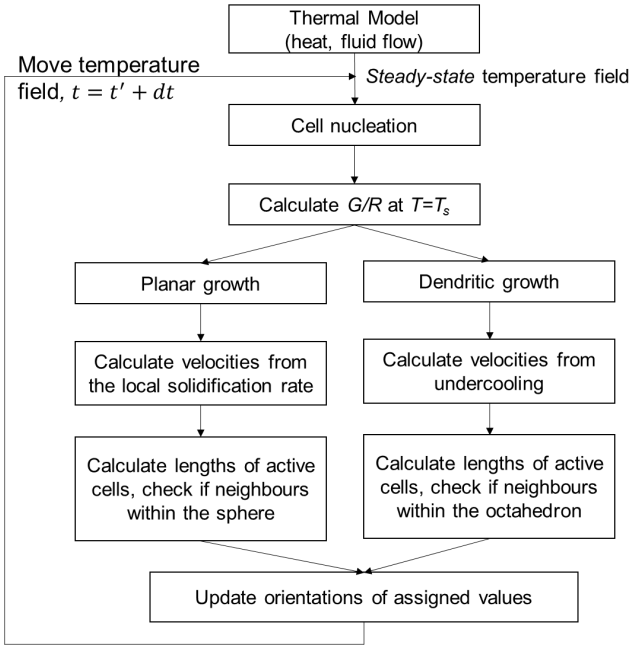


FIGURE 6.6: Flowchart of grain growth modelling using combined planar-dendritic cellular automata route.

6.4 Experimental Methods

To validate the proposed modelling process, a laser glazing of the TBC topcoat has been experimentally conducted by observing its microstructure formation. For this, a Ni-based superalloy Nimonic C263 was coated using an F4-MB plasma torch (Oerlikon-Metco) with commercially available powders for bondcoat (Co-32Ni-21Cr-8Al-0.5Y) and topcoat (7-8wt%Yttria Stabilised Zirconia, YSZ) via atmospheric plasma spraying (APS) process. For the laser glazing process, a single-mode Yb-doped CW fibre laser (SPI RedPower SP-100C, 1090nm wavelength) was used to melt the surface of TBC. After initial pre-optimisation of the process parameters to achieve a continuously remelted dense layer with an acceptable level of damage, the optimal power density of the laser was found to be 79,6 kW/cm^2. The laser power P at the workpiece and laser beam diameter d were fixed to 100W and 0.4 mm, respectively. To achieve various geometries of the melt pool, the scanning speed v was first varied between 0.5 mm/s and 300mm/s. In these conditions, the maximum scanning speed providing a continuous remelted layer was found to be 100 mm/s with an energy density of 250 J/cm^2, calculated through $E_p = \frac{P}{vd}$. To capture different grain morphologies, scanning speed was

then set to 2.5mm/s and 25 mm/s, which corresponds to energy densities of 10000 J/cm^2 and 1000 J/cm^2. After laser treatment, the samples were analysed with optical microscopy (Nikon), and the Nomarski prism was used to capture the small heigh variation of the dendritic structures. The curved surface of remelted tracks was analysed using a scanning electron microscope (SEM, Quanta Q650) in backscattered (BS) electron mode to capture the contrast between grains with different orientations. For image measurements, ImageJ software was used.

To reveal the crystal structure of the solidified material, samples were cut longitudinally near the middle of the remelted line, and then mechanically ground and polished to be in close proximity of the middle of the track. The cross-sections were analysed with electron backscatter diffraction (EBSD, Oxford Instruments). Prior to EBSD analysis, polished cross-sections were coated with a 10nm layer of carbon due to the non-conductive nature of YSZ, which reduces sample charging. Obtained EBSD maps were analysed with the aid of Oxford Crystal software.

6.5 Results and Discussion

6.5.1 Influence of fluid flow on melt pool geometry

Fluid motion within the liquid can affect the melt pool geometry significantly. Thermocapillary forces arising from the temperature gradient at the surface of the melt pool induce the flow of the liquid, creating a convective flow within the melt. While it is common to neglect the fluid flow due to its relatively low impact on the geometrical size of the melt pool, its impact on the *shape* of the interface can be significant, as shown in Fig. 6.7a. On the other hand, high energy density can lead to developed flow, reaching 45 mm/s when the energy densities of 10000 J/cm^2, which can further decrease to 0.1mm/s at 250 J/cm^2. To understand the impact of fluid flow within the liquid on the heat transfer in the workpiece, dimensionless groups can be used. Peclet number shows the ratio of convective and diffusive heat transport, defined as:

$$Pe = Re \cdot Pr = \frac{\boldsymbol{u}L}{\lambda} \tag{6.13}$$

where Re is the Reynolds number, Pr is the Prandtl number, $\boldsymbol{u}$ is the fluid velocity, L is characteristic length, and λ is thermal diffusivity defined as $\lambda = \frac{k}{\rho C_p}$, k is the thermal conductivity. Pe can also be calculated as a product of Reynold's number Re and Prandtl number Pr. The highest ratio of convective to diffusive heat transport was found at the trailing side of the melt pool, reaching 35% in the case of the highest energy density case, 10000 J/cm^2, shown in Fig. 6.7b. Then, the ratio of convective heat transfer to the combined heat transfer is 26%.

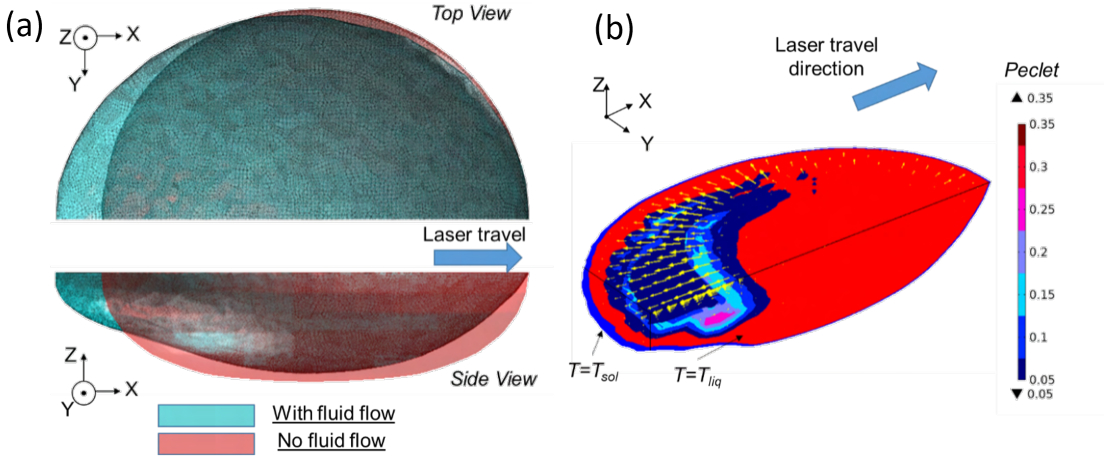


FIGURE 6.7: (a) Geometry of the melt pool with and without fluid motion within the pool. (b) Peclet distribution within the melt pool. Velocity vectors are shown in yellow. Energy density 10000 J/cm^2.

As a consequence, the developed fluid flow can change the semi-circular shape of the melt pool (red surface, Fig. 6.7a) to a droplet-like shape with a mostly straight trailing edge, curving to a nearly vertical boundary at the surface (cyan surface, Fig. 6.7a). Local spilling motion of the liquid, i.e., vorticity, is the highest at the trailing side of the pool, attributing to the elongation of the melt pool and straightening of its trailing edge.

Direct validations of the shape of the melt pool in-depth present a major difficulty. Instead, post-mortem EBSD scans of the solidified track will be presented. Assuming the solid-liquid interface is planar, instead of a continuous grain curling which could

be expected for a semi-spherical melt pool, the crystals were found to bend towards the direction of the scanning speed near the surface, as shown previously in Fig. 6.1.

6.5.2 Vertical columnar growth and horizontal columnar growth

In the set of experiments, unusual behaviour of grain growth was observed, as presented in Fig. 6.8a-d, which shows normal unidirectional vertical crystals, and long directed crystals, covering the surface of vertically grown crystals (also presented in a cross-cut in Fig. 6.10c). To reveal small fluctuations of the surface, Nomarski microscopy was used. In transparent samples, it is possible to gain the optical path information, where two orthogonally polarised beams are recombined through two birefringent wedges before observation. The varying optical density of the sample at peaks and valleys of a non-flat sample changes the apparent colour of the sample.

In high energy density conditions (Fig. 6.8a-b), the grains appear planar. The optical micrograph in Fig. 6.8a is brighter in the middle of the track due to the high curvature of the solidified track; a magnified image of the region in the red box is presented in Fig. 6.8b, where grain contrast was achieved by using backscattered electron image, sensitive to the density of the sample. For a tetragonal crystal, the apparent density of grain depends on its orientation as a consequence of varying packing density in different crystallographic directions. The smooth top surface suggests that the grain morphology remained planar in this case.

In decreased energy density conditions (Fig. 6.8c-d), the laser scanning speed increased from 2.5 to 25 mm/s. This, in turn, affected the local solidification rate, and the loss of interface stability is clear. 4 regions can be distinguished: (1) the planar region at the sides of the track, which transforms to a narrow (3) cellular mode and later to (3) dendritic mode (Fig. 6.8d). These groups are noted as *in-plane* to emphasise the elongation direction. The last group, *vertical* dendritic grains, is a clearly visible 180 µm wide region in the middle of the track. According to the experiment, this region has solidified above the median surface of the track mode

(Fig. 6.8c). Competition of the grain orientation is present in the dendritic zone in Fig. 6.8d, where the grain boundaries become bent instead of growing linearly.

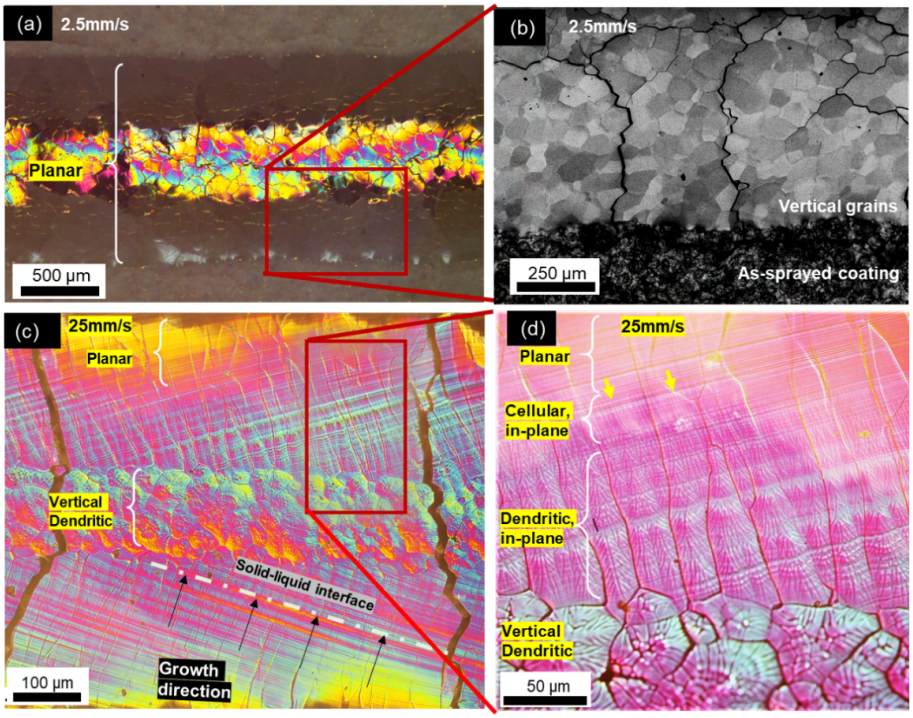


FIGURE 6.8: Micrographs of the top surface of the single track laser glazed thermal barrier coating at different laser scanning speeds: (a) 2.5mm/s, x5 magnification; (b) magnified backscattered SEM image of a marked region in a red box is shown in (a); (c) top surface of remelted track with a scanning speed of 25mm/s, x20 magnification and (d) x50 magnification of red box shown in (c).

By separating the current solid-liquid interface into planar and dendritic groups, and using the combined planar-dendritic cellular automata model, it is possible to capture different growth kinetics in diffusion-limited aggregation and interface-limited aggregation. In the case of a low solidification rate, all the interfaces remained planar, as will be demonstrated later. Grain solidification was captured entirely by the spherical growth algorithm, described in the previous chapter. The peculiar difference of the spherical approach is the unidirectional growth of the active cell representing the crystal front. Its growth velocity is the same as the rate of interface advance R and ensures that the whole interface shifts at the same rate and with no perturbations. In fact, this means that no competition among grains with different orientations is possible, and the growth is orientation-independent. Since the nucleated growing crystal inherits its original

orientation, the resultant texture of the solidified track repeats the original texture of the base material.

The predicted top surface reveals the grains are equidirectional with increasing grain size towards the centre (Fig. 6.9 a). Experimental results suggest that the grains are equidirectional however, the grain size in the middle of the track is similar to that at the sides. This difference arises from the assumption of a flat liquid surface in the thermal model. Due to the curved shape of the top surface, depressed in the middle (Fig. 6.8a), crystals reach the surface of the liquid sooner than the time predicted by the model. In the case of a combined planar-dendritic growth, happening with the energy density of 1000 J/cm^2, the grains undergo elongation towards the centre of the melt pool. The results are captured by the combined model, and the elongated dendritic grains found in the experimental results are also present in the predictions Fig. 6.9b. Besides the in-plane elongation, the model predicts the vertical dendritic grains in the middle with no elongation with a similar width of 200 µm Fig. 6.9b.

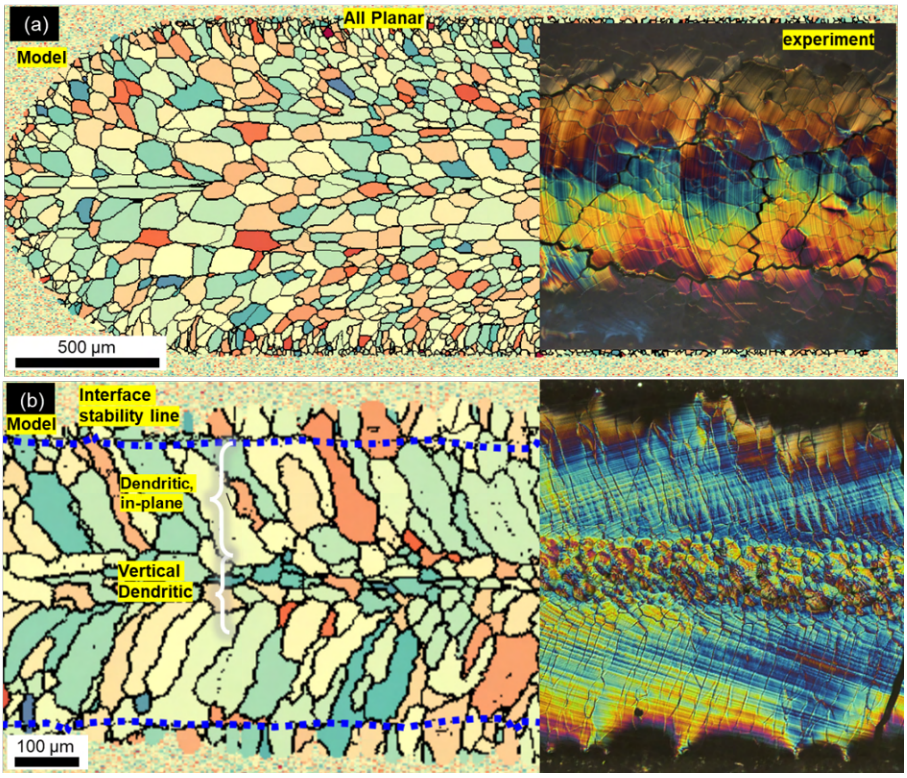


FIGURE 6.9: Top view of modelled and experimental grain structure for scanning speed of (a) 2.5mm/s and (b) 25mm/s.

It is worth noting that the in-plane grains (Fig. 6.8c-d) covered most of the surface

from the sides to the middle region with vertical dendritic grains, whereas in the case of planar growth the grain length is direction-independent. Here, an interplay of different phenomena occurs, which results in in-plane growing elongated grains. There can be at least two possible reasons for the in-plane columnar growth, "sealing" the remelted region. Firstly, convective and radiative heat transfer at the surface leads to an increased cooling rate at the surface. That is, when material solidifies in the bulk, the temperature decreases through conductive heat transfer. Due to a high melting point of zirconia (2680 ^{o}C [190]) and rather low thermal conductivity coefficient ($\sim$2 W/(Km)[117]), convective and radiative heat transfer plays a significant role in heat transfer. Gains at the surface, experiencing convective and radiative heat transfer in addition to conduction, have a higher heat loss (Fig. 6.10, a). Higher heat loss eventually increases the cooling rate, which gives the initial advantage in growth velocity at the surface even while morphology remains planar. Therefore, the grains at the side of the melt pool win the competition with the underlying vertical grains. Secondly, when the in-plane grain progresses towards the middle of the interface, the local solidification rate increases, breaking interface stability. Once the ratio between thermal gradient and solidification rate exceeds the critical value, the growth speed of the crystal is no longer limited by the solidification rate, and the grain undergoes dendritic growth. The growth of dendritic grains is not confined by the solidus line and the crystal progresses into the mushy zone, closing the underlying vertical grains (Fig. 6.10a, c). Somewhat similar results are often presented in the welded microstructure of metals, however, the underlying mechanism and microstructure are different. In the case of combined planar-dendritic growth, the cross-section consists of mostly vertical columnar grains. Metallic welds, in contrast, tend to grow towards the centre of the weld in the whole volume of the weld [43].

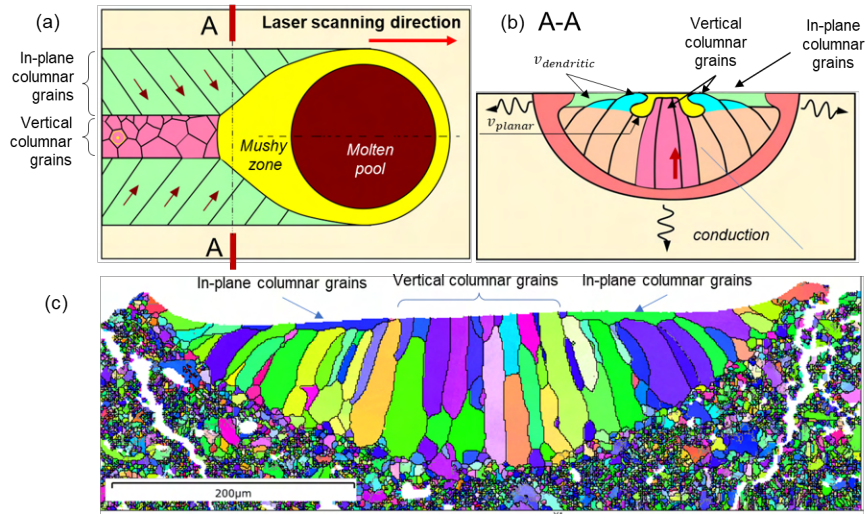


FIGURE 6.10: Illustration of the evolution of horizontal, vertical grains and grain surface sealing concept. (a) the top surface of the melt pool and solidification, indicating in-plane, or horizontal, columnar grains, and an area with vertically grown grains. (b) the cross-sectional sketch view. (c) EBSD of the transversal cross-section of track presented in Fig. 6.8c, showing vertical columnar grains and in-plane (horizontal) columnar grains.

6.5.3 Morphology analysis and its influence on the crystal microstructure

To further understand the behaviour of the melt pool, initial properties of the solid-liquid interface were analysed in terms of the thermal gradients G and solidification rate R, calculated as the projection of laser scanning speed on the normal to the interface. From Eq. (6.2), the critical morphology factor G/R is $2.4 \cdot 10^9 \frac{Ks}{m^2}$, dividing the solid-liquid interface into planar and dendritic groups, is presented in Fig. 6.11. In both analysed conditions, both solidification rate R and morphology factor G/R are highest at the trailing edge of the pool near the surface. In the case of high energy density input, 1000J/cm^2, the maximum solidification rate is 2.2 mm/s, which is close to the scanning speed of the laser (2.5 mm/s) due to a nearly vertical solid-liquid interface at the trailing edge. Minimum morphology factor of $3.7 \cdot 10^9 \frac{Ks}{m^2}$ (Fig. 6.11a-b) is higher than the critical value, and therefore no transition to dendritic solidification is present (Fig. 6.8a). The melt pool becomes elongated when the scanning speed is increased. In the case of the energy density of 100J/cm^2, the maximum solidification rate is 10.4 mm/s,

more than twice smaller than the corresponding laser scanning speed of 25 mm/s (Fig. 6.11c). The minimum morphology factor at the interface of $3.7 \cdot 10^8 \frac{Ks}{m^2}$ is smaller than the critical value of planar-dendritic transition, and the division line is shown in Fig. 6.11d. The interface, separated into planar and dendritic grains in Fig. 6.11f, suggests that the interface is perturbed in a nonlinear manner (also seen in the loss of interface stability line in Fig. 6.11d). Effectively, the crystals close to the surface begin exhibiting dendritic growth sooner than the underlying crystals and resulting in a higher rate of interface advance. This explains the occurrence of the top surface "sealed" by the elongated grains (Fig. 6.10c).

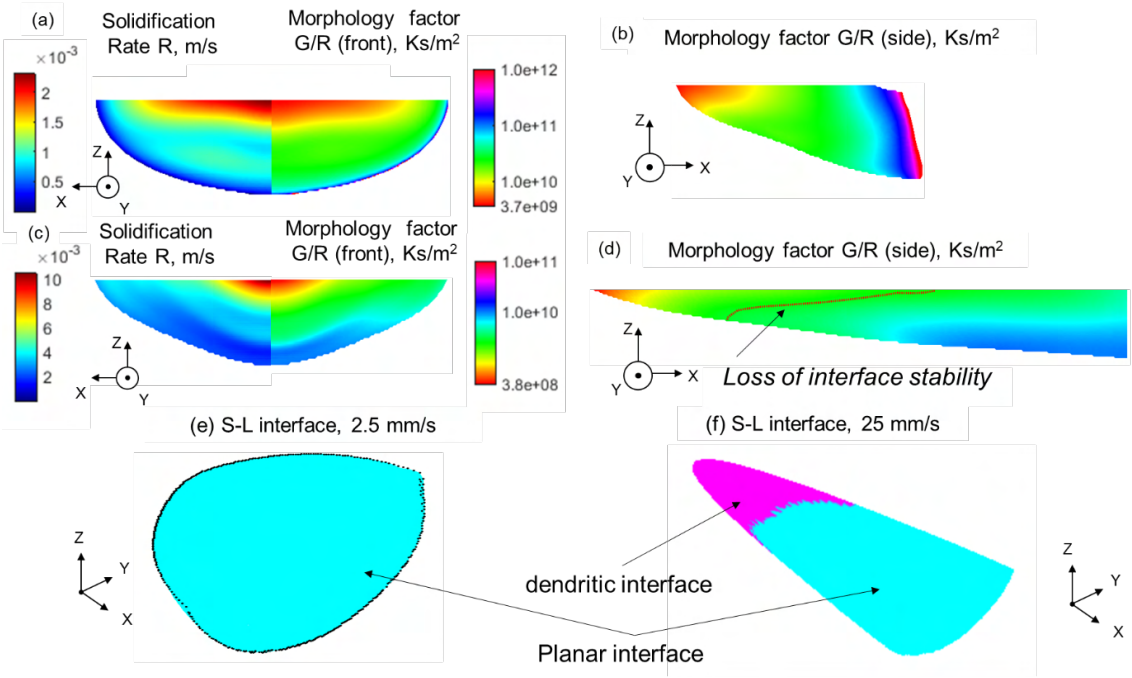


FIGURE 6.11: Predicted solidification rate and morphology factor for scanning speeds (a-b) 2.5 mm/s and (c-d) 25mm/s; (e-f) stability of solid-liquid interface. Colorbars of morphology rates are shared for (a-b) and (b-c).

Predicted grain geometry and orientation with its average misorientation from the Z axis are shown in Fig. 6.12. In the different sections shown in Fig. 6.12a mostly vertical growth behaviour is recognised. Mostly low misorientation angle is the result of the initial orientation of thermally sprayed coating, and no grain competition is detected. This matches well with the results of Han for pure metals [117] where planar solidification was assumed.

In the condition of higher solidification rates, the growth type changes drastically due to the presence of dendritic growth. The transversal cross-cuts, presented in Fig. 6.12b, suggest that initially planar growth at the solid-liquid boundary results in grain growth perpendicular to the solid-liquid interface. Grains with dendritic morphology, illustrated in a different colour scale, become elongated at the top surface. Growth of the crystal underneath the dendritic grain is suppressed due to the presence of a solid at the surface. While no evidence of such solidification behaviour was found in the literature, the modelled grain boundaries match well with our experimental results (Fig. 6.10c and Fig. 6.8c).

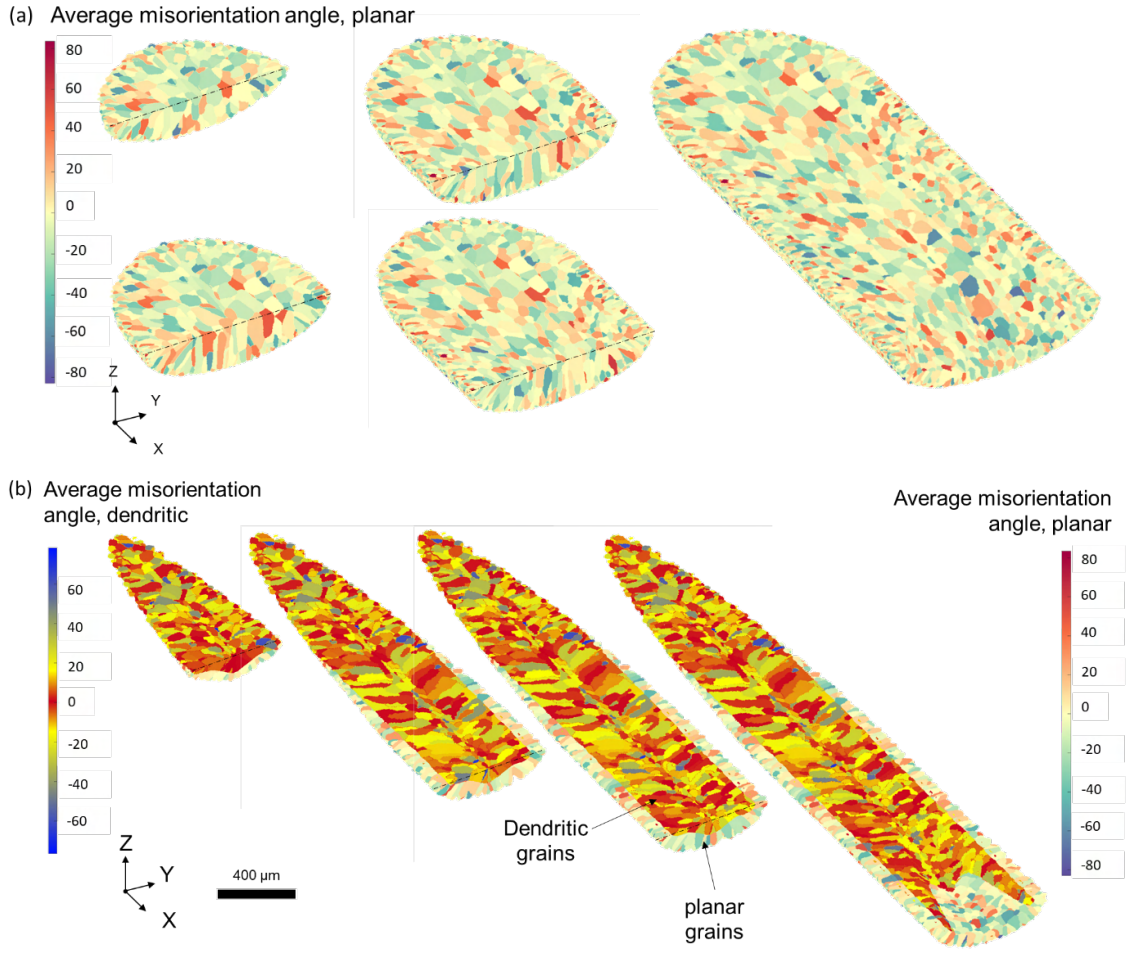


FIGURE 6.12: Grain evolution for (a) high energy density case (1000 J/cm2) and (b) moderate energy density case (100 J/cm2)

To validate the model, longitudinal cross-sectional cuts near the centre of the track were subjected to EBSD analysis. An obvious grain bending near the top surface is present, and the inclination of crystals is shown in Fig. 6.13b. The experimental

average inclination angle of the solidified track is 24^o, which is close to that obtained by the model (20^o, measured by bisecting the grains in both cases). The inclination of the grains is governed by the angle between the trailing edge of the melt pool and the heat source direction. The simulated melt pool, previously shown in Fig. 6.7, has a nearly linear trailing edge with an inclination angle of 21^o, as measured from the perpendicular axis. An obvious grain bending is present at the 50 µm thick surface layer (Fig. 6.13b) and was effectively captured by the proposed spherical growth algorithm (Fig. 6.13a). This effect is attributed to the change of the trailing edge from linear to semi-spherical (Fig. 6.7). The changing geometry of the solid-liquid interface affects the local solidification rate, i.e., grains closer to the surface are more aligned with the solidification direction and can propagate further.

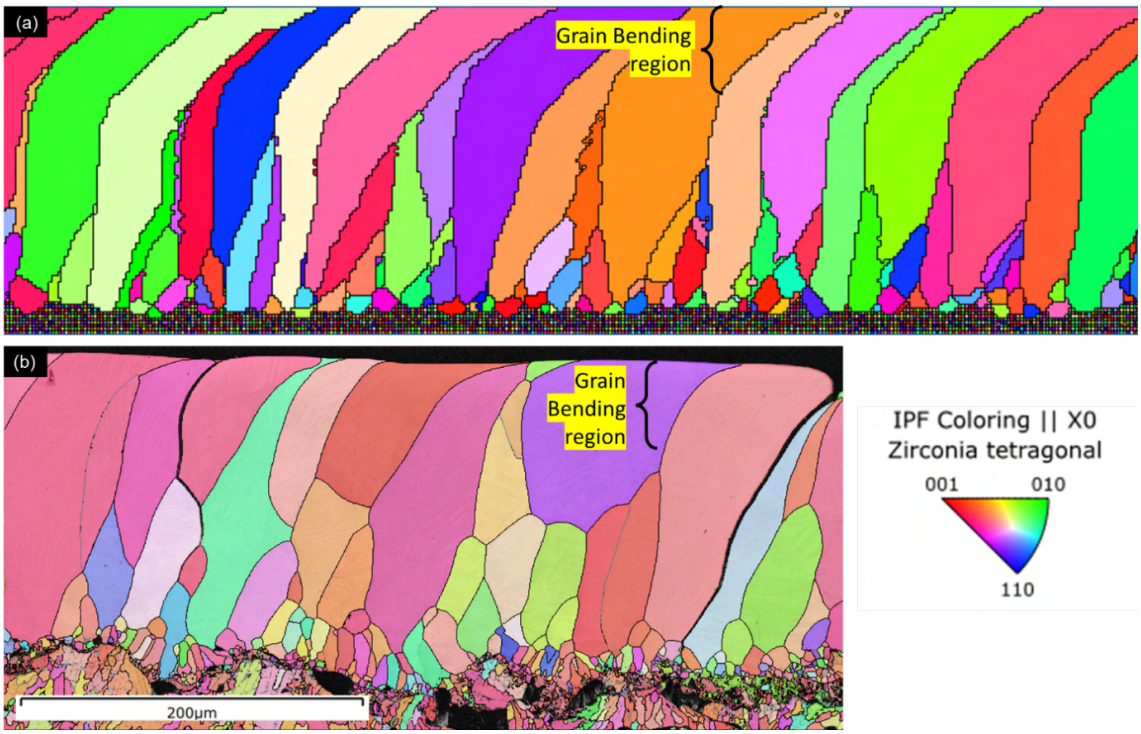


FIGURE 6.13: Grain boundaries and orientation map in longitudinal cross-sections (a) simulated microstructure; (b) EBSD scan. The corresponding energy density is 1000 J/cm^2.

Similar cross sections for a higher scanning speed (25 mm/s) are presented in Fig. 6.14. Compared to previously shown results with higher energy density input, the inclination angle has decreased, and new grains are present near the top surface in the experiment (Fig. 6.14b, indicated as competing grains) and can be predicted

by the proposed model (Fig. 6.14a). Since this is the region of dendritic solidification, the formation of this grain morphology can be attributed to the orientation-dependent growth near the top surface.

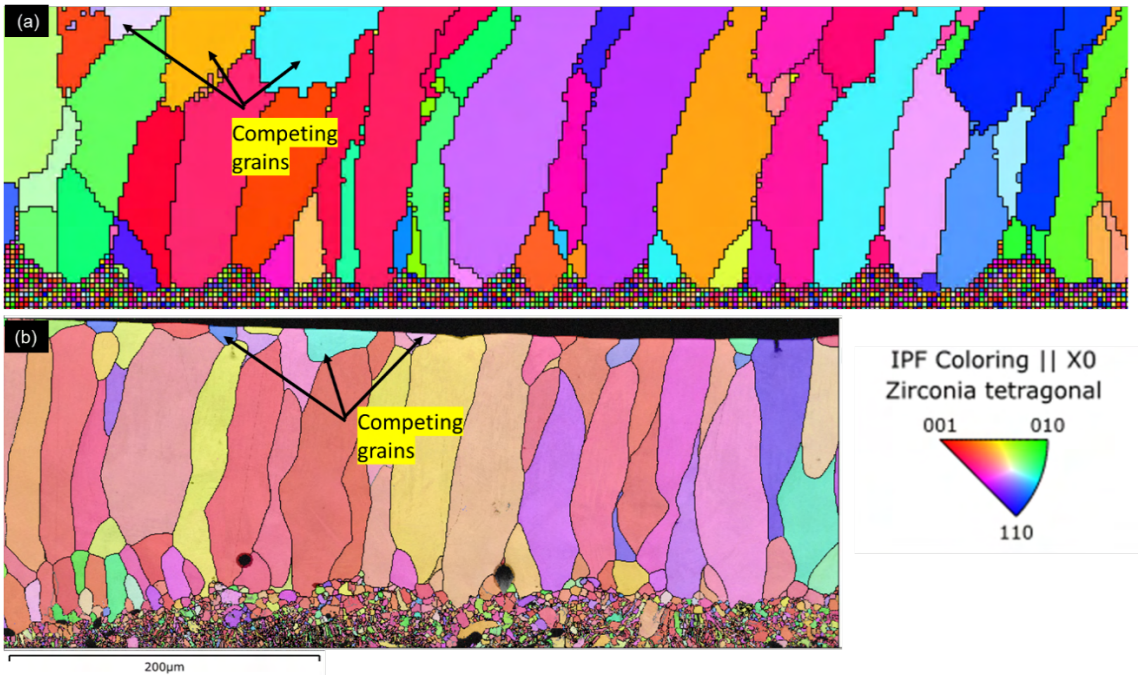


FIGURE 6.14: Grain boundaries and orientation map in longitudinal cross-sections (a) simulated microstructure; (b) EBSD scan. The corresponding energy density is 100 J/cm^2.

6.6 Summary

In this chapter, the grain formation mechanism in the laser glazing of YSZ has been studied. Various grain morphologies were observed in the laser-melted zirconia, including planar, cellular, and dendritic morphologies. It has been observed that the dendritic growth of laser-melted YSZ significantly affects the resultant microstructure and is responsible for grain surface sealing, reported for the first time. The grain inclination in the whole volume of solidified material was also found, and crystal bending was observed at the surficial layer when the crystals grow with a planar interface. To understand the grain formation mechanism a combined model enabling resolving diffusion-limited agglomeration, i.e., dendritic growth, and interface limited agglomeration, or planar growth is developed based on the Cellular Automata approach. The physical-based 3D

Cellular Automata-Finite Element model can resolve dendritic and planar growth phenomena simultaneously, allowing predictions of the grain structure characteristics. The main conclusion can be summarised as follows:

1. Fluid flow affects the shape of the melt pool. For accurate microstructure predictions, it is important to consider the liquid flow. Convection within the pool took up to 26% of the total heat transfer and affected the trailing edge of the melt pool most significantly. The influence of the fluid flow on the heat transfer decreases with increasing scanning speed.

2. Two coexisting solidification behaviours of laser-melted YSZ were observed, namely grain bending (crystals with curved grain boundary geometry under the surface) and grain surface sealing (in-plane surficial crystals cover vertical columnar grains). The formation mechanism was explained in terms of the different growth velocities of planar and dendritic interfaces.

3. The proposed multiscale model includes particular characteristics of orientation-independent growth that were captured by approximating the growing element as a sphere. To capture the tetragonal nature of the material, the growing element used in the decentered octahedron algorithms for FCC and BCC crystals was changed with consideration of corresponding crystallographic lattice constants. The modelling results were in good agreement with the experiments.

4. A novel combined cellular automata method is proposed, capturing specific aspects of planar and dendritic interfaces. By considering planar growth, resulting in curved grain geometry, and dendritic development, the model can expand the use of CA models and become a better physical representation of laser melting.

Chapter 7

Exploring new methods for local coating deposition

Recast layer, typically considered a negative side effect of laser machining, was found to form structures, which is presented in the current chapter. During the work on laser melting, described in the previous chapters, several experiments with controlled temperature gradients were performed. The initial aim of such experiments was to reduce the microcrack width in after laser melting, which commonly occurs in ceramic materials after solidification without thermal conditioning. The initial goal, diminish the solidification microcracks completely, the cracks after laser melting is in fact favourable, as it increases the thermomechanical compliance of the coating.

Careful examination of the results has shown that it is possible to deposit material arranged similarly to EB-PVD grown columns while being under atmospheric pressure. Very little scientific and industrial attention has been paid to the possibility of laser deposition in ambient conditions. To close this gap, two experimental setups for atmospheric pressure deposition were developed. The experimental results and formation mechanisms are presented and discussed in detail, as well as recommendations for further studies.

7.1 Introduction

Material deposition methods present a significant interest in industrial application, in particular to thermal barrier coatings of aerospace turbine engines. As it happens with engineering methods, deposition techniques present trade-off between coating resistance to the engine environment and its deposition costs. For example, air-plasma spraying technique is a cost-effective solution that has high deposition rates has generally worse performance than the slow vacuum-based processes such as EB-PVD. Nevertheless, there exist many deposition technologies having their benefits in particular aspect, and coating deposition technologies undergo extensive research. One of the most recent developments in deposition process is solution precursor plasma spray (SPS) and suspension plasma spray(SPPS), overcoming the limitation on the particle size for conventional APS process of 10-100 μm [142]. The latter allows to create new microstructures somewhat similar to vacuum-based techniques that cannot be deposited with APS process, which results in superior properties of the coating.

At the same time, both APS and SPS/SPPS processes are difficult to reproduce during on-wing maintenance due to miniaturisation challenges. However, combustion flame spraying, a simpler and older technique for coating deposition, can be used for coating application in-situ [273, 78]. Simpler design and lower temperatures of the propellant allowed to decrease the size of the spray gun and decrease the stand-off distance. However, CFS-based coating may experience worse mechanical interlocking and higher amount of unmolten particles.

Arguably, the biggest challenge of on-wing coating application is the confined space where deposition takes place. In this regard, lasers are perhaps one of the easiest to miniaturise energy sources, that are able to vaporise the material. However, very little attention was paid to the laser deposition of materials in atmospheric pressure conditions. To the best of author's knowledge, there is just a single work on atmospheric TBC deposition with a laser tool, performed by Ouyang et al. [231]. The authors used a microwave plasma generator as a propellant and green pulsed laser as a YSZ heating tool, achieving encouraging results for patch

repair with sub-micron width columns. Their solution due to the presence of plasma generator, their solution is difficult to miniaturise and challenging for in-situ coating application.

Although there are already dozens of material deposition techniques, very few studies have been dedicated to laser deposition in atmospheric pressure. To close this gap, this chapter aims to explore the possibilities of coating application via a laser source under atmospheric ambient conditions. A laser-based coating application is potentially easier to miniaturise and requires smaller stand-off distances than APS and SPS/SPPS, and may become a mature technology for coating deposition one day.

In this chapter, the exploratory results of utilisation of the laser beam will be presented, covering substrate-to-substrate TBC redeposition for microstructure modification, Liquid Droplet Laser Deposition method that can be used for production of splat-like coatings, and Atmospheric Vapour Laser Deposition (AVLD) method that can be used for manufacturing of the coating consisting of interconnected nanospheres. This will be supported with high-speed imaging of the laser target interaction and proposed coating deposition mechanisms.

7.1.1 Initial experiments: spiral path and crack suppression in laser melting

As a part of the laser-melting work, described in the previous chapters, an attempt to control solidification cracks was undertaken. Based on the idea of reducing the thermal gradient and slow heating and cooling, topcoat was melted with a spiral path. While such method creates lower thermal gradients, it can also create a vapour plume in the proximity of the substrate that has already been already hit by the laser and accumulated some energy. To our surprise, this has created columnar microstructure very similar to that of EB-PVD coatings, and did not require high vacuum, electron gun, or anything except for the laser. In this subsection, such initial experiment will be described in detail.

For the initial trials, a classical Archimedean spiral was chosen, which in polar coordinates (r, θ) can be written as follows:

$$r = a + b\theta \tag{7.1}$$

After transformation to Cartesian coordinates, the equations describing the spiral is:

$$x = \begin{cases} \frac{v_{max}}{2\pi n} \cdot t \cdot \sin\left(\frac{v_{max}}{R} \cdot t\right)\Big|_{(int\left[\frac{t}{\frac{2\pi nR}{v_{max}}}\right] mod 2)=0} \\ -\frac{v_{max}}{2\pi n} \cdot t \cdot \left[\frac{4\pi nR}{v_{max}} - t\right] \cdot \sin\left(\frac{v_{max}}{R} \cdot t\right) \cdot \left[\frac{4\pi n}{v} R - t\right]\Big|_{(int\left[\frac{t}{\frac{2\pi nR}{v_{max}}}\right] mod 2)=1} \end{cases} \tag{7.2}$$

$$y = \begin{cases} \frac{v_{max}}{2\pi n} \cdot t \cdot \cos\left(\frac{v_{max}}{R} \cdot t\right) + v_{travel} \cdot t\Big|_{(int\left[\frac{t}{\frac{2\pi nR}{v_{max}}}\right] mod 2)=0} \\ -\frac{v_{max}}{2\pi n} \cdot t \cdot \left[\frac{4\pi nR}{v_{max}} - t\right] \cdot \sin\left(\frac{v_{max}}{R} \cdot t\right) \cdot \left[\frac{4\pi n}{v} R - t\right] + v_{travel} \cdot t\Big|_{(int\left[\frac{t}{\frac{2\pi nR}{v_{max}}}\right] mod 2)=1} \end{cases} \tag{7.3}$$

Where R is the maximum radius of the spiral, n is the number of passes, v_{max} is the maximum scanning speed of the laser, and v_{travel} is the transverse speed of the laser or stage, t is time, and *mod* is the modulo operator. The solution of the above equation would result is presented graphically in Fig. 7.1. By controlling these 4 parameters, one can control the temperature distribution within the workpiece, expanding the possibilities of laser scanning from a simple straight line.

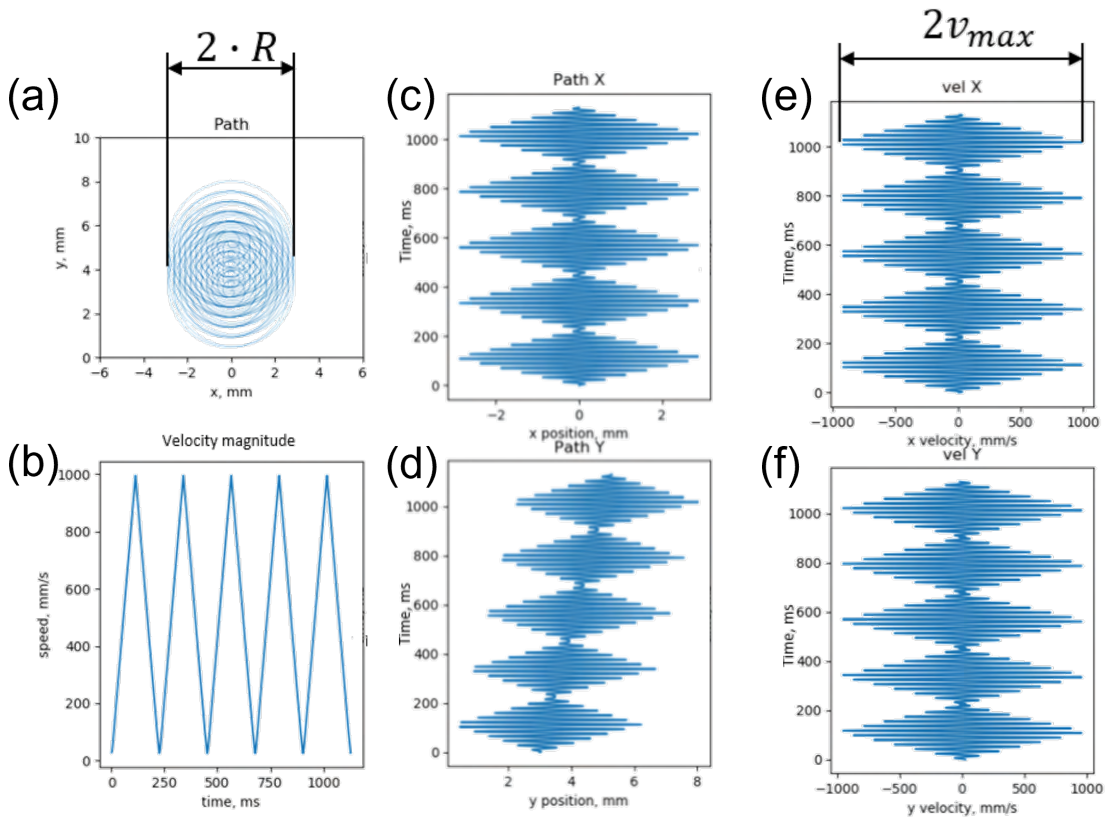


FIGURE 7.1: An example of the spiral path and corresponding kinematic conditions. (a) XY spiral path; time evolution of: (b) velocity magnitude, (c) X coordinate; (d) Y coordinate; (e) X velocity; (f) Y velocity.

In order to see the response of the material on the heating path, a mathematical solution of a set of equations must be found. For the computational efficiency of the preliminary study, non-linear phenomena such as fluid motion, phase change, and temperature-dependent material properties, were neglected. This allowed to use of the analytical solution of the heat equation using Green's functions, which can be written as follows:

$$T(x,y,z,t) = \frac{2\alpha}{k} q_0 \int_{\tau=0}^{t} \frac{1}{(4\pi\alpha(t-\tau))^{\frac{3}{2}}} \exp\left(-\frac{(x-x_{spot}(\tau))^2 + (y-y_{spot}(\tau))^2}{r^2+4\alpha(t-\tau)}\right) \cdot \exp\left(-\frac{z^2}{4\alpha(t-\tau)}\right) d\tau \tag{7.4}$$

By substituting the evolution of X and Y coordinates into the Eq. 7.4, one can obtain

the temperature field at any given time. Results with pre-optimised parameters are shown in Fig. 7.2 and 7.3.

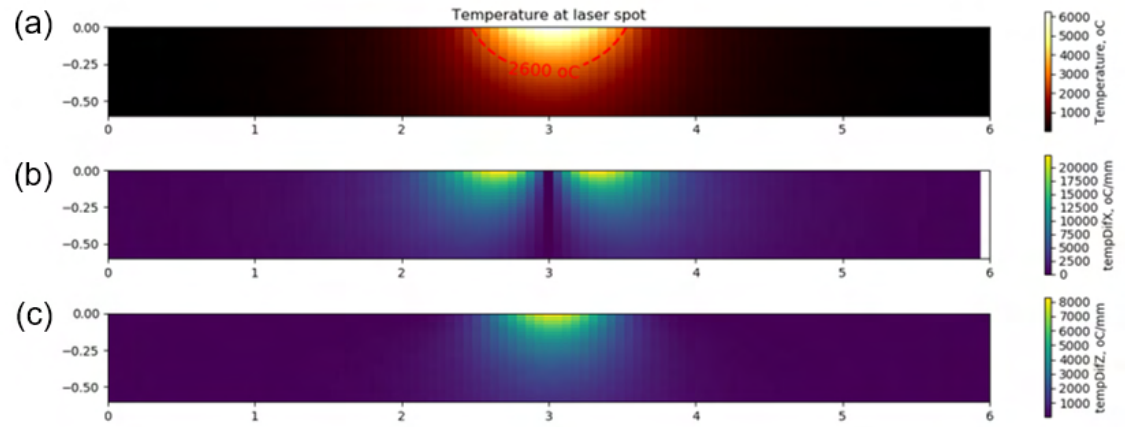


FIGURE 7.2: Slice of the temperature field in XZ direction with the standard line path, scanning speed $v_{travel} = 1.6\ mm/s$. (a) Temperature field, (b) temperature gradient in X direction (horizontal); (c) temperature gradient in Z direction (vertical).

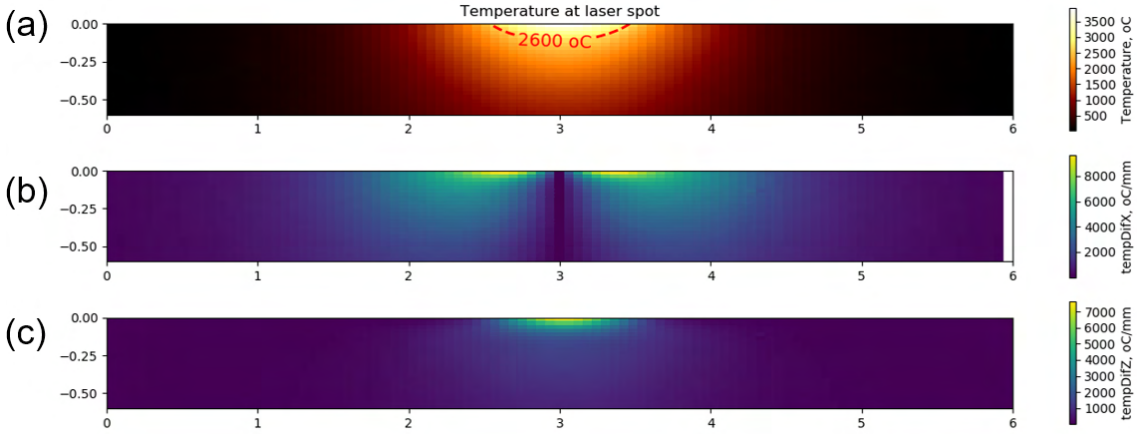


FIGURE 7.3: Slice of the temperature field in XZ direction with the spiral path with the following parameters: $R = 1\ mm$, $n = 100$, v_{max}= 1000 mm/s, and $v_{travel} = 0.01\ mm/s$.(a) Temperature field, (b) temperature gradient in X direction (horizontal); (c) temperature gradient in Z direction (vertical).

for comparison, the simple line scan, presented in Fig. 7.2 results in ∇T_x and ∇T_z is 22600 K/mm and 8100 K/mm, respectively. At the same time, the presented spiral path creates ∇T_x and ∇T_z od 9300 K/mm and 7400 K/mm, respectively.

One can assume that by minimising thermal gradient in the workpiece it would be possible to minimise thermal damage, i.e. microcracking, of the workpiece. A

possible approach to find the optimal conditions is to minimise the sum of the cost functions c_1, c_2 , and c_3:

$$c_1 = T_{i=\frac{N}{2},j=\frac{M}{2}} - T_{melt} c_2 = \sum_{i=1}^{N} (\frac{T_{i,j} - T_{i-1,j}}{\Delta x}) \cdot \frac{1}{N} c_3 = \sum_{i=1}^{M} (\frac{T_{i,j} - T_{i,j-1}}{\Delta z}) \cdot \frac{1}{M} \quad (7.5)$$

where N, M are the number of points in X and Z directions, respectively, $T_{i,j}$ is the temperature at X and Z, Δx and Δz are the spatial steps in X and Z directions. The c_1 is responsible for the melting of the workpiece, c_2 and c_3 is the sum of thermal gradients along X and Z coordinates. The cost functions can be calculated at the moment t when the laser is in the end of the spiral path with the period Δt:

$$t = (2 \cdot k + 1) \cdot \Delta t, k \subset \mathbb{N} \quad (7.6)$$

Such cost function experiences multiple local extrema, and different methods to find the global minima must be used. In the studies, a more sophisticated approach can be used.

Line scan and spiral scans were performed and presented in 7.4. The experiments were carried out with the SPI G3 nanosecond pulsed laser with a beam size of 0.6 mm and average power of 18.2W. 8wt%YSZ coating was deposited with the thickness of 350 μm onto the 110 μm layer of bondcoat (Co-32Ni-21Cr-8Al-0.5Y). Both coatings were deposited via the APS method onto 50 x 25 x 3 mm^3 Ni-based superalloy substrate (Nimonic C263).

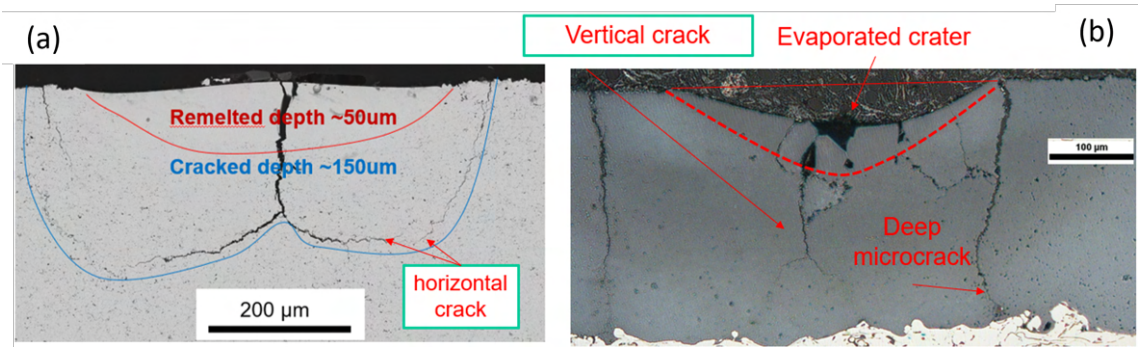


FIGURE 7.4: microstructure comparison of (a) line scan, v=5mm/s and (b) spiral scan with $R = 1\ mm$, $n = 100$, v_{max}= 1000 mm/s, and $v_{travel} = 0.01\ mm/s$.. SPI G3 nanosecond pulsed laser with a beam size of 0.6 mm, the average output power is 18.2W.

As it can be seen from the figures, without optimisation of the cost function the microcracks are still present in the topcoat. However, in contrast with the line scan conditions, the microcrack propagation direction becomes horizontal, in contrast with nearly vertical microcracks achieved via a spiral path.

Then, the spiral path was performed without shifting the spiral over the workpiece, i.e. $v_{travel} = 0\ mm/s$. The observations, presented in Fig. 7.5 a, reveal no microcracks under optical microscopy. Further observations via electron microscopy reveal very few solidification microcracks (Fig. 7.5 b).

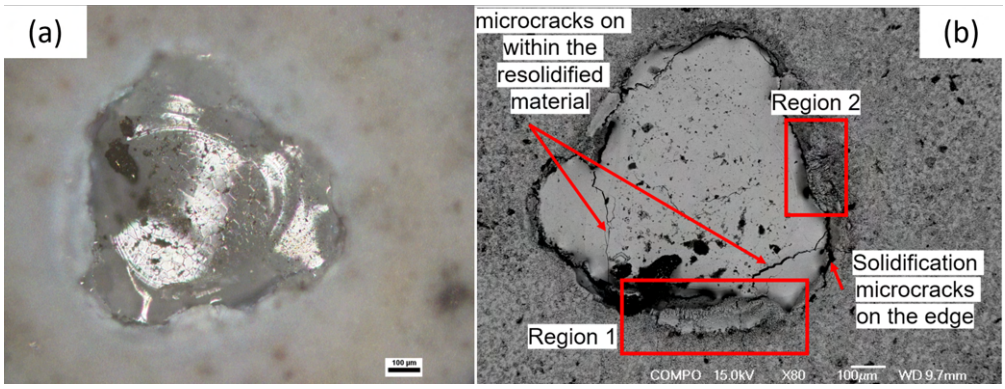


FIGURE 7.5: Optical and electron microscopy of spiral laser scans. (a) Bright field optical image, (b) SEM image. Performed with $R = 1\ mm$, $n = 3$, v_{max}= 1000 mm/s, and $v_{travel} = 0\ mm/s$, repeated 20 times for homogenous heating of the workpiece. SPI G3 nanosecond laser, laser spot size d=0.4mm

Interestingly, a rather unusual microstructure was formed on the sides of the molten crater, denoted as "Region 1" and "Region 2" in Fig. 7.5. This will be presented in

detail in the following section, with exploited approaches for material redeposition onto its own surface.

7.1.2 Substrate-to-substrate TBC re-deposition in atmospheric pressure

The spiral laser scanning path, used for decreasing thermal stresses and eventually reducing cracking, created favourable vapour growth conditions at the sides of the remelted area. Magnified view of Fig. 7.5 "Region 1" is shown in 7.6. As seen from the top, the melted region shrunk in size and created a tapered wall. This allowed revealing the microstructure from the top view. An obvious columnar microstructure with a column width of 3 to 5 μm and height of 15-20 μm were observed. In Fig. 7.6 a solidified splat, covering the column, is also visible, which can be a consequence of subsurface boiling and explosive material removal from the pool.

The deposited columns exhibit a feather-like structure with porous internal microstructure. A similar microstructure has been widely presented in EB-PVD deposited coatings. "Self-shadowing" effect is considered responsible for such porosity in low-pressure plasma spray and EB-PVD coatings [192]. As a consequence of internal porosity and small column size, the columns are susceptible to mechanical damage, and multiple broken columns were found, shown in Fig. 7.6 b.

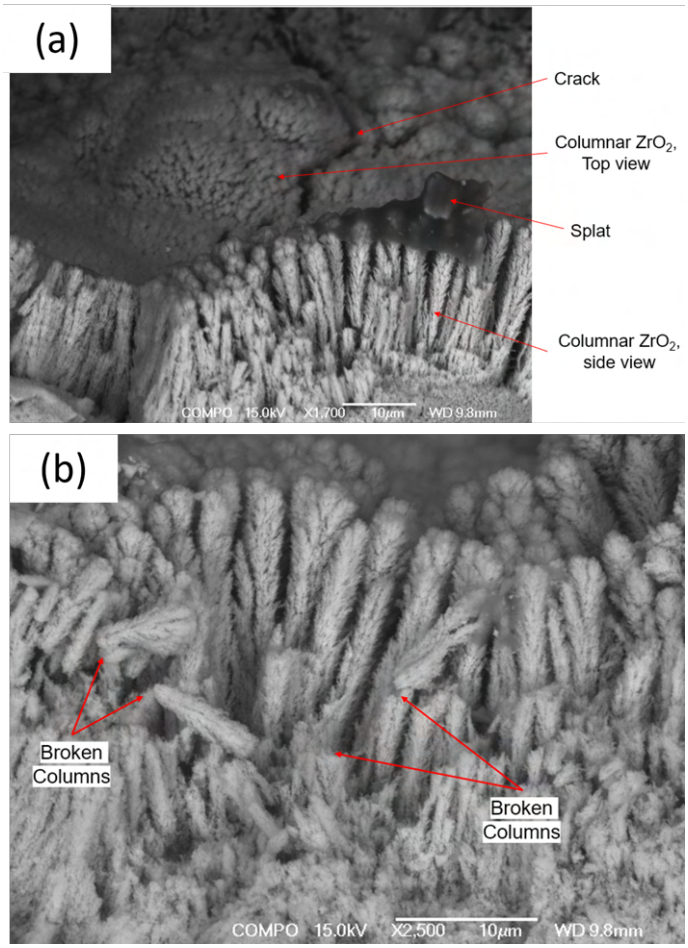


FIGURE 7.6: Vapour-grown YSZ, resolidified on the side of the molten pool (Region 1 in Fig. 7.5)
. (a) overview of columnar microstructure deposited in atmospheric environment; (b) high-magnification view of the vapour-grown columns.

In short pulse laser ablation and laser cutting, the affected material is typically removed in liquid form, e.g. dominant phase explosion in nanosecond ablation [251] and dominant melt expulsion in case of continuous wave cutting[41]. Such liquid droplets are then redeposited onto the surface of the sample with a high degree of oxidation (in the case of metals [284]) and are typically considered to be a negative side effect of laser processing.

In ultrashort pulse ablation, i.e. picosecond, femtosecond, and shorter pulses, the material is removed in vapourised state [126], which normally generates a low level of debris and redeposited material. As it was noted in the literature review, this mainly depends on the ratio between pulse duration of the laser τ_p and heat diffusion.

For low thermal conductivity materials, such as ZrO_2 and Y_2O_3 in particular, vaporisation can become a dominant removal mechanism.

An explanation of the observed phenomenon is schematically presented in Fig. 7.7. In Fig. 7.7 a-b, the surface and the central cross-section of the workpiece are presented, with a spiral laser path heating up, melting, and vaporising the surface. Such laser heating strategy generates low thermal gradients, i.e. the temperature drop along a given length l is reduced compared to a simple line scan of a laser. This, in turn, creates large areas of material with temperatures close to the melting point. At the centre of the spiral, the effective energy density of laser radiation is highest, which leads to material vaporisation (Fig. 7.7, b-c). In the magnified view of the side of the molten pool, presented in Fig. 7.7 c. The incoming laser radiation vaporises YSZ, and materials lose their molecules of YSZ in form of vapour. Vapour can partially absorb the incoming laser radiation, which may lead to molecule dissociation into ZrO_2 and Y_2O_3. This, at high laser power density, may dissociate into subsequent atoms, and later into ions and electrons, generating a plasma plume. After losing the energy on collisions, the opposite process of association takes place, creating again atoms and molecules, combining into clusters of molecules. Here, if the travel distance is short enough, the molecules and clusters of molecules would reach the surface of the workpiece with sufficient energy to get adhered to the surface. The oncoming atoms would generate internal porosity due to the well-studied shadowing effect [335]. The column width is controlled by the initial stage of material deposition, i.e. island nucleation.

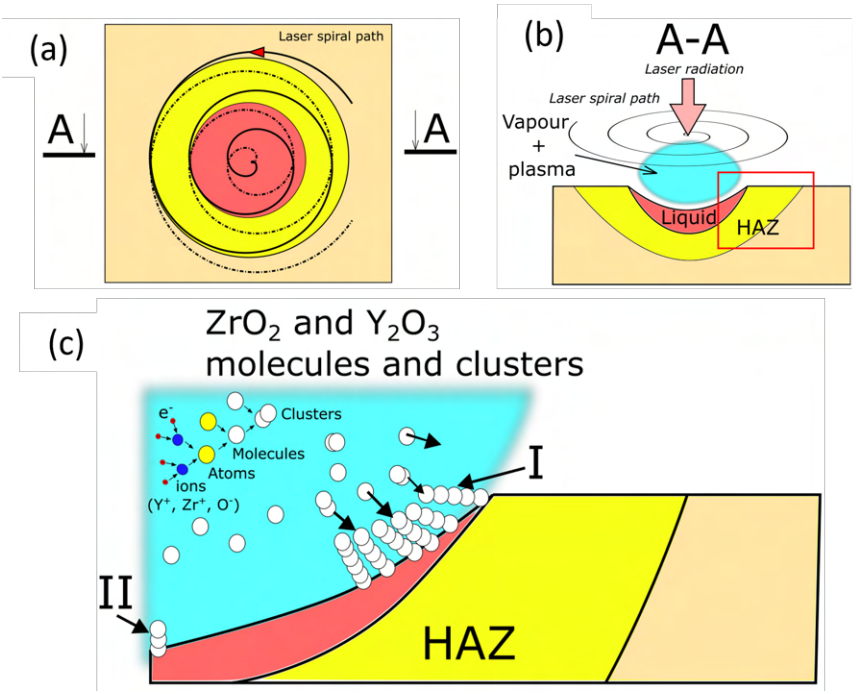


FIGURE 7.7: Schematic illustration of deposition process achieved via spiral path. (a) top view and the spiral trajectory of the laser beam; (b) cross-sectional view; (c) magnified view of the red box depicted in (b) illustrating the formation of the columnar microstructure. I denotes a column.

To the best of the author's knowledge, such structures have never been reported in the literature. A possible explanation for the formation of such patterns in atmospheric pressure, and why such microstructure has not been observed in the recast layer, is due to the two reasons:

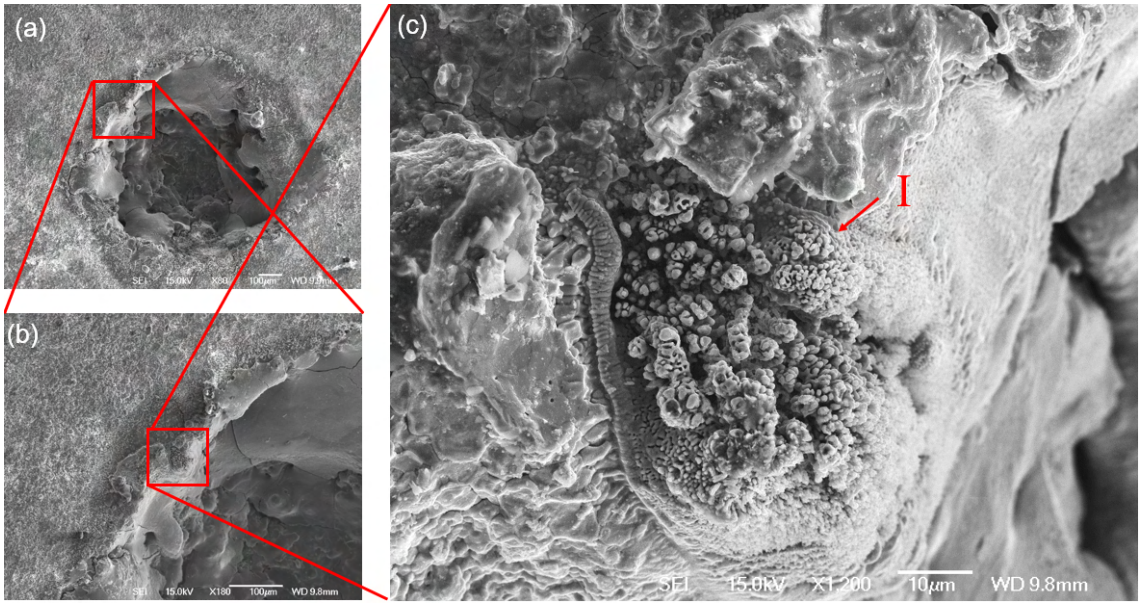
(i) Short distance between vapour and receiving surface. This is the direct consequence of material redeposition onto itself. The mean free path λ, calculated as $1/(\pi d^2 n_v)$, is a measure of volume scarcity, i.e. how long can an object travel without colliding with another object. In atmospheric conditions, it is less than just 60 nm for a ZrO_2 molecule. Essentially, this means that nearly direct contact of vapour with the substrate is necessary for creating "true" deposition from vapour. More collisions will lead to further cooling of the substance and the generation of larger clusters, which eventually condense into droplets of liquid.

(ii) Substrate temperature at the deposition zone is close to the melting point of the

deposited material. This is a direct consequence of low thermal gradients at the workpiece material, which does not often occur in laser processing. This allowed for high mobility of adatoms at the receiving surface and the formation of patterns typical for vapour deposition with substrate preheating.

Although no studies on material adhesion and general mechanical properties have been carried out, it should be noted that some of the columns were found broken (Fig. 7.6 b). Besides, adhesion of such structure also presents general interest, however, was out of the scope of this study.

In a set of similar experiments with a spiral laser scanning path, the unusual microstructure was found at a higher number of "circles", denoted as n. This effectively changes the amount of energy deposited per unit area, creates more aggressive material removal and was expected to generate larger structures. The results of this investigation are presented in Fig. 7.8 and 7.9, and show resemblance with the structure of corals.



u

FIGURE 7.8: SEM images of spiral laser scans performed with $R = 1\ mm$, $n = 100$, v_{max}= 1000 mm/s, and $v_{travel} = 0\ mm/s$, repeated 20 times for homogenous heating of the workpiece. SPI G3 nanosecond laser, laser spot size d=0.4mm. (a) low magnification; (b) magnified view of (a); (c) magnified view of (b) with the coral-like structure of the material.

It was assumed that this microstructure with separated columns was formed similarly to what was discussed above. However, due to the high energy density, the top surface of the columns has been melted and evaporated by subsequent spirals with high density.

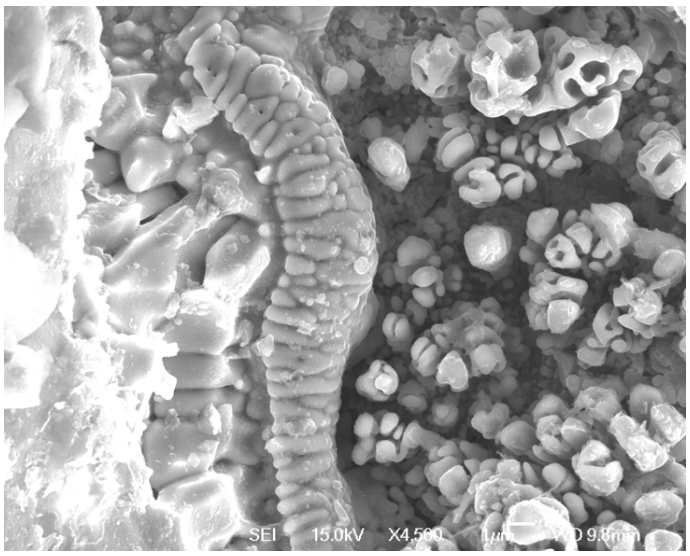


FIGURE 7.9: magnified view of the coral-like structure of YSZ depicted as I in 7.8

In order to investigate such redeposition as a microstructure modification technique in a continuous manner, the spiral path was modified in one dimension, such as:

$$x = v_{travel} \cdot t \tag{7.7}$$

$$y = \begin{cases} \frac{v_{max}}{2\pi n} \cdot t \cdot \sin\left(\frac{v_{max}}{R} \cdot t\right)\Big|_{(int\left[\frac{t}{\frac{2\pi nR}{v_{max}}}\right] mod 2)=0} \\ -\frac{v_{max}}{2\pi n} \cdot t \cdot \left[\frac{4\pi nR}{v_{max}} - t\right] \cdot \sin\left(\frac{v_{max}}{R} \cdot t\right) \cdot \left[\frac{4\pi n}{v} R - t\right]\Big|_{(int\left[\frac{t}{\frac{2\pi nR}{v_{max}}}\right] mod 2)=1} \end{cases} \tag{7.8}$$

In the scenario presented in Fig. 7.10 and 7.11, it should be noted that translational speed v_{travel} was purposely set to low values ($0.5\ mm/s$) in order to create high line overlapping and let the vapour plume remain longer at one spot. As a direct consequence of the high overlapping, this resulted in the deep removal of the topcoat (7.10 b).

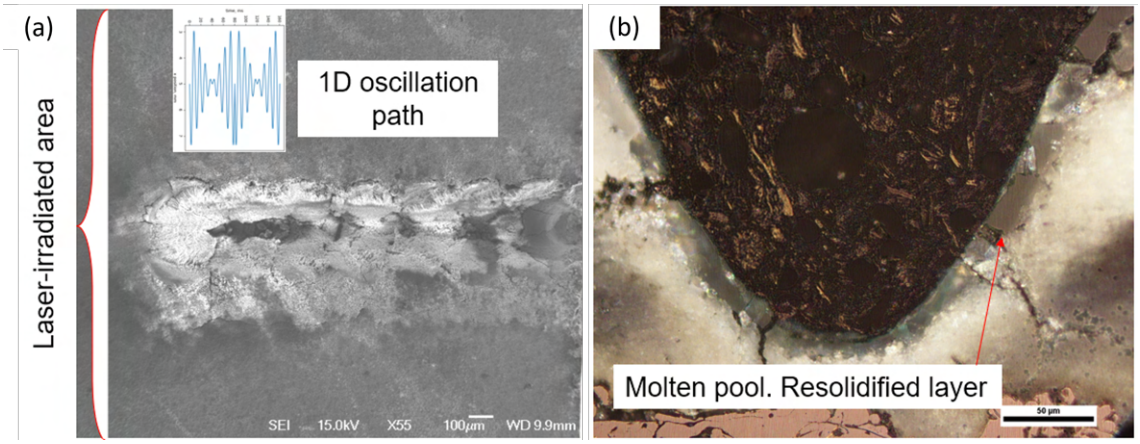


FIGURE 7.10: Microscope observations of spiral laser scans. (a) Top surface of the laser-affected surface of APS TBC with a 1D spiral path; (b)Cross-sectional micrograph showing material removal and melted layer. Laser parameters: $R = 2$ mm, $n = 200$, v_{max}= 1000 mm/s, and $v_{travel} = 0.5$ mm/s, SPI nanosecond laser.

High overlapping created conditions favourable for highly directional material deposition. Here, a highly porous, "feather"-like microstructure of the columns was found, as presented in 7.11. Such microstructure of the coating, due to its high internal porosity, can potentially create a coating with low thermal conductivity and better thermomechanical compliance.

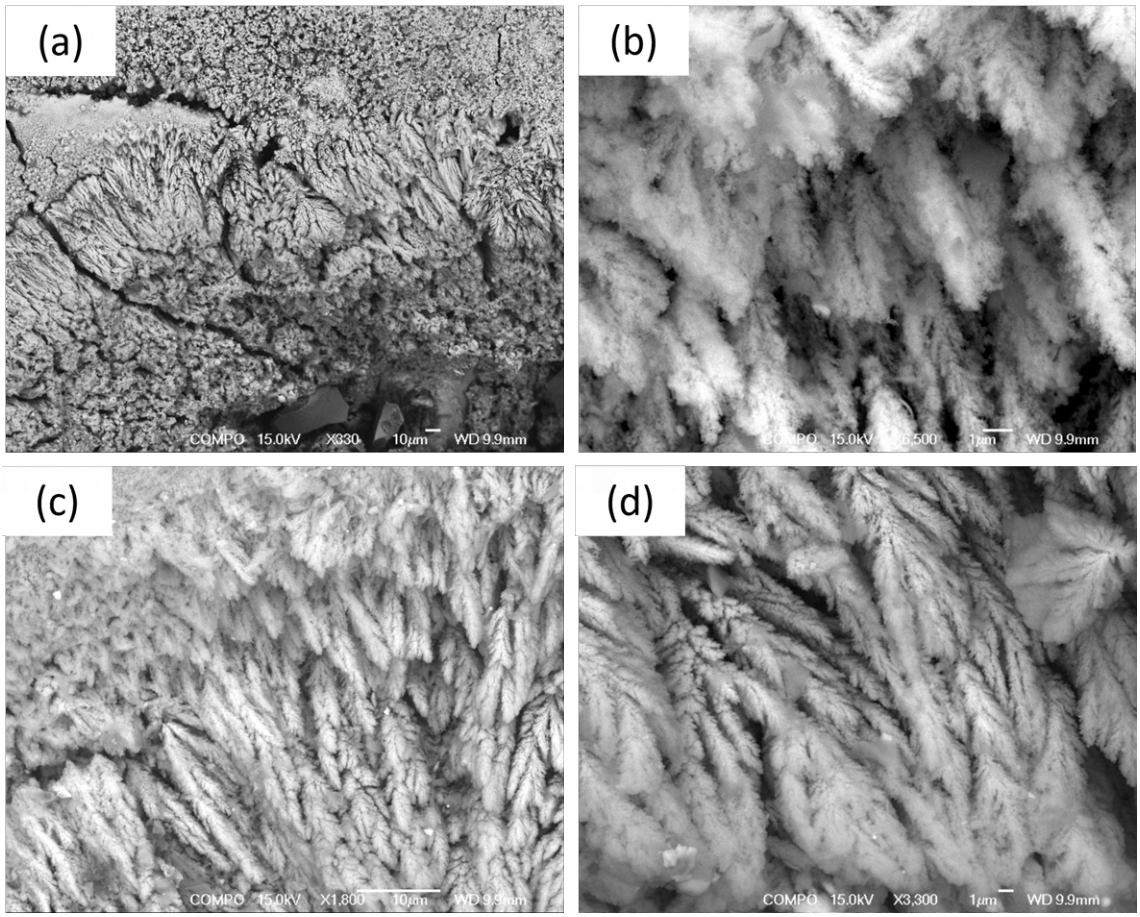


FIGURE 7.11: Top surface SEM observation of YSZ after 1D spiral laser pass, as shown in 7.10. (a) X630, (b) x6500, (c)x1800, (d)x3300

This section summarised experimental findings in substrate-to-substrate material redeposition. Unique columnar, feather-like, and coral-like microstructures were observed and presented above, which can be developed into surface microstructure modification techniques, restructuring dense, splat-like, or any other microstructure. Future studies may include a deeper characterisation of the coating crystal morphology, density, microstructure, and formation. Presented findings showed the very possibility of redeposited TBC with a certain and repeatable geometry and, possibly, can be developed into a favourable microstructure.

7.1.3 High-speed imaging of laser-substrate interaction

To understand more about the physical phenomena governing structure modification, a high-speed imaging technique was employed. it should be noted

that the available frame rate did not allow to reveal shock wave formation or to distinguish between different separate pulses, instead, this investigation was mainly focused on mass transfer.

In Fig. 7.12, a series of high-speed images is presented. It can be seen that a highly emissive region is present once the initial pulse hits the workpiece, caused by the formation of plasma and its further recombination into vapour. After 40 μs, the vapour plume disappeared and only several droplets can be distinguished. Similarly, after 80 μs from the initial irradiation, several droplets can be seen with a sign of vapour plume with decreased emittance. After 5 seconds and on of workpiece heating, no plasma/vapour formation was found, however, the amount of liquid ejecta increased significantly. After 15 seconds of laser irradiation, there have been no signs of vapour or droplets formation, with a heated region of the TBC.

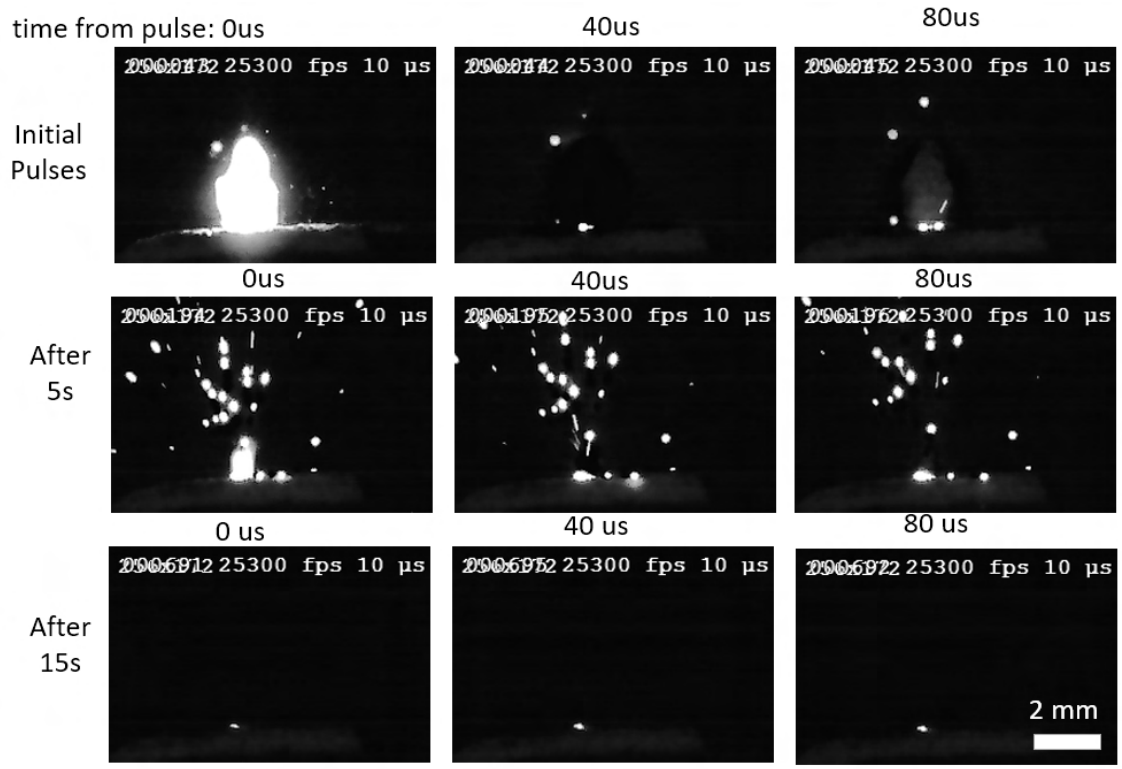


FIGURE 7.12: High-speed imaging of laser ablation of APS-sprayed 8wt%YSZ coating. Frame rate 25300 frames/s, exposure time 10 μs. Time from the pulse denotes the time passed from a pivoting pulse at the beginning (initial pulses row), after 5 and 15 seconds of laser irradiation. SPI G3 laser, average laser power 18.2W, laser spot size 50.5 μm, pulse repetition frequency 35kHz. Static irradiation.

Previously presented fine microstructure (Fig.7.10 and Fig. 7.11) suggests that the

microstructure was deposited from vapour phase. At the same time, with static irradiation, the vapour forms only at the irradiation of several initial pulses (Fig. 7.12). Later, the vapour/plasma does not appear abundantly. Instead, a liquid melt pool of TBC is formed which, under incoming laser radiation, leads to subsurface boiling and melt explosion, ejecting material in the liquid phase. Further irradiation does not remove any material, likely due to its absence in the irradiation zone.

Although the laser-material interaction has a probabilistic nature, especially in the case of heterogeneous coating with multiple scattering planes, defects, microcracks, pores, changing optical properties, etc., it should also be noted that the time between separate laser pulses is 29 μs, the exposure time is 10 μs, and the time between 2 frames is 40 μs. Therefore, there is a possibility that the pulse hit between 2 consecutive frames, forming a vapour/plasma plume, which has had a longer. To understand this further, either a higher frame rate camera is needed. Instead, a longer exposure time was used in the next experiment, capturing the temporal evolution of the laser-workpiece interaction.

Trying to capture most of the ablation vapour plume, the shutter time was minimised such as the exposure time was 45μs, and the time between the frames was 56 μs. Such results are presented in Fig. 7.13, depicting thermal processes within the plume. At the initial frame, a bright plasma plume is formed (red arrow, Fig. 7.13, a), which later cools down and has 2 distinctive areas with high emittance (red arrow, Fig. 7.13, b) and lower emittance (yellow arrow, Fig. 7.13, b) regions. The plume can be also seen after 112 μs and 168 μs of irradiation (Fig. 7.13, c and d). The density of liquid ejecta gradually increases and reaches its maximum after 68 and 224μs, and neither vapour nor liquid droplets were found after 280 μs irradiation.

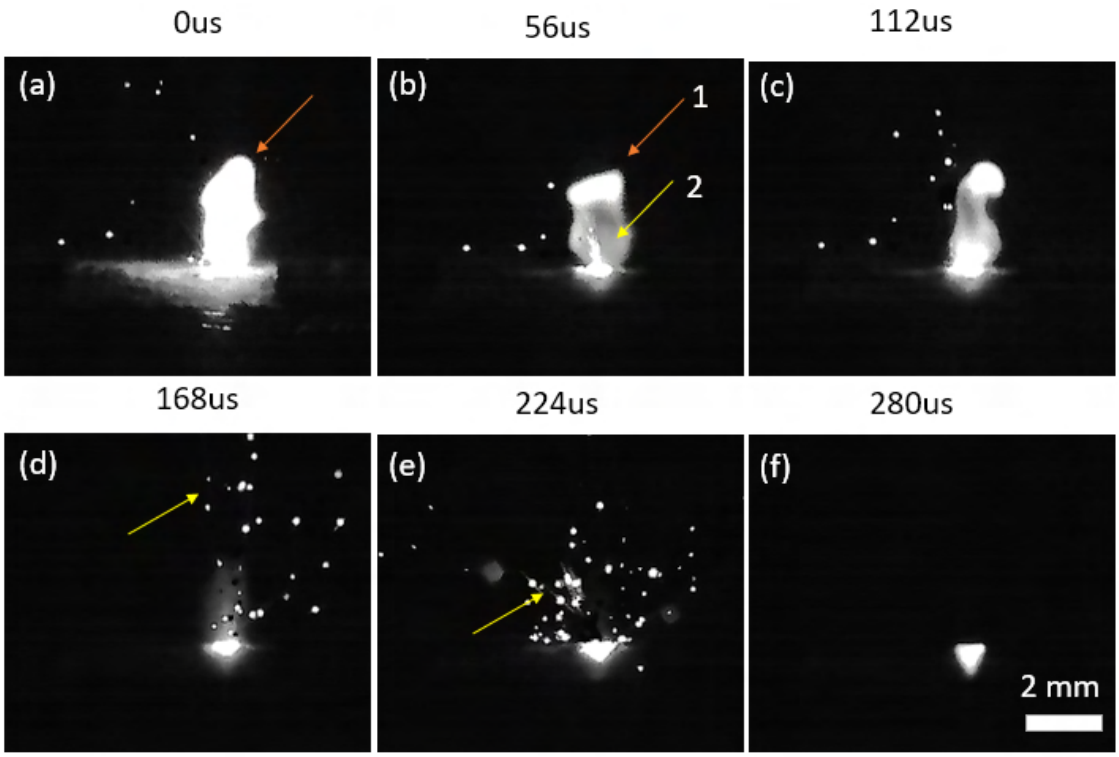


FIGURE 7.13: High-speed imaging of laser ablation of APS-sprayed 8wt%YSZ coating. Frame rate 17860 frames/s (56 μs frame-to-frame time), exposure time 45 μs. Time from the pulse denotes the time passed from a pivoting initial pulse. SPI G3 laser, average laser power 18.2W, laser spot size 50.5 μm, pulse repetition frequency 35kHz. Static irradiation.

These findings support previously discussed findings. Vapour plume and liquid ejecta tend to decrease with time, as the system approaches thermodynamic equilibrium. In conclusion, to form a vapour plume is essential to hit a new area of the workpiece in order to continuously create vapourised material, and cannot be achieved with static irradiation.

An interesting observation was documented when examining the behaviour of picosecond irradiation, presented in Fig. 7.14. Initially, the laser pulse formed a liquid droplet (Fig. 7.14, a) which rose up due to increased pressure at the substrate surface. Consequent laser pulse vaporised more material underneath(Fig. 7.14, b), and, unexpectedly, the next pulse hit the liquid droplet (Fig. 7.14, c), and generated a spray of finer droplets. A somewhat similar method, although more predictable and repeatable, is employed for generating extreme ultraviolet (EUV) light, where a CO_2 laser creates small droplets of tin which are then heated by a

secondary laser, eventually emitting high-energy photons [213].

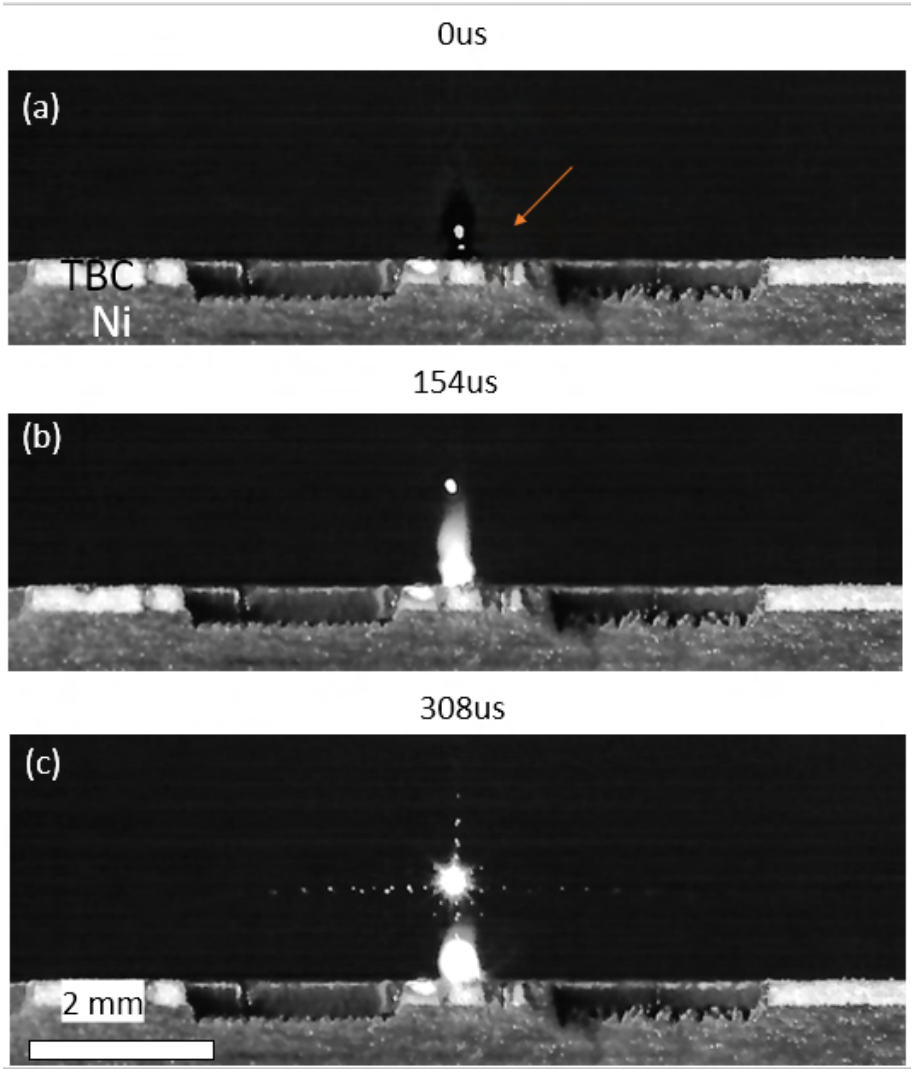


FIGURE 7.14: High-speed imaging of laser ablation of APS-sprayed 8wt%YSZ coating with a picosecond laser irradiation. Frame rate 6500 frames/s (154 μs frame-to-frame time), exposure time 140 μs. Time from the pulse denotes the time passed from a pivoting initial pulse. EKSPLA 1064, average laser power 3.5W, laser spot size 35 μm, pulse repetition frequency 4kHz. Static irradiation

7.2 Experimental methods

Aside from the general equipment used in other investigations discussed in the Methodology chapter, here specific information regarding the development of the deposition rig is presented.

7.2.1 Substrate and target materials

Stainless steel 304L was used as the substrate material in all the tests. Although the ideal material for the tests would be a nickel superalloy, such as Nimonic C263 or Inconel 718, stainless steel was used due to its price and availability. It was assumed a reasonable assumption since the primary interest of the study is microstructure formation rather than the processes at the interface between substrate and coating. However, it should be noted that in comparison with Nimonic C263, stainless steel 304L is more prone to high-temperature oxidation and has a lower coefficient of thermal expansion than that of Nimonic C263 ($17.3 \cdot 10^{-7}$ [249] and $11.0 \cdot 10^{-7}$ [96] at 100°C, correspondingly), which can result in higher thermal expansion mismatch with YSZ ($8.5 \cdot 10^{-7}$ at 100°C [257]). For reference purposes, the composition of 304L steel is presented in the table 7.1.

El.	Fe	Cr	Ni	Mn	Mo	Si	S	C	P	Cu	Co	N	V
wt.%	69.9	17.7	7.9	1.75	0.32	0.015	0.006	0.025	0.03	0.84	0.17	0.07	0.1

TABLE 7.1: Elemental composition (wt%) of AISI 304L stainless steel used as substrates in the deposition experiment [234]

Stainless steel plates 0.8mm thick were cut to size via abrasive waterjet, cleaned in methanol in an ultrasonic bath and rinsed with deionised water. To activate the surface prior to deposition, substrates were immersed in acetone for 5 minutes, then in isopropanol for 2 minutes, and rinsed with distilled water to remove all the residue.

The target material, i.e. the donor sample for deposition, was chosen to be close to that of 8wt%YSZ topcoats. Although targets for EB-PVD deposition and powders for thermal spraying are available with the composition matching state-of-the-art topcoats with 8wt%YSZ, the geometrical shape and size are dictated by the state-of-the-art setup. Due to a certain experimental setup configuration, these geometries, typically thick disks with diameters ranging from 50 to 250 mm, could not be used in the setup. On the other hand, it is possible to sinter the powders used for thermal spraying to exact size and shape, however, without significant efforts, this may result in low repeatability of the target microstructure, i.e. its

porosity, geometrical cylindricity and circularity tolerances. Thermo-optical properties of the target were of utmost importance, i.e. melting point, thermal conductivity, coefficient of thermal expansion, laser absorptance, and the choice of deposition target fell on standardised ZrO_2 cylinders widely used as a grinding media. The composition of used targets (Pingxiang Bastian New Materials) is presented in table 7.2.

El.	ZrO_2	Y_2O_3	Al_2O_3	Fe_2O_3	SiO_2	TiO_2	MgO	Na_2O_3
wt.%	94.7±0.6	4.9±0.5	0.3±0.1	¡0.01	¡0.01	¡0.01	¡0.01	¡0.01

TABLE 7.2: Elemental composition (wt%) of ZrO_2 deposition targets.

Although the composition of the target is seemingly similar to that of topcoats, according to the YSZ phase diagram, the phase content of the targets is not metastable, non-transformable tetragonal *t'*. These targets have high hardness and high fracture toughness and are therefore used as grinding media. The 4.9wt% of yttria acting as a stabiliser results in a transformable tetragonal phase, where transformation toughening is the responsible mechanism for crack closure. While this gives an incredible strength to 4.9wt%YSZ, the use of such in thermal barrier coatings is limited due to its low-temperature stability, whereas upon heating the crystal structure of transformable YSZ transforms into monoclinic+cubic phases under relatively low temperatures, below 500 °C [87, 108]. Since the phase content of deposited coating was not of primary interest, YSZ targets with different content of the stabiliser have been used as an available alternative. The influence of a lower stabiliser content of 4% shifts the phase diagram, however, the difference in thermo-optical properties were considered negligible for the proof-of-concept studies.

7.2.2 Deposition rig design

This subsection describes the experimental setups used to produce target-to-substrate deposition. 2 versions are presented here utilising different approaches for substrate heating and target movement.

Deposition rig v1: conductive heating design

First experiments of target-to-substrate deposition were performed with the apparatus presented in Fig. 7.15. The substrate temperature was controlled via 2 conductive heaters (8786067XX Rauschert, Germany) had been used to preheat the stainless steel substrate. The substrate temperature in the experiments with this rig was fixed to 400°C. The target was fixed on a geared DC brushless motor which was rotating at 2000 RPM. The laser was aimed at the flat surface of the target, and the angle between the laser and the flat surface of the target was fixed at 45°. The target-substrate distance plays an important role in the deposition process and could be adjusted in a wide range. However, due to mechanical tolerance limitations, the minimum distance achievable with this setup was 0.9mm.

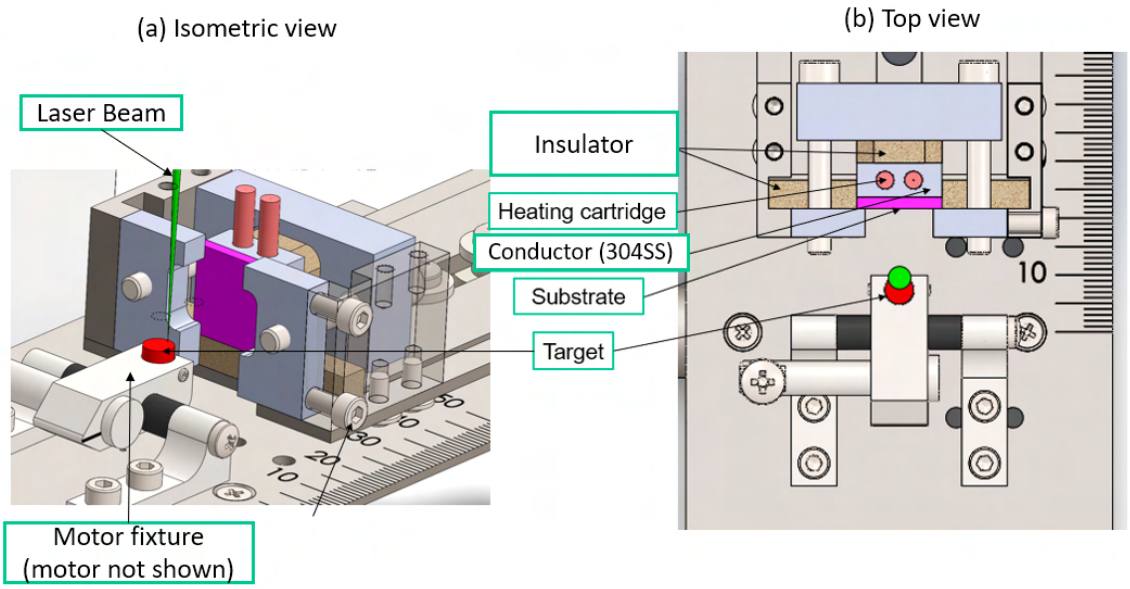


FIGURE 7.15: First design iteration of deposition rig, utilising conduction heating and wide range of target-substrate distances.

Deposition rig v2: radiative heating design

In the first design iteration, poor repeatability resulted in inconsistent experiments and was addressed via a fine and independent positioning of the substrate and target. To achieve predictable heating of the substrate and simpler sample loading and unloading, radiative heating approach was prefered to conduction heating. For

this, an infrared bulb (Osram HLX 64635) with a gold-coated focusing reflector was used which can focus the beam in a spot of approximately 5 mm.

The second design iteration of the rig addressed some of the issues of the previous rig, aiming to achieve more precise control of target-substrate distance and higher temperatures of the substrate. The design of the rig is presented in Fig. 7.16.

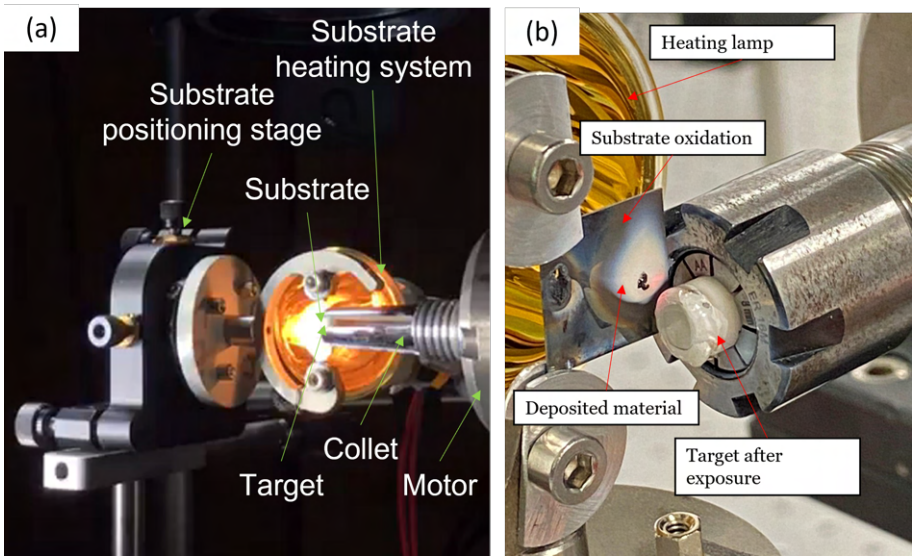


FIGURE 7.16: Final deposition rig setup utilising radiation heating and narrow of target-substrate distance range with fine control. (a) Equipment during the substrate heating; (b) apparatus after the experiment with deposited coating.

The front surface temperature was calibrated with a K-type thermocouple, presented in Fig.7.17. Each point of the calibration curve, shown in Fig.7.17 b, was taken after 5 minutes of heating when the system achieved thermal equilibrium with the environment. It was possible to achieve temperatures as high as 860 °C with this method. The substrate temperature in the experiments with this rig was fixed to 500°C unless mentioned otherwise.

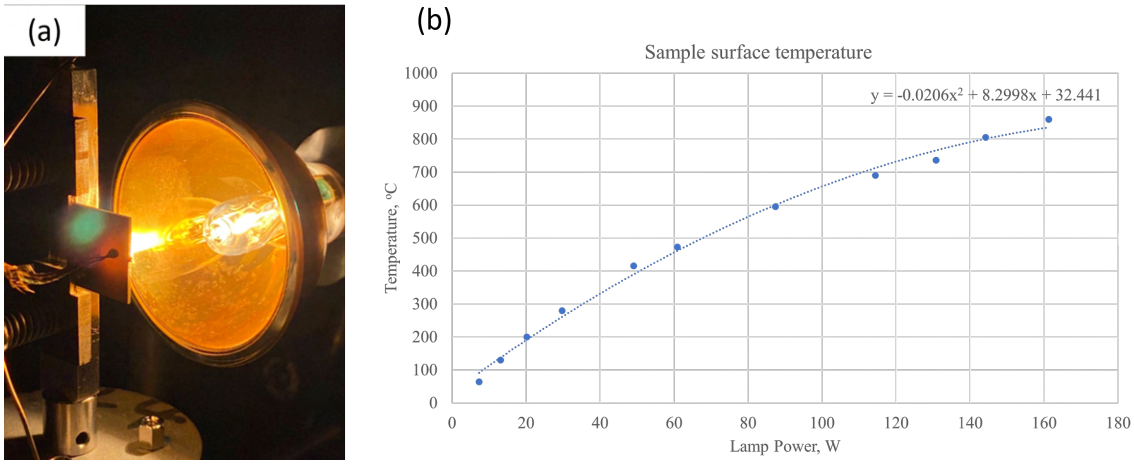


FIGURE 7.17: Calibration process of the heating equipment. (a) photograph of the heated substrate with a thermocouple. (b) the front surface temperature of a 0.8mm thick sample after thermal equilibrium.

7.3 Results and Discussion

7.3.1 Initial deposition results (Deposition rig v1)

Two distinguished experiments will be described in the current subsection, achieved with the first design of the rig. Although the setup suffered issues with the repeatability of the parameters, the results generally presented a substrate coated with splat-like deposits. The presented results were achieved with the SPI G3 nanosecond pulsed laser with a laser spot size of 0.2mm, average power at the target of 18.2 W, and pulse repetition frequency of 35kHz.

Droplet deposition

A typical and repeatable example of the target-to-substrate deposition experiments is presented in Fig. 7.18. The surface of the stainless steel substrate after rolling is shown in Fig. 7.18, with pronounced long valleys and pits, and an optically reflective surface. After deposition, the surface was covered with solidified liquid splats close to spherical in shape, illustrated in Fig. 7.18, b.

Typical droplet size was 1 to 6 μm. In contrast with APS coatings, the liquid droplets did exhibit high deformation and remained semi-spherical. The reason behind this is the low velocity of the droplets once the substrate surface is reached. The main

source of acceleration for the droplets is recoil pressure formed by the laser heating and vaporisation of the target.

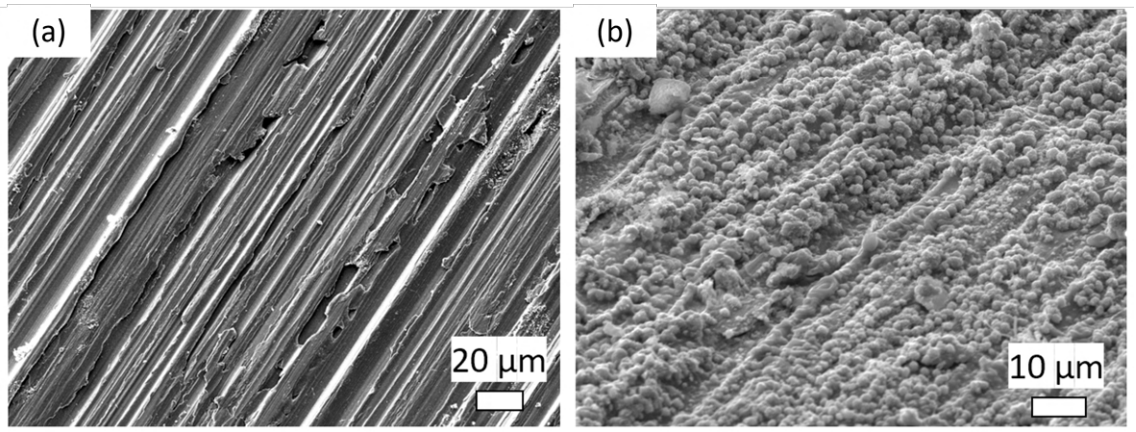


FIGURE 7.18: Substrate surface (a) before and (b) after the deposition experiment with SPI G3 nanosecond laser.

Whisker formation

Another experiment that took place happened accidentally and could not be repeated, however, still presented. In the simplistic rig design, the YSZ target was coupled to the motor with glue. Upon 10 seconds of irradiation, the target heated up and expanded enough to break the glue, as shown in Fig. 7.19. Soon afterwards, as depicted in Fig. 7.19, b, the target fell to the side and continued rotating the side, driven by recoil pressure. In this case, the target-substrate distance decreased significantly, therefore laser-generated YSZ vapour was closer to the substrate.

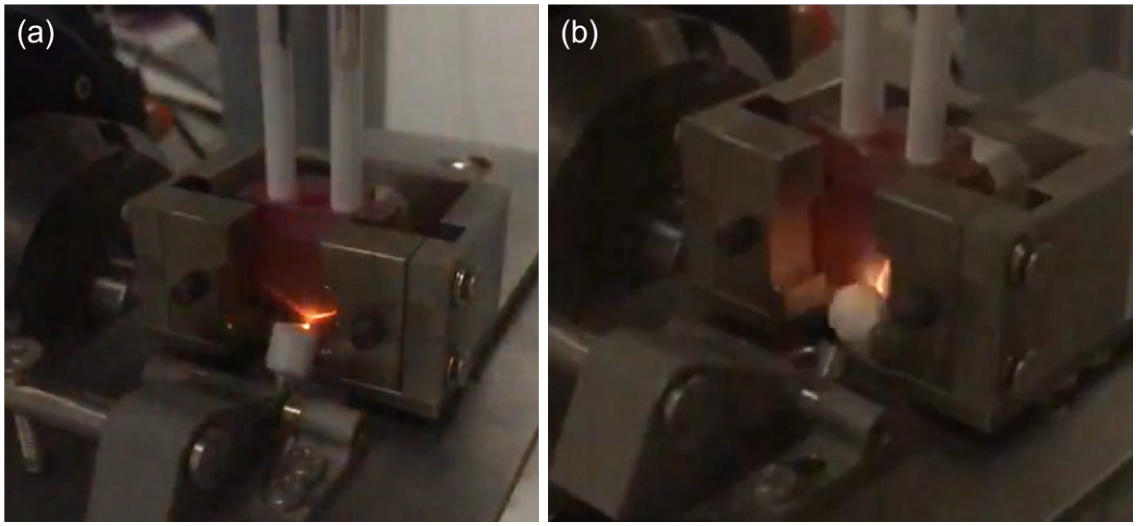


FIGURE 7.19: Experimental deposition rig v.1 in action. (a) Normal operation with the substrate with visible laser spot and ablation plume; (b) Flipped sample rotating on its cylindrical side.

SEM observations of the deposited mictrostructure are presented in Fig. 7.20. Large (tens to hundreds of μm) splats of YSZ were noticed, which was a result of prolonged radiation at a single spot causing an increased size of the melt pool and larger size of the splats. Interestingly, the splats are covered with elongated whisker-like columns with a sub-micron diameter, 5-10 μm long. A similar microstructure was reposted by Ouyang et al. [233]; the authors used a short pulse laser for material ejection and creating a vapour plume that was deposited on the YSZ surface (partially removed), and a radio frequency plasma torch for preheating and vapour propelling.

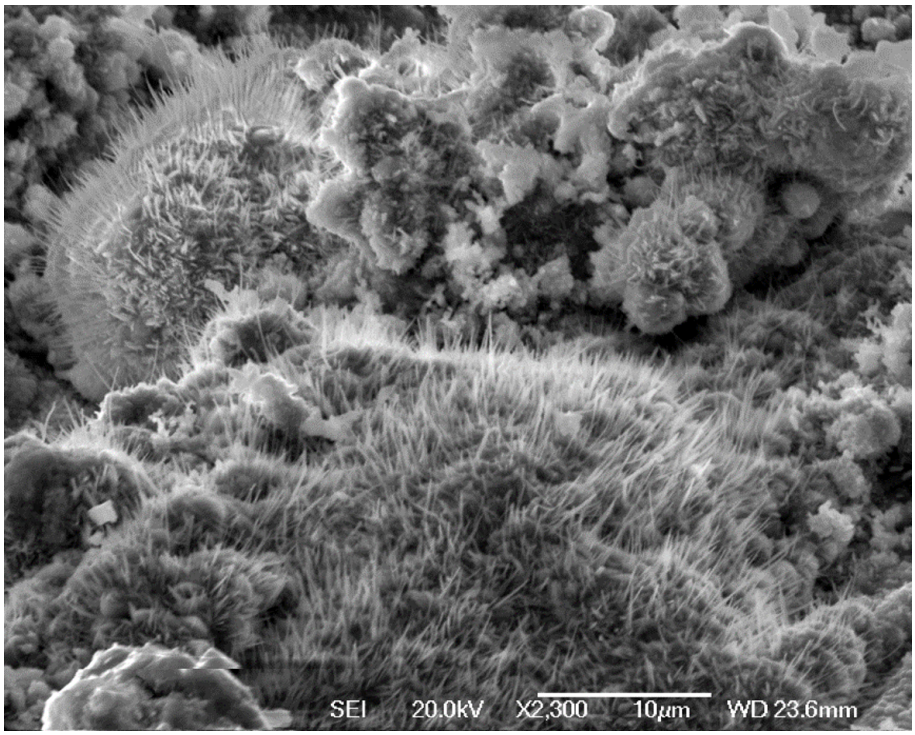


FIGURE 7.20: Deposition of sub-micron whisker-like YSZ with SPI G3 laser.

Although investigations of the properties of the samples were out of the scope of this study, it would be reasonable to assume that the sub-micron diameter whisker-like microstructure of the YSZ, arguably, may exhibit properties significantly different from that of a larger column, although of the same composition[264]. J.E. Gordon [106] found this phenomenon in small glass cylinders and attributed a significant increase of mechanical properties in smaller samples to the lower amount of dislocations within the structure. Moreover, similar microstructures, although of different materials, are often fabricated by means of wet chemistry and due to the high specific area of the nanowhiskers find applications in chemical and biological sensors[362].

Many methods have been reported on nanowhiskers deposition techniques, most often Vapour-Liquid-Solid (VLS) methods, an essential detail allowing for the whisker to grow is a liquid globule of a different material, which acts as a catalyst for the chemical reaction, typically studied with gold-silicon droplets on a silicon substrate [337, 264].

A possible explanation for whisker growth in the presented experiment is as follows.

Initially, the substrate surface was covered with a layer of YSZ by means of droplet transfer, depicted in Fig. 7.21, a. Once the target changed its orientation and rotation, the flux of vapour has increased, and after losing its energy on collisions with ambient air, condensed into nanometre-scale droplets, shown in Fig. 7.21, b. With time, the size of the droplets increases by absorption of the neighbouring vapour particles, eventually meeting the surface (Fig. 7.21, b). The incoming vapour flux is partially "absorbed" by the liquid nanodroplet, which eventually becomes the tip of the whisker, Fig. 7.21, c. Possibly, such droplets may remain liquid and, considering the impurities of the target material and alloy nature of YSZ, enable the VLS growth mechanism. Such droplet may remain liquid due to the following reasons:

1. Incoming heat flux from the vapour adatoms.

2. Impurities of the YSZ. Composition of YSZ used in these studies include some lower melting point oxides, such as Na_2O_3 (851°C) and Fe_2O_3 (1565°C). On such a small scale, the composition of the nano- droplet may be shifted towards the impurity and lower the melting point.

3. Size-dependent melting point of materials, or melting-point depression. In particular, the melting point sharply decreases for particles smaller than 50 nm and allows for temperature drop in order of several hundreds of degrees [370].

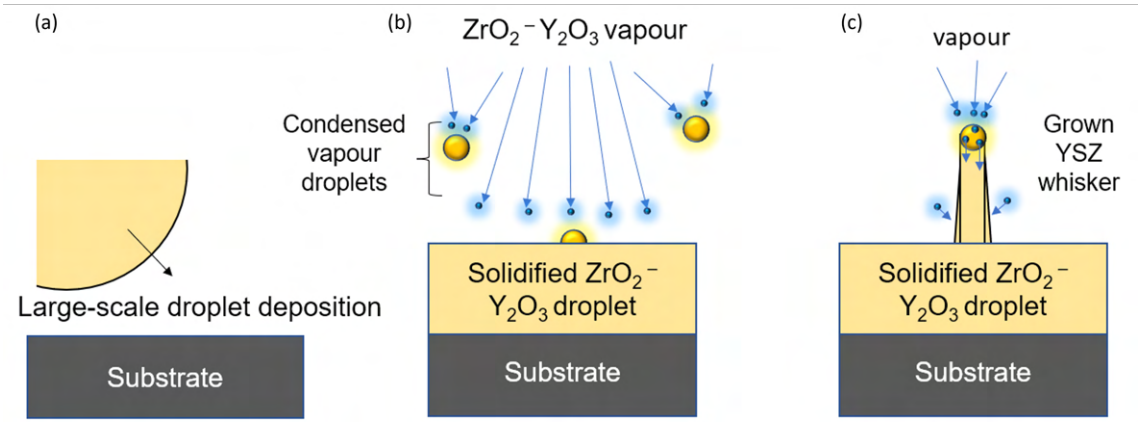


FIGURE 7.21: Deposition mechanism of whisker-structured YSZ

Further studies of YSZ whiskers, in particular their strength, exact size, morphology, and composition, although of scientific interest, are out of the scope

of the current study, which aims at investigating the general possible microstructures in the atmospheric environment.

7.3.2 High-speed imaging of laser-target interaction

In order to understand and control the deposition process, the interaction of the laser beam and the target is of utmost importance. For deposition from the vapour phase, it is important to bring the vapour plume as close as possible to the substrate, thus reducing the number of collisions with the ambient environment. All the lasers available were studied, and, as can be expected, higher laser power generates a larger vapour plume. The results presented in the rest of this chapter are performed with an SPI redPower continuous wave laser with the average output power at the workpiece of 88W.

High-speed footage of laser-target interaction, presented in Fig. 7.22, shows the evolution of target response to laser irradiation. At the initial stage, Fig. 7.22, a-b, the laser is absorbed by the target. First signs of material ejection in form of vapour or liquid starts after at least 312 μs (Fig. 7.22, c). The laser is tightly focused onto the target surface and results in a power density of 24.9 MW/cm^2 if the beam elongation at the curved surface is neglected. The such power density was sufficient for melting of the sample and creating conditions for boiling, eventually ejecting the liquid droplets from the melt pool as a consequence of the melt pool boiling. This creates a steady stream of liquid droplets.

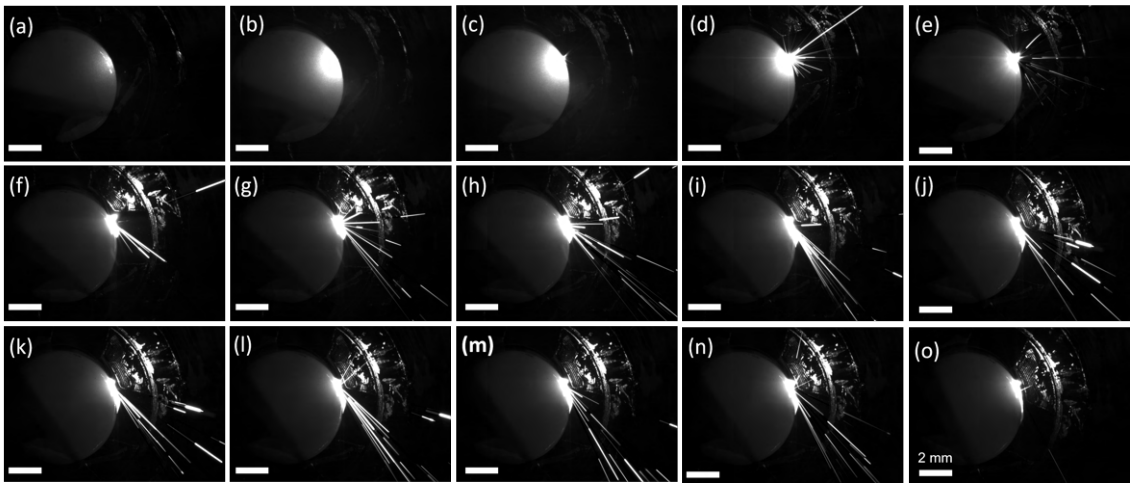


FIGURE 7.22: High-speed imaging of laser ablation of 4.9wt%YSZ target close to the focal plane. T Time step between images is 154 μs (frame rate is 6500 frames/s), exposure time 151 ms. Average power 88W, beam waist 30 μm (increased on a curved surface). Linear velocity at the target surface is 44 mm/s.

Such behaviour of the melt pool will be further employed to demonstrate the possibilities of splat-like coating deposition, or Liquid Droplet Laser Deposition (LDLD). In comparison with the state-of-the-art APS process, the laser directly melts the YSZ target and generates a flow of microdroplets, instead of feeding a high-temperature plasma for particle melting. In the LDLD approach, acceleration of the droplets is done purely by the laser process, i.e. by generating high recoil pressure at the surface.

The velocity of the droplets is stochastic in its nature and will depend on the local conditions of the melt pool, place of the ejection, local target material parameters, e.g. laser absorptance and roughness, precipitation content, etc. To measure the velocity of the droplets, a similar high-speed imaging experiment took place. The speed was measured as the length of the track after the droplet that travelled this distance l_{track} during the period of camera exposure time $t_{exposure}$, and the highest speed, calculated as $\nu_{droplet} = l_{track}/t_{exposure}$, was 39 m/s (see Fig. 7.23).

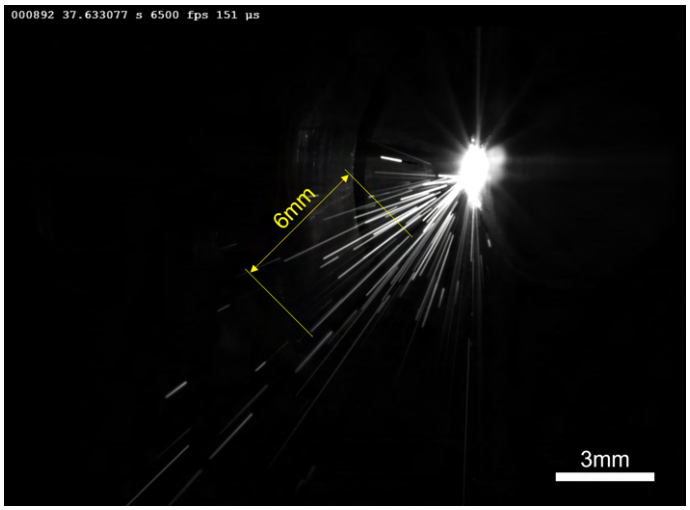


FIGURE 7.23: High-speed imaging of laser ablation of 4.9wt%YSZ target close to the focal plane. The time step between images is 154 μs (frame rate is 6500 frames/s), exposure time 151 ms. Average power 88W, beam waist 30 μm (increased on a curved surface). Linear velocity at the target surface is 44 mm/s.

The range of powder velocities in the APS process is typically 150-300 m/s [205, 375]. This is significantly higher than what has been achieved with the presented method, peaking at 39m/s. In the case of coating application, this may result in lower particle deformation and consequently lower coating adhesion. However, the presented results were limited by the apparatus available and should be treated as a proof-of-concept rather than an industrial solution. This can be solved by, for instance, adding a separate droplet acceleration, e.g. by means of airflow. Another possible approach is to create a steady moving melt pool at the surface of the target via continuous irradiation and use a second pulsed laser aimed at the melt pool, to generate boiling conditions and high enough recoil pressures, while maintaining the necessary average power with the first laser.

In order to suppress liquid ejection from the melt pool, the laser power density was decreased. In Fig. 7.26, where a steady vapour plume is visible (denoted with orange arrow) with increased laser spot size. The corresponding irradiance is 0.56MW/cm$_2$ 0.14MW/cm$_2$ in Fig. 7.26, a and b, respectively. The size of the vapour plume was 1.8mm and 0.9mm and was directed perpendicularly to the target surface. This will further be used to enable Atmospheric Vapour Laser Deposition (AVLD).

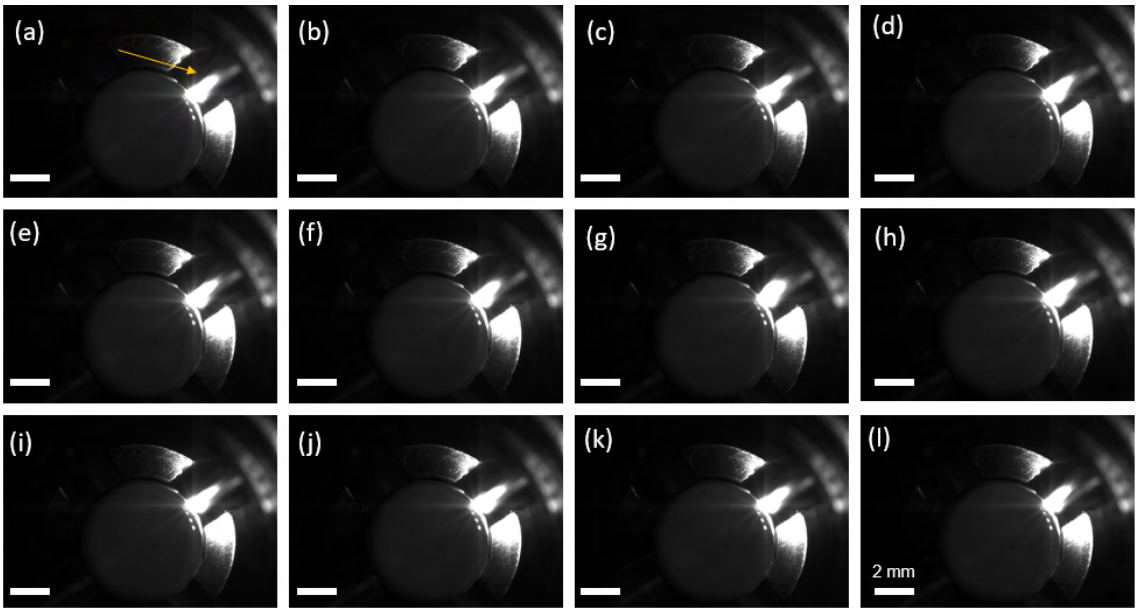


FIGURE 7.24: A series of high-speed images laser ablation of 4.9wt%YSZ target with a laser spot size of 0.2mm. The orange arrow indicates the vapour plume. The Time step between images is 154 μs (frame rate is 6500 frames/s), exposure time is 151 ms. Average power 88W. Linear velocity at the target surface is 44 mm/s.

The vapour/plasma plume does not change its size or shape with time, as shown in a series of images in Fig. 7.24 allowing to generate a predictable plume of energised particles for their deposition.

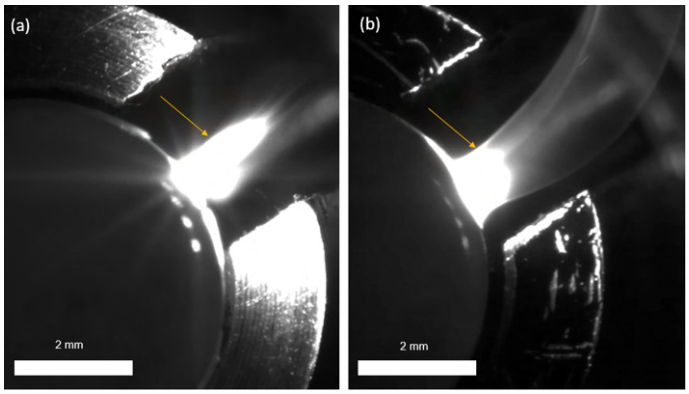


FIGURE 7.25: High-speed imaging of laser ablation of 4.9wt%YSZ target with defocused beam: (a) laser spot size of 0.2mm and (b) 0.4mm. The orange arrow indicates the vapour plume. Exposure time 151 ms. Average power 88W. Linear velocity at the target surface is 44 mm/s.

After prolonged continuous irradiation of the target surface, a molten pool is generated, as shown in Fig. 7.26. Surprisingly, no splashing was detected even after continuous irradiation for several seconds.

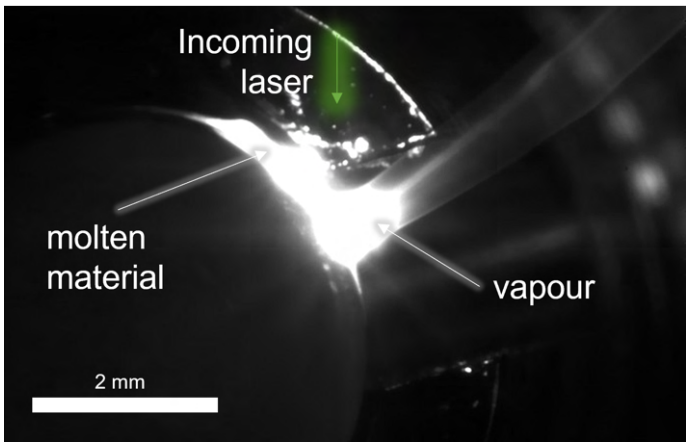


FIGURE 7.26: High-speed imaging of laser ablation of 4.9wt%YSZ target with a beam size of 0.4mm after prolonged irradiation. The orange arrow indicates the vapour plume. Exposure time 151 ms. Average power 88W. Linear velocity at the target surface is 44 mm/s.

However, for the sake of target cooling and its mechanical integrity, continuous irradiation was separated into pulses of 10ms pulse duration with 90ms of dwelling time between pulses. This allowed some level of target cooling by convection and radiation.

Two different concepts for generating a flow of high-temperature particles were found via high-speed imaging. This was then developed into Liquid Droplet Laser Deposition (LDLD) and Atmospheric Vapour Laser Deposition (AVLD) techniques, presented in the following subsections.

7.3.3 Liquid droplet laser deposition (LDLD) method

To take advantage of the droplet formation and acceleration directly from the pool, the preheated substrate is located directly at the path of the droplet allowing their solidification at the substrate surface, as shown in Fig. 7.27.

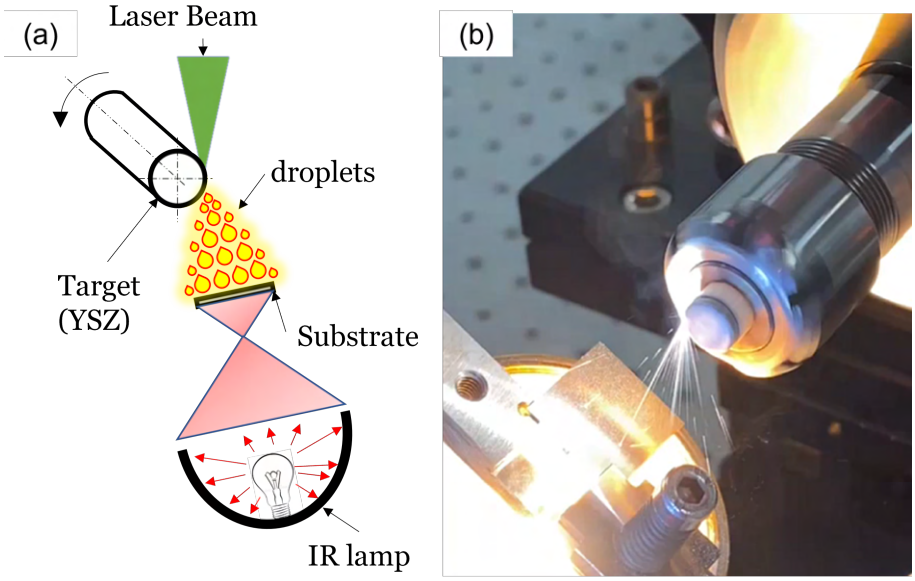


FIGURE 7.27: Liquid droplet laser deposition (LDLD) process. (a) schematic view showing droplet formation; (b) photograph was taken during the experiment.

As it was previously shown in the high-speed footage, the high power density of the laser can generate conditions necessary for melt removal from the pool, presumably by boiling YSZ within the pool. A similar phenomenon is often encountered in laser sputtering, which is considered a thermal side effect of laser ablation.

The reason for such liquid removal from the pool falls into one of the following categories: phase explosion, also known as "explosive boiling", and subsurface boiling. Melt expulsion by the recoil pressure plays an insignificant role given the long distances a droplet may travel.

However, the actual removal mechanisms have been a field of scientific debate. Kelly and Miotello [151] argued about the physical existence of the "subsurface heating" phenomenon.

Generally, *phase explosion* is attributed to high fluence and short pulse irradiation. As proposed by Martynyuk in the early works on explosive boiling [203], boiling cannot occur at short and ultrashort pulse irradiation since the timescale does not allow for heterogeneous nucleation of bubbles. Thus, the liquid approaches the critical thermodynamic temperature and homogenous nuclei form resulting in explosive relaxation of the surface into a mixture of vapour and equilibrium liquid

droplets.

Subsurface heating, an alternative explosion mechanism, initially proposed by Dabby and Paek [56]. The authors assumed that upon high-intensity laser irradiation, subsurface temperatures exceed that of the surface temperature by up to 3000K; as a result, the material is removed in an explosive manner.

According to Kelly and Miotello [151], this phenomenon was considered wrong for two reasons: i original authors neglected vaporisation without reasonable justification, which lead to exaggerated results; (ii) original model of Dabby and Paek used the Dirichlet boundary conditions at the surface, and fixed surface temperature to melting and vaporisation temperatures in different works. Kelly et al. argued that this case is valid only for the case of very slow heating (normal boiling, when this boundary condition is not fixed), or for very fast boiling, i.e. explosive boiling when the temperature approaches critical temperature. The corrected model of Kelly and Miotello shows that the subsurface temperature exceeds the surface temperature only by a few degrees.

Nonetheless, in the case of YSZ melting, the subsurface heating mechanism is proposed to be responsible for material ejection. While the assumptions of Kelly et al. are reasonable, both considerations, whether critical decomposition or subsurface heating, lack a crucial property of zirconia-based ceramics: its low absorptance coefficient in its fully dense state for infrared radiation. In contrast with TBCs, fully dense YSZ does not have an abundance of internal defects, i.e. microcracks and pores, and the absorption by inelastic scattering is limited.

At 1μm wavelength, the absorptance of dense cubic YSZ is only 300 1/cm [178], and according to Beer-Lambert law, the laser irradiance decreases e times after passing 33 μm into the material, and $(1-e)$ portion of the beam will still propagate further. At the same time, the surface of the target exhibit cooling by convection and radiation. At the same time, the incoming radiation penetrates through the ceramic and heats it up from the inside. Besides, the duration of the process is far from short and ultrashort pulse ablation, and the surface has sufficient time for homogenous bubble nucleation.

The deposited droplets at the substrate are presented in Fig. 7.28. Solidified droplets of different shapes were found at the surface, such as flat and round splats(Fig. 7.28, a), flat splats with raptured border (Fig. 7.28, b-c), nearly spherical splats that did not have sufficient kinetic energy at the substrate surface (flat and round splats(Fig. 7.28, d, f). The size of the splats was generally in a wide range between 4 and 50 *mu*m (7.28, e-f).

In thermal spraying, substrate preheating is considered the parameter responsible for the splat shape [180]. Besides, the jetting dynamics also depend on the velocity of the splat at the moment of impact, its size, and its temperature at the moment of impact. The variation of these parameters in the droplets leads to different shapes of the splats.

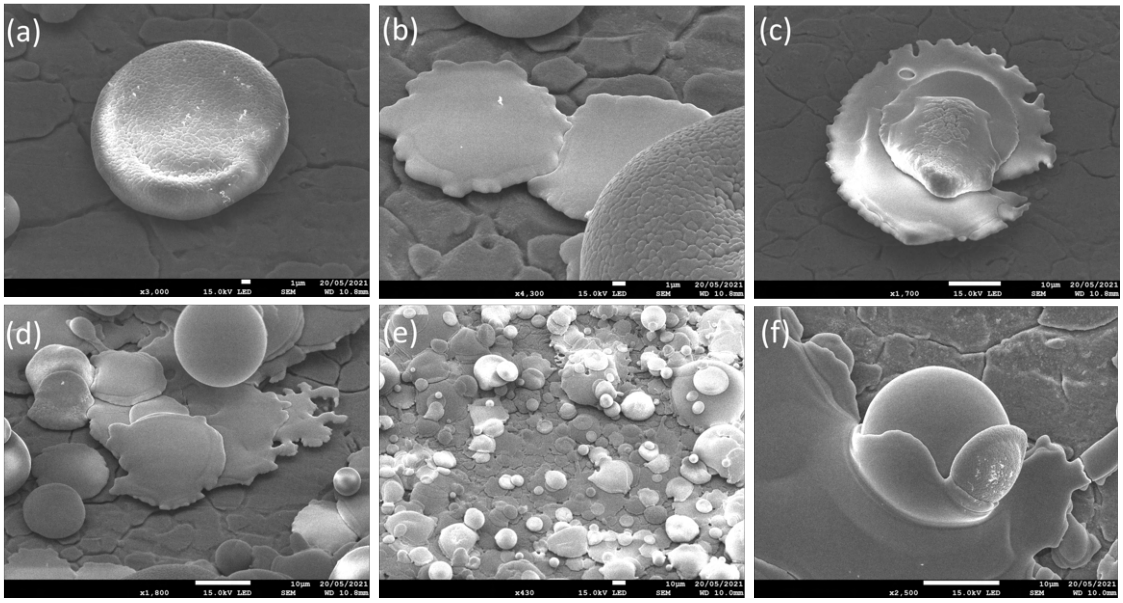


FIGURE 7.28: Various splat shapes achieved with LDLD method. Average power 88W, beam waist 30 μm. Linear velocity at the target surface is 44 mm/s, and target-substrate distance is 5mm.

EDS analysis, presented in Fig.7.29 confirms that the splat have zirconium in their composition.

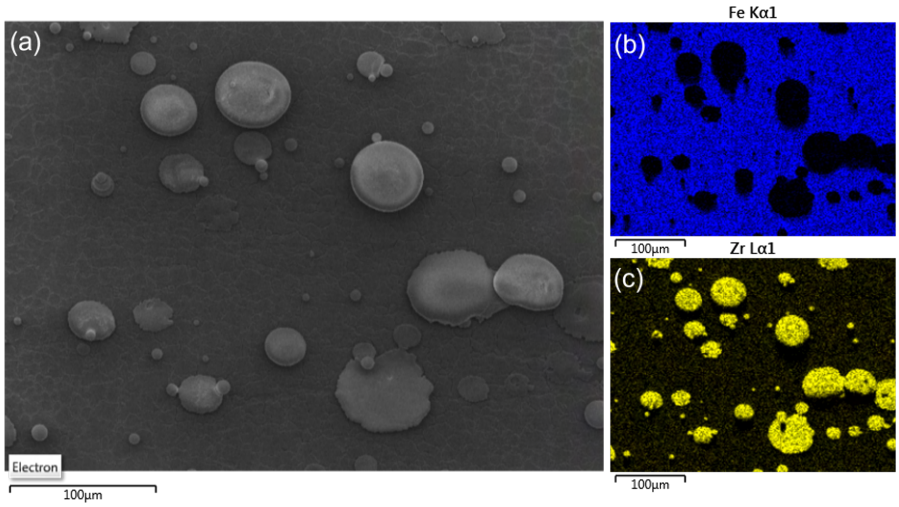


FIGURE 7.29: BSE image and corresponding Fe and Zr elemental map of the substrate after LDLD process. Average power 88W, beam waist 30 μm. Linear velocity at the target surface is 44 mm/s, and target-substrate distance is 5mm.

Although the surface of the splats presented above is nearly always smooth, some examples previously shown in Fig. 7.28, c, and Fig. 7.30 reveal the loss of planar stability of solid-liquid interface during splat solidification; cooling rates as high as $10^8 K/s$ can be expected [28]. According to the study of Liu et al. [190], a stable planar interface is typical for high cooling rates due to complete solute trapping. At relatively low thermal gradients, cellular solidification was observed.

This is the opposite with the interface stability findings discussed in the previous chapter, where an increase in cooling rate GR (interface velocity R in particular) resulted in the loss of interface stability; in laser melting of YSZ the interface velocities R were relatively low, therefore resulting in low cooling rates $G \cdot R$. Besides, such patterns are generally present on large and thick splats, i.e. far from the interface with metal, which reduces the heat flow to the metallic substrate and generates lower cooling rates.

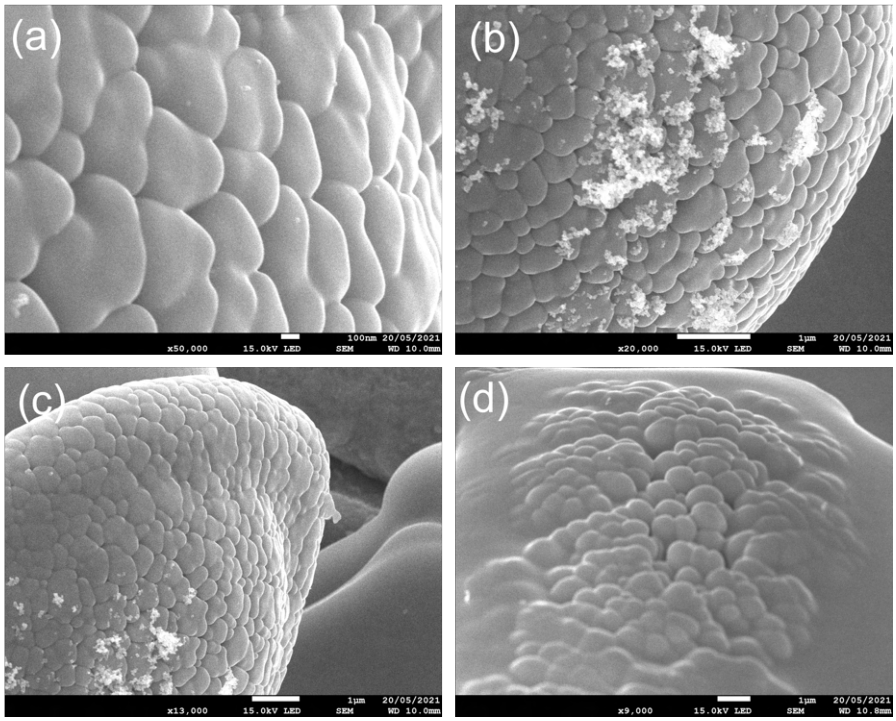


FIGURE 7.30: BSE images showing cellular solidification of YSZ splays. Average laser power 88W, beam waist 30 μm. Linear velocity at the target surface is 44 mm/s, and target-substrate distance is 5mm.

After a prolonged experiment, it is possible to achieve good coverage of the surface. A side of the sample is shown in Fig. 7.31, where the sample underwent 60 seconds of LDLD deposition. Although the majority of the splats have flattened and the amount of spherical splats is insignificant, a shadow exists under the substrate in Fig. 7.31 a, which is a sign of coating delamination. Although adhesion tests have not been carried out in the current study, the adhesion of the initial layer to the substrate may be limited. This is in part due to the low speed of the ejected droplets. There is another possible reason for coating delamination: mismatch of coefficient of thermal expansion between 4.9wt%YSZ and stainless steel coating, and the delamination could start during the cooling phase.

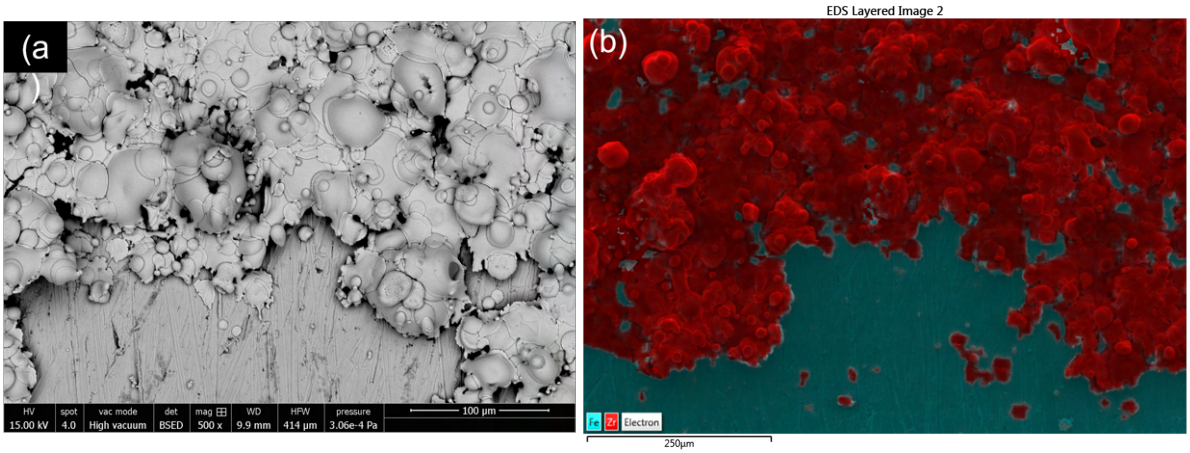


FIGURE 7.31: BSE image and corresponding EDS map showing sample coverage with the coating at the side of the coating. Average laser power 88W, beam waist 30 μm. Linear velocity at the target surface is 44 mm/s, target-substrate distance is 5mm, and laser irradiation time is 120 seconds.

A general overview of the coating achievable with such a method is shown in Fig. 7.32. All the surface is covered with generally small splats. A large number of spherical particles (note large spherical droplets with signs of dendritic solidification in Fig. 7.32, b) signalising some amount of low-velocity droplets. Porosity is particularly evident in Fig. 7.32, c. High magnification BS image, shown in Fig. 7.32, d, reveals the short (¡5 μm) microcracks within the splats formed as a consequence of stress relaxation during cooling.

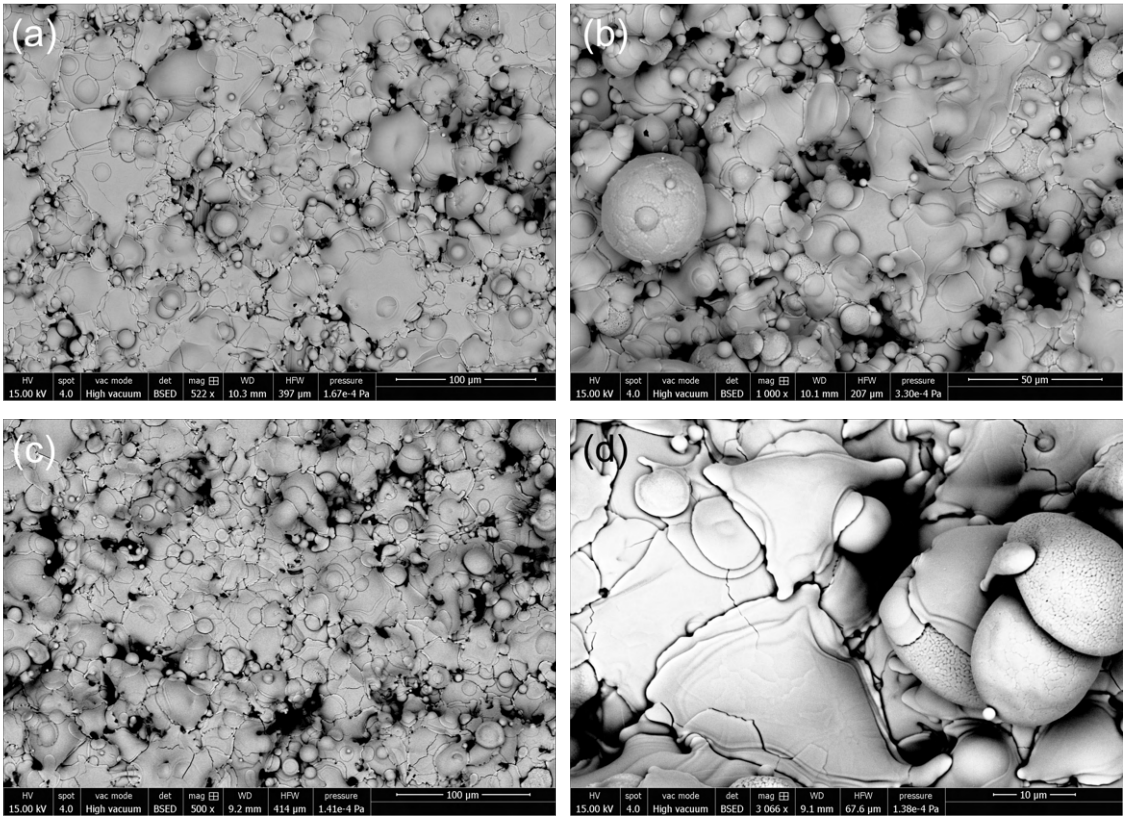


FIGURE 7.32: BSE images showing the surface topology and coating coverage at different magnifications and instances. (a) 522x; (b) 1000x; (c) 500x ; (d) 3066x. Average laser power 88W, beam waist 30 μm. Linear velocity at the target surface is 44 mm/s, target-substrate distance is 5mm, and laser irradiation time is 120 seconds.

A comparison of YSZ deposited via state-of-the-art APS method and proposed LDLD under the same magnification is shown in 7.32. Typical defects of APS coating are present in LDLD coating as well, such as pores and microcracks; the unmolten spherical globules present in APS coating cannot exist in LDLD coating since all the deposited material undergoes phase transformation, however, the droplets with low deformation present a very similar defect.

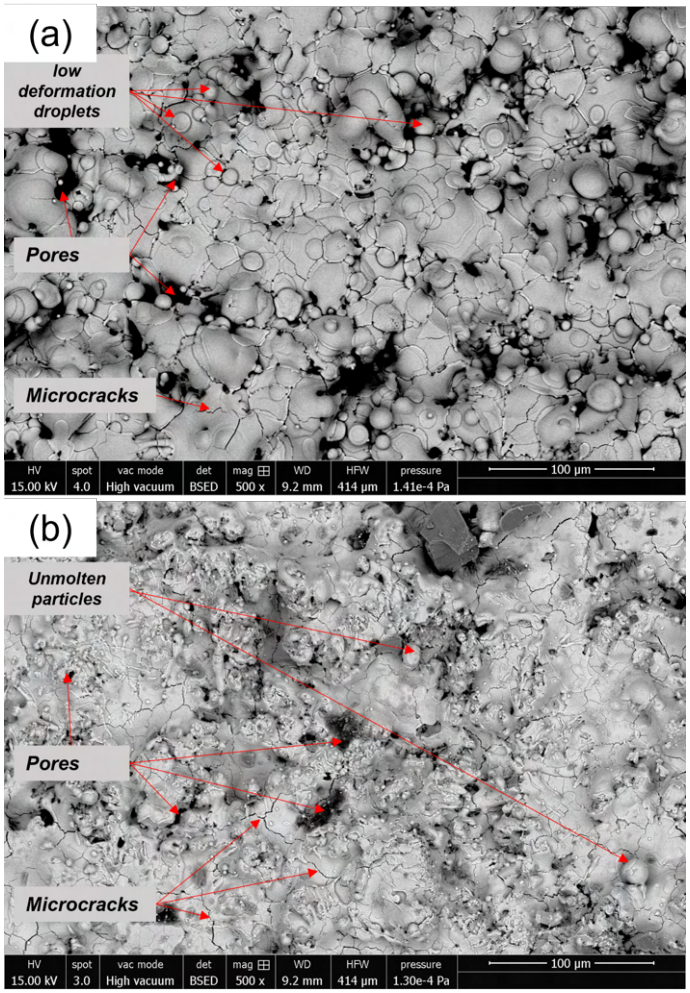


FIGURE 7.33: BSE images showing surface topology and typical defects present in (a) LDLD coating; (b) APS coating. 500x magnification.

The main issue with the LDLD manufactured coatings is their inconsistent velocity and the particle distribution which potentially may be tailored with appropriate laser apparatus. Previously, the subsurface heating model was discussed and proposed as a response mechanism for material removal from the liquid pool. This results in the formation of a relatively large melt pool and explosion from its whole volume. The process may benefit from at least two potential modifications into the laser system:

• Using a short-pulse, such as a nanosecond, high output average laser. The nature of a nanosecond laser pulse may change the removal mechanism from subsurface heating to explosive boiling at the surface. Explosive boiling is known to happen at a thermodynamic critical point, i.e. the endpoint temperature of the equilibrium curve, at which the substance is both vapour and liquid coexist. In this case, the

supercritical interface breaks down and explodes, which may result in the finer size of the droplets and their higher acceleration. Besides, as the critical point is generally higher than the boiling point (and, to the best of the author's knowledge, remains unknown for ZrO_2), this would create a higher initial temperature of the vapour and higher recoil pressures.

• By changing the wavelength of the laser, e.g. by using a second or higher harmonic generator or switching to excimer or gas lasers, it is possible to change the depth of laser penetration through the coating. At shorter wavelengths, e.g. green or UV and below, the absorptance of YSZ increases [178] and can result in shallower melt pools with more homogenous temperature distribution.

7.3.4 Atmospheric Vapour Laser Deposition (AVLD) method

The lower power density of the incoming laser radiation at the target material can generate conditions favourable for steady-state vaporisation. As it was shown with the aid of high-speed imaging, low power densities and sufficient laser power melt the target and create a steady plasma plume at the surface of the melt pool. It was assumed that the plume in the plasma state due to its high vibrant emission in a wide wavelength spectrum, caused by continuous atom excitation, ionisation, and recombination with an electron; however, vapour and plasma terms are used here interchangeably for the partially ionised vapour.

The apparatus used for v is presented in Fig. 7.34. A rotating target acts as a material donor which is irradiated with a laser such that a steady vapour plume is generated. It is important to suppress other material ejection mechanisms, particularly subsurface heating and phase explosion in order to achieve consistent deposition from the vapour phase. Such conditions can be achieved via parameter optimisation of laser processing, i.e. laser fluence, power density, average power, and target rotation speed. To increase adhesion, the substrate was heated with an infrared lamp up to 250, 500, and 750°C. The laser irradiation time was 30 seconds unless stated otherwise.

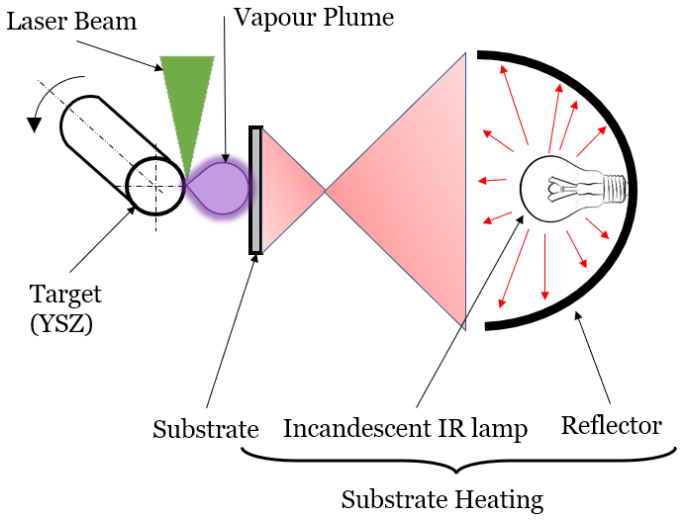


FIGURE 7.34: schematic view of Atmospheric Vapour Laser Deposition (AVLD) technique

A typical coating and its microstructure achieved via the AVLD method are presented in Fig. 7.35, which was achieved with the substrate temperature of 200°C at 200μm target-substrate distance. Part of the coating was mechanically removed with tweezers to show the cross-section, as seen in Fig. 7.35, a-b. The microstructure of the coating is highly porous and consists of interconnected spheres with a sub-micron diameter (Fig. 7.35).

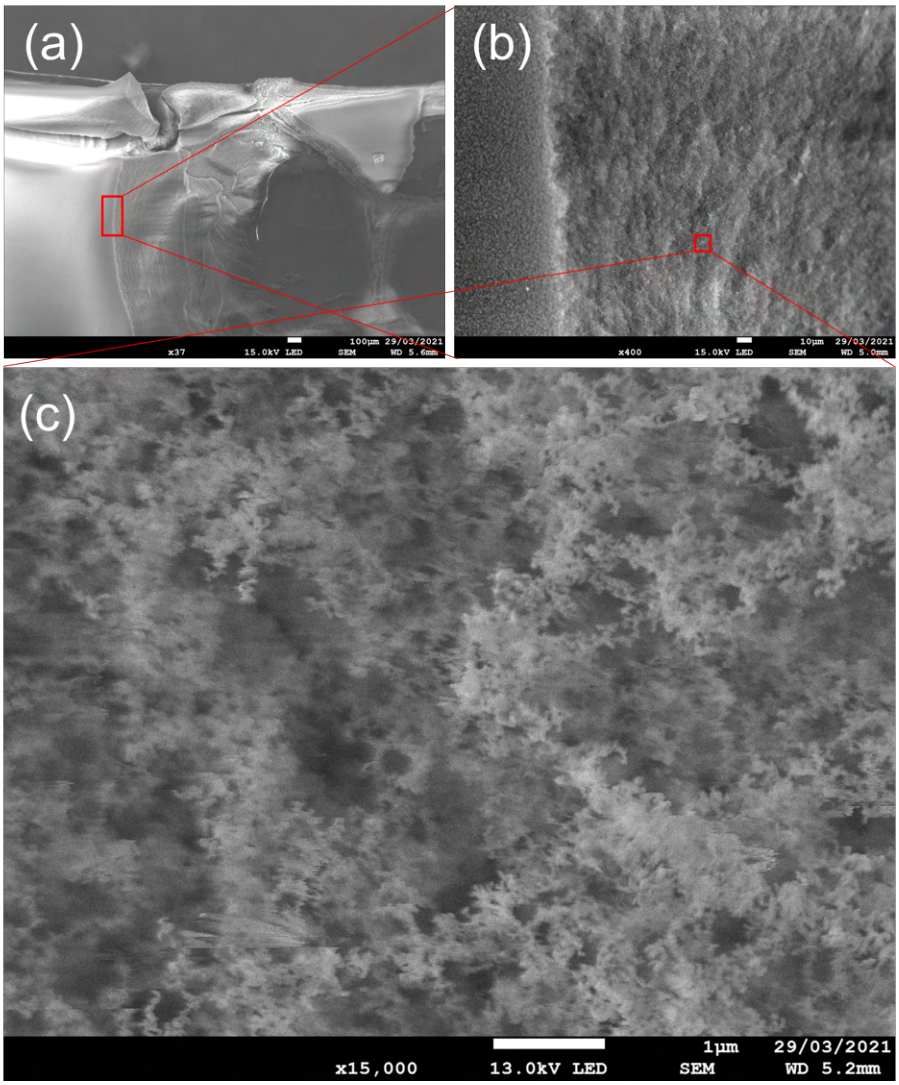


FIGURE 7.35: Top view of the deposited coating via AVLD method, BSE SEM images at different magnifications: (a) x37; (b) x400; (c) x15 000. Substrate temperature 250°C, average laser power 88W, beam waist 200 μm. Linear velocity at the target surface is 44 mm/s, target-substrate distance is 200μm.

Similar tests have been carried out at different substrate temperatures (500°C and 750°C), however, the influence of substrate temperature on the coating microstructure was not observed, and the coating still consists of nearly 100 μm spheres, an example achieved with 750°C is shown in Fig. 7.36. Although the substrate temperature can be expected to promote adhesion, which was out of the scope of this study, higher substrate temperatures may also increase the sintering of neighbouring nanospheres. Nevertheless, such behaviour was not observed as both 250°C and 750°C substrate temperatures lead to similar sintering conditions.

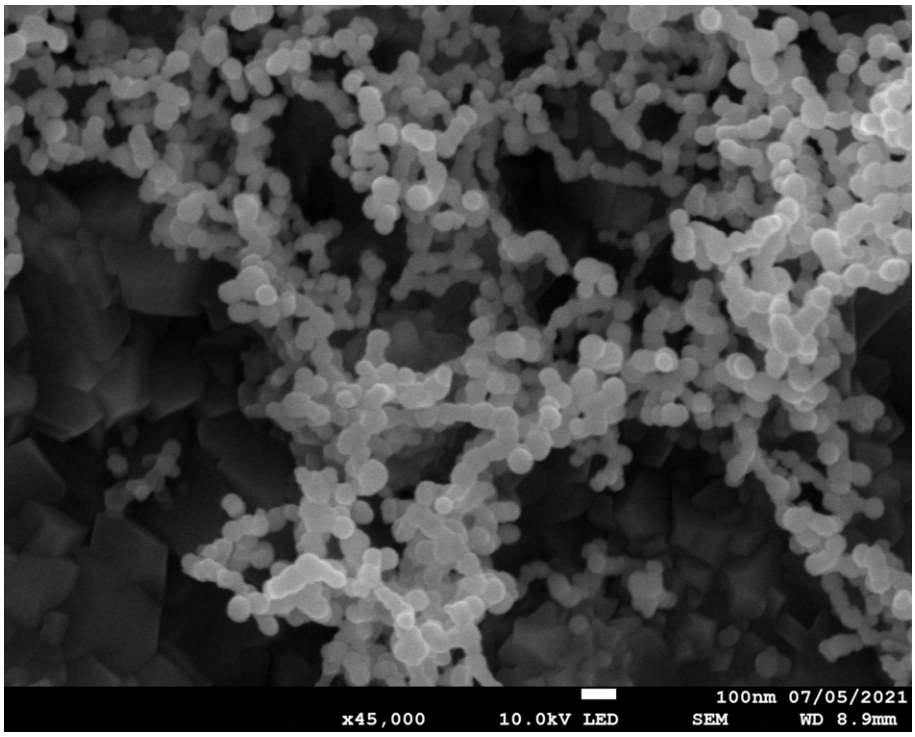


FIGURE 7.36: High magnification SE image of interconnected YSZ nanospheres deposited via AVLD method, x45 000. Substrate temperature 750°C, average laser power 88W, beam waist 200 μm. Linear velocity at the target surface is 44 mm/s, target-substrate distance is 200μm.

The target substrate distance is another important parameter in the AVLD deposition method. Large target-substrate distance lead to collisional loss of internal energy of the vapour and condensed liquid droplets. At the same time, a small target-substrate distance would inevitably cause thermal damage to the substrate, and at target-substrate distances of 100 μm, the substrate was melted through due to the incoming heat from the vapour. On the other hand, larger target-substrate distances lead to complete loss of coating adhesion, and the deposited coating at target-substrate distances of 600 μm or more quickly de-bonded from the substrate during cooling. However, as shown in Fig. 7.37, the coating still remained at 500 μm target-substrate distance and had a similar microstructure to that with smaller separation distances.

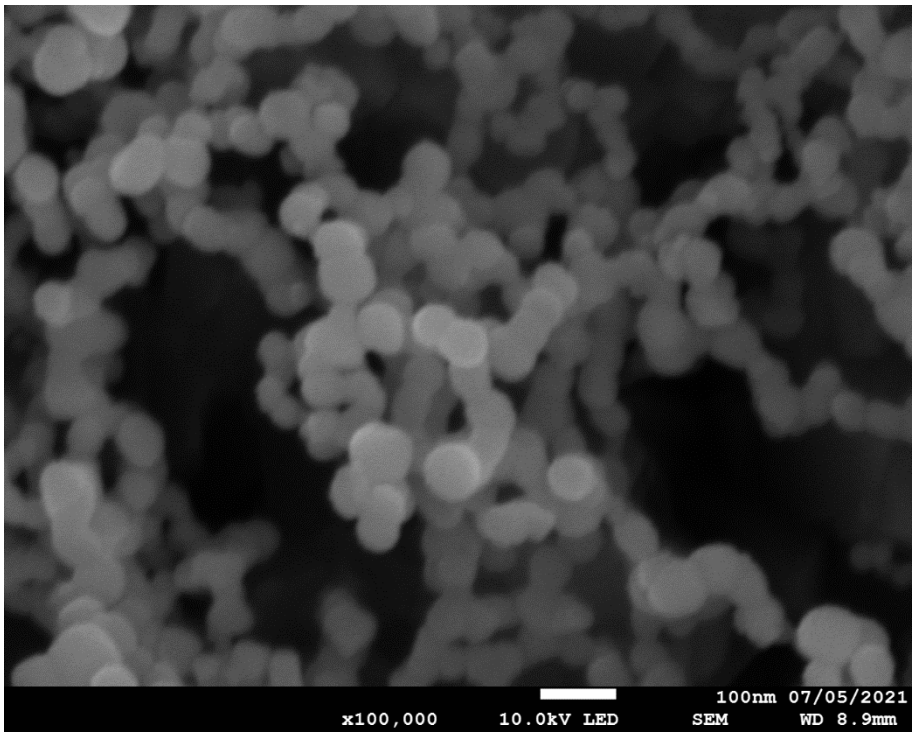


FIGURE 7.37: High magnification SE image of interconnected YSZ nanospheres deposited via AVLD method, x100 000. Substrate temperature 750°C, average laser power 88W, beam waist 200 μm. Linear velocity at the target surface is 44 mm/s, target-substrate distance is 500μm.

A long microcrack and detail of the fracture are shown in Fig. 7.38. Presumably, the microcrack appeared mechanically, as the prolonged thermal cracking of such a porous structure is unlikely. The microcrack appeared due to the rapture of the interlinks between the sintered spheres (Fig. 7.38, c). The high porosity of the coating and random intertwining of the coating is assumed to influence the mechanical properties of the YSZ resulting in the low ultimate strength of such coating and, if such method is used for producing thermal barrier coatings, may compromise erosion resistance. Nonetheless, such high porosity of the coating may be beneficial in low-mechanical impact applications. The thermal conductivity of such coating can be expected to be smaller than that of typical APS coatings, as well as the high thermomechanical compliance. Future work can be attributed to examining the properties of the coating, in particular thermal conductivity and yield strength. To increase the mechanical properties of the coating, a second thermal exposure step may be used. This is a typical step for sol-gel-produced coatings promoting interconnections between the nanoparticles and the coating with the

substrate[169].

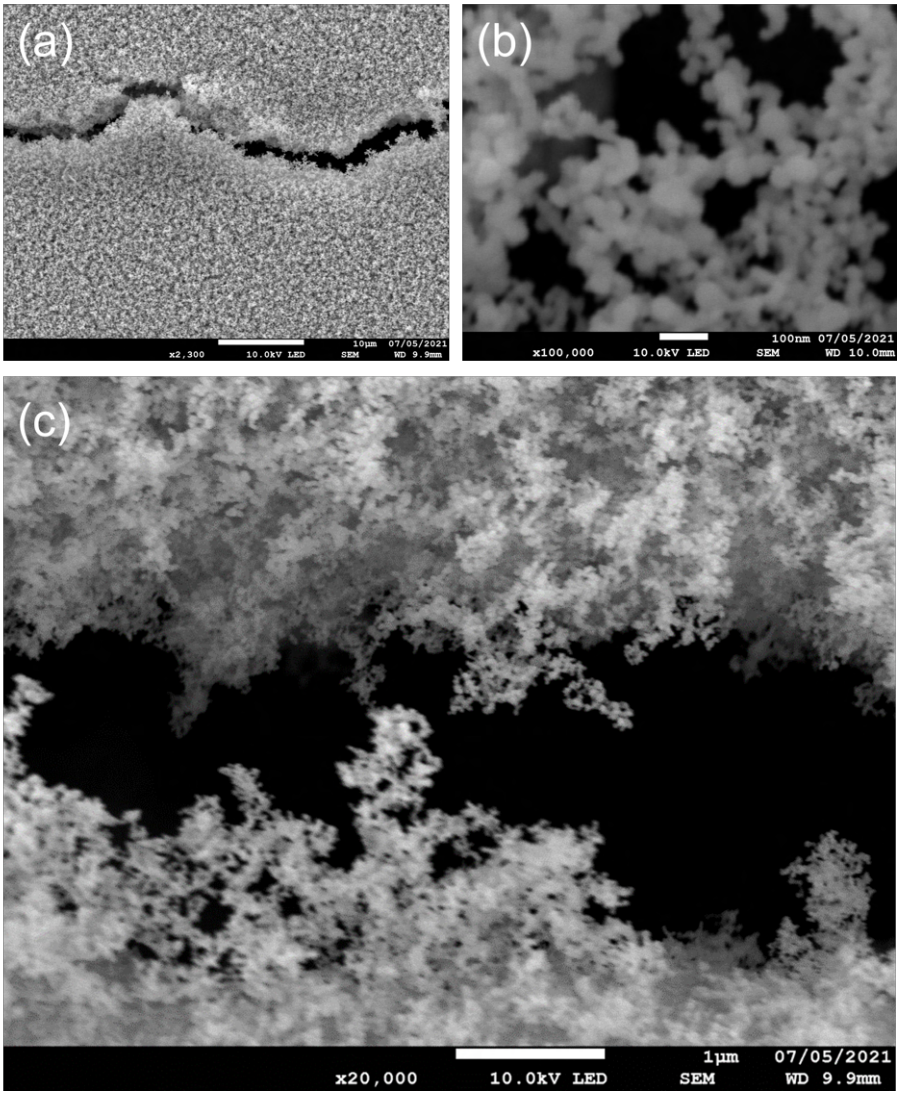


FIGURE 7.38: Top view of a long microcrack at different magnifications. (a) x2300 view showing crack propagation; (b) x100 000 view close to fracture surface; (c) x20 000 view fracture of a porous AVLD structure. Conditions: substrate temperature 750 ° C, average laser power 88W, beam waist 200 μm. Linear velocity at the target surface is 44 mm/s, target-substrate distance is 500μm.

The microstructure of the coating resembles that of the sol-gel-produced coatings [62]. However, in contrast with wet-chemistry methods, there is no chemical waste after the process, typically involving expensive precursors and strong acids for reaction catalysis and requiring drying steps [310].

In contrast with chemical mechanisms of gel formation, the AVLD formation mechanism is purely based on the thermal process. The incoming radiation creates

conditions favourable exclusively for vaporisation as a material removal mechanism. The material is vaporised and may further dissolve into Zr, Y, and O atoms with their further ionisation. Surrounding ambient air is present at 101 kPa has a significant concentration and results in a low mean free path (compared to vacuum conditions) and collisions with air molecules cool down the vaporised molecules. After losing energy on collisions, the molecules condensate and create clusters of removed material, and quick cooling conditions in the atmosphere result in a smaller size of the clusters. The clusters of YSZ remain liquid and after further collisions with air will generate nanoparticles. In fact, this is one of the top-down methods for generating nanoparticles of various materials [322]. However, if the substrate is situated sufficiently close to the target, the droplet will be deposited onto the substrate. Subsequent droplets will continue deposition onto the substrate forming islands of the coating. The incoming liquid droplets of condensed material may solidify on the fly, or remain liquid/partially liquid and solidify at the underlying sphere creating a randomly interconnected network of nanospheres. It should be noted that the whisker deposition was not possible within the tested range of parameters at the AVLD setup. This was attributed to the low density of the generated vapour.

At the lowest target-substrate distance, 150μm, and shorter laser irradiation time (5 seconds), an alternative microstructure was observed, shown in Fig. 7.39. The top view reveal formation of another type of porosity: porosity between the formed columns (Fig. 7.39 a-b). The size of the columns was in the range of 5...10 μm, while the column separation distance was 1 μm or less. A closer look at the column, shown in Fig. 7.39, c, reveals that the coating still consists of sintered nanospheres. The formation of seemingly structured porosity in a random process was attributed to the shadowing effect similar to that of EB-PVD produced coatings, when the solidified molecules block the surface under themself and suppress further deposition [334].

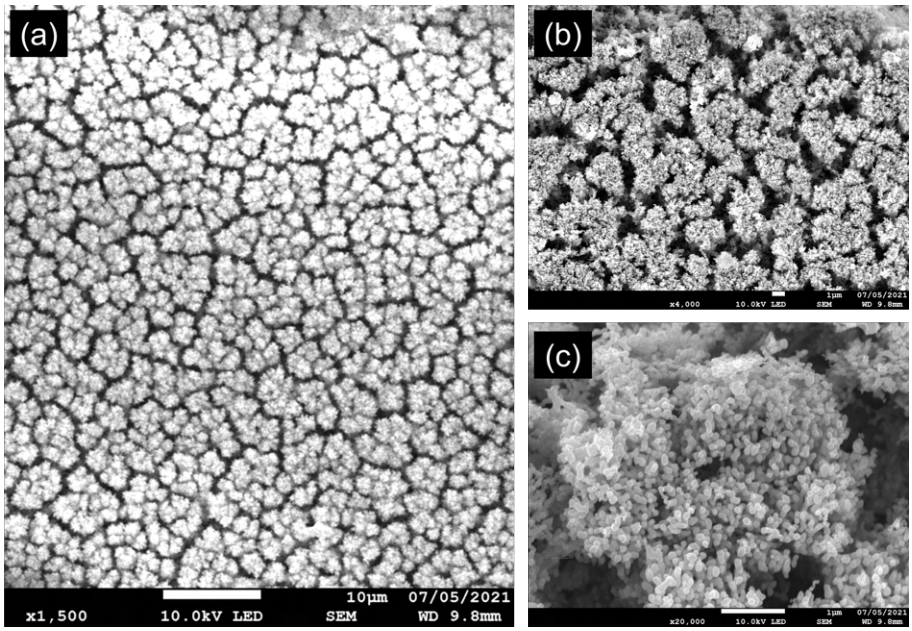


FIGURE 7.39: Top surface SEM images of the central area of the substrate after deposition. (a) x1500 showing the formation of pseudo-columns; (b) close view of the columns (x4000); (c) Microstructure of the column consisting of sintered nanospheres. Conditions: substrate temperature 750°C, average laser power 88W, beam waist 200 μm. Linear velocity at the target surface is 44 mm/s, and target-substrate distance is 150μm. laser irradiation time 30 seconds.

7.4 Summary

In this chapter, several deposition methods have been demonstrated with a focus on coating microstructure. This includes substrate-to-substrate and s family of target-to-substrate deposition methods. Various microstructures have been observed, and formation mechanisms have been proposed. Due to the early-stage research, the repeatability of the apparatus was limited, and further scientific and for the further industrial use of this information statistical studies will be required.

Substrate-to-substrate deposition was found to create highly structured columnar and feather-like coatings. Repeatable redeposition patterns consisting of separated columns were found when using a spiral laser path, effectively preheating the substrate and simultaneously generating a vapour plume for its further deposition. Future work can be dedicated to developing substrate-to-substrate deposition as a coating modification technique to locally recreate columnar microstructure for better thermal fatigue performance. Moreover, this technique

can be further used to restructure CFS/APS sprayed coatings on-wing as a part of coating restoration.

Target-to-substrate deposition techniques in atmospheric pressure were presented here. To date, attention to laser deposition techniques in atmospheric pressure was limited. The reason for neglecting this field are oxidation and the short mean free path, eventually oxidising the coating material and/or losing the energy on the way to the substrate. In the case of oxides, such as ZrO_2 and Y_2O_3 oxidation does not present an issue. In the process of investigations, three different coating formation processes were observed:

• *Liquid droplet laser deposition (LDLD).* These conditions were generated with a high power density of the laser source. The LDLD coating consists of splats and has defects similar to that of thermally sprayed coatings, including microcracking, porosity, and unmelted particles (low deformation particles). Future work can be dedicated to the optimisation of the setup parameters. In particular, a short pulse laser source may be highly beneficial in this regard. Continuous wave irradiation creates conditions of subsurface melting and may result in lower vapour pressures than that of phase explosion. phase explosion, in turn, can generate high recoil pressures and propel the droplets more efficiently.

• *Whiskers formation.* Formation of sub-micron long columns of YSZ was found. Vapour-Liquid-Solid (VLS) mechanism was assumed responsible for coating formation, however, the exact reason remains unknown. Further studies may be dedicated to the recreation of the conditions, and developing this into an atmospheric pressure whisker deposition technique.

• *Atmospheric Vapour Liquid Deposition (AVLD).* Reliable and repeatable formation of interconnected nanospheres in a relatively large process window was shown. Coatings with high porosity and potentially advanced thermal protection properties and high thermomechanical compliance were shown. Future work can be dedicated to achieving control of demanded properties such as porosity, mechanical strength, and adhesion. The development of a sintering step may further help to promote coating strength and adhesion.

As this study was dedicated to exploring the range of possible coatings, coating characterisation was attributed to future work for all types of presented coatings. Studies on coating porosity, thermal conductivity, mechanical strength, and adhesion strength will help to understand the range of possible applications of such coatings and the potential optimisation of the deposition methods based on the analysis.

Chapter 8

General Conclusions

In this thesis, various applications of laser on thermal barrier coatings have been investigated. The primary focus of the work was dedicated to: (i) investigating the microstructure modification of thermal barrier coatings for improved coating performance; (ii) analysis of the coating performance after laser modification and comparison against the as-sprayed APS coatings in simulated in-engine environment; (iii) understanding the laser melting phenomena and grain growth mechanics in solidified thermal barrier coating; (iv) investigating the possible ways to deposit thermal barrier coatings with the aid of a laser tool. The general conclusions of the work are as follows.

8.1 TBC microstructure modification through laser ablation and laser melting approach

Combined laser ablation–laser melting TBC modification approach has been proposed and discussed theoretically. Increase of thermomechanical compliance of the coating was achieved by minimising the in-plane Young's modulus, which was performed with the aid of pulsed laser ablation, and laser melting was performed with a continuous wave laser source. This, in contrast with the laser glazing technique, allows to tailor thermomechanical compliance of the coating while simultaneously applying a protective layer.

It was found that ultrashort pulse picosecond laser ablation can lead to selective ablation of the topcoat with minimal damage to the bondcoat. Such results have not been observed in nanosecond ablation regime, which was explained in terms of thermallisation of the bondcoat lattice with a nanosecond and longer pulses. Material removal mechanisms in short pulse and ultrashort pulse ablation are significantly different; melt expulsion and phase explosion were found to dominate the removal mechanism in short pulse ablation, while the decrease in pulse duration of the laser promotes direct vaporisation of the topcoat. Non-linear effects, resulting from different nature of the topcoat and bondcoat demonstrated the ability to reflect the laser radiation internally thus generating voids inside the material.

The second step of the modification approach is generation of a dense layer enabling mechanical and chemical protection of the underlying lamellar coating. Laser malting of previously grooved TBCs was proven possible, in particular generation of continuous dense layer. In presented study, the coating was grooved in one dimension, thus simplifying the laser melting process. It was found that the dense layer generates cracks as a result of solidification, and these cracks, where possible, align with the underlying grooves.

Unusual crystal formation upon solidification was found in the melting stage, "grain surface sealing". This creates a "sealing" layer of thin surficial layer of grains. This phenomenon was examined and explained in a separate study on grain growth.

8.2 Performance assessment and microstructure characterisation of laser modified thermal barrier coatings

Laser-modified samples of were compared against as-sprayed APS coatings in a number of tests simulating in-engine conditions. The effects of artificially induced porosity after coating deposition, combined with surface densification, generating

vertical and sealed pores via laser beam processing showed that such technique have several advantages against the as-sprayed coating.

Due to surface densification, the erosion resistance of the coating after modification was raised by an average of 8.6 times compared to the as-sprayed coatings. Due to the increased depth of the glazed zone, no significant volume fracture of the densified region was observed. The removal mechanism during erosion tests was changed from splat loss at the splat-splat interface to gradual grinding removal of the coating.

CMAS resistance of the modified coatings was improved due to limiting the CMAS propagation paths into the TBC. While the molten CMAS infiltrates through the porous APS TBC, the modified coating alters CMAS infiltration behaviour; molten silicates in this case propagate through thin crack channels within the dense layer, and later contained within the volume of the groove connected to the microcrack. Higher-temperature CMAS infiltration test was found to remove the whole as-sprayed coating in an explosive manner during cooling phase, while the modified coating remained on the cmponent after the test.

Due to the coating's higher strain tolerance, the thermal cycling life of the coating was extended by 11%. Edge delamination was found responsible for as-sprayed coating failure, while buckling became the dominating failure mechanism for the modified coatings.

After both mechanical impact of erosive particles and thermal cycling, X-ray diffraction demonstrated the presence of a ferroelastic domain switching in the laser-modified state of the YSZ coating. Such behaviour wasn't observed in coatings that had been sprayed. The tensile residual stress within the topcoat layer, arising from thermal spraying process, was reduced using by using melting. The laser-modified coating produced substantial compressive stresses in the thin surficial region, but the as-sprayed coating showed signs of stress relaxation after erosion.

8.3 On the importance of interface stability in cellular automata models: planar and dendritic solidification in laser melted YSZ

Two distinct effects formed during laser melting, were observed in solidified topcoats: grain surface sealing and grain bending. Such effects occur in different conditions and both effects were explained as a consequence of different growth types in diffusion-limited aggregation and interface-limited aggregation, eventually creating planar and dendritic grain morphologies. Besides, various grain morphologies were observed in the laser-melted zirconia, including planar, cellular, and dendritic morphologies.

To explain this, a predictive mathematical tool was developed based on the Cellular Automata(CA) approach. In contrast with already existing CA models, the planar solidification have not found attention in the field.

Fluid flow was found to alter the shape of the melt pool significantly. It is crucial to take the liquid flow into account for precise microstructure predictions. The trailing edge of the melt pool was most severely impacted by internal convection, which accounted for up to 26% of the total heat transfer. With increased scanning speed, the fluid flow's impact on heat transfer reduces.

The proposed multiscale model includes particular characteristics of orientation-independent growth that were captured by approximating the growing element as a sphere. To capture the tetragonal nature of the material, the growing element used in the decentered octahedron algorithms for FCC and BCC crystals was changed with consideration of corresponding crystallographic lattice constants. The modelling results were in good agreement with the experiments.

Grain bending (crystals with bent grain boundary geometry under the surface) and grain surface sealing were found to coexist while laser-melted YSZ solidified (in-plane surficial crystals cover vertical columnar grains). Changing growth velocity in planar and dendritic interfaces were used to describe the creation mechanism.

8.4 Laser deposition in atmospheric pressure

In this work, the possibility of TBC deposition in atmospheric pressure was demonstrated. An area that has been overlooked both academically and industrially showed that different microstructure of the coating may be achieved. Formation mechanisms for each of the deposited microstructure were proposed and discussed.

Substrate-to-substrate deposition, i.e. recast formation with a particular set of parameters, can create columnar microstructure similar to the TBC microstructure deposited from vapour in high vacuum conditions. Formation of columnar, "feather"-like, and "coral"-like microstructure was demonstrated by using a spiral path of the laser beam. Columns with 3-5 μm width and 15-20 μm height were demonstrated.

Two types of target-to-substrate deposition with a laser tool was discovered here.

With the aid of laser melting and recoil pressure it is possible to create a thermal barrier coating, which was attributed to "Liquid droplet laser deposition (LDLD)". Similarly to thermal spraying techniques, LDLD relies on propelled liquid droplets of the material to be deposited; in contrast with thermal spraying, LDLD forms liquid droplets from a bulk material, unlike typically used powder, and phase transition to liquid is an inevitable outcome of the process.

Deposition from vapour phase under atmospheric pressure with the laser tool was found to create a coating consisting of interconnected solidified YSZ nanospheres, which was attributed to "Atmospheric Vapour Liquid Deposition" (AVLD). Coatings produced with this method is characterised with high porosity and potentially high thermomechanical compliance.

Chapter 9

Future Work

In this chapter, potential future work arising from the thesis is discussed. More work is needed to overcome current limitations of the TBC modification technique, and enhance our understanding of the laser melting and laser deposition processes.

9.1 TBC microstructure modification through laser ablation and laser melting approach

The reduction of the glazed layer's thickness, which is what leads to high thermal stresses during thermal cycling, is a primary goal for an optimal modification strategy. This makes creating such a coating even more challenging because, in this case, the thickness of the glazed layer also depends on the width of the previously machined grooves. Other laser manufacturing techniques might be applied in other investigations even though the tools that were accessible were limited. The thickness of the glazed layer can be reduced by either reducing the numerical aperture of the focusing lens, which entails widening the beam at the entrance, or by shortening the lens' focal distance, which will eventually reduce the laser spot size.

Another method of laser spot size minimisation is the decrease of the laser wavelength from 1064nm to higher harmonics, e.g. 532 nm or 355 nm and above, or use excimer laser source. The latter will also promote laser absorption within

the TBC, as zirconia-based ceramics are known to have poor absorption of near-infrared irradiation [37].

Mathematical modelling of the phenomenon may help to better understand the desired geometry of the grooves. While this study was based on simplified calculations of thermal expansion mismatch and its minimisation, the actual physical phenomenon within the TBC layer is rather complex. A comprehensive physical model of TBCs under thermal loads will be beneficial for both building an understanding of the TBC evolution after modification, as well as allow to optimise the grooving and melting geometries.

With further industrialisation of this technique, repeatability of the work should be checked statistically over large set of data in order to ensure repeatable results both of the ablation and melting processes.

9.2 Performance assessment and microstructure characterisation of laser modified thermal barrier coatings

Further work toward TBCs with desired elastic modulus ratio, in particular through thermomechanical modelling, should be carried out in order to obtain thermal barrier coatings with desired characteristics. Besides, the width of the microcracks at the dense layer after laser melting was recognised to be responsible for an increased thermal shock resistance [315].

While the number of samples was limited in this work, the results clearly indicate significant improvement in the erosion resistance of the coating. However, with further use of this technique, erosion resistance of the samples should be measured with a larger set of samples.

Grooving the topcoat in perpendicular dimensions would potentially benefit the coating. Together with careful control of the thickness and geometry of the glazed

layer, this can suppress buckling failure. A pattern of grooves generated at the dense layer can serve this purpose, thus decreasing compressive thermal stresses.

Potentially, wider microcracks would increase the thermomechanical compliance of the topcoat. The width of these cracks may be controlled by the groove pitch and/or ambient temperature during laser melting. At the same time, there is a trade-off between the crack width and resistance of the coating to oxidation, i.e. larger cracks would be a better short path for oxygen penetration to the bondcoat. With regard to CMAS resistance, increasing the crack width would lead to a higher flow rate of molten silicates toward the grooves, and lower CMAS performance.

Minimisation of the groove width will allow for wider parameter range in the laser melting step, and, consequently, reduce the thickness of the dense layer. As buckling was found to dominate the failure mechanism in modified coatings, main efforts should address this failure in order to enhance the properties of the modified coating. One way to reduce it is by adding a third processing step, where the surface of the glazed TBC will be ablated down to the required level. To optimise this step, instead of removal of the whole coating the glazed layer may be covered with grooves, thus repeating the underlying microstructure of the coating. This will allow to reduce the thermal expansion stresses within the glazed layer.

Alterations to the groove are possible, including partial thickness grooving and cascaded groove depths, which may further increase the thermal cycling performance. Various groove geometries with internal voids, the possibility of which was demonstrated in the ultrashort laser ablation regime, may be further developed.

Different laser melting strategies, such as discussed discontinuous and semi-continuous laser melting may be advantageous in conditions where high thermomechanical compliance is more important than resistance to mechanical attacks.

9.3 On the importance of interface stability in cellular automata models: planar and dendritic solidification in laser melted YSZ

In he presented work, the influence of planar and dendritic solidification regimes was demonstrated on laser melted topcoats. To build a better understanding of the process, the model should be validated on a variety of simpler materials, in particular, BCC and FCC metals.

The effects of grain bending and grain surface sealing on the properties of the solidified material may be addressed in the future studies. Mechanical, electrical, magnetic properties of materials are known to depend on the crystal structure of the workpiece. Optimisation of the grain orientation and geometry may allow to build materials with unprecedented properties in the future.

The key feature of the proposed model is its ability to distinguish different solidification modes, and adjust the velocity of the process respectively. Presented model is based on the LGK models for dendritic growth, which makes the model relatively fast, compared to the models assuming complete dendrite formation since the diffusion equation can be neglected. Moreover, the planar solidification modelling is significantly faster to calculate than even the LGK model due to simple vectorisation of the solution. Future work may address these advantages of the model and generate an inverse model for grain growth, thus allowing to find the necessary laser parameters for desired grain geometry.

Future work may be also dedicated to the investigation of the influence of planar and dendritic solidification on resultant orientation of the remelted coating. It as noted that planar solidification mode is likely to be indifferent to the orientation of the seed crystal, while dendritic growth causes orientation competition of the neighbouring crystals and results in selection of preferred orientation. APS TBCs typically have a characteristic [100] texture resulting from rapid solidification of the droplets. Therefore, it was difficult to build certain conclusions of orientation

evolution during laser melting; separate study on the evolution of orientation in planar and dendritic growths, conducted with random initial orientation and stong but varied texture of the initial workpiece material, will promote understanding in the origin of crystal orientation.

9.4 Laser deposition in atmospheric pressure

As this study was dedicated to exploring the range of possible coating microstructures, limited attention was paid to the properties of the resultant coatings. A comprehensive study on the mechanical characteristics, in particular adhesion strength and adhesion mechanisms, are necessary to enable any of the proposed techniques. For substrate-to-substrate deposition, i.e. surface modification with surficial columnar microstructure, mechanical strength, coating porosity, and thermal conductivity must be studied. Besides, the microstructure deviation within a given set of conditions was out of the scope of this work, however should be addressed in future studies.

In order to understand coating performance, a series of tests in simulated engine conditions must me performed; in particular, resistance of the AVLD coatings to mechanical damage should be checked and porosity of the coating optimised based on this data. LDLD coatings would also suffer from erosion damage due to multiple splat interfaces and limited splat-to-splat bonding; thermal shock characteristics of the coatings, in particular LDLD-produced topcoats, must be checked.

Based on the results, the LDLD technique may be further optimised in terms of particle velocity. Particle velocities in the proposed process were much lower than that of the typical APS speeds (30m/s against 150-200m/s). While the main source for the speed in APS process is the propellant gas accelerating the particles, LDLD relies on liquid ejection mechanics and the associated vapour pressure. Increasing the velocity of the droplets may lead to better mechanical interlocking of splats and better adhesion of the coating. This can be done by adding an external acceleration source, e.g. from combustion, plasma, or adding high pressure gas.

However, the size of the droplets is in LDLD deposition was found to be approx. 5-20 μm, resulting in low active surface area useful for acceleration. Another method would rely on changing the laser source and adjusting the laser parameters. In the present study, the laser used for LDLD deposition is a continuous wave source. Applying the same technique with a pulsed laser, in particular with the widely used Q-switched lasers providing high power densities, will enhance the recoil pressure and increase the velocity of the droplets. Besides, the properties of the LDLD-produced coating, such as resistance to molten silicates and erosion, may be enhanced with laser glazing or combined modification approach, proposed in this work.

With regard to AVLD technique, it was possible to achieve a coating consisting from nanospheres. While the properties of the coating was not measured within this study, it would be safe to assume based on the SEM images that the adhesion strength as well as mechanical strength of the coating is limited due to a low sphere-to-sphere contact surface. One of the ways to optimise this is to introduce a sintering step, where a high temperature can be applied to the coating in order to promote coating cohesion and adhesion.

References

[1] Raheleh Ahmadi-Pidani, Reza Shoja-Razavi, Reza Mozafarinia, and Hossein Jamali. Improving the thermal shock resistance of plasma sprayed cysz thermal barrier coatings by laser surface modification. *Optics and Lasers in Engineering*, 50(5):780–786, 2012.

[2] S. Ahmaniemi, P. Vuoristo, T. Mäntylä, F. Cernuschi, and L. Lorenzoni. Modified thick thermal barrier coatings: Thermophysical characterization. *Journal of the European Ceramic Society*, 24(9):2669–2679, 2004.

[3] Naveed Ahmed, Saied Darwish, Abdulrehman M Alahmari, and Muhammad Ali Shar. Micro-channels by nd: Yag laser beam machining: fabrication, microstructures, and micro-hardness profiles. *The International Journal of Advanced Manufacturing Technology*, 85(9):1955–1968, 2016.

[4] KM Ahmmed, Colin Grambow, and Anne-Marie Kietzig. Fabrication of micro/nano structures on metals by femtosecond laser micromachining. *Micromachines*, 5(4):1219–1253, 2014.

[5] Taotao Ai, Fen Wang, Xiaoming Feng, and Miaomiao Ruan. Microstructural and mechanical properties of dual ti3alc2–ti2alc reinforced tial composites fabricated by reaction hot pressing. *Ceramics International*, 40(7):9947–9953, 2014.

[6] Javed Akram, Pradeep Chalavadi, Deepankar Pal, and Brent Stucker. Understanding grain evolution in additive manufacturing through modeling. *Additive Manufacturing*, 21(February):255–268, 2018.

[7] Stephen Akwaboa, Patrick Mensah, and Ravinder Diwan. Effects of thermal radiation on air plasma spray (aps) coated gas turbine blade. *Proceedings of*

the ASME Turbo Expo, 4(PARTS A AND B):627–633, 2010.

[8] Nisar Ali, Shazia Bashir, Mahreen Akram, Khaliq Mahmood, et al. Effect of dry and wet ambient environment on the pulsed laser ablation of titanium. *Applied surface science*, 270:49–57, 2013.

[9] Julian M Allwood, Tom HC Childs, Adam T Clare, Anjali KM De Silva, Vimal Dhokia, Ian M Hutchings, Richard K Leach, David R Leal-Ayala, Stewart Lowth, Candice E Majewski, et al. Manufacturing at double the speed. *Journal of Materials Processing Technology*, 229:729–757, 2016.

[10] Robert Almgren. Variational algorithms and pattern formation in dendritic solidification. *Journal of computational physics*, 106(2):337–354, 1993.

[11] SI Anisimov, BL Kapeliovich, TL Perelman, et al. Electron emission from metal surfaces exposed to ultrashort laser pulses. *Zh. Eksp. Teor. Fiz*, 66(2):375–377, 1974.

[12] AFM Arif, BS Yilbas, and BJ Abdul Aleem. Laser cutting of thick sheet metals: Residual stress analysis. *Optics and Laser Technology*, 41(3):224–232, 2009.

[13] M. Asta, C. Beckermann, A. Karma, W. Kurz, R. Napolitano, M. Plapp, G. Purdy, M. Rappaz, and R. Trivedi. Solidification microstructures and solid-state parallels: Recent developments, future directions. *Acta Materialia*, 57(4):941–971, 2009.

[14] Kellar Autumn, Metin Sitti, Yiching A Liang, Anne M Peattie, Wendy R Hansen, Simon Sponberg, Thomas W Kenny, Ronald Fearing, Jacob N Israelachvili, and Robert J Full. Evidence for van der waals adhesion in gecko setae. *Proceedings of the National Academy of Sciences*, 99(19):12252–12256, 2002.

[15] Aysegul Aygun. *Novel Thermal Barrier Coatings (TBCs) that are resistant to high temperature attack by CaO-MgO-Al2O3-SiO2 (CMAS) glassy deposits.* PhD thesis, The Ohio State University, 2008.

[16] Aysegul Aygun, Alexander L Vasiliev, Nitin P Padture, and Xinqing Ma. Novel thermal barrier coatings that are resistant to high-temperature attack by glassy deposits. *Acta Materialia*, 55(20):6734–6745, 2007.

[17] M. J. Aziz. Model for solute redistribution during rapid solidification. *Journal of Applied Physics*, 53(2):1158–1168, 1982.

[18] M. J. Aziz and W. J. Boettinger. On the transition from short-range diffusion-limited to collision-limited growth in alloy solidification. *Acta Metallurgica Et Materialia*, 42(2):527–537, 1994.

[19] Peter Baldus, Martin Jansen, and Dieter Sporn. Ceramic fibers for matrix composites in high-temperature engine applications. *Science*, 285(5428):699–703, 1999.

[20] Vamsi Krishna Balla, Partha P Bandyopadhyay, Susmita Bose, and Amit Bandyopadhyay. Compositionally graded yttria-stabilized zirconia coating on stainless steel using laser engineered net shaping (lens™). *Scripta Materialia*, 57(9):861–864, 2007.

[21] Narottam P Bansal and Sung R Choi. Properties of cmas glass from desert sand. *Ceramics international*, 41(3):3901–3909, 2015.

[22] L Barilleau, G Duchateau, B Chimier, G Geoffroy, and V Tikhonchuk. Influence of non-collisional laser heating on the electron dynamics in dielectric materials. *Journal of Physics D: Applied Physics*, 49(48):485103, 2016.

[23] Dieter Bauerle. *Laser processing and chemistry*. Springer Science and Business Media, 2013.

[24] Mohamad Bayat, Sankhya Mohanty, and Jesper Henri Hattel. A systematic investigation of the effects of process parameters on heat and fluid flow and metallurgical conditions during laser-based powder bed fusion of ti6al4v alloy. *International Journal of Heat and Mass Transfer*, 139:213–230, 8 2019.

[25] G Bertrand and R Mévrel. Zirconia coatings realized by microwave plasma-enhanced chemical vapordeposition. *Thin Solid Films*,

292(1-2):241–246, 1997.

[26] Tania Bhatia, Alper Ozturk, Liangde Xie, Eric H Jordan, Baki M Cetegen, Maurice Gell, Xinqin Ma, and Nitin P Padture. Mechanisms of ceramic coating deposition in solution-precursor plasma spray. *Journal of materials research*, 17(9):2363–2372, 2002.

[27] Bharat Bhushan. *Encyclopedia of nanotechnology*. Number 544.1. Springer Dordrecht, Netherlands, 2012.

[28] L Bianchi, AC Leger, M Vardelle, A Vardelle, and P Fauchais. Splat formation and cooling of plasma-sprayed zirconia. *Thin Solid Films*, 305(1-2):35–47, 1997.

[29] Mario Birkholz. *Thin film analysis by X-ray scattering*. John Wiley and Sons, 2006.

[30] Srikanth Bontha, Nathan W Klingbeil, Pamela A Kobryn, and Hamish L Fraser. Thermal process maps for predicting solidification microstructure in laser fabrication of thin-wall structures. *Journal of Materials Processing Technology*, 178(1-3):135–142, 2006.

[31] Srikanth Bontha, Nathan W Klingbeil, Pamela A Kobryn, and Hamish L Fraser. Effects of process variables and size-scale on solidification microstructure in beam-based fabrication of bulky 3d structures. *Materials Science and Engineering: A*, 513:311–318, 2009.

[32] V Bruyere, C Touvrey, and P Namy. Comparison between phase field and ale methods to model the keyhole digging during spot laser welding. *Proceedings of the 2013 COMSOL Conference*, pages 1–7, 2013.

[33] Wit C Bushko and Vijay K Stokes. Solidification of thermoviscoelastic melts. part ii: Effects of processing conditions on shrinkage and residual stresses. *Polymer Engineering and Science*, 35(4):365–383, 1995.

[34] Jeppe Byskov-Nielsen, Juha-Matti Savolainen, Martin Snogdahl Christensen, and Peter Balling. Ultra-short pulse laser ablation of metals: threshold fluence,

incubation coefficient and ablation rates. *Applied Physics A*, 101(1):97–101, 2010.

[35] Gunduz Caginalp and Paul Fife. Phase-field methods for interfacial boundaries. *Physical Review B*, 33(11):7792, 1986.

[36] XQ Cao, R Vassen, and D Stoever. Ceramic materials for thermal barrier coatings. *Journal of the European Ceramic Society*, 24(1):1–10, 2004.

[37] D. Cha and D. Axinte. Transient thermal model of nanosecond pulsed laser ablation: Effect of heat accumulation during processing of semi-transparent ceramics. *International Journal of Heat and Mass Transfer*, 173:121227, 2021.

[38] D Cha, OG Diaz, Z Liao, D Gilbert, D Axinte, J Kell, A Norton, M O'Key, MR Osborne, and D Main. Development of a novel system for in-situ repair of aeroengine airfoil via pulsed laser ablation. *Journal of Manufacturing Systems*, 55:126–131, 2020.

[39] NK Chaudhury, R Gupta, and S Gulia. Sol-gel technology for sensor applications. *Defence Science Journal*, 57(3):241, 2007.

[40] J I E Chen. Modelling of laser welding of aluminium using comsol multiphysics. 2020.

[41] Kai Chen and Y Lawrence Yao. Striation formation and melt removal in the laser cutting process. *Journal of Manufacturing Systems*, 18(2):43–53, 1999.

[42] Shanshan Chen, Lola Brown, Mark Levendorf, Weiwei Cai, Sang-Yong Ju, Jonathan Edgeworth, Xuesong Li, Carl W Magnuson, Aruna Velamakanni, Richard D Piner, et al. Oxidation resistance of graphene-coated cu and cu/ni alloy. *ACS nano*, 5(2):1321–1327, 2011.

[43] Shijia Chen, Gildas Guillemot, and Charles André Gandin. Three-dimensional cellular automaton-finite element modeling of solidification grain structures for arc-welding processes. *Acta Materialia*, 115:448–467, 2016.

[44] WR Chen, X Wu, BR Marple, RS Lima, and PC Patnaik. Pre-oxidation and tgo growth behaviour of an air-plasma-sprayed thermal barrier coating. *Surface and Coatings Technology*, 202(16):3787–3796, 2008.

[45] Xi Chen. Calcium–magnesium–alumina–silicate (cmas) delamination mechanisms in eb-pvd thermal barrier coatings. *Surface and Coatings Technology*, 200(11):3418–3427, 2006.

[46] Ying Chen, Chun Li, Xiaofeng Zhao, and Ping Xiao. Measurements and understanding of the stiffness of an air plasma sprayed thermal barrier coating. *Surface and Coatings Technology*, 394:125678, 2020.

[47] Zefei Cheng, Jiasheng Yang, Fang Shao, Xinghua Zhong, Huayu Zhao, Yin Zhuang, Jinxing Ni, and Shunyan Tao. Thermal stability of ysz coatings deposited by plasma spray–physical vapor deposition. *Coatings*, 9(8):464, 2019.

[48] Jerome Chevalier, Sylvain Deville, Etienne Munch, Romain Jullian, and Frederic Lair. Critical effect of cubic phase on aging in 3 mol yttria-stabilized zirconia ceramics for hip replacement prosthesis. *Biomaterials*, 25(24):5539–5545, 2004.

[49] Wen-Tung Chien and Shiann-Chin Hou. Investigating the recast layer formed during the laser trepan drilling of inconel 718 using the taguchi method. *The International Journal of Advanced Manufacturing Technology*, 33(3):308–316, 2007.

[50] Sung Ryul Choi, John W. Hutchinson, and A. G. Evans. Delamination of multilayer thermal barrier coatings. *Mechanics of Materials*, 31(7):431–447, 1999.

[51] Sang Ok Chwa and Akira Ohmori. Thermal diffusivity and erosion resistance of zro2-8 wt. y2o3 coatings prepared by a laser hybrid spraying technique. *Thin Solid Films*, 415(1-2):160–166, 2002.

[52] David R Clarke, Matthias Oechsner, and Nitin P Padture. Thermal-barrier coatings for more efficient gas-turbine engines. *MRS bulletin*, 37(10):891–898, 2012.

[53] DR Clarke and CG Levi. Materials design for the next generation thermal barrier coatings. *Annual review of materials research*, 33(1):383–417, 2003.

[54] E Courtin, Philippe Boy, Thierry Piquero, Julien Vulliet, Nathalie Poirot, and Christel Laberty-Robert. A composite sol–gel process to prepare a ysz electrolyte for solid oxide fuel cells. *Journal of Power Sources*, 206:77–83, 2012.

[55] Nicholas Curry, Matthias Leitner, and Karl Korner. High-porosity thermal barrier coatings from high-power plasma spray equipment—processing, performance and economics. *Coatings*, 10(10):957, 2020.

[56] F Dabby and Un-Chul Paek. High-intensity laser-induced vaporization and explosion of solid material. *IEEE Journal of Quantum Electronics*, 8(2):106–111, 1972.

[57] Narendra B Dahotre and Sandip Harimkar. *Laser fabrication and machining of materials*. Springer Science and Business Media, 2008.

[58] S. A. David and T. DebRoy. Current issues and problems in welding science. *Science*, 257(5069):497–502, 1992.

[59] Walt A De Heer, Claire Berger, Xiaosong Wu, Phillip N First, Edward H Conrad, Xuebin Li, Tianbo Li, Michael Sprinkle, Joanna Hass, Marcin L Sadowski, et al. Epitaxial graphene. *Solid State Communications*, 143(1-2):92–100, 2007.

[60] T. DebRoy. Hl wei, js zuback, t. mukherjee, jw elmer, jo milewski, am beese, a. wilson-heid, a. de, and w. zhang,"additive manufacturing of metallic components—process, structure and properties. *Progr. Mater. Sci.*, 92:112–224, 2018.

[61] T. Debroy and S. A. David. Physical processes in fusion welding. *Reviews of Modern Physics*, 67(1):85–112, 1995.

[62] Amir Dehghanghadikolaei, Jamal Ansary, and Reza Ghoreishi. Sol-gel process applications: A mini-review. *Proc. Nat. Res. Soc*, 2(1):02008–02029, 2018.

[63] Elodie Delon, Florence Ansart, S Duluard, Jean-Pierre Bonino, Daniel Monceau, Aurélie Rouaix, Ronan Mainguy, Carole Thouron, André Malié, Aurélien Joulia, et al. Outstanding durability of sol-gel thermal barrier coatings reinforced by ysz-fibers. *Journal of the European Ceramic Society*, 38(14):4719–4731, 2018.

[64] SR Dhineshkumar, Muthukannan Duraiselvam, S Natarajan, SS Panwar, Trilochan Jena, and Muhammed Anaz Khan. Enhancement of strain tolerance of functionally graded lati2al9o19 thermal barrier coating through ultra-short pulse based laser texturing. *Surface and Coatings Technology*, 304:263–271, 2016.

[65] Francesca Di Niso, Caterina Gaudiuso, Teresa Sibillano, Francesco Paolo Mezzapesa, Antonio Ancona, and Pietro Mario Lugarà. Role of heat accumulation on the incubation effect in multi-shot laser ablation of stainless steel at high repetition rates. *Optics express*, 22(10):12200–12210, 2014.

[66] Hong-qiang Dou, Cai-zhen Yao, Hao Liu, Yi Wan, Ren-jie Ding, Xiao-dong Yuan, and Shi-zhen Xu. Femtosecond laser ablation of al-mg alloy in vacuum and air. *Applied Surface Science*, 447:388–392, 2018.

[67] Julie M. Drexler, Angel L. Ortiz, and Nitin P. Padture. Composition effects of thermal barrier coating ceramics on their interaction with molten ca-mg-al-silicate (cmas) glass. *Acta Materialia*, 60(15):5437–5447, 2012.

[68] Julie M. Drexler, Kentaro Shinoda, Angel L. Ortiz, Dongsheng Li, Alexander L. Vasiliev, Andrew D. Gledhill, Sanjay Sampath, and Nitin P. Padture. Air-plasma-sprayed thermal barrier coatings that are resistant to high-temperature attack by glassy deposits. *Acta Materialia*, 58(20):6835–6844, 2010.

[69] EASA. European aviation environmental report 2019. (TO-01-18-673-EN-N):112, 2019.

[70] Shane M Eaton, Haibin Zhang, Peter R Herman, Fumiyo Yoshino, Lawrence Shah, James Bovatsek, and Alan Y Arai. Heat accumulation effects in femtosecond laser- written waveguides with variable repetition rate. 13(12):2496–2504, 2005.

[71] EKSPLA. Atlantic he series laser. technical description and user manual. 2014.

[72] G. A. El-Awadi, S. Abdel-Samad, and Ezzat S. Elshazly. Hot corrosion behavior of ni based inconel 617 and inconel 738 superalloys. *Applied Surface Science*, 378:224–230, 2016.

[73] Epstein. Trends in thermal and propulsive efficiency. 1998.

[74] LJ Espinoza-Pérez, Eddie López-Honorato, and Luis A González. Development of zro2 and ysz coatings deposited by pe-cvd below 800° c for the protection of ni alloys. *Ceramics International*, 46(10):15621–15630, 2020.

[75] Anthony Glyn Evans, DR Mumm, JW Hutchinson, GH Meier, and FS Pettit. Mechanisms controlling the durability of thermal barrier coatings. *Progress in materials science*, 46(5):505–553, 2001.

[76] Zhengjie Fan, Rujia Wang, Xuesong Mei, Xiaofeng Zhang, Xiaomao Sun, Jianlei Cui, Wenqiang Duan, and Wenjun Wang. Microstructure evolution in yttria stabilized zirconia during laser hybrid induction modification. *Journal of Alloys and Compounds*, 810:151898, 2019.

[77] Huanjie Fang, Weize Wang, Jibo Huang, and Dongdong Ye. Investigation of cmas resistance of sacrificial plasma-sprayed mullite-ysz protective layer on 8ysz thermal barrier coating. *Corrosion Science*, 173:108764, 2020.

[78] Francesco Fanicchia. In-situ patch repair of thermal barrier coatings. *PhD Thesis submitted to the University of Nottingham for the degree of Doctor of Philosophy*, 2017.

[79] Yang Feng, Tian-shun Dong, Guo-lu Li, Ran Wang, Guo-zheng Ma, Xiang-wei Zhao, and Qi Liu. The roles of stress in the thermal shock failure of ysz tbcs before and after laser remelting. *Journal of Alloys and Compounds*, 828:154417, 2020.

[80] JM Fishburn, MJ Withford, DW Coutts, and JA Piper. Study of the fluence dependent interplay between laser induced material removal mechanisms in metals: Vaporization, melt displacement and melt ejection. *Applied surface science*, 252(14):5182–5188, 2006.

[81] Marianne M Francois, Amy Sun, Wayne E King, Neil Jon Henson, Damien Tourret, Ccut Allan Bronkhorst, Neil N Carlson, Christopher Kyle Newman, T Haut, Jozsef Bakosi, et al. Modeling of additive manufacturing processes for metals: Challenges and opportunities. *Current Opinion in Solid State and Materials Science*, 21(4):198–206, 2017.

[82] M. Froend, V. Ventzke, F. Dorn, N. Kashaev, B. Klusemann, and J. Enz. Microstructure by design: An approach of grain refinement and isotropy improvement in multi-layer wire-based laser metal deposition. *Materials Science and Engineering A*, 772(November 2019):138635, 2020.

[83] David Furrer and Hans Fecht. Ni-based superalloys for turbine discs. *Jom*, 51(1):14–17, 1999.

[84] Ch A. Gandin and M. Rappaz. A 3d cellular automaton algorithm for the prediction of dendritic grain growth. *Acta Materialia*, 45(5):2187–2195, 1997.

[85] Ch-A Gandin and Michel Rappaz. A coupled finite element-cellular automaton model for the prediction of dendritic grain structures in solidification processes. *Acta metallurgica et materialia*, 42(7):2233–2246, 1994.

[86] Ashish Ganvir. *Microstructure and thermal conductivity of liquid feedstock plasma sprayed thermal barrier coatings*. PhD thesis, University West, 02 2016.

[87] Ashish Ganvir. *Microstructure and thermal conductivity of liquid feedstock plasma sprayed thermal barrier coatings*. PhD thesis, University West, 2016.

[88] Huajian Gao, Xiang Wang, Haimin Yao, Stanislav Gorb, and Eduard Arzt. Mechanics of hierarchical adhesion structures of geckos. *Mechanics of materials*, 37(2-3):275–285, 2005.

[89] JR Vargas Garcia and Takashi Goto. Thermal barrier coatings produced by chemical vapor deposition. *Science and Technology of Advanced Materials*, 4(4):397–402, 2003.

[90] Jacquelynn KM Garofano, Harris L Marcus, and Mark Aindow. Characterization of microstructural effects in a percussion laser-drilled powder metallurgy ni-based superalloy. *Journal of materials science*, 44(2):680–684, 2009.

[91] Jacquelynn KM Garofano, Harris L Marcus, and Mark Aindow. Nanoscale carbide precipitation in the recast layer of a percussion laser-drilled superalloy. *Scripta Materialia*, 61(10):943–946, 2009.

[92] RC Garvie, RH Hannink, and RT Pascoe. Ceramic steel? *Nature*, 258(5537):703, 1975.

[93] M Gell, DN Duhl, DK Gupta, and KD Sheffler. Advanced superalloy airfoils. *JOM*, 39(7):11–15, 1987.

[94] Maurice Gell, Krishnakumar Vaidyanathan, Brent Barber, Jiangtian Cheng, and Eric Jordan. Mechanism of spallation in platinum aluminide/electron beam physical vapor-deposited thermal barrier coatings. *Metallurgical and Materials Transactions A: Physical Metallurgy and Materials Science*, 30(2):427–435, 1999.

[95] Shaoning Geng, Ping Jiang, Lingyu Guo, Xuesong Gao, and Gaoyang Mi. Multi-scale simulation of grain/sub-grain structure evolution during solidification in laser welding of aluminum alloys. *International Journal of Heat and Mass Transfer*, 149, 2020.

[96] S Genna, C Leone, B Palumbo, and F Tagliaferri. Statistical approach to fiber laser microcutting of nimonic® c263 superalloy sheet used in effusion cooling system of aero engines. *Procedia Cirp*, 33:520–525, 2015.

[97] Reza Ghasemi, Reza Shoja-Razavi, Reza Mozafarinia, and Hossein Jamali. Laser glazing of plasma-sprayed nanostructured yttria stabilized zirconia thermal barrier coatings. *Ceramics International*, 39(8):9483–9490, 2013.

[98] Reza Ghasemi, Reza Shoja-Razavi, Reza Mozafarinia, Hossein Jamali, Morteza Hajizadeh-Oghaz, and Raheleh Ahmadi-Pidani. The influence of laser treatment on hot corrosion behavior of plasma-sprayed nanostructured yttria stabilized zirconia thermal barrier coatings. *Journal of the European Ceramic Society*, 34(8):2013–2021, 8 2014.

[99] Partha Sarathi Ghosh, Abhishek Sen, Somnath Chattopadhyaya, Shubham Sharma, and Jujhar Singh. applied sciences prediction of transient temperature distributions for laser welding of dissimilar metals. *applied sciences*, 2021.

[100] Anindya Ghoshal, Michael J. Walock, Muthuvel Murugan, Clara Mock, Luis Bravo, Marc Pepi, Andy Nieto, Andrew Wright, Jian Luo, Nishan Jain, Alison Flatau, and Larry Fehrenbacher. Governing parameters influencing cmas adhesion and infiltration into environmental/thermal barrier coatings in gas turbine engines. *Proceedings of the ASME Turbo Expo*, 6:1–11, 2019.

[101] Dominic Giguère, Gilles Olivié, François Vidal, Stéphanie Toetsch, Guillaume Girard, Tsuneyuki Ozaki, Jean-Claude Kieffer, Ossama Nada, and Isabelle Brunette. Laser ablation threshold dependence on pulse duration for fused silica and corneal tissues: experiments and modeling. *JOSA A*, 24(6):1562–1568, 2007.

[102] C. Giolli, A. Scrivani, G. Rizzi, F. Borgioli, Giovanni Bolelli, and L. Lusvarghi. Failure mechanism for thermal fatigue of thermal barrier coating systems. *Journal of Thermal Spray Technology*, 18(2):223–230, 2009.

[103] Przemysław Golewski and Tomasz Sadowski. The influence of tbc aging on crack propagation due to foreign object impact. *Materials*, 12(9):1488, 2019.

[104] Sheng-kai Gong, Liang Deng, Xiao-fang Bi, and Hui-bin Xu. Thermal barrier effect of ceramic thermal barrier coatings. *Acta Aeronautica et Astronautica Sinica*, 21(164), 2000.

[105] Marek Goral, Radosław Swadźba, and Tadeusz Kubaszek. Tem investigations of tgo formation during cyclic oxidation in two-and three-layered thermal barrier coatings produced using lpps, cvd and ps-pvd methods. *Surface and Coatings Technology*, 394:125875, 2020.

[106] James Edward Gordon. *The new science of strong materials: or why you don't fall through the floor*, volume 27. Princeton University Press, 2006.

[107] Takashi Goto. Thermal barrier coatings deposited by laser cvd. *Surface and Coatings Technology*, 198(1-3):367–371, 2005.

[108] Thomas Götsch, Wolfgang Wallisch, Michael Stöger-Pollach, Bernhard Klötzer, and Simon Penner. From zirconia to yttria: Sampling the ysz phase diagram using sputter-deposited thin films. *Aip Advances*, 6(2):025119, 2016.

[109] Cheng Gu, Colin D. Ridgeway, and Alan A. Luo. Examination of dendritic growth during solidification of ternary alloys via a novel quantitative 3d cellular automaton model. *Metallurgical and Materials Transactions B: Process Metallurgy and Materials Processing Science*, 50(1):123–135, 2019.

[110] Hongbo Guo, Seiji Kuroda, and Hideyuki Murakami. Microstructures and properties of plasma-sprayed segmented thermal barrier coatings. *Journal of the American Ceramic Society*, 89(4):1432–1439, 2006.

[111] Bhupendra K Gupta, Gilbert Farmer, and Alan Walker. Thick thermal barrier coating having grooves for enhanced strain tolerance, 10 1997. US Patent 5,681,616.

[112] E Gyorgy, IN Mihailescu, P Serra, A Perez Del Pino, and JL Morenza. Crown-like structure development on titanium exposed to multipulse nd: Yag

laser irradiation. *Applied Physics A*, 74(6):755–759, 2002.

[113] Morteza Haeri and Mohammad Haeri. Imagej plugin for analysis of porous scaffolds used in tissue engineering. *Journal of Open Research Software*, 3(1), 2015.

[114] Morteza Hajizadeh-Oghaz, Reza Shoja Razavi, and Mohammad Reza Loghman-Estarki. Synthesis and characterization of non-transformable tetragonal ysz nanopowder by means of pechini method for thermal barrier coatings (tbcs) applications. *Journal of sol-gel science and technology*, 70(1):6–13, 2014.

[115] Rihong Han, Wenchao Dong, Shanping Lu, Dianzhong Li, and Yiyi Li. Modeling of morphological evolution of columnar dendritic grains in the molten pool of gas tungsten arc welding. *Computational Materials Science*, 95:351–361, 2014.

[116] Rihong Han, Yiyi Li, and Shanping Lu. Macro-micro modeling and simulation for the morphological evolution of the solidification structures in the entire weld. *International Journal of Heat and Mass Transfer*, 106:1345–1355, 2017.

[117] Rihong Han, Shanping Lu, Wenchao Dong, Dianzhong Li, and Yiyi Li. The morphological evolution of the axial structure and the curved columnar grain in the weld. *Journal of Crystal Growth*, 431:49–59, 2015.

[118] Rihong Han, Shanping Lu, Wenchao Dong, Dianzhong Li, and Yiyi Li. Multi-scale simulation for the columnar to equiaxed transition in the weld pool. *ISIJ International*, 56(6):1003–1012, 2016.

[119] Sang Heon Han, Yeon Seung Lee, JR Cho, and Kyun Ho Lee. Efficiency analysis of air-fuel and oxy-fuel combustion in a reheating furnace. *International Journal of Heat and Mass Transfer*, 121:1364–1370, 2018.

[120] Niels Hansen. Hall-petch relation and boundary strengthening. *Scripta Materialia*, 51(8 SPEC. ISS.):801–806, 2004.

[121] KSKS Sree Harsha. *Principles of vapor deposition of thin films*. Elsevier, 2005.

[122] Ahmet Hasçalık and Mustafa Ay. Co2 laser cut quality of inconel 718 nickel–based superalloy. *Optics and Laser Technology*, 48:554–564, 2013.

[123] D Hasselman, Lloyd F Johnson, Larry D Bentsen, RAHMATHULLAH SYED, HONG LIM LEE, and MICHAEL V SWAIN. Thermal diffusivity and conductivity of dense polycrystalline zr0. *Am. Ceram. Soc. Bull*, 66(5):799–806, 1987.

[124] Wenting He. Deposition mechanisms of thermal barrier coatings (tbcs) manufactured by plasma spray-physical vapor deposition (ps-pvd). 2017.

[125] C Henkes and H Olivier. Flow characterization of a detonation gun facility and first coating experiments. *Journal of thermal spray technology*, 23(5):795–808, 2014.

[126] Sonja Hermann, Nils-Peter Harder, Rolf Brendel, Dirk Herzog, and Heinz Haferkamp. Picosecond laser ablation of sio2 layers on silicon substrates. *Applied Physics A*, 99(1):151–158, 2010.

[127] Arthur H Heuer, R Chaim, and V Lanteri. The displacive cubic→ tetragonal transformation in zro2 alloys. *Acta metallurgica*, 35(3):661–666, 1987.

[128] AD Hewitt. Technology of oxy-fuel gas processes. part 1: General principles involved. 1972.

[129] C. J. Howard, R. J. Hill, and B. E. Reichert. Structures of zro2 polymorphs at room temperature by high-resolution neutron powder diffraction. *Acta Crystallographica Section B*, 44(22):116–120, 1988.

[130] Yingbin Hu, Weilong Cong, Xinlin Wang, Yuanchen Li, Fuda Ning, and Hui Wang. Laser deposition-additive manufacturing of tib-ti composites with novel three-dimensional quasi-continuous network microstructure: effects on strengthening and toughening. *Composites Part B: Engineering*, 133:91–100, 2018.

[131] Yingbin Hu, Fuda Ning, Weilong Cong, Yuanchen Li, Xinlin Wang, and Hui Wang. Ultrasonic vibration-assisted laser engineering net shaping of zro2-al2o3

bulk parts: Effects on crack suppression, microstructure, and mechanical properties. *Ceramics International*, 44(3):2752–2760, 2018.

[132] IATA. Economic per formance of the airline industry. *2020 End-year report*, 2020.

[133] T Ihle and H Muller-Krumbhaar. Fractal and compact growth morphologies in phase transitions with diffusion transport. *Physical Review E*, 49(4):2972, 1994.

[134] Powder Technologies Inc. Elemental composition of and properties of afrl 03 test dust.

[135] R. P. INGEL and D. LEWIS III. Lattice parameters and density for y2o3-stabilized zro2. *Journal of the American Ceramic Society*, 69(4):325–332, 1986.

[136] Nicolau Iralal Morar, Rajkumar Roy, Jorn Mehnen, Sundar Marithumu, Simon Gray, Tracey Roberts, and John Nicholls. Investigation of recast and crack formation in laser trepanning drilling of cmsx-4 angled holes. 2018.

[137] Eric Irissou, Jean-Gabriel Legoux, Anatoly N Ryabinin, Bertrand Jodoin, and Christian Moreau. Review on cold spray process and technology: part i—intellectual property. *Journal of Thermal Spray Technology*, 17(4):495–516, 2008.

[138] Hossein Jamali, Reza Mozafarinia, Reza Shoja-Razavi, and Raheleh Ahmadi-Pidani. Comparison of hot corrosion behaviors of plasma-sprayed nanostructured and conventional ysz thermal barrier coatings exposure to molten vanadium pentoxide and sodium sulfate. *Journal of the European Ceramic Society*, 34(2):485–492, 2014.

[139] Hyung-Jun Jang, Dong-Ho Park, Yeon-Gil Jung, Jung-Chel Jang, Sung-Churl Choi, and Ungyu Paik. Mechanical characterization and thermal behavior of hvof-sprayed bond coat in thermal barrier coatings (tbcs). *Surface and Coatings Technology*, 200(14-15):4355–4362, 2006.

[140] BZ Janos, E Lugscheider, and P Remer. Effect of thermal aging on the erosion resistance of air plasma sprayed zirconia thermal barrier coating. *Surface and Coatings Technology*, 113(3):278–285, 1999.

[141] R. L. Jones. Some aspects of the hot corrosion of thermal barrier coatings. *Journal of Thermal Spray Technology*, 6(1):77–84, 1997.

[142] Eric H Jordan, Chen Jiang, and Maurice Gell. The solution precursor plasma spray (spps) process: a review with energy considerations. *Journal of Thermal Spray Technology*, 24(7):1153–1165, 2015.

[143] Eric H Jordan, L Xie, M Gell, NP Padture, B Cetegen, A Ozturk, X Ma, J Roth, TD Xiao, and PEC Bryant. Superior thermal barrier coatings using solution precursor plasma spray. *Journal of Thermal Spray Technology*, 13(1):57–65, 2004.

[144] Jan Fong Jue and Anil V Virkar. Fabrication, microstructural characterization, and mechanical properties of polycrystalline t'-zirconia. *Journal of the American Ceramic Society*, 73(12):3650–3657, 1990.

[145] Kai Kadau, Jose Antonio Pascual-gutierrez, and Atin Sharma. Turbine component thermal barrier coating with vertically aligned, engineered surface and multifurcated groove features, 3 2018. US Patent App. 15/547,709.

[146] Wang Kai, Peng Hui, Guo Hongbo, and Gong Shengkai. Effect of sintering on thermal conductivity and thermal barrier effects of thermal barrier coatings. *Chinese Journal of Aeronautics*, 25(5):811–816, 2012.

[147] Hyun Wook Kang, Ho Lee, and Ashley J Welch. Laser ablation in a liquid-confined environment using a nanosecond laser pulse. *Journal of Applied physics*, 103(8):083101, 2008.

[148] Jin Kawakita, Hiroshi Katanoda, Makoto Watanabe, Kensuke Yokoyama, and Seiji Kuroda. Warm spraying: An improved spray process to deposit novel coatings. *Surface and Coatings Technology*, 202(18):4369–4373, 2008.

[149] Jin Kawakita, Tadashi Shinohara, Seiji Kuroda, Masato Suzuki, and Satoshi Sodeoka. Fabrication of nano-sized oxide composite coatings and photo-electric conversion/electron storage characteristics. *Surface and Coatings Technology*, 202(16):4028–4035, 2008.

[150] PL Ke, YN Wu, QM Wang, J Gong, C Sun, and LS Wen. Study on thermal barrier coatings deposited by detonation gun spraying. *Surface and Coatings Technology*, 200(7):2271–2276, 2005.

[151] Roger Kelly and Antonio Miotello. Comments on explosive mechanisms of laser sputtering. *Applied Surface Science*, 96:205–215, 1996.

[152] Can Kerse, Hamit Kalaycıoğlu, Parviz Elahi, Barbaros Çetin, Denizhan K Kesim, onder Akçaalan, Seydi Yavaş, Mehmet D Aşık, Bulent oktem, Heinar Hoogland, et al. Ablation-cooled material removal with ultrafast bursts of pulses. *Nature*, 537(7618):84–88, 2016.

[153] A Keyvani, M Saremi, M Heydarzadeh Sohi, and Z Valefi. A comparison on thermomechanical properties of plasma-sprayed conventional and nanostructured ysz tbc coatings in thermal cycling. *Journal of alloys and compounds*, 541:488–494, 2012.

[154] Muhammed Anaz Khan, Muthukannan Duraiselvam, S. S. Panwar, Trilochan Jena, and S. R. Dhineshkumar. Improvement of strain tolerance of functionally graded tbcs through laser surface micro-texturing. *Journal of Materials Science*, 52(2):696–708, 2017.

[155] Muhammed Anaz Khan, Muthukannan Duraiselvam, SS Panwar, Trilochan Jena, and SR Dhineshkumar. Thermo-mechanical characterization of laser textured lamgal11o19/ysz functionally graded thermal barrier coating. *Surface and Coatings Technology*, 321:146–155, 2017.

[156] Y. Khattari, T. El Rhafiki, N. Choab, T. Kousksou, M. Alaphilippe, and Y. Zeraouli. Apparent heat capacity method to investigate heat transfer in a composite phase change material. *Journal of Energy Storage*, 28(August 2019):101239, 2020.

[157] John A. Kilner. Feel the strain. *Nature Materials*, 7(11):838–839, 2008.

[158] Erich H Kisi and CJ Howard. Crystal structures of zirconia phases and their inter-relation. In *Key Engineering Materials*, volume 153, pages 1–36. Trans Tech Publ, 1998.

[159] VI Konov, TV Kononenko, EN Loubnin, F Dausinger, and D Breitling. Pulsed laser deposition of hard coatings in atmospheric air. *Applied Physics A*, 79(4-6):931–936, 2004.

[160] M Konter and M Thumann. Materials and manufacturing of advanced industrial gas turbine components. *Journal of Materials Processing Technology*, 117(3):386–390, 2001.

[161] S. Kou and Y. Le. Welding parameters and the grain structure of weld metal - a thermodynamic consideration. *Metallurgical transactions. A, Physical metallurgy and materials science*, 19 A(4):1075–1082, 1988.

[162] Sindo Kou. *WELDING METALLURGY*. John Wiley and Sons, Inc, 2003.

[163] R Kromer, S Costil, C Verdy, S Gojon, and H Liao. Laser surface texturing to enhance adhesion bond strength of spray coatings–cold spraying, wire-arc spraying, and atmospheric plasma spraying. *Surface and Coatings Technology*, 352:642–653, 2018.

[164] R Kromer, F Mauget, L Despres, S Costil, and J Cormier. Thermo-mechanical fatigue evaluation of a thermal barrier coating bond-coatless system. *Materials Science and Engineering: A*, 756:130–141, 2019.

[165] Robin Kromer, Jonathan Cormier, Sophie Costil, Damien Courapied, Laurent Berthe, and Patrice Peyre. High temperature durability of a bond-coatless plasma-sprayed thermal barrier coating system with laser textured ni-based single crystal substrate. *Surface and Coatings Technology*, 337:168–176, 2018.

[166] Stephan Krämer, James Yang, Carlos G. Levi, and Curtis A. Johnson. Thermochemical interaction of thermal barrier coatings with molten

cao-mgo-al 2o 3-sio 2 (cmas) deposits. *Journal of the American Ceramic Society*, 89(10):3167–3175, 2006.

[167] SI Kudryashov, AA Samokhvalov, EI Ageev, AA Petrov, and VP Veiko. Ultrasonic characterization of dry and wet nanosecond laser ablation of solids. *International Journal of Heat and Mass Transfer*, 127:1095–1100, 2018.

[168] Vijay Kumar and K Balasubramanian. Progress update on failure mechanisms of advanced thermal barrier coatings: A review. *Progress in Organic Coatings*, 90:54–82, 2016.

[169] Chih-Wei Kuo, Yun-Hwei Shen, I-Ming Hung, Shaw-Bing Wen, Huey-Er Lee, and Moo-Chin Wang. Effect of y2o3 addition on the crystal growth and sintering behavior of ysz nanopowders prepared by a sol–gel process. *Journal of alloys and compounds*, 472(1-2):186–193, 2009.

[170] S Kuroda, T Fukushima, and S Kitahara. Generation mechanisms of residual stresses in plasma-sprayed coatings. *Vacuum*, 41(4-6):1297–1299, 1990.

[171] SCTW Kuroda and TW Clyne. The quenching stress in thermally sprayed coatings. *Thin solid films*, 200(1):49–66, 1991.

[172] Seiji Kuroda, Jin Kawakita, Makoto Watanabe, and Hiroshi Katanoda. Warm spraying—a novel coating process based on high-velocity impact of solid particles. *Science and technology of advanced materials*, 2008.

[173] W. Kurz and D.J. Fisher. Fundamentals of solidification. pages 139–140, 1992.

[174] Si Kyaw, Arthur Jones, Mark A.E. Jepson, Tom Hyde, and Rachel C. Thomson. Effects of three-dimensional coating interfaces on thermo-mechanical stresses within plasma spray thermal barrier coatings. *Materials and Design*, 125:189–204, 2017.

[175] Konstantinos Kyprianidis. *Future Aero Engine Designs: An Evolving Vision*, pages 3–24. 11 2011.

[176] JS Langer. Models of pattern formation in first-order phase transitions. In *Directions in Condensed Matter Physics: Memorial Volume in Honor of Shang-Keng Ma*, pages 165–186. World Scientific, 1986.

[177] Petra A Langjahr, Rainer Oberacker, and Michael J Hoffmann. Long-term behavior and application limits of plasma-sprayed zirconia thermal barrier coatings. *Journal of the American Ceramic Society*, 84(6):1301–1308, 2001.

[178] Angel Larrea, Daniel Sola, Miguel Angel Laguna-Bercero, José Ignacio Peña, Rosa Isabel Merino, and VM Orera. Self-supporting thin yttria-stabilised zirconia electrolytes for solid oxide fuel cells prepared by laser machining. *Journal of The Electrochemical Society*, 158(10):B1193, 2011.

[179] Laurent J Lewis and Danny Perez. Laser ablation with short and ultrashort laser pulses: Basic mechanisms from molecular-dynamics simulations. *Applied Surface Science*, 255(10):5101–5106, 2009.

[180] Chang-Jiu Li and Jing-Long Li. Evaporated-gas-induced splashing model for splat formation during plasma spraying. *Surface and Coatings Technology*, 184(1):13–23, 2004.

[181] Fang Li, Xiaoguan Chen, Wenhu Lin, Hua Pan, Xin Jin, and Xueming Hua. Nanosecond laser ablation of al-si coating on boron steel. *Surface and Coatings Technology*, 319:129–135, 2017.

[182] Guang-Rong Li, Li-Shuang Wang, and Guan-Jun Yang. Achieving self-enhanced thermal barrier performance through a novel hybrid-layered coating design. *Materials and Design*, 167:107647, 2019.

[183] Yanping Lian, Zhengtao Gan, Cheng Yu, Dmitriy Kats, Wing Kam Liu, and Gregory J. Wagner. A cellular automaton finite volume method for microstructure evolution during additive manufacturing. *Materials and Design*, 169:107672, 2019.

[184] Bo Liang and Chuanxian Ding. Thermal shock resistances of nanostructured and conventional zirconia coatings deposited by atmospheric plasma spraying.

Surface and Coatings Technology, 197(2-3):185–192, 2005.

[185] Curt H Liebert, Richard E Jacobs, Stephan Stecura, C Robert Morse, Curth Liebert, Richard E Jacobs, Stephan Stecura, and C Robert Morse. Durability of zirconia thermal-barrier ceramic coatings on air-cooled turbine blades in cyclic jet engine operation. *Nasa Technical Memorandum*, (September), 1976.

[186] Rogerio S Lima and Basil Richard Marple. Toward highly sintering-resistant nanostructured zro2-7wt.% y2o3 coatings for tbc applications by employing differential sintering. *Journal of Thermal Spray Technology*, 17(5):846–852, 2008.

[187] RS Lima, A Kucuk, and CC Berndt. Evaluation of microhardness and elastic modulus of thermally sprayed nanostructured zirconia coatings. *Surface and Coatings Technology*, 135(2-3):166–172, 2001.

[188] RS Lima, A Kucuk, and CC Berndt. Integrity of nanostructured partially stabilized zirconia after plasma spray processing. *Materials Science and Engineering: A*, 313(1-2):75–82, 2001.

[189] Dong Rong Liu, Shuhao Wang, and Wentao Yan. Grain structure evolution in transition-mode melting in direct energy deposition. *Materials and Design*, 194:108919, 9 2020.

[190] H Liu, HR Salimi Jazi, M Bussmann, and J Mostaghimi. Experiments and modeling of rapid solidification of plasma-sprayed yttria-stabilized zirconia. *Acta Materialia*, 57(20):6013–6021, 2009.

[191] Huagang Liu, Wenxiong Lin, Zhenyuan Lin, Lingfei Ji, and Minghui Hong. Self-organized periodic microholes array formation on aluminum surface via femtosecond laser ablation induced incubation effect. *Advanced Functional Materials*, 29(42):1903576, 2019.

[192] S-H Liu, Juan P Trelles, Anthony B Murphy, W-T He, Jia Shi, Shan Li, C-J Li, C-X Li, and H-B Guo. Low-pressure plasma-induced physical vapor

deposition of advanced thermal barrier coatings: Microstructures, modelling and mechanisms. *Materials Today Physics*, 21:100481, 2021.

[193] X Liu, D Du, and G Mourou. Laser ablation and micromachining with ultrashort laser pulses. *IEEE journal of quantum electronics*, 33(10):1706–1716, 1997.

[194] Patrick Lorazo, Laurent J Lewis, and Michel Meunier. Short-pulse laser ablation of solids: from phase explosion to fragmentation. *Physical review letters*, 91(22):225502, 2003.

[195] DKY Low, L Li, and AG Corfe. Effects of assist gas on the physical characteristics of spatter during laser percussion drilling of nimonic 263 alloy. *Applied surface science*, 154:689–695, 2000.

[196] Guoxin Lu, David W Sokol, Yongkang Zhang, and Jeff L Dulaney. Nanosecond pulsed laser-generated stress effect inducing macro-micro-nano structures and surface topography evolution. *Applied Materials Today*, 15:171–184, 2019.

[197] A Luz, D Balint, and K Nikbin. A finite element model for tbc damage detection and lifetime prediction. 2008.

[198] Xinqing Ma, Fang Wu, Jeff Roth, Maurice Gell, and Eric H Jordan. Low thermal conductivity thermal barrier coating deposited by the solution plasma spray process. *Surface and Coatings Technology*, 201(7):4447–4452, 2006.

[199] Atsushi Maeda, Yingjun Jin, and Takashi Kuboki. Light press of sheet metal edge for reducing residual stress generated by laser cutting considering mechanical properties and intensity of residual stress. *Journal of Materials Processing Technology*, 225:178–184, 2015.

[200] Satyapal Mahade, Abhilash Venkat, Nicholas Curry, Matthias Leitner, and Shrikant Joshi. Erosion performance of atmospheric plasma sprayed thermal barrier coatings with diverse porosity levels. *Coatings*, 11(1):86, 2021.

[201] Boguslaw Major. Laser processing for surface modification by remelting and alloying of metallic systems. *Materials Surface Processing by Directed Energy*

Techniques, pages 241–274, 2006.

[202] Manuela Martena, D. Botto, P. Fino, S. Sabbadini, M. M. Gola, and C. Badini. Modelling of tbc system failure: Stress distribution as a function of tgo thickness and thermal expansion mismatch. *Engineering Failure Analysis*, 13(3 SPEC. ISS.):409–426, 2006.

[203] MM Martynyuk. Phase explosion of a metastable fluid. *Combustion, Explosion and Shock Waves*, 13(2):178–191, 1977.

[204] Donald M Mattox. *Handbook of physical vapor deposition (PVD) processing*. William Andrew, 2010.

[205] Georg Mauer, Robert Vaßen, and Detlev Stöver. Atmospheric plasma spraying of yttria-stabilized zirconia coatings with specific porosity. *Surface and coatings technology*, 204(1-2):172–179, 2009.

[206] Clare McDaniel, Aiden Flanagan, and Gerard M O'Connor. Evidence for increased incubation parameter in multi-pulse ablation of a pt: Ss alloy using a femtosecond laser at high repetition rates. *Applied surface science*, 295:1–7, 2014.

[207] Oerlikon Metco. Conicraly amdry 995c powder product details.

[208] Oerlikon Metco. Yttria stabilized zirconia metco 204b-ns powder product details.

[209] Robert A Miller. *Analysis of the response of a thermal barrier coating to sodium and vanadium doped combustion gases*. Lewis Research Center, NASA, 1979.

[210] Robert A Miller, James L Smialek, and Ralph G Garlick. Phase stability in plasma-sprayed, partially stabilized zirconia-yttria. 1981.

[211] Antonio Miotello and Roger Kelly. Critical assessment of thermal models for laser sputtering at high fluences. *Applied Physics Letters*, 67(24):3535–3537, 1995.

[212] Kashmiri Lal Mittal and Antonio Pizzi. *Adhesion promotion techniques: technological applications*. CRC Press, 1999.

[213] Hakaru Mizoguchi, Takashi Saitou, and Taku Yamazaki. Development status of high power euv light source development for exposure in semiconductor mass production. *Komatsu Tech. Rep.*, 63:18–24, 2017.

[214] Mohammad Sadegh Mohebbi and Vasily Ploshikhin. Implementation of nucleation in cellular automaton simulation of microstructural evolution during additive manufacturing of al alloys. *Additive Manufacturing*, 36:101726, 2020.

[215] Atieh Moridi, SEYYED MOSTAFA Hassani-Gangaraj, Mario Guagliano, and Ming Dao. Cold spray coating: review of material systems and future perspectives. *Surface Engineering*, 30(6):369–395, 2014.

[216] M. F. Morks, C. C. Berndt, Y. Durandet, M. Brandt, and J. Wang. Microscopic observation of laser glazed yttria-stabilized zirconia coatings. *Applied Surface Science*, 256(21):6213–6218, 2010.

[217] COMSOL Multiphysics. Cfd module user 's guide. *COMSOL Multiphysics*, page 598, 2016.

[218] D. R. Mumm and G. A. Evans. Mechanisms controlling the performance and durability of thermal barrier coatings. *Key Engineering Materials*, 197:199–230, 2001.

[219] Hari Singh Nalwa. *Deposition and processing of thin films*. Academic press, 2002.

[220] Pramoda K Nayak, Chan-Jung Hsu, Sheng-Chang Wang, James C Sung, and Jow-Lay Huang. Graphene coated ni films: a protective coating. *Thin Solid Films*, 529:312–316, 2013.

[221] J. R. Nicholls, M. J. Deakin, and D. S. Rickerby. A comparison between the erosion behaviour of thermal spray and electron beam physical vapour deposition thermal barrier coatings. *Wear*, 233-235:352–361, 1999.

[222] John R Nicholls, Y Jaslier, and DS Rickerby. Erosion and foreign object damage of thermal barrier coatings. In *Materials science forum*, volume 251, pages 935–948. Trans Tech Publ, 1997.

[223] LAUGE FUGLSANG NIELSEN. Elasticity and damping of porous materials and impregnated materials. *Journal of the American Ceramic Society*, 67(2):93–98, 1984.

[224] Andy Nieto, Michael Walock, Anindya Ghoshal, Dongming Zhu, William Gamble, Blake Barnett, Muthuvel Murugan, Marc Pepi, Chris Rowe, and Robert Pegg. Layered, composite, and doped thermal barrier coatings exposed to sand laden flows within a gas turbine engine: Microstructural evolution, mechanical properties, and cmas deposition. *Surface and Coatings Technology*, 349:1107–1116, 2018.

[225] Stephen Norman, Mikhail N Zervas, Andrew Appleyard, Michael K Durkin, Ray Horley, Malcolm P Varnham, Johan Nilsson, and Yoonchan Jeong. Latest development of high-power fiber lasers in spi. In *Fiber Lasers: Technology, Systems, and Applications*, volume 5335, pages 229–237. International Society for Optics and Photonics, 2004.

[226] Hisaichi Ohnabe, Shoju Masaki, Masakazu Onozuka, Kaoru Miyahara, and Tadashi Sasa. Potential application of ceramic matrix composites to aero-engine components. *Composites Part A: Applied Science and Manufacturing*, 30(4):489–496, 1999.

[227] RM Osgood, HH Gilgen, and R Krchnavek. Laser assisted cvd process for vlsi microfabrication. In *Conference on Solid State Devices and Materials*, pages 427–428. Business Cent for Academic Soc Japan, 1984.

[228] Patrick I. O'Toole, Milan J. Patel, Chao Tang, Dayalan Gunasegaram, Anthony B. Murphy, and Ivan S. Cole. Multiscale simulation of rapid solidification of an aluminium–silicon alloy under additive manufacturing conditions. *Additive Manufacturing*, 48(PA):102353, 2021.

[229] Kenjiro Oura, VG Lifshits, AA Saranin, AV Zotov, and M Katayama. *Surface science: an introduction*. Springer Science and Business Media, 2013.

[230] JH Ouyang, S Nowotny, A Richter, and E Beyer. Characterization of laser clad yttria partially-stabilized zro2 ceramic layers on steel 16mncr5. *Surface and Coatings Technology*, 137(1):12–20, 2001.

[231] Zihao Ouyang. Deposition of yttria-stabilized zirconia thermal barrier coatings by laser-assisted plasma coating at atmospheric pressure. 2011.

[232] Zihao Ouyang, Tae-Seung Cho, and David N Ruzic. Deposition of ysz thin films by atmospheric plasma-assisted pulsed laser ablation. *IEEE Transactions on Plasma Science*, 40(11):2850–2852, 2012.

[233] Zihao Ouyang, Liang Meng, Priya Raman, Tae S Cho, and DN Ruzic. Laser-assisted plasma coating at atmospheric pressure: production of yttria-stabilized zirconia thermal barriers. *Journal of Physics D: Applied Physics*, 44(26):265202, 2011.

[234] W Pacquentin, N Caron, and R Oltra. Effect of microstructure and chemical composition on localized corrosion resistance of a aisi 304l stainless steel after nanopulsed-laser surface melting. *Applied Surface Science*, 356:561–573, 2015.

[235] Nitin P. Padture, Maurice Gell, and Eric H. Jordan. Thermal barrier coatings for gas-turbine engine applications. *Science*, 296(5566):280–284, 2002.

[236] NP Padture, KW Schlichting, T Bhatia, A Ozturk, B Cetegen, EH Jordan, M Gell, S Jiang, TD Xiao, PR Strutt, et al. Towards durable thermal barrier coatings with novel microstructures deposited by solution-precursor plasma spray. *Acta materialia*, 49(12):2251–2257, 2001.

[237] Pedram Parandoush and Altab Hossain. A review of modeling and simulation of laser beam machining. *International journal of machine tools and manufacture*, 85:135–145, 2014.

[238] T Patterson, A Leon, B Jayaraj, J Liu, and YH Sohn. Thermal cyclic lifetime and oxidation behavior of air plasma sprayed conicraly bond coats for thermal

barrier coatings. *Surface and Coatings Technology*, 203(5-7):437–441, 2008.

[239] Danny Perez and Laurent J Lewis. Ablation of solids under femtosecond laser pulses. *Physical review letters*, 89(25):255504, 2002.

[240] Danny Perez and Laurent J Lewis. Molecular-dynamics study of ablation of solids under femtosecond laser pulses. *Physical review B*, 67(18):184102, 2003.

[241] Manfred Peters, Bilge Saruhan-Brings, and Uwe Schulz. Advanced coatings for blades of future aero engines. In *Proc. Eur. Air Space Conf*, pages 26–29, 2009.

[242] A Petitbon, L Boquet, and D Delsart. Laser surface sealing and strengthening of zirconia coatings. *Surface and Coatings Technology*, 49(1-3):57–61, 1991.

[243] Jon Petzing, Jeremy Coupland, and Richard K Leach. The measurement of rough surface topography using coherence scanning interferometry. 2010.

[244] Andrew W Phelps and Lynne Pfledderer. Development of a naturalistic test media for dust ingestion cmas testing of gas turbine engines. 2014.

[245] Katherine C Phillips, Hemi H Gandhi, Eric Mazur, and SK Sundaram. Ultrafast laser processing of materials: a review. *Advances in Optics and Photonics*, 7(4):684–712, 2015.

[246] C Piconi and G Maccauro. Zirconia as a ceramic biomaterial. *Biomaterials*, 20(1):1–25, 1999.

[247] Lisa Pin, Florence Ansart, Jean-Pierre Bonino, Yannick Le Maoult, Vanessa Vidal, and Philippe Lours. Processing, repairing and cyclic oxidation behaviour of sol–gel thermal barrier coatings. *Surface and Coatings Technology*, 206(7):1609–1614, 2011.

[248] A. Pineau, G. Guillemot, D. Tourret, A. Karma, and Ch A. Gandin. Growth competition between columnar dendritic grains – cellular automaton versus phase field modeling. *Acta Materialia*, 155:286–301, 2018.

[249] Reeju Pokharel, Anirban Patra, Donald W Brown, Bjørn Clausen, Sven C Vogel, and George T Gray III. An analysis of phase stresses in additively manufactured 304l stainless steel using neutron diffraction measurements and crystal plasticity finite element simulations. *International Journal of Plasticity*, 121:201–217, 2019.

[250] Tresa M Pollock and Sammy Tin. Nickel-based superalloys for advanced turbine engines: chemistry, microstructure and properties. *Journal of propulsion and power*, 22(2):361–374, 2006.

[251] Cristian Porneala and David A Willis. Observation of nanosecond laser-induced phase explosion in aluminum. *Applied physics letters*, 89(21):211121, 2006.

[252] N Eswara Prasad and Russel JH Wanhill. *Aerospace materials and material technologies*, volume 3. Springer, 2017.

[253] Guillaume Pujol, Florence Ansart, Jean-Pierre Bonino, André Malié, and Sarah Hamadi. Step-by-step investigation of degradation mechanisms induced by cmas attack on ysz materials for tbc applications. *Surface and Coatings Technology*, 237:71–78, 2013.

[254] Kobayashi R. Dynamics of interfaces in systems of reaction diffusion (fractals and related topics). *RIMS Kokyuroku*, 614:39–54, 1987.

[255] Ondrej Racek, Christopher C Berndt, DN Guru, and J Heberlein. Nanostructured and conventional ysz coatings deposited using aps and ttpr techniques. *Surface and Coatings Technology*, 201(1-2):338–346, 2006.

[256] Gediminas Raciukaitis, Marijus Brikas, Paulius Gecys, and Mindaugas Gedvilas. Accumulation effects in laser ablation of metals with high-repetition-rate lasers. (May), 2008.

[257] Miladin Radovic, Edgar Lara-Curzio, Rosa M Trejo, H Wang, and Porter. Thermophysical properties of ysz and ni-ysz as a function of temperature and

porosity. *Advances in Solid Oxide Fuel Cells II: Ceramic Engineering and Science Proceedings*, 27(4):79–85, 2009.

[258] Narendran Raghavan, Ryan Dehoff, Sreekanth Pannala, Srdjan Simunovic, Michael Kirka, John Turner, Neil Carlson, and Sudarsanam S Babu. Numerical modeling of heat-transfer and the influence of process parameters on tailoring the grain morphology of in718 in electron beam additive manufacturing. *Acta Materialia*, 112:303–314, 2016.

[259] Mohamed N Rahaman, Jacob R Gross, Rollie E Dutton, and Hsin Wang. Phase stability, sintering, and thermal conductivity of plasma-sprayed zro2–gd2o3 compositions for potential thermal barrier coating applications. *Acta Materialia*, 54(6):1615–1621, 2006.

[260] Michel Rappaz, Ch A Gandin, Jean-Luc Desbiolles, and Ph Thevoz. Prediction of grain structures in various solidification processes. *Metallurgical and Materials Transactions A*, 27(3):695–705, 1996.

[261] Ashok K Ray, DK Das, B Venkataraman, PK Roy, B Goswami, Nilima Roy, SK Das, N Parida, S Tarafder, S Chaudhuri, et al. Characterization of rupture and fatigue resistance of tbc superalloy for combustion liners. *Materials Science and Engineering: A*, 405(1-2):194–200, 2005.

[262] André Reck, André Till Zeuner, and Martina Zimmermann. Fatigue behavior of non-optimized laser-cut medical grade ti-6al-4v-eli sheets and the effects of mechanical post-processing. *Metals*, 9(8):843, 2019.

[263] Roger C Reed. *The superalloys: fundamentals and applications*. Cambridge university press, 2008.

[264] Gunther Richter, Karla Hillerich, Daniel S Gianola, Reiner Monig, Oliver Kraft, and Cynthia A Volkert. Ultrahigh strength single crystalline nanowhiskers grown by physical vapor deposition. *Nano Letters*, 9(8):3048–3052, 2009.

[265] Joseph David Rigney and Ramgopal Darolia. Thermal barrier coating with improved erosion and impact resistance and process therefor, 9 2003. US Patent 6,620,525.

[266] Frank L Riley. *Structural ceramics: fundamentals and case studies*. Cambridge University Press, 2009.

[267] Ibiye Aseibichin Roberts, CJ Wang, R Esterlein, M Stanford, and DJ Mynors. A three-dimensional finite element analysis of the temperature field during laser melting of metal powders in additive layer manufacturing. *International Journal of Machine Tools and Manufacture*, 49(12-13):916–923, 2009.

[268] Theron M. Rodgers, Jonathan D. Madison, and Veena Tikare. Simulation of metal additive manufacturing microstructures using kinetic monte carlo. *Computational Materials Science*, 135:78–89, 2017.

[269] Theron M Rodgers, Jonathan D Madison, Veena Tikare, and Michael C Maguire. Predicting mesoscale microstructural evolution in electron beam welding. *Jom*, 68(5):1419–1426, 2016.

[270] M. Rolchigo. Use of cellular automata-based methods for understanding material-process-microstructure relations in alloy-based additive processes. *Thesis*, pages 1–30, 2018.

[271] M. R. Rolchigo and R. LeSar. Application of alloy solidification theory to cellular automata modeling of near-rapid constrained solidification. *Computational Materials Science*, 163(December 2018):148–161, 2019.

[272] Rolls-Royce. The all-new rolls-royce trent 7000. *Airinsight*, 322(10):891–921, 2014.

[273] Rolls-Royce. Flare - 'flame spray adder for in-situ patch repair of aero-engine combustors'. *UK Research and Innovation*, 322(10):891–921, 2015.

[274] Andrew R Roosen and Jean E Taylor. Modeling crystal growth in a diffusion field using fully faceted interfaces. *Journal of computational physics*, 114(1):113–128, 1994.

[275] Daniel Rosenthal. The theory of moving sources of heat and its application of metal treatments. *Transactions of ASME*, 68:849–866, 1946.

[276] Francesco Ruffino and Maria Grazia Grimaldi. Nanostructuration of thin metal films by pulsed laser irradiations: A review. *Nanomaterials*, 9(8):1133, 2019.

[277] Y Saito, G Goldbeck-Wood, and H Muller-Krumbhaar. Numerical simulation of dendritic growth. *Physical Review A*, 38(4):2148, 1988.

[278] S Sampath, X Jiang, A Kulkarni, J Matejicek, DL Gilmore, and RA Neiser. Development of process maps for plasma spray: case study for molybdenum. *Materials Science and Engineering: A*, 348(1-2):54–66, 2003.

[279] Uwe Schulz. Phase transformation in eb-pvd yttria partially stabilized zirconia thermal barrier coatings during annealing. *Journal of the American Ceramic Society*, 83(4):904–910, 2000.

[280] Uwe Schulz, Bilge Saruhan, Klaus Fritscher, and Christoph Leyens. Review on advanced eb-pvd ceramic topcoats for tbc applications. *International Journal of Applied Ceramic Technology*, 1(4):302–315, 2004.

[281] Carsten Schäfer, Herbert M. Urbassek, and V. Leonid Zhigilei. Metal ablation by picosecond laser pulses: A hybrid simulation. *Physical Review B - Condensed Matter and Materials Physics*, 66(11):1154041–1154048, 2002.

[282] HG Scott. Phase relationships in the zirconia-yttria system. *Journal of materials science*, 10(9):1527–1535, 1975.

[283] I. P. Semenova, R. Z. Valiev, E. B. Yakushina, G. H. Salimgareeva, and T. C. Lowe. Strength and fatigue properties enhancement in ultrafine-grained ti produced by severe plastic deformation. *Journal of Materials Science*, 43(23-24):7354–7359, 2008.

[284] HK Sezer, L Li, M Schmidt, AJ Pinkerton, B Anderson, and P Williams. Effect of beam angle on haz, recast and oxide layer characteristics in laser

drilling of tbc nickel superalloys. *International Journal of Machine Tools and Manufacture*, 46(15):1972–1982, 2006.

[285] Benjamin Shassere, Duncan Greeley, Alfred Okello, Michael Kirka, Peeyush Nandwana, and Ryan Dehoff. Correlation of microstructure to creep response of hot isostatically pressed and aged electron beam melted inconel 718. *Metallurgical and Materials Transactions A: Physical Metallurgy and Materials Science*, 49(10):5107–5117, 2018.

[286] Yumeng Shi, Wu Zhou, Ang-Yu Lu, Wenjing Fang, Yi-Hsien Lee, Allen Long Hsu, Soo Min Kim, Ki Kang Kim, Hui Ying Yang, Lain-Jong Li, et al. van der waals epitaxy of mos2 layers using graphene as growth templates. *Nano letters*, 12(6):2784–2791, 2012.

[287] Kentaro Shinoda, Yoichi Kojima, and Toyonobu Yoshida. In situ measurement system for deformation and solidification phenomena of yttria-stabilized zirconia droplets impinging on quartz glass substrate under plasma-spraying conditions. *Journal of thermal spray technology*, 14(4):511–517, 2005.

[288] AK Singh, TRG Kutty, and Sucharita Sinha. Pulsed laser deposition of corrosion protective yttrium oxide (y2o3) coating. *Journal of Nuclear Materials*, 420(1-3):374–381, 2012.

[289] H Singh, BS Sidhu, D Puri, and S Prakash. Use of plasma spray technology for deposition of high temperature oxidation/corrosion resistant coatings–a review. *Materials and Corrosion*, 58(2):92–102, 2007.

[290] Dalip Singh Mehta and Vishal Srivastava. Quantitative phase imaging of human red blood cells using phase-shifting white light interference microscopy with colour fringe analysis. *Applied Physics Letters*, 101(20):203701, 2012.

[291] JG Smeggil. Some comments on the role of yttrium in protective oxide scale adherence. *Materials Science and Engineering*, 87:261–265, 1987.

[292] JL Smialek, DT Jayne, JC Schaeffer, and WH Murphy. Effects of hydrogen annealing, sulfur segregation and diffusion on the cyclic oxidation resistance

of superalloys: a review. *Thin solid films*, 253(1-2):285–292, 1994.

[293] Y. H. Sohn, K. Vaidyanathan, M. Ronski, E. H. Jordan, and M. Gell. Thermal cycling of eb-pvd/mcraly thermal barrier coatings: Ii. evolution of photo-stimulated luminescence. *Surface and Coatings Technology*, 146-147:102–109, 2001.

[294] Thomas Sourmail. Coatings for high-temperature application. 2009.

[295] Gosipathala Sreedhar, MD Masroor Alam, and V. S. Raja. Hot corrosion behaviour of plasma sprayed ysz/al2o3 dispersed nicraly coatings on inconel-718 superalloy. *Surface and Coatings Technology*, 204(3):291–299, 2009.

[296] Akella Srikanth, G Mohammed Thalib Basha, and B Venkateshwarlu. A brief review on cold spray coating process. *Materials Today: Proceedings*, 22:1390–1397, 2020.

[297] Mihai Stafe, Aurelian Marcu, and Niculae N Puscas. Material removal and deposition by pulsed laser ablation and associated phenomena. In *Pulsed Laser Ablation of Solids*, pages 143–214. Springer, 2014.

[298] Stephan Stecura. Two-layer thermal barrier coating for turbine airfoils-furnace and burner rig test results. 1976.

[299] MJ Stiger, NM Yanar, MG Topping, FS Pettit, and GH Meier. Thermal barrier coatings for the 21st century. *Zeitschrift fur Metallkunde*, 90(12):1069–1078, 1999.

[300] Donna Strickland and Gerard Mourou. Compression of amplified chirped optical pulses. *Optics communications*, 55(6):447–449, 1985.

[301] EC Subbarao. Ceramic dielectrics for capacitors. *Ferroelectrics*, 35(1):143–148, 1981.

[302] Ramesh Subramanian. Segmented thermal barrier coating and method of manufacturing the same, 3 2004. US Patent 6,703,137.

[303] X. K. Sun, Jian Zhang, Yelong Chu, Wei Liu, Baozhi Cui, and Zhidong Zhang. Dependence of magnetic properties on grain size of α-fe in nanocomposite (nd, dy)(fe, co, nb, b)5.5/α-fe magnets. *Applied Physics Letters*, 74(12):1740–1742, 1999.

[304] Josefine Svenungsson, Isabelle Choquet, and Alexander F.H. Kaplan. Laser welding process - a review of keyhole welding modelling. *Physics Procedia*, 78(August):182–191, 2015.

[305] RJ Takahashi, JMK Assis, F Piorino Neto, and DAP Reis. Heat treatment for tgo growth on nicraly for tbc application. *Materials Research Express*, 6(12):126442, 2020.

[306] Wenda Tan and Yung C. Shin. Multi-scale modeling of solidification and microstructure development in laser keyhole welding process for austenitic stainless steel. *Computational Materials Science*, 98:446–458, 2015.

[307] Kirubel Teferra and David J. Rowenhorst. Optimizing the cellular automata finite element model for additive manufacturing to simulate large microstructures. *Acta Materialia*, 213:116930, 2021.

[308] W. A. Tiller, K. A. Jackson, J. W. Rutter, and B. Chalmers. The redistribution of solute atoms during the solidification of metals. *Acta Metallurgica*, 1(4):428–437, 1953.

[309] W Tillmann, I Baumann, P Hollingsworth, and I-A Laemmerhirt. Influence of the spray angle on the properties of hvof sprayed wc–co coatings using (- 10+ 2 um) fine powders. *Journal of thermal spray technology*, 22(2-3):272–279, 2013.

[310] Jorge Torres-Rodríguez, Jozsef Kalmar, Melita Menelaou, Ladislav Čelko, Karel Dvořak, Jaroslav Cihlář, Jaroslav Cihlař Jr, Jozef Kaiser, Enikő Győri, Péter Veres, et al. Heat treatment induced phase transformations in zirconia and yttria-stabilized zirconia monolithic aerogels. *The Journal of Supercritical Fluids*, 149:54–63, 2019.

[311] E Toyserkani and N Rasti. Ultrashort pulsed laser surface texturing. pages 441–453, 2015.

[312] Z. T. Trautt and Y. Mishin. Capillary-driven grain boundary motion and grain rotation in a tricrystal: A molecular dynamics study. *Acta Materialia*, 65:19–31, 2014.

[313] JP Trelles and JVR Heberlein. Simulation results of arc behavior in different plasma spray torches. *Journal of thermal spray technology*, 15(4):563–569, 2006.

[314] R Trivedi and W Kurz. Dendritic grpwth. *International Materials Reviews*, 39(2):49–74, 1994.

[315] P. C. Tsai, J. H. Lee, and C. S. Hsu. Hot corrosion behavior of laser-glazed plasma-sprayed yttria-stabilized zirconia thermal barrier coatings in the presence of v2o5. *Surface and Coatings Technology*, 201(9-11 SPEC. ISS.):5143–5147, 2007.

[316] PC Tsai, HL Tsai, and David C Tu. Study of processing variables in laser glazing plasma-sprayed thermal barrier coatings. *Materials Science and Engineering: A*, 165(2):167–173, 1993.

[317] Pi Chuen Tsai, Jiing Herng Lee, and Chi Lung Chang. Improving the erosion resistance of plasma-sprayed zirconia thermal barrier coatings by laser glazing. *Surface and Coatings Technology*, 202(4-7):719–724, 2007.

[318] Koji Tsukuma, Kuniyoshi Ueda, and Masahiko Shimada. Strength and fracture toughness of isostatically hot-pressed composites of al2o3 and y2o3-partially-stabilized zro2. *Journal of the American Ceramic Society*, 68(1):C–4, 1985.

[319] RC Tucker Jr. Introduction to coating design and processing. *Thermal Spray Technology*, 5:76–88, 2013.

[320] SPI Lasers UK. Sp-100c-0013-r0006 product manual. 2005.

[321] SPI Lasers UK. G3.0 pulsed fibre laser, technical report. 2007.

[322] Marc Ullmann, Sheldon K Friedlander, and Andreas Schmidt-Ott. Nanoparticle formation by laser ablation. *Journal of Nanoparticle Research*, 4(6):499–509, 2002.

[323] A Van der Drift. Evolutionary selection, a principle governing growth orientation in vapour-deposited layers. *Philips Res. Rep*, 22(3):267, 1967.

[324] G Van Tendeloo and S Amelinckx. Group-theoretical considerations concerning domain formation in ordered alloys. *Acta Crystallographica Section A: Crystal Physics, Diffraction, Theoretical and General Crystallography*, 30(3):431–440, 1974.

[325] Robert Vassen, Maria Ophelia Jarligo, Tanja Steinke, Daniel Emil Mack, and Detlev Stover. Overview on advanced thermal barrier coatings. *Surface and Coatings Technology*, 205(4):938–942, 2010.

[326] Robert Vaßen, Franziska Traeger, and Detlev Stöver. Correlation between spraying conditions and microcrack density and their influence on thermal cycling life of thermal barrier coatings. *Journal of Thermal Spray Technology*, 13(3):396–404, 2004.

[327] Gnanamoorthi Venkadesan and Jayaram Muthusamy. Experimental investigation of al2o3/8ysz and ceo2/8ysz plasma sprayed thermal barrier coating on diesel engine. *Ceramics International*, 45(3):3166–3176, 2019.

[328] Céline Viazzi, Jean-Pierre Bonino, and Florence Ansart. Synthesis by sol-gel route and characterization of yttria stabilized zirconia coatings for thermal barrier applications. *Surface and Coatings Technology*, 201(7):3889–3893, 2006.

[329] Céline Viazzi, Jean-Pierre Bonino, Florence Ansart, and Antoine Barnabé. Structural study of metastable tetragonal ysz powders produced via a sol–gel route. *Journal of Alloys and Compounds*, 452(2):377–383, 2008.

[330] Tamás Vicsek. Pattern formation in diffusion-limited aggregation. *Physical Review Letters*, 53(24):2281–2284, 1984.

[331] M. H. Vidal-Setif, N. Chellah, C. Rio, C. Sanchez, and O. Lavigne. Calcium-magnesium-alumino-silicate (cmas) degradation of eb-pvd thermal barrier coatings: Characterization of cmas damage on ex-service high pressure blade tbcs. *Surface and Coatings Technology*, 208:39–45, 2012.

[332] Vaughan R Voller, CR Swaminathan, and Brian G Thomas. Fixed grid techniques for phase change problems: a review. *International Journal for Numerical Methods in Engineering*, 30(4):875–898, 1990.

[333] Konstantin Von Niessen and Malko Gindrat. Plasma spray-pvd: a new thermal spray process to deposit out of the vapor phase. *Journal of thermal spray technology*, 20(4):736–743, 2011.

[334] Kunihiko Wada, Norio Yamaguchi, and Hideaki Matsubara. Effect of substrate rotation on texture evolution in zro2-4 mol.% y2o3 layers fabricated by eb-pvd. *Surface and coatings technology*, 191(2-3):367–374, 2005.

[335] Kunihiko Wada, Norio Yamaguchi, and Hideakis Matsubara. Microstructure modification of yttria-stabilized zirconia layers prepared by eb-pvd. *Journal of the Ceramic Society of Japan*, 111(1300):883–889, 2003.

[336] Anja M Waetjen, Dominik A Polsakiewicz, Ingo Kuhl, Rainer Telle, and Horst Fischer. Slurry deposition by airbrush for selective laser sintering of ceramic components. *Journal of the European Ceramic Society*, 29(1):1–6, 2009.

[337] a RS Wagner and s WC Ellis. Vapor-liquid-solid mechanism of single crystal growth. *Applied physics letters*, 4(5):89–90, 1964.

[338] Dongsheng Wang, Zongjun Tian, Lida Shen, Zhidong Liu, and Yinhui Huang. Effects of laser remelting on microstructure and solid particle erosion characteristics of zro2-7wtplasma spraying. *Ceramics International*, 40(6):8791–8799, 2014.

[339] Houxiao Wang, Sukai Zhu, Guoxiang Xu, Wei Zhou, Lin Li, Dao Hua Zhang, Naifei Ren, Kaibo Xia, and Chunhui Shi. Influence of ultrasonic vibration on

percussion drilling performance for millisecond pulsed nd: Yag laser. *Optics and Laser Technology*, 104:133–139, 2018.

[340] Li Wang, Yuelan Di, Haidou Wang, Yuncai Zhao, and Shuai Li. On crack evolution with texturization of bonding layer in thermal barrier coating. *Journal of the European Ceramic Society*, 2021.

[341] N Wang, S Mokadem, M Rappaz, and W Kurz. Solidification cracking of superalloy single-and bi-crystals. *Acta Materialia*, 52(11):3173–3182, 2004.

[342] Xuezhi Wang, Wei Huang, Chao Zhu, Qingying Chen, Srikanth Pilla, and Gongying Liang. Porosity effects on oxygen ions diffusion in the yttria-stabilized zirconia (ysz) by molecular dynamics simulation. *Journal of Molecular Liquids*, 265:31–35, 2018.

[343] Yan Wang, Geoffrey Darut, Xiao Tao Luo, Thierry Poirier, Jorge Stella, Hanlin Liao, and Marie Pierre Planche. Influence of preheating processes on the microstructure of laser glazed ysz coatings. *Ceramics International*, 43(5):4606–4611, 2017.

[344] Yazhao Wang, Zhonghua Zhu, Shengdi Ta, Zeyu Cheng, Peng Zhang, Ninghan Zeng, Bernard Albert Goodman, Shoulei Xu, and Wen Deng. Optical properties of yttria-stabilized zirconia single-crystals doped with terbium oxide. *Crystals*, 12(8):1081, 2022.

[345] Rudolf Weber, Thomas Graf, Peter Berger, Volkher Onuseit, Margit Wiedenmann, Christian Freitag, and Anne Feuer. Heat accumulation during pulsed laser materials processing. 22(9):5279–5284, 2014.

[346] H. L. Wei, J. W. Elmer, and T. DebRoy. Three-dimensional modeling of grain structure evolution during welding of an aluminum alloy. *Acta Materialia*, 126:413–425, 2017.

[347] H. L. Wei, J. Mazumder, and T. DebRoy. Evolution of solidification texture during additive manufacturing. *Scientific Reports*, 5(1):1–7, 2015.

[348] HL Wei, JW Elmer, and Tarasankar DebRoy. Origin of grain orientation during solidification of an aluminum alloy. *Acta Materialia*, 115:123–131, 2016.

[349] HL Wei, JW Elmer, and Tarasankar DebRoy. Crystal growth during keyhole mode laser welding. *Acta Materialia*, 133:10–20, 2017.

[350] J Wei, Y Ye, Z Sun, L Liu, and G Zou. Control of the kerf size and microstructure in inconel 738 superalloy by femtosecond laser beam cutting. *Applied Surface Science*, 370:364–372, 2016.

[351] RG Wellman and JR Nicholls. A review of the erosion of thermal barrier coatings. *Journal of Physics D: Applied Physics*, 40(16):R293, 2007.

[352] Richard G Wellman, MJ Deakin, and JR Nicholls. The effect of tbc morphology on the erosion rate of eb pvd tbcs. *Wear*, 258(1-4):349–356, 2005.

[353] G Weyl, A Pirri, and R Root. Laser ignition of plasma off aluminum surfaces. *AIAA Journal*, 19(4):460–469, 1981.

[354] BD White, O Kesler, and Lars Rose. Air plasma spray processing and electrochemical characterization of sofc composite cathodes. *Journal of Power Sources*, 178(1):334–343, 2008.

[355] Douglas E Wolfe, Jogender Singh, and Krishnan Narasimhan. Synthesis and characterization of multilayered tic/tib2 coatings deposited by ion beam assisted, electron beam–physical vapor deposition (eb–pvd). *Surface and Coatings Technology*, 165(1):8–25, 2003.

[356] YN Wu, FH Wang, WG Hua, J Gong, C Sun, and LS Wen. Oxidation behavior of thermal barrier coatings obtained by detonation spraying. *Surface and Coatings Technology*, 166(2-3):189–194, 2003.

[357] Feiyu Xiong, Chenyang Huang, Orion L. Kafka, Yanping Lian, Wentao Yan, Mingji Chen, and Daining Fang. Grain growth prediction in selective electron beam melting of ti-6al-4v with a cellular automaton method. *Materials and Design*, 199:109410, 2021.

[358] Junzhen Xiong, Xinqi Yang, Wei Lin, and Kaixuan Liu. Evaluation of inhomogeneity in tensile strength and fracture toughness of underwater wet friction taper plug welded joints for low-alloy pipeline steels. *Journal of Manufacturing Processes*, 32:280–287, 2018.

[359] S. Q. Xu, C. Zhu, and Y. Zhang. Effects of laser remelting and oxidation on nicraly/8y2o3-zro2 thermal barrier coatings. *Journal of Thermal Spray Technology*, 27(3):412–422, 2018.

[360] Cong Yang, Qingyan Xu, and Baicheng Liu. Gpu-accelerated three-dimensional phase-field simulation of dendrite growth in a nickel-based superalloy. *Computational Materials Science*, 136:133–143, 2017.

[361] T-Y Brian Yang, William L Kruer, and M Richard. More and a. bruce langdon. absorption of laser light in overdense plasmas by sheath inverse bremsstrahlung. *Phys. Plasmas*, 2:3146–3154, 1995.

[362] Tao Yang, Enhui Wang, Fuqiang Wang, Kuochih Chou, and Xinmei Hou. Fabrication of ordered mullite nanowhisker array with surface enhanced raman scattering effect. *Scientific reports*, 5(1):1–7, 2015.

[363] Bekir Sami Yilbas, SS Akhtar, and C Karatas. Laser hole cutting into ti-6al-4v alloy and thermal stress analysis. *The International Journal of Advanced Manufacturing Technology*, 59(9):997–1008, 2012.

[364] BS Yilbas, SS Akhtar, and C Karatas. Laser trepanning of a small diameter hole in titanium alloy: temperature and stress fields. *Journal of Materials Processing Technology*, 211(7):1296–1304, 2011.

[365] Bo-Shi Yuan, Di Wang, Yuan Dong, Wei Zhang, and Guang-Yong Jin. Experimental study of the morphological evolution of the millisecond–nanosecond combined-pulse laser ablation of aluminum alloy. *Applied optics*, 57(20):5743–5748, 2018.

[366] I. Zaplatynsky. Performance of laser-glazed zirconia thermal barrier coatings in cyclic oxidation and corrosion burner rig tests. *Thin Solid Films*,

95(3):275–284, 1982.

[367] I Zaplatynsky. The effect of laser glazing on life of zr02 tbc's in cyclic burner rig tests. 1986.

[368] Zane Zelča, Silvija Kukle, and Jānis Kajaks. Short natural fibers reinforced polyolefin composites. *Materials Science. Textile and Clothing Technology*, 11:6–11, 2016.

[369] T. Zhai, X. P. Jiang, J. X. Li, M. D. Garratt, and G. H. Bray. The grain boundary geometry for optimum resistance to growth of short fatigue cracks in high strength al-alloys. *International Journal of Fatigue*, 27(10-12):1202–1209, 2005.

[370] M Zhang, M Yu Efremov, F Schiettekatte, EA Olson, AT Kwan, SL Lai, T Wisleder, JE Greene, and LH Allen. Size-dependent melting point depression of nanostructures: Nanocalorimetric measurements. *Physical Review B*, 62(15):10548, 2000.

[371] Panpan Zhang, Fuhai Li, Xiaofeng Zhang, Zhihui Zhang, Feifei Zhou, Luquan Ren, and Min Liu. Thermal shock resistance of thermal barrier coatings with different surface shapes modified by laser remelting. *Journal of Thermal Spray Technology*, 28(3):417–432, 2019.

[372] Qi Zhang, Daniel Sando, and Valanoor Nagarajan. Chemical route derived bismuth ferrite thin films and nanomaterials. *Journal of Materials Chemistry C*, 4(19):4092–4124, 2016.

[373] XB ZHANG, W ZHANG, et al. Laser-induced ablation and laser drilling of dd6 nickel-based single-crystal alloy by nanosecond and picosecond lasers. *Applied laser*, 34(6):551–556, 2014.

[374] Xiancheng Zhang, Makoto Watanabe, and Seiji Kuroda. Effects of residual stress on the mechanical properties of plasma-sprayed thermal barrier coatings. *Engineering Fracture Mechanics*, 110(4):314–327, 2013.

[375] Lidong Zhao, Klaus Seemann, Arne Fischer, and Erich Lugscheider. Study on atmospheric plasma spraying of al2o3 using on-line particle monitoring. *Surface and Coatings Technology*, 168(2-3):186–190, 2003.

[376] Wanqin Zhao and Zhishui Yu. Self-cleaning effect in high quality percussion ablating of cooling hole by picosecond ultra-short pulse laser. *Optics and Lasers in Engineering*, 105:125–131, 2018.

[377] X Zhao, X Wang, and P Xiao. Sintering and failure behaviour of eb-pvd thermal barrier coating after isothermal treatment. *Surface and Coatings Technology*, 200(20-21):5946–5955, 2006.

[378] B Zheng, Y Zhou, JE Smugeresky, JM Schoenung, and EJ Lavernia. Thermal behavior and microstructural evolution during laser deposition with laser-engineered net shaping: Part i. numerical calculations. *Metallurgical and materials transactions A*, 39(9):2228–2236, 2008.

[379] Lei Zheng, Zhang Maicang, and Dong Jianxin. Hot corrosion behavior of powder metallurgy rene95 nickel-based superalloy in molten nacl-na2so4 salts. *Materials and Design*, 32(4):1981–1989, 2011.

[380] Leonid V Zhigilei, Zhibin Lin, and Dmitriy S Ivanov. Atomistic modeling of short pulse laser ablation of metals: connections between melting, spallation, and phase explosion. *The Journal of Physical Chemistry C*, 113(27):11892–11906, 2009.

[381] X Zhong, Y Wang, Z Xu, Y Zhang, J Zhang, and X Cao. Influence of laser-glazing on hot corrosion resistance of yttria-stabilized zirconia tbc in molten salt mixture of v2o5 and na2so4. *Materials and corrosion*, 60(11):882–888, 2009.

[382] Kai-Ge Zhou, Freddie Withers, Yang Cao, Sheng Hu, Geliang Yu, and Cinzia Casiraghi. Raman modes of mos2 used as fingerprint of van der waals interactions in 2-d crystal-based heterostructures. *ACS nano*, 8(10):9914–9924, 2014.

[383] D. Zhu and R.A. Miller. Sintering and creep behavior of plasma-sprayed zirconia- and hafnia-based thermal barrier coatings. *Surface and Coatings Technology*, 108-109(1-3):114–120, 1998.